Nano Studies

12

2015

Nano Studies

12

2015

Nano Studies, 2015, 12

UDG [53 + 54 + 620.22] (051.2)
N – 21

Nano Studies is a biannual scientific journal published in Georgia.

Nano Studies' topics of interest include Nanoscience and Nanotechnology, and related problems of Physics, Chemistry and Materials Science.

Nano Studies publish following categories of scientific articles: research papers, communications, reviews and discussions.

Nano Studies publish scientific articles in English and also in Georgian and in Russian.

Summaries of all the articles of **Nano Studies** are referred in **Georgian Abstracts Journal** and are accessible in **Tech Inform** (Georgia's Central Institute for Scientific and Technical Information) database: **http://www.tech.caucasus.net**

Full-texts of articles published in **Nano Studies** are free-accessible at the journal's web-site: **www.NanoStudies.org**

Editor & Publisher: **Levan Chkhartishvili**
Editorial Assistant: **Tamar Berberashvili**

Address of Editorial Office: **Department of Engineering Physics**
Georgian Technical University
Campus 4, Room 307
77 Merab Kostava Avenue
Tbilisi, 0175, Georgia
www.NanoStudies.org

E-mail: **chkharti2003@yahoo.com**
Phone: **995 322 37 19 42**
Mobile: **995 599 34 07 36**

Publishing House **Nekeri**

ISSN 1987 – 8826

CONTENTS

Proceedings of the ICANM 2015: International Conference & Exhibition on Advanced & Nano Materials (August10–12, 2015, Ottawa, Ontario, Canada)

Regular Papers

Science History Pages

Chronicle

POLYETHERIMIDE–GRAPHENE COMPOSITE FOR CORROSION PROTECTION OF STAINLESS STEEL 304

H. Alhumade, A. Yu, A. Elkamel

University of Waterloo
Department of Chemical Engineering
Waterloo, Ontario, Canada
halhumade@uwaterloo.ca

Accepted October 19, 2015

Abstract

Polyetherimide–Graphene is investigated as corrosion protection coating on a Stainless Steel 304 substrate. Graphene is incorporated in the polymeric matrix using the in-situ polymerization approach. The dispersion of the filler is observed using Scanning Electron Microscopy and Transmission Electron Microscopy. The graphene based composite is cured by thermal imidization under vacuum to avoid degradation of the hosting polymer. The influences of incorporating graphene in the corrosion protection property of the hosting polymer in addition to the long-term performance of the protective coating are investigated. It was concluded that the addition of graphene may enhance the corrosion inhibition of stainless steel at a very low loading of the filler. This finding is supported by the observed results after conducting electrochemical techniques such as Tafel polarization and electrochemical impedance spectroscopy. Adhesion of the protective coating to the metal substrate is evaluated before and after 30 days of exposure to a 3.5 wt. % NaCl corrosive medium in order to confirm the long-time performance of the coating.

1. Introduction

The deterioration of metals due to the electrochemical reactions that take place between the metals and the surrounding is a phenomenon known as corrosion. This electrochemical process causes threats to both economy and industry in various fields. Therefore, an increasing number of studies have focused on approaches to mitigate corrosion in different environments. One of these approaches is designing a hybrid coating material that can extend the lifetime of various materials by attenuating the corrosion rates and also add to the valuable mechanical properties of the coated materials. Various coatings materials such as nanocomposites, hydrophobic and also organic-inorganic coatings have already excelled in mitigating corrosion on different metals substrates [1]. The use of protective coating to extend the lifespan of materials is a widely utilized technique is fields such as pipeline, construction and automobile industry. Stainless Steel 304 (SS304) is one of those metals that are extensively utilized in industry and this is attributed to the valuable properties of SS304 such as the significant thermal and electrical conductivity, corrosion resistance in addition to the fact that SS304 is formable and wieldable [2]. However, in a chloride rich environment, studies revealed that SS304 may corrode more intensively [3].

In polymeric composites, the fillers materials may act as barriers that shield corrosive agents such as water and oxygen molecules. Furthermore, the incorporation of fillers in a polymeric matrix may add to the various mechanical properties of the coated materials especially when organic-inorganic composites are formed. Clays, nanotubes and silicon dioxide are examples of nanofillers can be found in various forms such as layer, tubular and spherical. A number of materials have been tested as protective coatings however; the lack of adhesion between at the interface between the protective material and the metals substrates is what limit the use of such protective coatings in certain mediums [4]. Polyetherimide (PEI) has already been utilized to mitigate corrosion and this is attributed the substantial adhesion property of the material to various metals substrates. In addition to adhesion, PEI is chemically stable, has low dielectric constant and thermal expansion coefficient [5]. The combination of these valuable properties made PEI an ideal coating material for corrosion inhibition purposes. However, these valuable properties might be enhanced by the incorporation of fillers in the polymeric matrix.

Graphene is widely utilized in manufacturing of polymers composites for different purposes. This can be attributed to advantages properties of graphene such as low density and high aspect ratio over other fillers such as clay [6]. Studies have revealed that graphene may enhance mechanical, thermal and dielectric properties of different polymers in addition to gas permeability and corrosion protection [7]. In this study, PEI–G (PEI/G) composites are synthesized and tested as corrosion protective coatings on SS304 substrates in a 3.5 wt. % Sodium Chloride solution. The protection properties of the prepared coatings are evaluated using electrochemical measurements such as Tafel polarization and electrochemical impedance spectroscopy (EIS). Furthermore, the interface adhesion between the protective coatings and metal substrates is examined once the coating is synthesised. Moreover, the long term performance of the protective coatings is also evaluated by conducting the adhesion test after exposing the coated substrates to the corrosive medium for 30 days.

2. Experimental

2.1. Materials and instruments

A polished and cleaned SS304 foil with 0.002 inch thickness was used as substrate (Mc-Master-Carr), 4,4-Bisphenol A Dianhydride (BPADA) (Polysciences Inc.) was heated under vacuum at 60 °C for 3 h in order to remove moisture residue. N-Methyl-2-pyrrolidione (NMP) and m-Phenylenediamine (mPDA) (Sigma Aldrich) were used as received. Graphene nanoplatelets (xGnp-C-750) (XG-Sciences) were used as fillers. According to the supplier, the graphene platelets have an average particle diameter of less than 2 μm and an average surface area of 750 m^2 / g.

2.2. Coating preparation

Polyetherimide-Graphene composite were prepared and coated on a clean SS304 substrates according to the procedures outlined in **Figure 1**. The protective coatings were prepared without graphene to produce (PEI) and with 0.1 wt. % graphene to produce (PEI/$G_{0.1}$) protective coatings.

The PEI/$G_{0.1}$ coating was synthesis by first dispersing 6.4 mg graphene in 35 ml NMP and the suspension was stirred and bath sonicated for 1 h each. 1.1 g of mPDA was dissolved in a separate 35 ml of NMP and stirred until a clear solution was observed. The graphene suspension and the mPDA solution were mixed and the mixture was stirred and bath sonicated for an hour each. The polymerization step was initiated by adding 5.3 g of BPADA to the mixture and the monomers were allowed to react overnight under nitrogen purge to produce a Polyamic acid-Graphene (PAA–G) solution. PAA–G solution was applied on a polished and cleaned SS304 substrate using a fine brush and the thickness was controlled (50 ± 1 μm) using a film applicator (Paul N.Gardner Company Inc.). Finally, the PAA–G was heated under vacuum for 10 h at 70 °C to recover most of the NMP solvent and subsequently cured under vacuum at 100 °C, 150 °C and 205 °C for 2 h each to complete the imidization and produce the PEI/$G_{0.1}$ coating. Similar procedures were followed to prepare PEI coating without the addition of the graphene suspension.

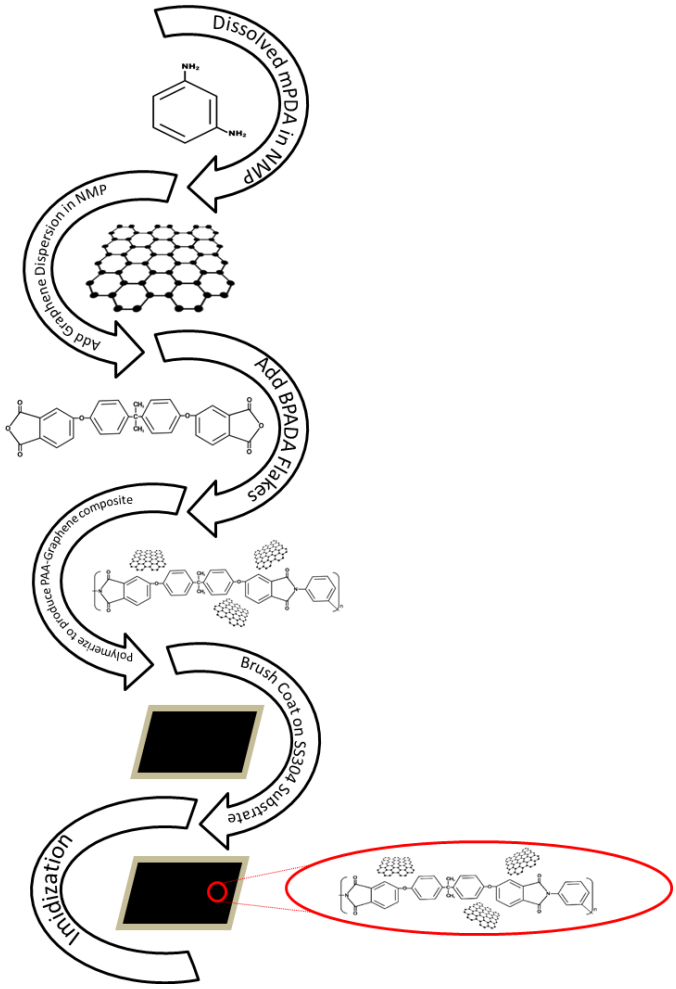

Figure 1. PEI/$G_{0.1}$ Coating Synthesis on a SS304 Substrate.

2.3. Morphology characterization

The morphology of the PEI/G composite was examined using Scanning Electron Microscopy (SEM) (Zeiss LEO 1550) and Transmission Electron Microscopy (TEM) (Philips CM-10 TEM). For SEM analysis, the coated SS304 substrate was fixed on the SEM holder using

a carbon tape before coating with gold using the gold sputtering technique with 120 s deposition time. The TEM sample was prepared by scrapping part of the coating from the coated substrate by a sharp knife and the collected sample was dispersed in methanol for 5 min, fished with a TEM copper grid and left to dry under vacuum at ambient temperature.

2.4. Adhesion test

The adhesion test was performed twice, once after the synthesis of the coating and again after 30 days of exposure to the corrosive medium. The test was conducted according to ASTM-3359D standard using a tape test kit with an 11 tooth 1 mm spacing blade (Paul N. Gardner Company Inc.).

2.5. Electrochemical Measurements

All electrochemical measurements were conducted using VSP–300 workstation (Uniscan Instruments Ltd.) with double-jacketed 1 L corrosion cell using a three electrode configuration. Here, a coated / uncoated SS304 with exposed area of 1 cm^2 was used as the working electrode (WE), two graphite rods were used as the auxiliary electrodes (AE) and a Silver / Silver Chloride (Ag / AgCl) electrode as the reference electrode (RE). The corrosion cell was covered with multi-holes Teflon cap to allow the insertion of the electrodes and a 3.5 wt. % NaCl solution was used as the electrolyte. The potential of the working electrode was allow stabilizing for 30 min and then recorded as the open circuit potential or the corrosion potential (E_{corr}) before conducting any electrochemical measurements. Moreover, impedance spectroscopy was carried out before Tafel polarization tests. Furthermore, all raw measurements were collected three times in order to confirm the reproducibility of the data. Bio-Logic EC-Lab software was used to extract the corrosion potential and the corrosion current (I_{corr}).

The impedance behaviour of the samples were recorded at a frequency range of 100 kHz to 100 mHz in order to produce the Nyquist plots, while Tafel plots were obtained by scanning the potential of the working electrodes from –500 to 500 mV above the corrosion potential at a rate of 10 mV/min. I_{corr} was extracted by finding the intersection between the linear portion of the anodic and the cathodic lines in the Tafel plots and this I_{corr} was used to calculate the corrosion rate (R_{corr}) using equation (1) as per the ASTM G102 standard:

$$R_{corr} = [0.13 \times I_{corr} \times EW] / [A \times \rho]. \quad (1)$$

In the above equation, EW is the equivalent weight of SS304 (25.12 g), ρ is the density (8.03 g / cm^3) and A is the sample exposed area (1 cm^2).

3. Results and discussion

3.1. Morphology

Both SEM and TEM were used to capture the dispersion of graphene in PEI matrix. **Figure 2**, depicts the dispersion in the polymeric matrix at high and low magnifications using SEM, while **Figure 3** depicts the dispersion using TEM. In both figures the graphene platelets were manifested in stacked graphene sheets.

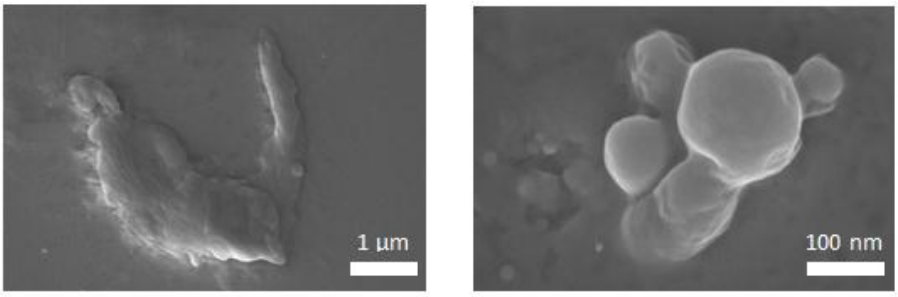

Figure 2. SEM images of Graphene dispersion in PEI/$G_{0.1}$ Composite.

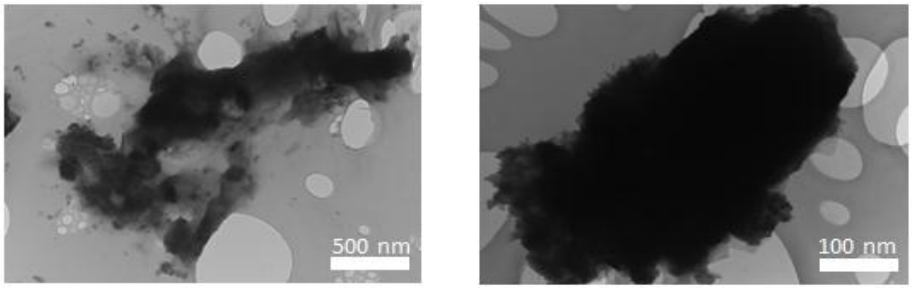

Figure 3. TEM images of Graphene dispersion in PEI/$G_{0.1}$ Composite.

3.2. Adhesion

The corrosion process can be excelled by the accumulation of the various corrosive agents at the interface between the coating and the metal substrate. Therefore, a substantial adhesion between the coating and the substrate is always a desire. Here, the interface adhesion is evaluated according to the ASTM D3359 standard using the tape adhesion kit. **Figure 4** depicts the post adhesion test results on PEI/$G_{0.1}$ coating before and after 30 days of exposure to the corrosive medium. The figure represents the noble interface adhesion between the coating and the substrate, where no peelings from the protective coatings were observed before and after the exposure. The coatings received 5B (0 % peeling) rating according to the ASTM standard. This confirms the robust adhesion as well as the long term durability of the protective PEI/$G_{0.1}$ coating.

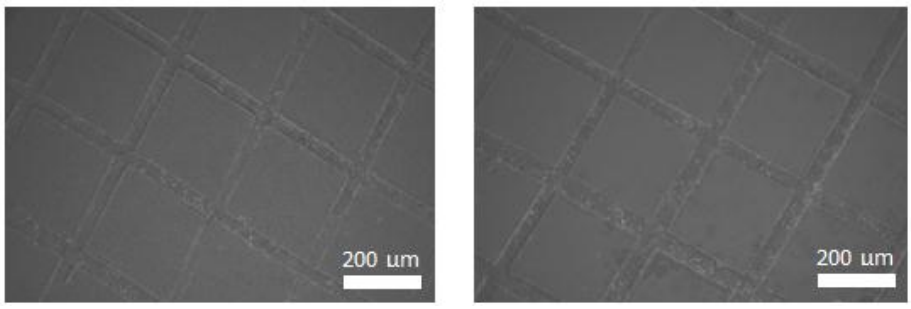

(a) (b)

Figure 4. SEM images of post adhesion test of PEI/$G_{0.1}$ Composite (a) before and (b) after 30 days exposure to the 3.5 wt. % NaCl solution.

3.3. Cyclic voltammetry and impedance spectroscopy

Tafel polarization and Impedance spectroscopy were utilized to evaluate the electrochemical behaviour of the bare and coated SS304 substrate. **Figure 5**, depicts the Tafel plots for bare, PEI and PEI/$G_{0.1}$ coated SS304 substrates. These plots were used to extract

valuable corrosion parameters such as corrosion potential and corrosion current. The corrosion current was recorded as the intersection between the extrapolation of the linear portions of the anodic and the cathodic curves. All extracted corrosion parameters are reported in Table 1, where a positive shift was observed in the corrosion potential after coating the SS304 substrate with PEI and a further shift was observed as a result of incorporating the graphene in the PEI matrix. Furthermore, coating the SS304 substrate with PEI and the incorporation of graphene attenuated both the corrosion currents and the corrosion rates of coated substrates. The reported results indicate that coating SS304 with PEI may slow the deterioration rate of SS304 and this rate can be further attenuated by the incorporation of graphene. The protection efficiency (P_{EF}) is another parameter that can be calculated using equation (2) to reflect the degree of corrosion mitigation a protective coating may deliver. The protection efficiencies for both PEI and PEI/$G_{0.1}$ were computed and reported in **Table 1**, where the P_{EF} magnitudes confirm that an enhancement in corrosion mitigation can be achieved by coating the substrate with PEI and this enhancement can be further excelled by incorporating graphene in the polymeric matrix.

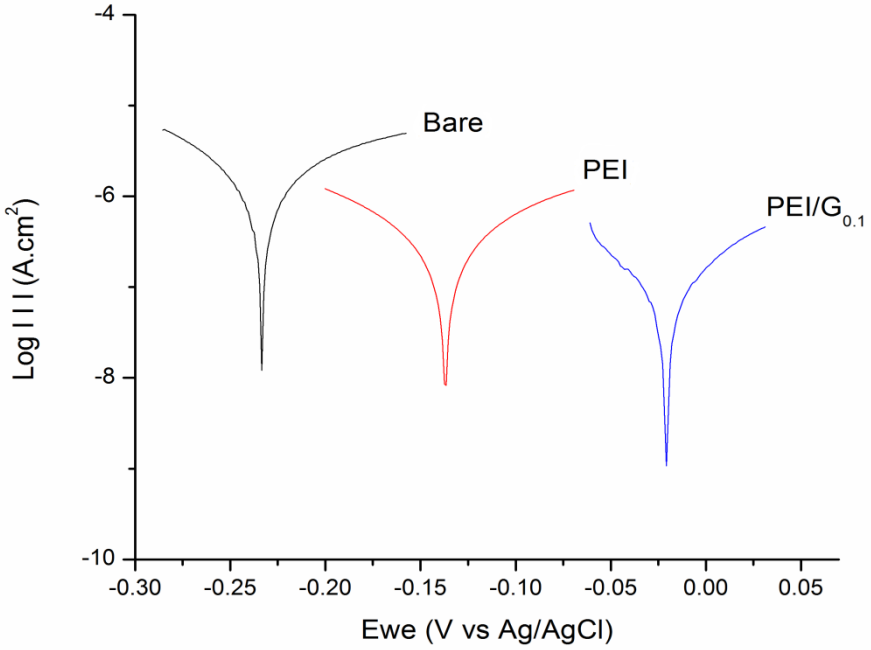

Figure 5: Tafel plots of bare and coated SS304 substrates.

Table 1. Corrosion parameters extracted from potentiodynamic measurements for bare SS304, PEI and PEI/$G_{0.1}$ coated SS304 substrates in 3.5 wt. % NaCl solution.

Sample	Corrosion parameters extracted from Tafel plots			
	$E_{corr.}$ [mV vs Ag/AgCl]	$I_{corr.}$ [µA/cm²]	$R_{corr.}$ [MPY]	P_{EF} [%]
SS304	–244	3.29	1.33	–
PEI	–161	1.00	0.40	69.6
PEI/$G_{0.1}$	–29.6	0.07	0.03	97.8

$$PEF\ [\%] = [1 - I_{corr.} / I^{\circ}_{corr.}] \times 100, \quad (2)$$

where, $I^{\circ}_{corr.}$ represents the corrosion current of the bare SS304 substrate.

Impedance is a complex resistance that may results from passing an alternative current through a circuit. In this study, the impedance behaviours of the bare and coated substrates

were investigated. Moreover, equivalent circuits, which are depicted in **Figure 6** were used to model the impedance behaviour of the bare and coated substrates. In these circuits, CPE is a constant phase elements and W is the Warburg impedance, while Rs, Rp and Rch represent the electrolyte, polarization and charge transfer resistances, respectively.

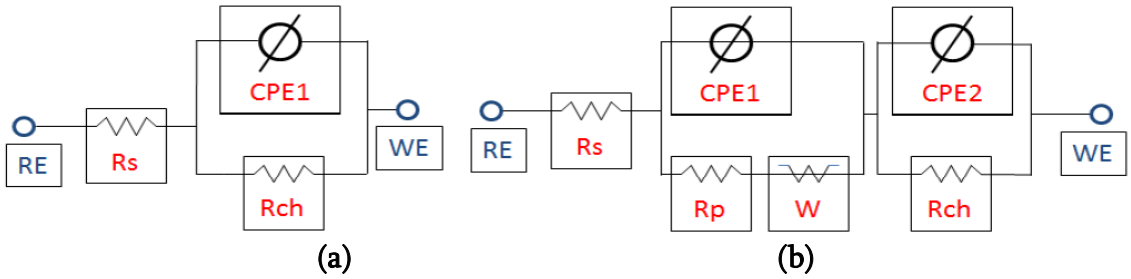

Figure 6. Equivalent circuits to model the impedance behaviour of (a) bare and (b) coated SS304 substrate.

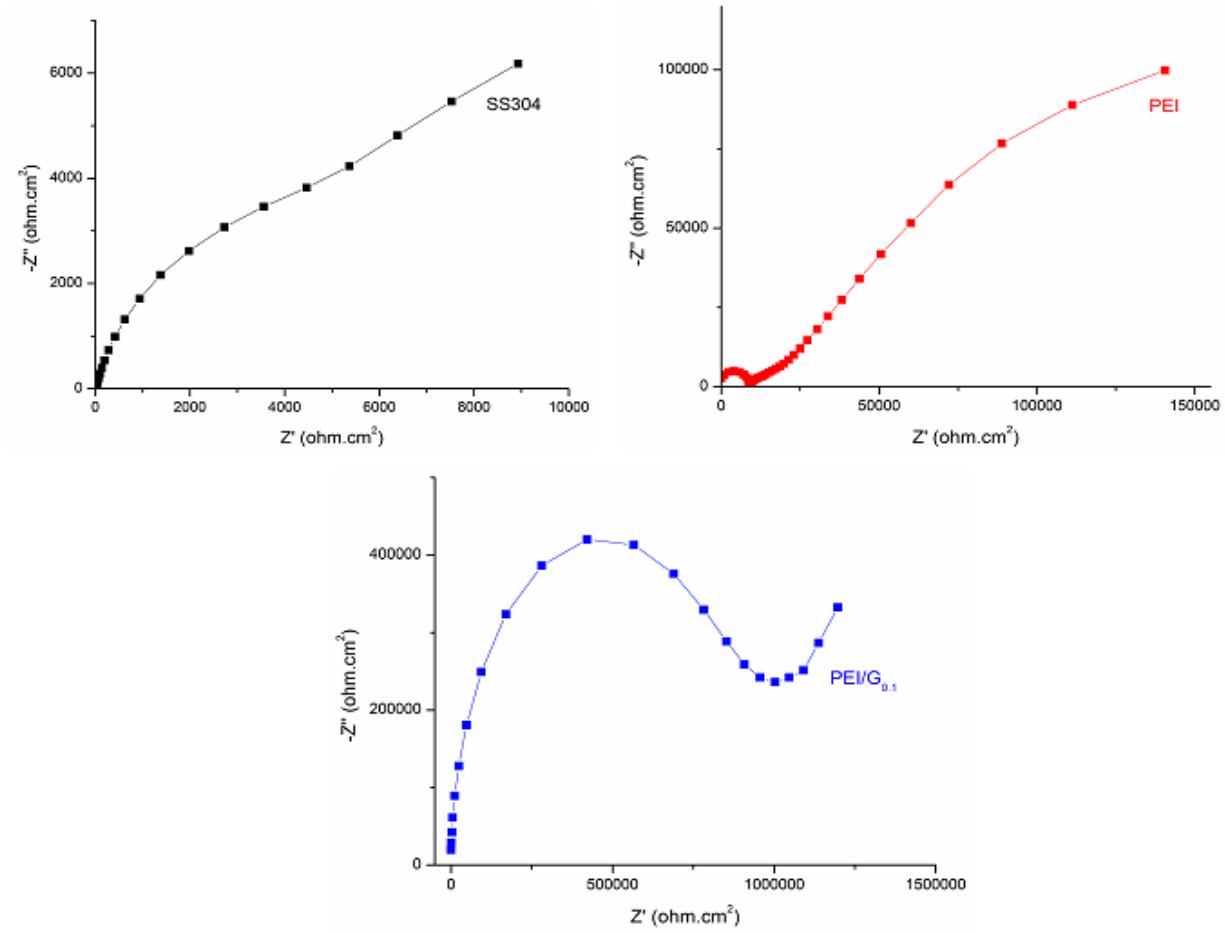

Figure 7. Impedance behaviour of bare and coated SS304 substrates.

Figure 7 depicts the Nyquist plots for bare and coated substrates, where it was observed that the fitting data obtained from the equivalent circuits fit well to the raw impedance data. These fittings were used to evaluate the various elements in the equivalent circuits. The variations in the magnitudes of these elements may be used to evaluate the corrosion mitigation properties of the PEI and PEI/$G_{0.1}$ protective coatings. Indeed, an increase in the charge transfer resistance reflects an enhancement in corrosion inhibition. The charge transfer resistance obtained from the fittings are $7.0 \cdot 10^3$, $1.0 \cdot 10^4$ and $8.6 \cdot 10^5$ $\Omega \cdot cm^2$ for bare, PEI and PEI/$G_{0.1}$ coated SS304, respectively.

Reported results from both Tafel polarization and impedance spectroscopy measurements revealed that PEI may enhance the corrosion mitigation on SS304 substrate. Furthermore, a small loading of graphene may further excel this corrosion inhibition property.

4. Conclusion

In this study, Polyetherimide/graphene composite was synthesised using in situ polymerization and thermal imidization. The dispersion of the filler was captured using SEM and TEM. The corrosion protection properties of the coatings were evaluated using Tafel polarization and EIS. Moreover, the interface adhesion between the metal substrate and the PEI/$G_{0.1}$ coating was evaluated as per the ASTM standard D3359.

The study revealed that PEI/G coating with a small load of filler 0.1 wt. % may prolong the lifetime of coated substrate in a 3.5 wt. % NaCl solution. This enhancement in corrosion protection property of PEI can be attributed to the ability of dispersed graphene nanoplatelets in prolonging pathway for corrosive agents to reach the coated substrate.

Acknowledgements

The authors would like to acknowledge the financial support by the Petroleum Institute, Abu Dhabi through research Project # 66. The authors also acknowledge the financial support and Mr. Alhumade full scholarship from the Ministry of Education, Saudi Arabia.

References

1. L. Cecchetto, D. Delabouglise, J.-P. Petit. On the mechanism of the anodic protection of aluminium alloy AA5182 by emeraldine base coatings: Evidences of a galvanic coupling. Electrochim. Acta, 2007, 52, 11, 3485-3492.
2. A. Vasinonta, J. L. Beuth, M. L. Griffith. A process map for consistent build conditions in the solid freeform fabrication of thin-walled structures. J. Manuf. Sci. & Eng., 2001, 123, 4, 615-622.
3. G. Kang, Q. Kan, J. Zhang, Y. Sun. Time-dependent ratchetting experiments of SS304 stainless steel. Int. J. Plasticity, 2005, 22, 5, 858-894.
4. K. C. Chang, C. H. Hsu, H. I. Lu, W. F. Ji, C. H. Chang, W. Y. Li, T. L. Chuang, J. M. Yeh, W. R. Liu, M. H. Tsai. Advanced anticorrosive coatings prepared from electroactive Polyimide/graphene nanocomposites with synergistic effects of redox catalytic capability and gas barrier properties. Express. Polym. Lett., 2014, 8, 4, 243-255.
5. S. Kumar, T. Rath, R. N. Mahaling, C. S. Reddy, C. K. Das, K. N. Pandey, R. B. Srivastava, S. B. Yadaw. Study on mechanical, morphological and electrical properties of carbon nanofiber / polyetherimide composites. Mater. Sci. & Eng. B, 2007, 141, 1, 61-70.
6. D. Prasai, J. C. Tuberquia, R. R. Harl, G. K. Jennings, K. I. Bolotin. Graphene: corrosion-inhibiting coating. ACS Nano, 2012, 6, 2, 1102-1108.
7. B. P. Singh, B. K. Jena, S. Bhattacharjee, L. Besra. Development of oxidation and corrosion resistance hydrophobic graphene oxide-polymer composite coating on copper. Surf. Coat. Tech., 2013, 232, 475-481.

ONE STEP 10 MINUTE MICROWAVE SYNTHESIS OF SILVER NANOPARTICLES USING MANNAN

J. A. L. Hartman, N. Christian, P. Couture,
K. M. Hart, J. Hinds, S. Marinelli, A. O. Pinchuk

University of Colorado at Colorado Springs
Department of Physics and Energy Sciences
Colorado Springs, Colorado, USA
jhartman@uccs.edu

Accepted October 19, 2015

Abstract

Silver nanoparticles have been synthesized using a rapid 10 minute, one-step microwave synthesis method by the reduction of Ag^+ ions in an aqueous solution of mannan, which is the linear polysaccharide polymer of the reducing sugar mannose and the natural ligand for the mannose receptor. The mannan functions as the sole reducing, encapsulating, and stabilizing agent in the microwave synthesis. The nanoparticles were characterized using UV-visible spectroscopy and nanoparticle size was estimated using dynamic light scattering and scanning electron microscopy. The average size of the silver nanoparticles was estimated to be 79.00 ± 3.99 nm with a surface plasmon resonance peak at 433 ± 0.71 nm. The silver nanoparticles were observed for 3 months for stability with no noticeable aggregation.

1. Introduction

Noble metal nanoparticles (NPs) are of interest for applications in a number of areas including chemistry, optics, and biomedical science [1 – 4]. Silver nanoparticles (AgNPs) exhibit unique optical [5] and chemical properties when compared to those of bulk silver [6]. AgNPs prepared by specific synthesis methods using monosaccharides or polysaccharides [4, 7] have been shown to exhibit applications in cell targeting [8, 9].

Despite the beneficial properties of AgNPs, issues of cytotoxicity [10, 11] are of concern because some stabilizers and reducing agents [12] used in the synthesis of AgNPs pose biological safety threats [13]. Traditional NP syntheses often reduce the metal salt precursor by a chemical reducing agent while using an additional encapsulating agent to stabilize the NPs. Microwave assisted syntheses have advantages over traditional heating due to rapid initial heating resulting in superior reaction yield while minimizing reaction time [14]. Microwave assisted techniques have been reported for AgNP synthesis using monosaccharides [7] and soluble starch [2]. Mannan, the linear polysaccharide of the reducing sugar mannose, is the ligand for the mannose receptor. Mannan-functionalized NPs possess biological applications including cell targeting [8], binding to E. coli [15], sentinel lymph node detection [16], detection of lectins

[17] and colorimetric bioassays [18]. The techniques reported for the synthesis of mannan-functionalized NPs involve a synthesis time of 2.5 to 48 h [17, 18]; the mannan is added as a capping agent through self-assembly, with additional chemicals used as reducing agents. A rapid one-step technique for the synthesis of mannan functionalized AgNPs in which the mannan functions as the sole reducing, encapsulating, and stabilizing agent has not been reported to our knowledge. We present a 10 min one-step microwave polysaccharide-assisted technique for the synthesis of stable AgNPs reduced and encapsulated with mannan that does not use additional reducing agents.

2. Experimental: materials and methods

2.1. Materials

Analytical grade chemicals and solvents were purchased from Sigma Aldrich and used without further purification. Silver nitrate ($AgNO_3$, CAS: 7761-88-8, ACS Reagent 99+ %) was used as the metal salt precursor, and mannan from *Saccharomyces Cerevisiae* (CAS: 9036-88-8) was used as the reducing, encapsulating, and stabilizing agent. DDI (distilled deionized) H_2O was used for all experiments. CEM glass 10 mL microwave reaction vessels with single use lids were used for the microwave synthesis.

2.2. Instrumentation

All nanoparticle syntheses were performed using a Discover SP (CEM Corporation, Matthews, NC) laboratory grade microwave synthesizer [19]. Optical characterization was performed using a PerkinElmer Lambda 1050 UV–Vis spectrometer. Hydrodynamic diameter data for the nanoparticle size distribution was obtained by using a Brookhaven Instruments ZetaPALS zeta potential dynamic light scattering (DLS) analyser with ZetaPlus Version 4.20 particle sizing software. Images of the nanoparticles were obtained using a TESCAN Vega 3G scanning electron microscope (SEM). The measurement tool of the SEM software was implemented for obtaining the particle size distribution histograms from the SEM image.

2.3. Solution preparation and synthesis procedure

Preparation of mannan solution and silver nitrate solution of desired weight percentage

The aqueous solutions of mannan (9 % w/w) and $AgNO_3$ (19 % w/w) were prepared by dissolving the appropriate mass of mannan and $AgNO_3$ into DDI H_2O. The solutions were kept in a dark refrigerator to preserve the quality of the solution.

Preparation and procedure for microwave synthesis

Previously reported techniques were modified [1, 2, 14] for the developed one step microwave synthesis of AgNPs reduced solely by mannan.. The reaction mixture was prepared using 2 mL of DDI H_2O and 0.5 mL of mannan solution; the volume of $AgNO_3$ solution was calculated from the desired mass ratio of $AgNO_3$: mannan. The solutions were loaded into capped glass microwave vessels that are designed to withstand high temperature and pressure reactions. The parameters of the microwave synthesis (time, temperature, and pressure) were optimized for reaction yield using the Box-Benhken design [14] by performing trials with

various combinations of time, temperature, and mass ratio of $AgNO_3$: mannan. For each set of reaction parameters, identical samples were synthesized in quintuplicate to confirm repeatability and to establish statistical confidence.

2.4. Characterization

UV–Visible spectroscopy

UV–Vis spectroscopy was used to measure the absorbance spectra of the AgNPs. Optical quality cuvettes were used and samples were characterized at full strength when performing UV-Vis spectroscopy. The spectra were collected with the samples at room temperature. Statistical confidence was obtained through collection of the spectra for all quintuplicate samples. The sample whose reaction parameters produced the narrowest SPR band and maximum absorbance, indicative of a narrow distribution of nanoparticles, was selected for further characterization using DLS and SEM.

Dynamic light scattering

The average hydrodynamic diameter of the AgNPs was found using DLS. For DLS measurements, the backscatter angle was set to 90 ° and the wavelength of the laser was 657 nm. To ensure consistency in measurements, optical cuvettes were used for all samples and appropriate dilutions with DDI H_2O were performed immediately before each analysis. The data collection was completed at a temperature of 25 °C and measurements were taken over 5 min. The dust cutoff was modified accordingly such that the baseline index of the measurements remained at 98 % or greater. The reported diameters for each identical sample are the mean of the DLS measurements obtained from the quintuplicate samples.

Scanning electron microscopy

A TESCAN Vega 3G scanning electron microscope was used to obtain the SEM image. Because the nanoparticles are encapsulated by the linear polymer mannan, excess mannan needed to be removed from the sample via centrifugation [19] in order to obtain a clear SEM image. Samples were subjected to centrifugation at 16,000 g for 20 min. The supernatant was then discarded and the resultant pellet containing the NPs was reconstituted in water and centrifuged at 16,000 g for 10 min. This process was repeated four times. The final pellet solution was reconstituted in a solution of water, which was evenly dispersed over conductive ITO-coated glass using a SCS G3-8 spin-coating machine by Cookson Electronics. The machine was operated at 650 rpm for 30 s, and the spin-coated sample was allowed to dry for 24 hours on the ITO coated glass prior to the SEM characterization. The centrifugation process allowed for the nanoparticles to be imaged by SEM with minimal interference from the mannan encapsulation.

3. Results and discussion

3.1. Optimization of microwave parameters

In order to evaluate the effect of varying the reaction parameters, trials were synthesized with various combinations of time (5, 10, 15, 20, 30 min), temperature (90, 100, 110, 120, 125, and 130 °C, and mass ratio of $AgNO_3$: mannan (1 : 30, 1 : 40). Preliminary experiments determined that varying the initial weight concentrations of the prepared $AgNO_3$ or mannan

solutions did not have an effect on the NPs synthesized. Upon completion of successful microwave synthesis, the color of the solution in the vessel gradually changed from light yellow to yellow to light amber and finally dark amber, indicating the formation of AgNPs [3, 14, 20].

In optimizing the reaction temperature, the decomposition points of the reducing agent and metal salt precursor were taken into consideration. Mannan and silver nitrate have a decomposition points of 133 and 444 °C, respectively. Therefore, the microwave synthesis was performed at temperatures of 90, 100, 110, 120, 125, and 130 °C. However, due to the enhanced reaction yield and superheating of the microwave [21], the maximum temperature for optimal synthesis was found to be 120 °C. Above 120 °C, the SPR in UV–Vis absorption spectra began to widen and the color of the solution changed, indicative of aggregations; while below 120 °C, the solution possessed a very faint yellow color and minimal SPR, indicative of a solution that was not fully reduced. While optimizing the reaction time, it was determined that 5 min was not sufficient enough for the metal precursor to be fully reduced. After increasing the reaction time beyond 10 min, the SPR peak sufficiently broadened, indicating decreased monodispersity of the solution. In optimizing the mass ratio of $AgNO_3$: mannan, increasing the mass ratio of $AgNO_3$: mannan up to 1 : 40 $AgNO_3$: mannan resulted in higher reaction yield and a slightly narrower SPR peak when normalized. Therefore, the optimal synthesis parameters were determined to be 10 min at 120 °C with a mass ratio of 1 : 40 $AgNO_3$: mannan. Upon completion of successful microwave synthesis, the solution in the vessel possessed the characteristic amber color of AgNP solutions [14], as shown in **Figure 1**.

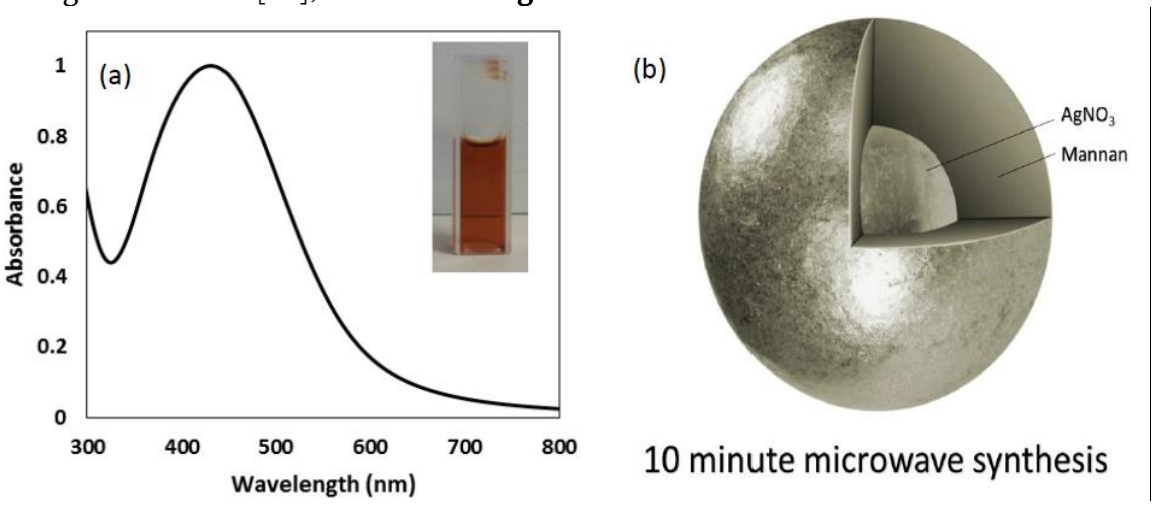

Figure 1. (a) Representative UV–Vis absorption spectrum of a sample from the optimized synthetic parameters: 1 : 40 (mass ratio) $AgNO_3$: Mannan at 120 °C for 10 min. The data presented is averaged over the quintuplicate samples. Inset photo shows a picture of the nanoparticles from the optimal synthesis. (b) Illustration of the encapsulation of the AgNPs by the mannan.

3.2. Characterization of AgNPs through UV–Vis absorption spectra

Synthesis of the AgNPs was first confirmed from the resulting SPR in the absorbance spectra of the nanoparticles obtained from UV-Vis spectroscopy. Evidence of the formation of mannan-encapsulated AgNPs was apparent from the surface plasmon absorption maximum [22] at 433 ± 0.71 nm [23]. Analysis of the UV-Vis absorption spectra illustrated that the successful synthesis is sensitive to the reaction time, temperature, and mass ratio of the $AgNO_3$: mannan. Representative spectra are shown in **Figures 2a**, **b**, and **c** to illustrate the sensitivity of the

synthesis to the reaction parameters. The UV-Vis spectra presented are averaged over identical quintuplicate synthesized samples. The optimized reaction parameters were determined to be 10 minutes, 120°C, and 1 : 40 $AgNO_3$: mannan, in which strong and narrow SPR absorption [24] was observed. The UV–Vis spectrum of this sample is displayed in **Figure 1**. The surface plasmon absorption maximum occurs at 433 ± 0.71 nm and has a full width at half maximum of 185 ± 1.41 nm. This is comparable to the SPR maxima reported for similar sugar-based synthetic routes using polysaccharides and additional reducing agents, which range between 420 – 445 nm [2 – 4, 7, 13, 20, 25, 26].

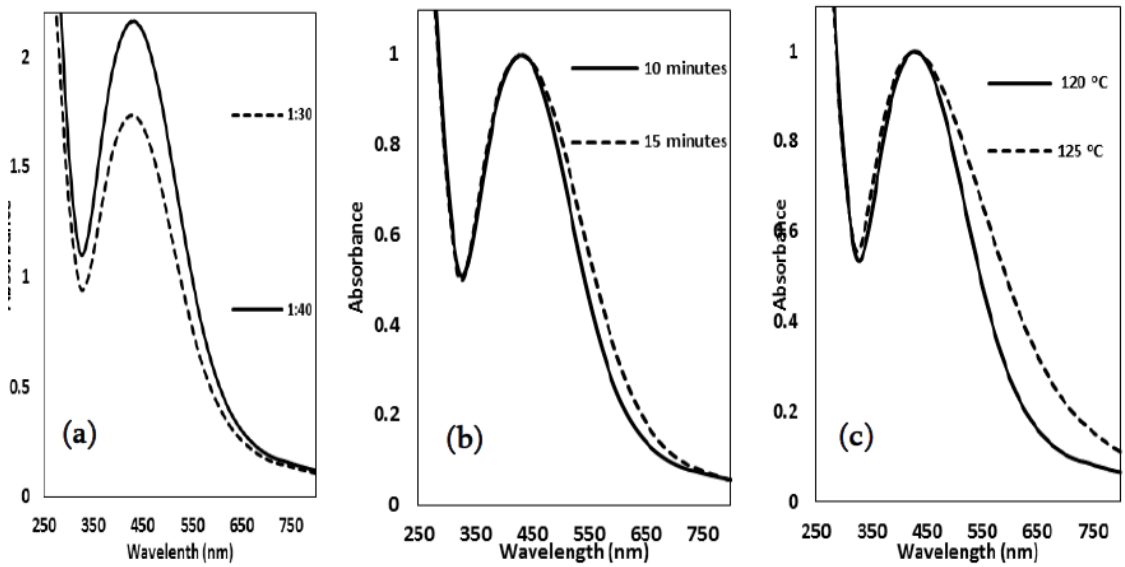

Figure 2. Illustration of the effect of (a) mass ratio of $AgNO_3$: Mannan; (b) reaction time; and (c) temperatures on the absorption spectra of mannan-stabilized AgNPs.

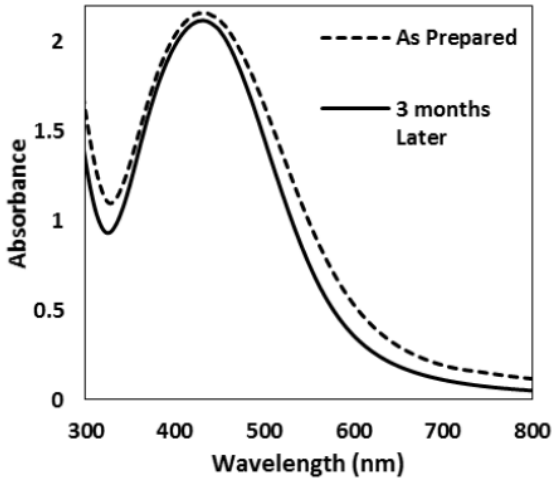

Figure 3. Illustration of time stability of the AgNPs examined through the absorption spectra. The SPR for the AgNPs on the day of synthesis was 433 nm; 3 months later, the SPR was 431 nm. The SPR peak did not broaden with time, indicative of low or minimal aggregation in terms of time stability.

The stability of colloidal AgNPs can indicate successful AgNP synthesis [12]. Time stability is an important property required for numerous applications including direct coating of biomaterials, devices, and medical textiles [27]. Additionally, the synthesis of stable AgNPs with limited agglomeration for long periods of time is important for biological and antibacterial

applications [27]. The colloidal AgNP solutions were stable for a period of up to 3 months and no noticeable aggregation occurred. As shown in **Figure 3**, the UV–Vis absorption spectra did not exhibit any changes indicative of aggregation. This indicates that the linear polysaccharide polymer mannan functions as an effective protective and stabilizing agent for the formation of the AgNPs. The stability of mannan-capped AgNPs is expected due to the attachment of the linear polysaccharide polymer mannan that encapsulates the surface of the nanoparticles [3].

3.3. Size analysis of AgNPs by dynamic light scattering and scanning electron microscopy

To confirm the qualitative results obtained from the absorbance spectra and the value of the surface plasmon absorption peak, direct characterization of the nanoparticle size was performed using DLS and SEM. The value reported for hydrodynamic diameter was obtained by averaging the value over the quintuplicate samples. The average hydrodynamic diameter was 91.80 ± 3.70 nm. Although hydrodynamic diameter is larger than the actual particle size [28, 29], it is an important parameter to study in regards to *in vivo* migration of NPs.

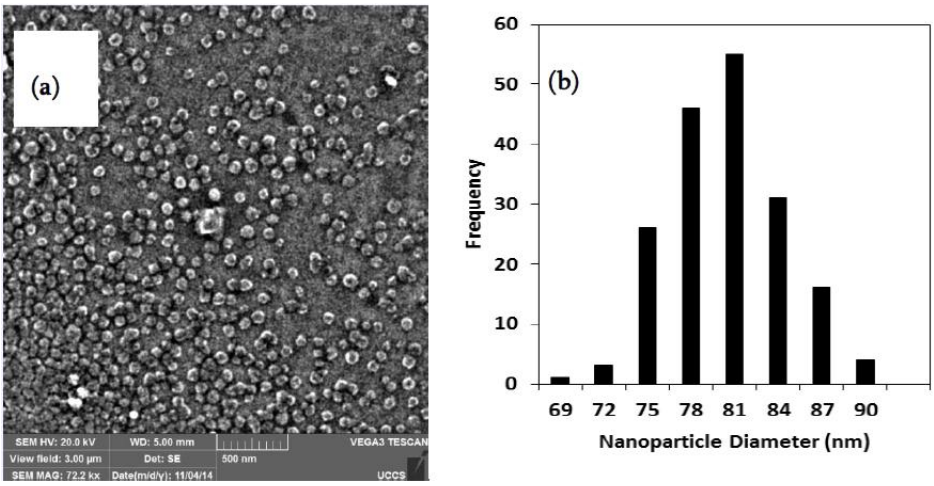

Figure 4. (a) SEM image of mannan-AgNPs. (b) Histogram of the size distribution of AgNPs obtained from the SEM image. 183 nanoparticles were counted and the average nanoparticle size was found to be 79.00 ± 3.99 nm.

Characterization using SEM imaging confirms that the NPs are smaller than their hydrodynamic diameter. The SEM image is presented in **Figure 4a**. The actual size of the nanoparticles was confirmed using the measurement tool in the SEM software. 183 nanoparticles were counted in this SEM image. The average actual diameter was found to be 79.00 ± 3.99 nm, which is less than the hydrodynamic diameter measured by DLS. The actual particle diameter is expected to be smaller than the hydrodynamic diameter [28, 29]. A histogram of the actual particle size distribution from this SEM image is displayed in **Figure 4b**.

3.4. Control experiments

To ensure that mannan does play a critical role in the synthesis of AgNPs, control experiments were performed. No SPR absorption band was observed when the synthesis was performed without mannan. This verifies that the nanoparticle formation was solely a result of

the reduction of the $AgNO_3$ by the mannan and not from any self-reduction of the $AgNO_3$ when exposed to the thermal heating of the microwave. Additionally, a control experiment using the identical reagents and reaction parameters through a traditional heating reflux condenser reaction was performed. No nanoparticles were formed in 10 min, illustrating that the microwave synthesis has the advantage of the rapid synthesis time (10 min). After the reaction solution was boiling for 3.5 h, it was found that similar results were obtained; however, the yield of the reaction was significantly lower, as shown in **Figure 5**. The comparison between the syntheses demonstrated that the microwave synthesis resulted in higher absorbance while reducing the synthesis time from 3.5 h to 10 min.

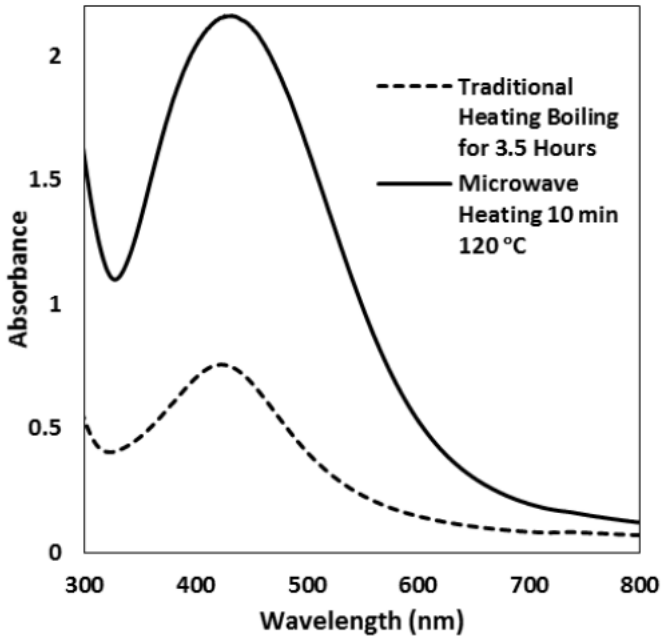

Figure 5. Comparison of 1 : 40 $AgNO_3$: Mannan synthesis using the 10 min microwave synthesis versus a 3.5 h traditional heating synthesis. The absorbance is significantly higher for the microwave synthesis.

4. Conclusion

In conclusion, a rapid one-step microwave synthesis using mannan, the linear polysaccharide form of the reducing sugar mannose, was developed the preparation of stable AgNPs that are encapsulated and functionalized with mannan. Mannan functions as the sole reducing, encapsulating, and stabilizing agent in the reaction. The mannan-functionalized AgNPs were characterized using UV–Vis spectroscopy to measure the absorbance spectrum, DLS to measure the hydrodynamic diameter, and SEM to measure the actual diameter of the AgNPs. The SPR peak of the absorbance spectrum was 433 ± 0.71 nm. The hydrodynamic diameter was found to be 91.80 ± 3.70 nm from the DLS, and the actual diameter was determined to be 79.00 ± 3.99 nm using the SEM. Biological applications using mannan-functionalized AgNPs to bind to the mannose receptor are now possible without concerns of cytotoxicity due to additional reducing or stabilizing agents required in the synthesis of the AgNPs.

Acknowledgements

Thanks to Dr. Jiang for his advice and review on this Project.

This work is supported by funding from the Center for Biofrontiers Institute, University of Colorado at Colorado Springs.

References

1. H. Huang, X. Yang. Synthesis of polysaccharide-stabilized gold and silver nanoparticles: a green method. Carbohydr. Res., 2004, 339, 2627-2631.
2. N.. Vigneshwaran, R. P. Nachane, R. H. Balasubramanya, P. V. Varadarajan. A novel one-pot “green” synthesis of stable silver nanoparticles using soluble starch. Carbohydr. Res., 2006, 341, 2012-2018.
3. S. K. Mehta, S. Chaudhary, M. Gradzielski. Time dependence of nucleation and growth of silver nanoparticles generated by sugar reduction in micellar media. J. Colloid Interface Sci., 2010, 343, 447-453.
4. K. P. Bankura, D. Maity, M. M. R. Mollick, D. Mondal, B. Bhowmick, M. K. Bain, A. Chakraborty, J. Sarkar, K. Acharya, D. Chattopadhyay. Synthesis, characterization and antimicrobial activity of dextran stabilized silver nanoparticles in aqueous medium. Carbohydr. Polymers. 2012, 89, 1159- 1165.
5. A. Pinchuk, U. Kreibig, A. Hilger. Optical properties of metallic nanoparticles: influence of interface effects and interband transitions. Surf. Sci., 2004, 557, 269-280.
6. K. M. M. Abou El-Nour, A. Eftaiha, A. Al-Warthan, R. A. A. Ammar. Synthesis and applications of silver nanoparticles. Arab. J. Chem., 2010, 3, 135-140.
7. C. Pettegrew, Z. Dong, M. Z. Muhi, S. Pease, M. A. Mottaleb, M. R. Islam. Silver nanoparticle synthesis using monosaccharides and their growth inhibitory activity against gram-negative and positive bacteria. ISRN Nanotechnol., 2014, 2014, 1-8.
8. Z. Cui, C.-H. Hsu, R. J. Mumper. Physical characterization and macrophage cell uptake of mannan-coated nanoparticles. Drug Dev. Ind. Pharm., 2003, 29, 689-700.
9. Z. Ghotbi, A. Haddadi, S. Hamdy, R. W. Hung, J. Samuel, A. Lavasanifar. Active targeting of dendritic cells with mannan-decorated PLGA nanoparticles. J. Drug Target., 2011, 19, 281-292.
10. H.-J. Yen, S.-H. Hsu, C.-L. Tsai. Cytotoxicity and immunological response of gold and silver nanoparticles of different sizes. Small, 2009, 5, 1553-1561.
11. C. Liu, P. Zhang, X. Zhai, F. Tian, W. Li, J. Yang, Y. Liu, H. Wang, W. Wang, W. Liu. Nano-carrier for gene delivery and bioimaging based on carbon dots with PEI-passivation enhanced fluorescence. Biomater., 2012, 33, 3604-3613.
12. V. K. Sharma, R. A. Yngard, Y. Lin. Silver nanoparticles: green synthesis and their antimicrobial activities. Adv. Colloid Interface Sci., 2009, 145, 83-96.

13. H. Peng, A. Yang, J. Xiong. Green, microwave-assisted synthesis of silver nanoparticles using bamboo hemicelluloses and glucose in an aqueous medium. Carbohydr. Polym. 2013, 91, 348-355.
14. G. A. Kahrilas, L. M. Wally, S. J. Fredrick, M. Hiskey, A. L. Prieto, J. E. Owens. Microwave-assisted green synthesis of silver nanoparticles using orange peel extract. ACS Sustain. Chem. Eng., 2014, 2, 367-376.
15. C. Lin, Y. Yeh, C. Yang, C. Chen, G. Chen, C. Chen, Y. Wu. Selective binding of mannose-encapsulated gold nanoparticles to type 1 pili in *Escherichia coli*. J. Am. Chem. Soc.,2002, 124, 3508-3509.
16. B. E. Ocampo–García, F. D. M. Ramírez, G. Ferro–Flores, L. M. de León–Rodríguez, C. L. Santos–Cuevas, E. Morales–Avila, C. A. de Murphy, M. Pedraza–López, L. A. Medina, M. A. Camacho–López. (99m)Tc-labelled gold nanoparticles capped with HYNIC-peptide / mannose for sentinel lymph node detection. Nucl. Med. Biol., 2011, 38, 1-11.
17. D. C. Hone, A. H. Haines, D. A. Russell. Rapid, quantitative colorimetric detection of a lectin using mannose-stabilized gold nanoparticles. Langmuir, 2003, 19, 7141-7144.
18. C. L. Schofield, A. H.. Haines, R. A. Field, D. A. Russell. Silver and gold glyconanoparticles for colorimetric bioassays. Langmuir, 2006, 22, 6707-6711.
19. Y. Luo, X. Sun, Rapid, single-step preparation of dendrimer-protected silver nanoparticles through a microwave-based thermal process. Mater. Lett., 2007, 61, 1622-1624.
20. M. Darroudi, M. Bin Ahmad, A. H. Abdullah, N. A. Ibrahim. Green synthesis and characterization of gelatin-based and sugar-reduced silver nanoparticles. Int. J. Nanomed., 2011, 6, 569-574.
21. M. Tsuji, M. Hashimoto, Y. Nishizawa, M. Kubokawa, T. Tsuji. Microwave-assisted synthesis of metallic nanostructures in solution. Chem., 2005, 11, 440-452.
22. K. L. Kelly, E. Coronado, L. L. Zhao, G. C. Schatz. The optical properties of metal nanoparticles: The influence of size, shape, and dielectric environment. J. Phys. Chem B, 2003, 107, 668-677.
23. S. He, J. Yao, P. Jiang, D. Shi, H. Zhang, S. Xie, S. Pang, H. Gao. Formation of silver nanoparticles and self-assembled two-dimensional ordered superlattice. Langmuir, 2001, 17, 1571-1575.
24. J. L. Elechiguerra, J. L. Burt, J. R. Morones, A. Camacho–Bragado, X. Gao, H. H. Lara, M. J. Yacaman. Interaction of silver nanoparticles with HIV-1. J. Nanobiotechnol., 2005, 3, 6.
25. J. Pal, M. K. Deb. Microwave synthesis of polymer coated silver nanoparticles by glucose as reducing agent. Indian J. Chem., 2012, 51, 821-824.
26. Y. Abboud, A. Eddahbi, A. El Bouari, H. Aitenneite, K. Brouzi, J. Mouslim. Microwave-assisted approach for rapid and green phytosynthesis of silver nanoparticles using aqueous onion (Allium cepa) extract and their antibacterial activity. J. Nanostruct. Chem., 2013, 3, 84.
27. H. J. Lee, S. G. Lee, E. J. Oh, H. Y. Chung, S. I. Han, E. J. Kim, S. Y. Seo, H. D. Ghim, J. H. Yeum, J. H. Choi. Antimicrobial polyethyleneimine-silver nanoparticles in a stable colloidal dispersion. Colloids Surf. B, 2011, 88, 505-511.

28. R. De Palma, S. Peeters, M. J. Van Bael, H. Van Den Rul, K. Bonroy, W. Laureyn, J. Mullens, G. Borghs, G. Maes. Silane ligand exchange to make hydrophobic superparamagnetic water-dispersible. Chem. Mater., 2007, 19, 1821-1831.
29. J. Zheng, Y. Ding, B. Tian, Z. L. Wang, X. Zhuang. Luminescent and Raman active silver nanoparticles with polycrystalline structure. J. Am. Chem. Soc., 2008, 130, 10472-10473.

MICRO-NANO STRUCTURED SUPERHYDROPHOBIC POLYMERIC POWDER COATINGS

M. S. Mozumder [1], A.-H. Mourad [2], H. Zhang [3], J. Zhu [3]

[1] UAE University
Chemical & Petroleum Engineering Department
Al Ain, Unired Aran Emirates
a.s.mozumder@uaeu.ac.ae
[2] UAE University
Mechanical Engineering Department
Al Ain, UAE,
ahmourad@uaeu.ac.ae
[3] Western University
Chemical & Biochemical Engineering Deptment
London, ON, Canada
hzhang1@uwo.ca, jzhu@uwo.ca

Accepted October 19, 2015

Abstract

This study demonstrates the development of polymeric superhydrophobic polymeric nanocomposite coatings by a solvent-free ultrafine powder coating (UPC) technique. The developed coatings produce water contact angles (CAs) of over 160 ° and sliding angle (SA) of less than 5 °. It is evident that the higher CA and lower SA of the low-energy coatings are attributed to the appropriate surface topography of micro- and / or nano-scales. Pull-off test of the coatings (i.e., maximum normal force tolerable before being detached from the substrates) confirmed their excellent adhesion to the underlying substrates. SEM images revealed the unique double-scale hierarchical (micro- and nano-) structures on the developed superhydrophobic surfaces. As an additional advantage, these superhydrophobic UPC technology eliminates the use of toxic solvents that are responsible for the hazardous emissions of VOCs.

1. Introduction

It is well known from the nature that lotus leaves are the best example of a non-wetting, super water repellent, and superhydrophobic surfaces. However, the superhydrophobicity of the lotus leaves does not come only from the epicuticular waxes, but also from their micro- and / or nano-scale hierarchical structures on top of the micropapillae [1]. Indeed, the combination of micro- and nano-scale structures (i.e., micron-sized papillae apart from each other by a micrometer scale distance and nanohair-like matters on each micropapillae) give lotus leaves the very high water CA but very low-sliding angle (SA). Therefore, mimicking

lotus leaves does not only require low-energy hydrophobic materials, but also needs to fabricate both micro- and / or nano-scale roughness on the top surfaces. Hence, surface roughness, combination of micro and / or nano-structures, plays the vital role to increase the water CA of the developed surfaces to the superhydrophobic range. Decisively, superhydrophobicity is attributed from both the surface chemical composition and the surface microstructure/roughness [2].

An enormous effort has already been made to develop lotus leaf-like micro-nanostructured superhydrophobic surfaces or coatings [3 – 16]. Among them, many different techniques were also employed to introduce desired micro and / or nano-roughness on the substrates of desired chemical and geometrical properties including plasma treatment [5, 11], chemical etching [8], chemical vapor deposition (CVD) [7], micropatterning [3, 4], lithography [12], etc. However, almost all of these techniques involved toxic solvent(s) usage that might be responsible for hazardous volatile organic compounds (VOC) emissions. However, powder coatings (PC) are considered as environmentally friendly as they eliminate the use of any solvent. In this paper, we will describe a solvent-free ultrafine powder coating (UPC) technology for creating polymeric superhydrophobic coatings on metallic substrates. The developed coatings are characterized by using scanning electron microscope (SEM) and compared with the microstructures of lotus leaf.

2. Experimental section

2.1. Preparation of superhydrophobic powder coatings

Superhydrophobic PCs were prepared by a solvent-free UPC technique using commonly available polymeric resins processed with nanosized additives. With this technique, ultrafine powder from polyester clearcoats with particle size between 15 and 20 mm were first produced. Since, these ultrafine powders fall in the category of Geldart Group C powders and did not flow well due to the dominant interparticle forces [17], special measures, by adding flow additives, were taken to overcome the flowability issue [18].

After resolving powders' flowability problem, low-energy nanoaddtives were added into the coating formulation to increase hydrophobicity of the coatings. At this stage 2.5 wt. % nanosized PTFE and 1.5 wt. % HNS (~ 100 nm average particle size) were dry-blended with the ultrafine polymeric resin mixtures so that they would provide superhydrophobicity as well as the desired micro- and nanostructures. The final powder mixture of ultrafine polymeric clear coat, nanosized flow additives, PTFE, and HNS were passed through a 32 μm sieve to further homogenize the mixture.

As shown in **Figure 1a**, polymeric resins, and curing, degassing, and flow agents were mixed and extruded to make homogeneous chips. The chips were then ground into ultrafine powders (15 – 20 μm) and dry blended with nanosized hydrophobic (PTFE and HNS) and flow additives. These ultrafine mixtures were electrostatically sprayed onto a grounded workpiece, and cured in a furnace (at 200°C, 10 min). Over-sprayed powders were recycled and reused.

Figure 1b illustrates the powder spraying and curing process. The powder mixture was sprayed with a corona spray gun (Surecoat, Nordson Corporation) on to an aluminum sample panel. Subsequently, the powder-coated substrates were cured in an oven at 200 °C for 10 min. Upon cured, the melted polymeric particles formed a homogeneous surface finish possessing

micro- and nanostructures as conceptualized in **Figure 1c**. However, due to the incorporation of hydrophobic particles into the coating formulation, the final coatings became superhydrophobic with desired micro- and nano-structures.

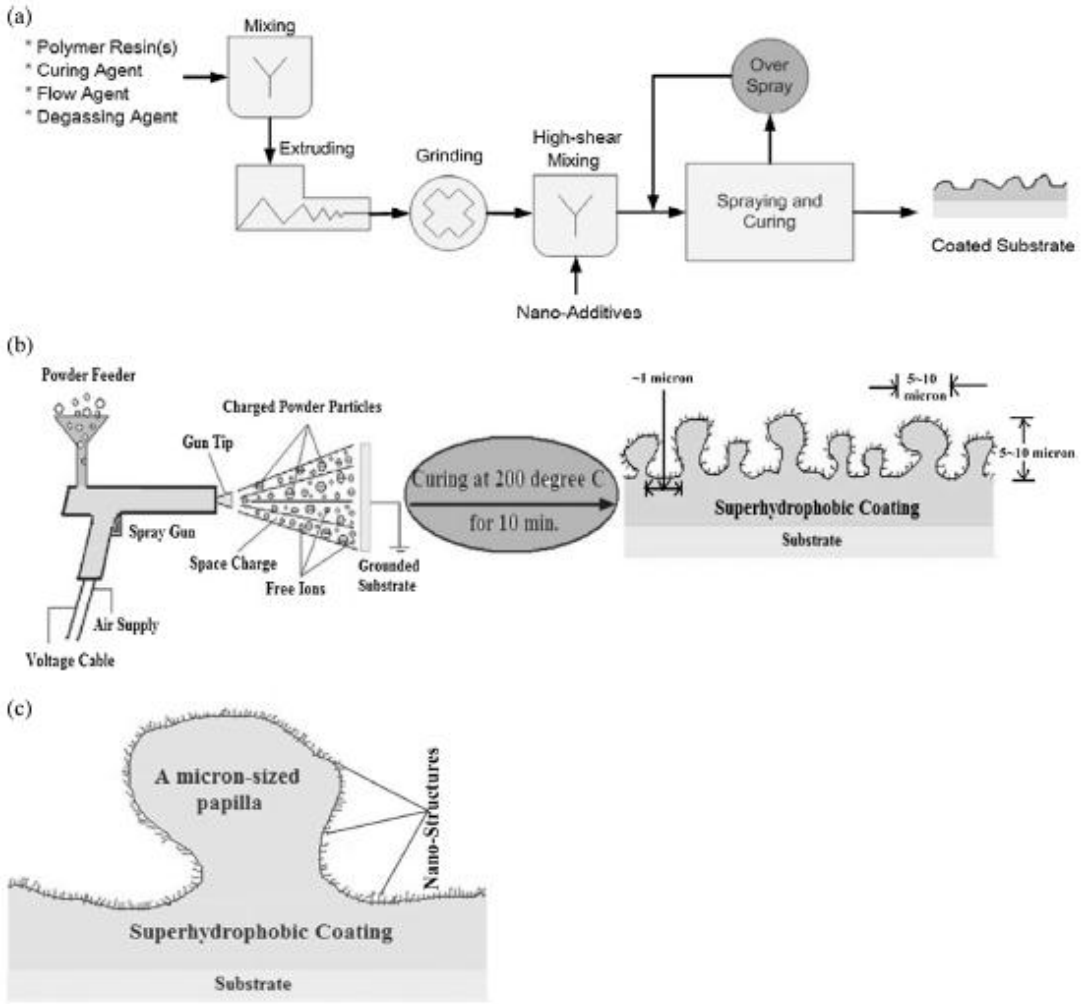

Figure 1. (a) Ultrafine polymeric PC process for superhydrophobic PC preparation. (b) Illustration of powder spraying and curing process. (c) Micro- and nano-structures in a micron-sized papilla.

2.2. Characterization of the developed coatings

2.2.1. Adhesion of the superhydrophobic coatings

The adhesion strength between the coating and the substrate was evaluated through an especially designed and fabricated loading system shown in **Figure 2**. Two aluminum rods of 10 mm diameter and 60 mm length were machined by turning machine. The polished face of each rod was brushed with a layer of super glue adhesive. The coated disc was loaded between the two brushed surfaces of the rods using two V-blocks. The arrangement was left to be cured / hardened for 5 min. Copper wires were introduced to the holes made at the ends of the two rods. The wires of the specimen were clamped to the crossheads of the MTS M/C, as shown in **Figure 1**. The maximum normal force applied on the coating sample, before being detached from the substrate, was measured.

Figure 2. Coating adhesion testing by MTS machine: coated samples were loaded as shown in the high-lighted section of the apparatus.

2.2.2. Scanning electron microscopy (SEM) of the superhydrophobic surfaces

The developed superhydrophobic surfaces were examined by SEM to verify their micro- and nano-structures. The prepared surfaces were cut into 10 mm × 10 mm square pieces which were mounted on metal stubs with the aid of adhesive carbon tape and were sputter coated with gold (15 nm thick layer). The gold-sputtered superhydrophobic surfaces were then carefully examined with a Hitachi S-2600 (Hitachi, Pleasonton, CA) SEM.

2.2.3. Contact angle and sliding angle measurements

Water CAs of the superhydrophobic surfaces were measured with a Rame–Hart 100 Goniometer equipped with a horizontal microscope. A 10ml droplet of deionized water was gently dispensed on the coated surfaces using a micrometric syringe (Gilmont Instrument). The static CA was measured by calculating the slope of the tangent to the drop at the liquid–solid–vapor interface line. The CA was measured in at least five different locations on the superhydrophobic panels. Statistical averages of the readings were reported. Moreover, SA was also used to evaluate superhydrophobicity of the developed coatings. SA was measured as the tilt angle at which the water droplet became unstable and rolled off from the surface.

2.2.4 . Durability test

A 100 % cotton cloth wrapped on a 1 × 1 × 1 cm^3 rubber head with 100 N normal force was exerted on the cured coating surfaces. The durability of superhydrophobicity was measured as the number of rubbing cycles performed before a significant change in water CA was observed.

3. Results and discussion

A solvent-free UPC technique, for the first time, has been utilized to develop superhydrophobic PC. Indeed, when the polymeric PC film was cured at 200 °C, the powder mixtures melted, homogenized, and spread onto the underlying substrates. During melting and spreading, the hydrophobic nanoparticles tended to move up to the top of the coatings and formed the nanostructures as the top-most layer on the cured polymeric resin. Moreover, due to the differences in surface energies between the nanosized hydrophobic PTFE and HNS, and

the other hydrophilic constituents of the mixture, micron-sized porous polymeric surfaces were developed upon melted and cured. Therefore, the micro porous nanostructured coatings resembled that of lotus leaf. Cross-sectional view of the finished superhydrophobic coatings was conceptualized in **Figure 1b**. **Figure 1c** further depicted a single micron-sized papilla that was covered with protruding nanostructures.

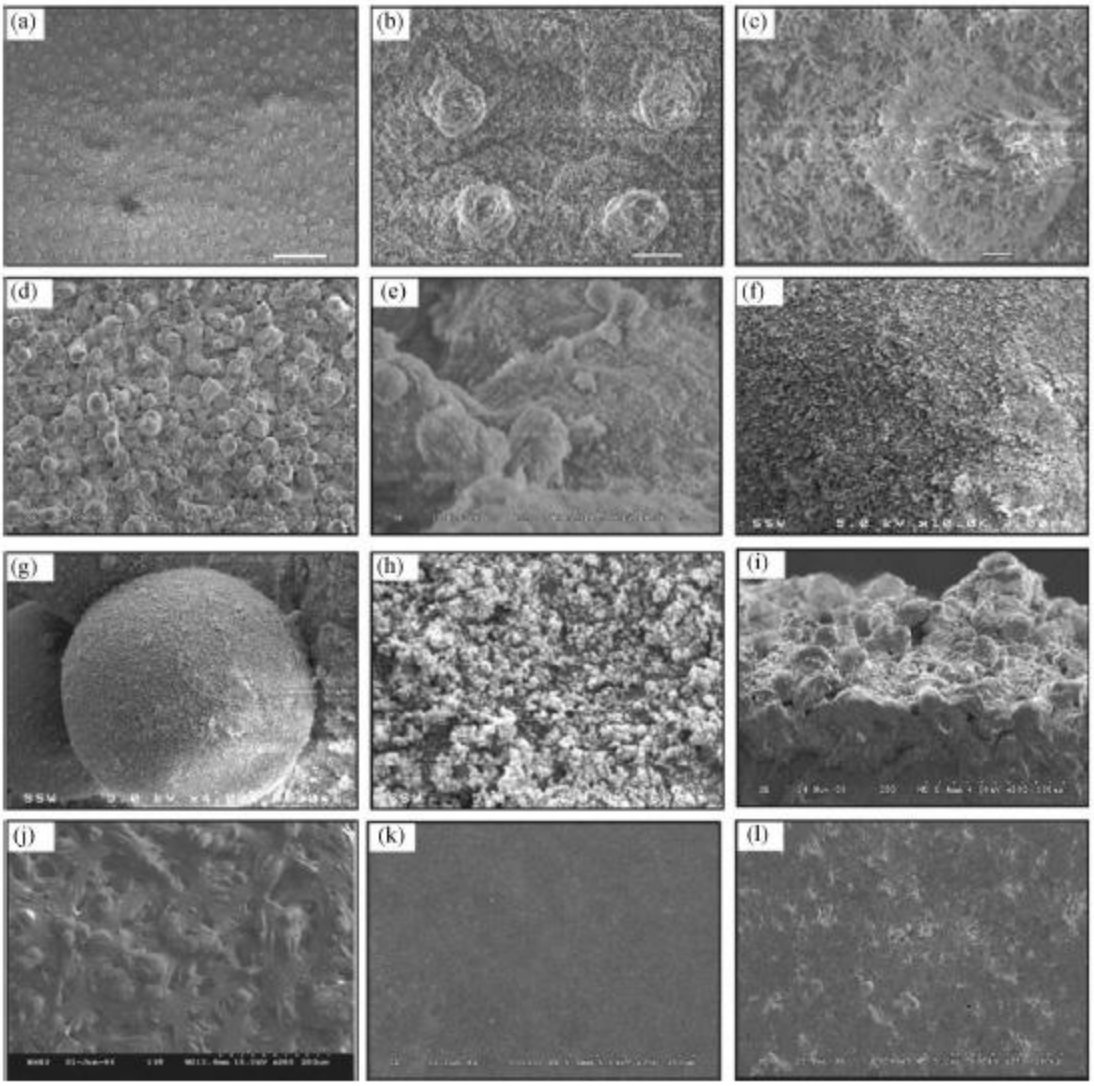

Figure 3. Micro- and nano-structures of lotus leaf (Nelumbo nucifera) (a–c) (Reproduced with permission from Ref. [19]. Copyright Royal Society of Chemistry, 2007) and that of superhydrophobic PC (d–i) and regular coatings and other hydrophobic coatings (j–l). (a) Top view of lotus leaf (bar = 50 μm). (b) Magnified view of lotus leaf taken from (a) (bar = 5 μm). (c) Magnification of a papillae from (b) (bar = 1 μm). (d) Top view of our superhydrophobic coating (bar = 100 μm). (e) Magnified section of (d) (bar = 5 μm). (f) Magnification of (e) (bar = 3 μm). (g) A micropapilla (bar = 7.5 μm). (h) Fabricated nanostructures on the micropapillae (bar = 600 nm). (i) Cross-sectional view of (d) (bar = 100 μm). (j). Top view of a regular coating (without any hydrophobic additive) (bar = 200 μm). (k) Top view of a coating containing 2 wt. % PTFE (bar = 200 μm). (l) Top view of a coating containing HNS only (bar = 200 μm).

SEM images confirmed the similarity of micro-and nano-structures present in the lotus leaf and in the developed superhydrophobic coatings. SEM images of **Figures 3a – c** showed the

double-scale hierarchical structures of lotus leaf in different magnifications [19] while **Figure 3d–I** showed the micro-nano-binary structures of the developed superhydrophobic PC. It is evident from these SEM images that the double-scale hierarchical structures of lotus leaf and of our superhydrophobic surfaces were almost interchangeable. Therefore, mimicking of lotus leaf was successfully achieved by UPC.

In particular, SEM image of Figure 3g depicts a single micropapilla (diameter ~ 7 mm) that is roofed with an enormous amount of nanostructures that is further magnified and shown in Figure 3h. The nano matters were 100 – 200 nm long and 40 – 70 nm in diameter; however, they formed bundles and developed submicron-sized (400 – 600 nm) valleys. Similar features (i.e., micron-sized elevations or micropapillae, submicron-sized valleys, and nanosized width of the nanostructures) of superhydrophobic surfaces were reported by other researchers with different approaches [20, 21]. In addition to the top views, Figure 3i shows the cross-sectional view of the superhydrophobic coating (shown in **Figure 3d**). The cross-sectional SEM image further confirmed the presence of micro- and nano-structures that made the developed coatings superhydrophobic in nature.

It is evident that the appropriate amount/ratio of low energy hydrophobic additives (i.e., PTFE and HNS) incorporated into the polymeric resin was responsible for those protruding micro-nano-textures. Our study showed that the ratio of PTFE to HNS of ~ 1.67 by which they were added to the polymeric resin resulted in the development of durable superhydrophobic coatings comprising of micro- and nano-structures. This claim is confirmed by the SEM images of another set of developed coatings (**Figures 3j – l**) that either did not contain any hydrophobic additive or did not possess optimum ratio of these additives. **Figure 3j** shows fairly smooth finish when neither PTFE nor HNS was used in the coating formulation and evidently did not exhibit superhydrophobicity. When 2 wt. % PTFE was included into the formula, porous structure were formed although they did not exhibit the desired combination of micron and nanosized features (**Figure 3k**).As a result, they did not achieve superhydrophobicity. Similarly, when only HNS was incorporated into the PC formulation keeping other ingredients the same, protruding micro-nanostructures were not formed as obviously (**Figur 3l**). Therefore, it is evident that the ratio of PTFE and HNS played a significant role in fabricating micro- and nano-structures onto the developed coatings, since our other trials involving different ratios of PTFE and HNS resulted in the existence of microstructures only or exhibited poor durability at the end.

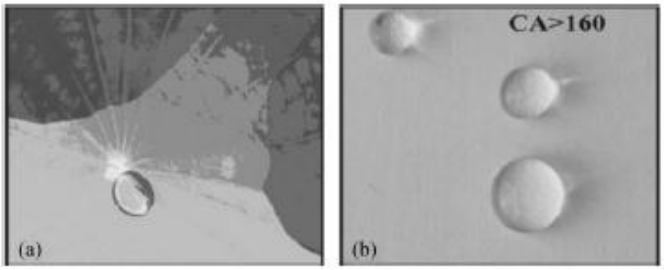

Figure 4. Water droplet formed sphere on lotus leaf (a) and on our superhydrophobic PC (b).

Figure 4 shows how easily water droplets formed spheres and rolled off on the lotus leaf and the comparison with polymeric superhydrophobic coating developed by UPC technology. On both surfaces water droplets formed very high CAs. The measured CA confirmed that the developed coating was as hydrophobic as the natural lotus leaf. Our superhydrophobic coatings

exhibited water CA of more than 160 °. Not only that, the water droplets were so unstable on the coated surfaces that they rolled off and ran away from the surfaces even when they were tilted less than 5 °. That gave the water SAs as minimum as possible, which is another important criteria for a surface to be superhydrophobic [4, 22]). It is interesting to report that while we tried to dispense them onto the coated surface to measure the water CA, the water droplets preferred more to be stick to the tip of the needle of the dispensing syringe. In some cases, water droplets repelled the coated surface so intensively that it was very difficult to place them on the superhydrophobic coatings. More interestingly, the droplets became unstable and ran away from the surface with an inclination of less than 5 °.

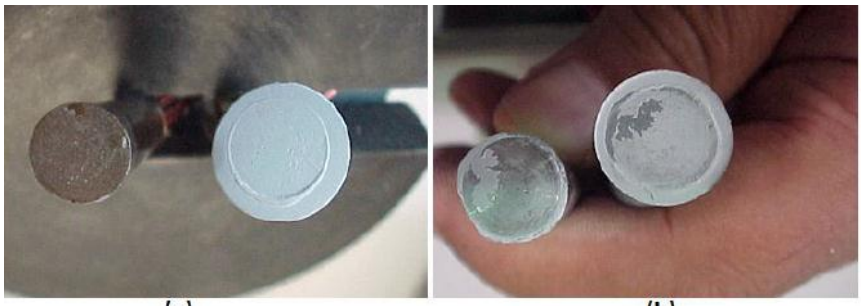

Figure 5. Adhesion tests; (a) before and (b) after being delaminated from the metallic substrate.

Furthermore, a novel coating sample loading system was designed and fabricated to measure the maximum load the coating can tolerate before being detached from the metallic substrates. The peak load and adhesion strength were found to be ~ 500 N and 11.3 MPa, respectively. Moreover, coating delamination is evident from **Figure 5** that shows two representative photographs of the same sample before (**a**) and after (**b**) being failed or detached under applied loads. It is evident from **Figure 3b** that the amount of the coating delaminated from the substrate is only about 30 % of the total area of the disc and the middle of the coating is still intact. This further exemplified the adhesion strength of the developed polymeric coatings. Indeed, superior coating adhesion could be attributed to the proper dispersion of nanoparticles, mechanical interlocking and chemical crosslinking of the polymers with other ingredients during the curing process of the coatings [23].

In addition to the superior coating adhesion, the developed surfaces also showed higher degree of durability in terms of their hydrophobicity. The wet cloth rubbing test revealed that the superhydrophobic coatings, which, were made of polyester clearcoat incorporated with nanosized PTFE, HNS, passed 2500 rubs with a change of water CA less than 10 °. In many cases, the coatings regained superhydrophobicity when they were dried up at ambient air. The reason behind the superb durability of the reported superhydrophobic surfaces lies in adhesion of the nano matters to the cured polyester resin and the rigidity of the micropapillae that indeed account into the overall length of the elevations/nanostructures.

Essentially, since no solvent was used in this unique polymeric superhydrophobic coating fabrication process, the reported UPC technique did not contribute into hazardous VOC emissions to the environment. Furthermore, this method also cut the cost of solvent(s). Moreover, solvent evaporation step (that consumes a significant amount of energy) was not needed to be included in our simple PC process. This further reduced the manufacturing costs of superhydrophobic surfaces.

4. Conclusion

Biomimetic polymeric superhydrophobic PC were successfully developed by the environmentally friendly, simple, and inexpensive PC technology. The created coatings revealed double-scale (both micro- and nano-) hierarchical structures that resembled those of natural lotus leaf. Subsequently they possessed infamous lotus effect as the finished surfaces superbly repelled water exhibiting very high water CAs. The developed coatings exhibited water CA of above 160 ° and SA of less than 5 ° that made them well comparable to the natural lotus leaf. The higher CA and lower SA were supposedly attributed to their unique dual-size (micro- and nano-scale) roughness leading to the minimization of surface energy. Furthermore, the developed superhydrophobic coatings were found to be superbly adherent to the substrates as well as retained their unique properties against the durability test performed.

Acknowledgements

The authors would like to acknowledge the funding from UAEU start-up research grant (MSM & AHM) and NSERC I2I grant (JZ) and to carry out this research.

References:

1. J. Zhai, et al. Physics, 2002, 31, 483.
2. S. Herminghaus. Europhys. Lett., 2000, 52, 165.
3. R. Furstner, et al. Langmuir, 2005, 21, 956.
4. M. Jin. Macromol. Rapid. Commun., 2005, 26, 1805.
5. S. H. Kim, et al. Langmuir, 2005, 21, 12213.
6. X. Y. Lu. Macromol. Rapid Commun., 2005, 26, 637.
7. M. Ma, et al. Macromol., 2005, 38, 9742.
8. B. T. Qian, Z. Q. Shen. Langmuir, 2005, 21, 9007.
9. H. Zhang, et al. Sci. Tech. Adv. Mater., 2005, 6, 236.
10. Q. Dou, et al. Macromol. Chem. Phys., 2006, 207, 2170.
11. S. C. Cho, et al. J. Mater. Chem., 2007, 17, 232.
12. Y. Lee, et al. Adv. Mater., 2007, 19, 2330.
13. H.-I. Hsiang, et al. Mater. Res. Bull., 2007, 42, 420.
14. P. V. Wal, U. Steiner. Soft Matter, 2007, 3, 426.
15. J. Seyfi, et al. Appl. Surf. Sci., 2015, 347, 224.
16. H. Wang, et al. Appl. Surf. Sci., 2015, 349, 724.
17. D. Geldart. Powd. Technol., 1973, 7, 285.
18. J. Zhu, H. Zhang. 2004, US Patent # 6,833,185.
19. Y. Liu, et al. J. Mater. Chem., 2007, 17, 1071.
20. B. He, et al. Langmuir, 2003, 19, 4999.
21. W. Lee, et al. Langmuir, 2004, 20, 7665.
22. A. Marmur. Langmuir, 2003, 19, 8343.
23. A. Lafabrier, et al. Prog. Org. Coat., 2014, 77, 1137.

MICROSTRUCTURE AND MECHANICAL PROPERTIES OF HEAT TREATED SELECTIVE LASER MELTING MANUFACTURED Ti-6Al-4V

D. D. Malka–Markovitz [1], A. Katsman [1], A. Shirizly [2], M. Bamberger [1]

[1] Technion – Israel Institute of Technology
Haifa, Israel
dennis@tx.technion.ac.il)
[2] RAFAEL
Haifa, Israel

Accepted October 19, 2015

Abstract

Investigation of microstructural evolution of pre and post heat treatment (HT) Selective Laser Melting (SLM) Ti-6Al-4V is presented. As received SLM samples composed of fine acicular α′ martensite within prior β grains were solution treated above the β-transus temperature, followed by a complementary HT within the α+β range. Non-monotonic change of microhardness as a function of HT temperature was observed. After low HT temperatures, the microstructure was composed mainly of martensitic α' phase, whereas, after high temperatures HT, bi-phasic microstructure with needle-like elongated α-phase grains and a mixture of lamellar α+β in between, was observed as the dominant microstructural component. The dependence of the properties and microstructure on heat treatment temperature will be discussed.

1. Introduction

Ti-6Al-4V is classified as an α+β alloy with 6 wt. % Aluminium stabilizing the hcp α phase and 4 wt. % Vanadium stabilizing the bcc β phase. The microstructures are divided into several types, namely grain boundary α ($\alpha_{G.B}$), primary α (called bi-modal microstructure when the globular α is surrounded by Widmanstätten plates), basketweave and martensite. Upon cooling from high temperatures (within or above the α+β region), the β phase transforms into several different types of morphologies, which strongly depend on the applied cooling rate.

Diffusion controlled transformations take place at slow cooling rates (CR < 20 C / s) [1], resulting in bi-modal microstructure when cooled from the α+β region. When cooled from the β region, initially, $\alpha_{G.B}$ is formed on the β grain boundaries, headed by nucleation and growth of parallel plates belonging to the same variant of the Burgers relationship inside the β grains, resulting in a Widmanstätten microstructure composed of several different orientation groups of parallel α plates within the retained β phase. This microstructure is often referred to as lamellar, whereas each group of parallel plates is referred to as α-colony. Slightly higher cooling rates favour nucleation over growth, resulting in a finer Widmanstätten structure composed of finer α-colonies. Past research [2] has shown that the colony size has a direct impact on mechanical properties.

High cooling rates (CR > 410 C / s) induce diffusionless transformation ($\beta \rightarrow \alpha' / \alpha''$) resulting in the formation of a martensitic phase which exists in two different structures: hcp distorted α′ acicular martensite and soft orthorhombic martensite – α″. Acicular α′ is distorted due to Vanadium supersaturation, whereas α′ is poorer in Vanadium, hence less distorted. The stability of the β phase depends on the dissolution of Vanadium. At temperatures close to β-transus ($T_\beta \approx 980$ °C), the β phase composed of 4 wt. % Vanadium and upon quenching, acicular α' is observed. Below the transus temperature, the β phase experiences a wide temperature-dependent compositional variation, as a lower temperature results in Vanadium enrichment of the β phase. Therefore, for low quenching temperatures, the β phase is stabilized and retained. This is the reason that, upon quenching from an intermediate temperature range of 750 – 900 °C, orthorhombic α″ is expected to form in addition to some retained β. A mixture of both α′ and α″ is expected upon quenching from and above the intermediate temperature range, however for higher quenching temperatures, the β phase is poorer in Vanadium, thus the formation of distorted α′ is favoured. During HT, the martensite phase rejects the supersaturated Vanadium atoms which remain in excess of the solubility limit, leading to its decomposition to produce thermodynamically stable α+β phases. For further information on Titanium alloys, the reader is referred to Refs. [3 – 5].

Selective Laser Melting (SLM) is an Additive Manufacturing (AM) technology which allows the producing components layer by layer out of powdered metal according to a 3D-CAD volume model. Detailed description of the process is brought in Refs. [6, 7]. SLM offers several distinctive advantages over the traditional processing, such as its ability to produce complex geometrical components, high material use efficiency and Near-Net-Shape production. However, due to the high temperature gradient induced by the laser beam and the subsequent fast cooling, the resulting component is thermally stressed and composed of non-equilibrium phases. In order to improve the mechanical properties of SLM fabricated components and satisfy the industrial needs, post HTs are required.

Very few information is available on SLM post HT Ti-6Al-4V in the literature. The goal of this research is to investigate the As-Received (AR) SLM manufactured Ti-6Al-4V microstructure and its evolution induced by different HTs.

2. Materials and methodes

The samples were manufactured by RAFAEL Israel using EOS M280 machine equipped with 200 W, Yb-fibre laser. Standard manufacturer conditions, as described in Ref. [8] were used to build the samples. Ti-6Al-4V 30μm powder with the composition given in **Table 1**, which ccorresponds to the ISO 5832-3, ASTM F1472 and ASTM B348 standards, manufactured by EOS, was used. All samples were stress relieved for 3 h at 650 °C in vacuum and furnace cooled (FC). These samples will be further addressed as the as-received (AR) samples.

Table 1. Chemical composition of the Ti-6Al-4V 30 μm powder used to produce SLM samples.

Ti	Al	V	O	N	H	Fe	C	Y
Bal.	6.19	3.98	0.12	0.018	0.02	0.18	0.004	< 0.001

Solution treatment of the AR samples was carried out for 1 hour at 1050^{0}C in an atmospheric environment, followed by Water Quenching (WQ). These samples will be further

addressed as Solution Treated and Water Quenched (STQ) samples. The HT was carried for two hours at the following temperatures: 950, 900, 850, 800, 750, 700 and 650 °C followed by FC with an approximate cooling rate of 0.02 C / s. These samples will be further addressed as Solution Treated, Water Quenched, Heat Treated and Furnace Cooled (STQHF) samples. The morphology was characterized by BSE mode in SEM (FEI Quanta 200 equipped with EDS), TEM (FEI Tecnai G² T20) and by optical microscopy (Reichert Polyvar). In order to reveal the microstructural features, the samples were etched with Kroll's reagent. The crystallography was examined by X-ray diffraction (Rigaku SmartLab) using Cu Kα radiation in a parallel beam configuration. The microhardness was measured with Shimadzu microhardness tester with an applied force of 2 kg for 15 s. In order to obtain statistical information, each sample was measured at 7 – 15 different locations. Young Modulus was estimated by ultrasonic wave measurements (Epoch 4) and the Yield Stress was estimated by tensile test of a dog bone sample, with its axis of symmetry perpendicular to the building direction.

3. Results and discussion

3.1. As received samples

The grain morphology of the Longitudinal Direction (LD) parallel to the SLM building direction and the Transverse Direction (TD) perpendicular to the building direction are shown in **Figures 1a** and **b**, respectively. The LD grain morphology was characterized by columnar grains elongated approximately parallel to the building direction. This grain morphology is typical of the SLM fabrication method [9, 10]. A high energy focused laser beam scans the deposited powder at a constant scan velocity. As the laser beam propagates, a steep temperature gradient is developed between the melted powder and its surroundings, leading to fast directional solidification as the previously deposited grains act as nucleation sites for epitaxial growth of the β phase. The rapid cooling from the β phase region induce non-equilibrium martensitic transformation β → α', resulting in long orthogonally oriented martensitic plates with acicular morphology located at the elongated prior β grains. The TD grain morphology is characterized by prior aquiaxed β grains (top view of the LD columnar elongated grains), which corresponds to the scan velocity of the laser beam composed of α' martensite with similar morphological features acquired for LD.

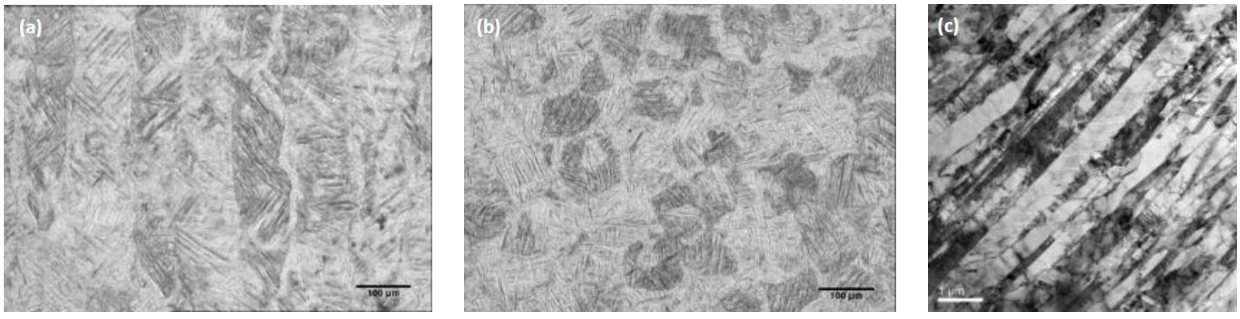

Figure 1. Microstructure of AR samples: (a) LD elongated grain morphology and (b) TD aquiaxed grain morphology, in (c) TEM higher magnification of acicular α'.

A higher magnification of the martensite phase (**Figure 1c**) reveals twins associated with the β → α' martensitic transformations. Various authors [5, 11, 12] reported the presence of dislocations and stacking faults within the α' phase.

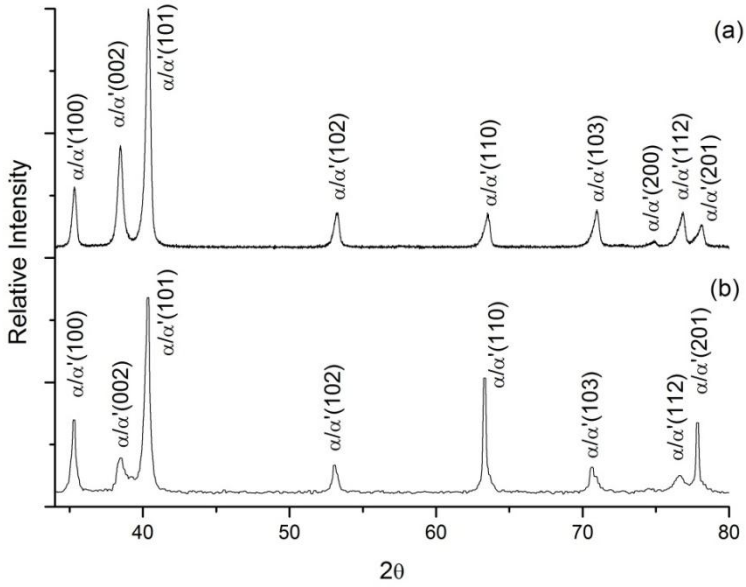

Figure 2. XRD patterns of (a) AR and (b) STQ samples.

The XRD pattern demonstrates broad peaks of hcp reflections, whereas reflections from the β-bcc phase were not detected (**Figure 2a**). Martensitic α' and α-phase have a hexagonal lattice with similar cell parameters, therefore it is complicated to distinguish these two phases from each other [13]. However, due to the fast cooling from the β region and the broadening of the peaks associated with microstrains developed during the martensitic transformations, it is reasonable to assume that the hcp phase is martensite.

3.2. Solution treated samples

STQ-TD shows significant grain growth and discernible grain boundaries compared to the AR-TD microstructure (**Figure 3a**). Acicular martensite α' was observed within the STQ grains. This result is in line with past research [1], which has shown that solution treatment of 1 hour at 1050^{0}C leads to complete decomposition of α' within the β grains (α'→β), which can grow in turn and transform into a new α' martensitic phase upon WQ.

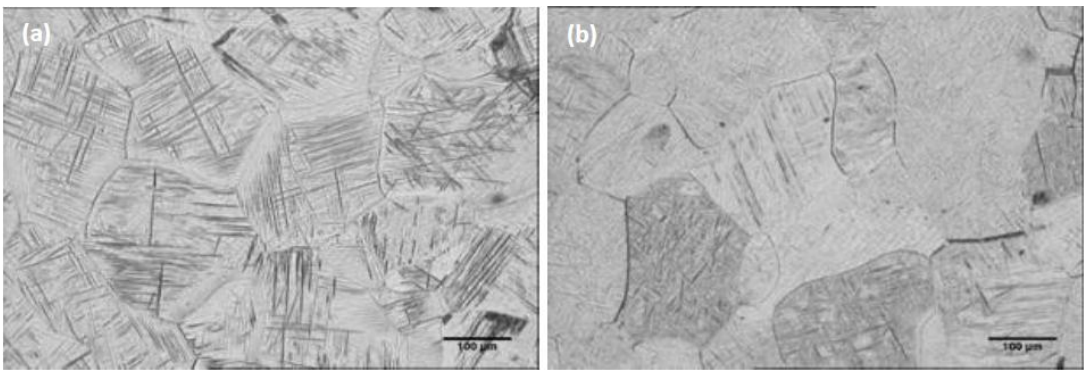

Figure 3. Microstructure of STQ: (a) aquiaxed morphology of TD and (b) LD.

The grain morphology of STQ-LD no longer contains elongated columnar grains and is composed mainly of equiaxial grains (**Figure 3b**). In order to investigate the LD grain morphology, two additional solution treatments were carried out. Samples held at 1050 °C for 1 h followed by FC or air cooling (AC) showed similar grain morphology with approximately the same typical dimensions. This leads to the conclusion that the grain morphology is

independent of the cooling regime, hence the structural changes occur during the solution treatment above the β-transus temperature. This result contradicts the observations of [14], claiming that the morphological change is due to a shearing mechanism which is related to martensitic transformations upon WQ from the β region.

One possible explanation for this observation can be correlated with the thermodynamically unstable β elongated columnar grains morphology, derived from the non-equilibrium SLM-fabrication. At 1050 °C, the thermal energy is sufficient to induce recovery and nucleation processes accounting for the new equiaxial grain morphology.

At higher magnification, STQ samples exhibit a martensitic microstructure characterized by long orthogonally oriented plates with acicular morphology, as obtained for AR. Microstructural investigation to evaluate the needle size of STQ and AR is still in progress.

The STQ-XRD pattern (**Figure 2b**) exhibited broad Ti-hcp reflections. No presence of β phase was discernible. As mentioned in the previous section, due to the high cooling rates and relatively broad peaks, it is reasonable to assume that the hcp phase is martensitic α'. Comparing the XRD pattern of AR to STQ, one can see the change in relative peak intensities, as can be vividly seen for {002} reflection. This observation is in line with the assumption that the nucleation process occurred during the isothermal holding at the β region. The newly formed grains have different crystallographic orientation, which results in different relative intensities acquired in STQ-XRD. For higher angles, a remarkable shift of STQ reflection towards lower angles is observed.

Table 2. Microhardness of AR and STQ samples.

	AR [HV 2 Kg]		STQ [HV 2 Kg]	
Microhardness	LD	TD	LD	TD
	370 ± 2	376 ± 5	400 ± 5	386 ± 9

Microhardness measurements that were carried out for both AR and STQ samples are presented in **Table 2**. In their research [14, 15] obtained higher hardness values for AR compared to STQ, resulting from the finer plate size of α' martensitic microstructure due to a high cooling rate which is typical of the SLM process. The higher microhardness of the STQ sample in the current study can be correlated with Oxygen dissolution during solutionizing in air. Kumar at al. demonstrated [16] a significant increase in microhardness of heat treated samples carried out in air due to Oxygen dissolution. This also explains the shift of hcp reflections in the STQ-XRD pattern to lower angles comparing to AR, due to the increase in the lattice parameters induced by oxygen dissolution within the Ti-hcp phase. Similar results were obtained in [17].

No significant difference between the TD and LD samples was observed, which implies that within the statistical error, TD and LD have similar microhardness properties. Past research showed that SLM-fabricated LD has preferential tensile properties [18, 19], however the observed variation is rather small.

3.3. Heat treated samples

STQHF LD and TD resolted in similar microstructural features, LD can be seen in **Figure 4**.

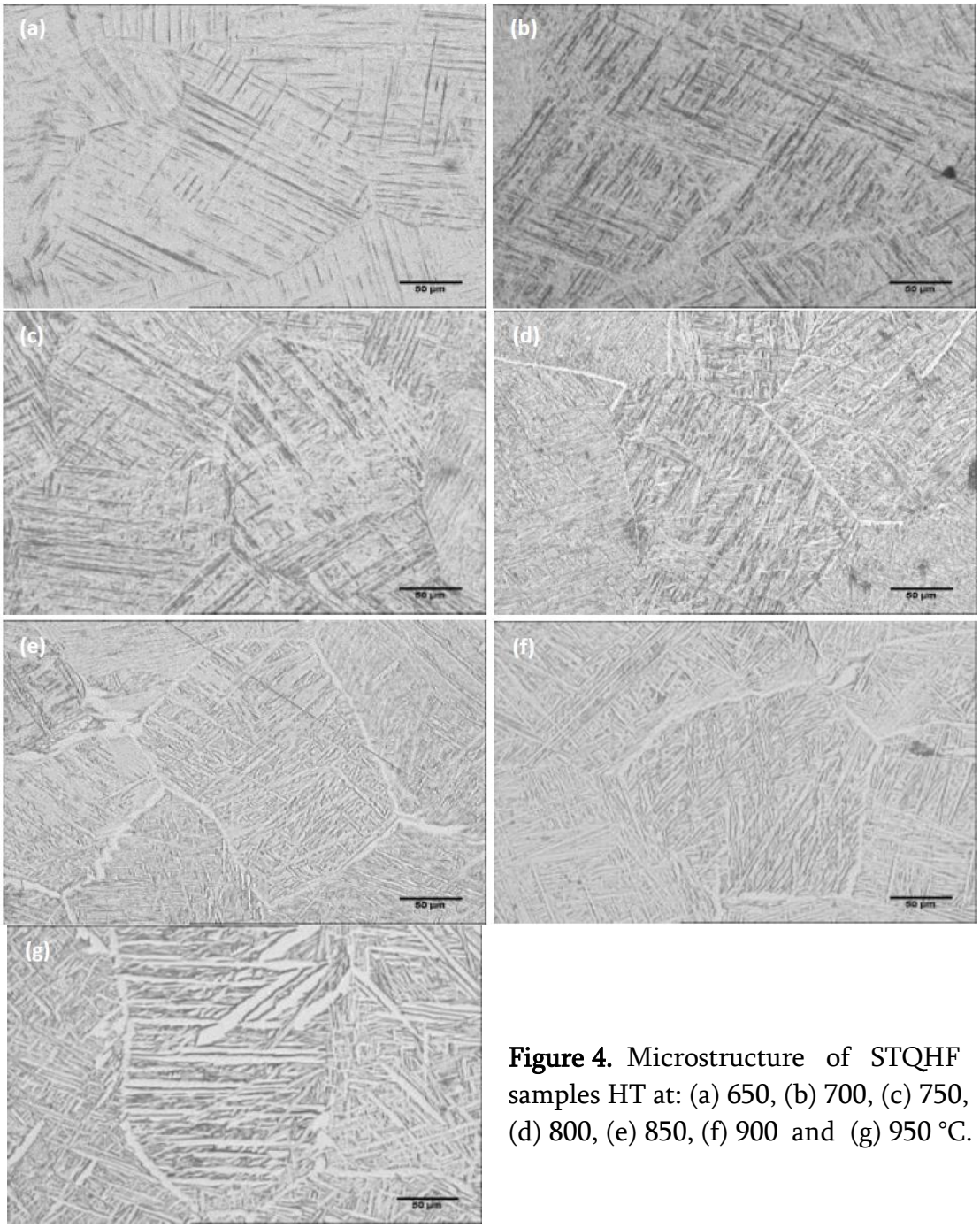

Figure 4. Microstructure of STQHF samples HT at: (a) 650, (b) 700, (c) 750, (d) 800, (e) 850, (f) 900 and (g) 950 °C.

Regardless of the HT temperature, similar size equiaxial primary β grains were observed. As expected, the size of STQHF grains corresponds with STQ since the sub-transus HT does not enable modification of the grain morphology.

Samples that were HT within the range of 650 – 800 °C (**Figure 4a**) exhibit typical martensitic microstructure comprised of long orthogonally oriented plates with acicular morphology. The BSE mode image of a sample heat treated at 650 °C (**Figure 5a**) exhibits a uniform contrast within the sample, with distinct darker martensitic plates. The dark contrast is associated with different crystallographic orientations rather than variation in the chemical composition. Grain boundaries can be seen in samples that were heat treated at 750 °C and above (**Figures 4c – g**), which is associated with precipitation of grain boundary-α phase ($\alpha_{G.B}$) in prior β grain boundaries.

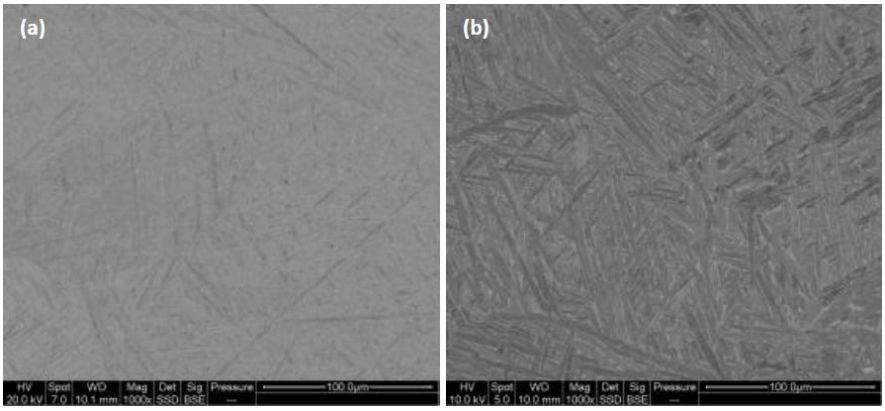

Figure 5. STQAF SEM-BSE mode of: (a) HT at 650 °C - no compositional contrast can be seen (b) HT at 900 °C – dark grey and bright grey contrast – α phase, white contrast – β phase.

In addition to martensite, elongated needle-like grains with typical α phase compositions (acquired by EDS) can be seen in a sample heat treated at 800 °C, which indicates partial decomposition of α' and formation of a thermodynamically stable α phase. A higher magnification revealed coarser plates with considerably less linear defects compared to AR and STQ samples (**Figure 6**). HRSEM-EDS and TEM-EDS composition investigation of samples heat treated below 800 °C is currently in progress.

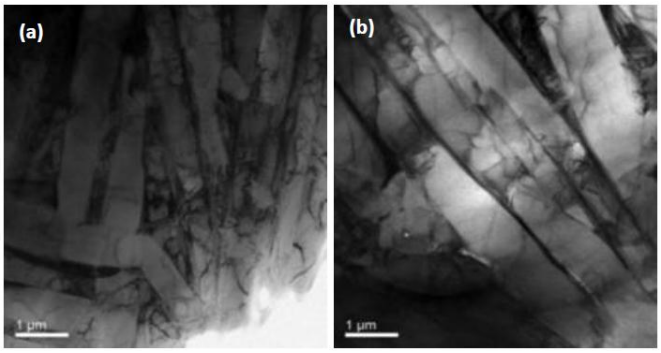

Figure 6. TEM images of samples heat treated at (a) 750 and (b) 800 °C.

HT within the range of 800 – 850 °C leads to high fracture martensite decomposition and subsequent formation of a biphasic microstructure (**Figures 4e – g** and higher magnification in **Figure 7**) composed of α+β lamellar morphology located between long parallel needle-like α grains, with very few colonies of untransformed martensitic plates. This result is in agreement with [20] observations. They showed that martensitic decomposition in Ti-6Al-4V is a time and temperature dependent process, corresponding with the Avrami equation. Full martensitic decomposition was achieved after HT at 800 °C for 1 h. The higher transformation temperature observed in the current study is expected due to oxygen dissolution in the samples mentioned in previous section. Oxygen is α phase stabiliser [4] which raises the α→β transformation temperature and subsequently the α'→α+β transition. Increased HT temperatures (900 – 950 °C) resulted in coarser bi-phasic microstructure. Similar microstructures were described in [21]. BSE mode in a sample heat treated at 900 °C (**Figure 5b**) demonstrated a vivid chemical composition difference between the darker, low Vanadium long parallel needle-like α plates (as well as smaller α plates within), and a Vanadium rich brighter β phase. EDS analysis at a range of 850 – 950 °C (**Table 3**) demonstrated typical compositions for the α and β phases. No statistical difference between the needle-like α and the lamellar α could be revealed.

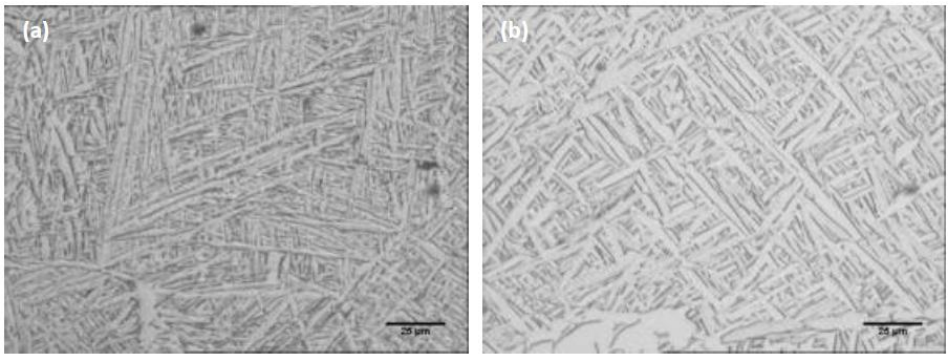

Figure 7. Microstructure of STQHF obtained at higher magnifications: images showing biphasic microstructure of samples heat treated at (a) 850 and (b) 950 °C.

Table 3. compositional EDS analyses of HT above 850 °C.

Sample	α [wt. %]			β [wt. %]		
	Ti	Al	V	Ti	Al	V
950 °C	92.0 ± 0.4	6.2 ± 0.1	1.8 ± 0.2	80.3 ± 1.6	2.2 ± 0.3	17.5 ± 1.9
900 °C	92.1 ± 0.5	6.0 ± 0.2	1.9 ± 0.5	79.7 ± 1.8	2.1 ± 0.1	18.2 ± 1.9
850 °C	91.8 ± 0.4	5.8 ± 0.1	2.4 ± 0.4	78.6 ± 0.8	2.5 ± 0.3	18.9 ± 1.8

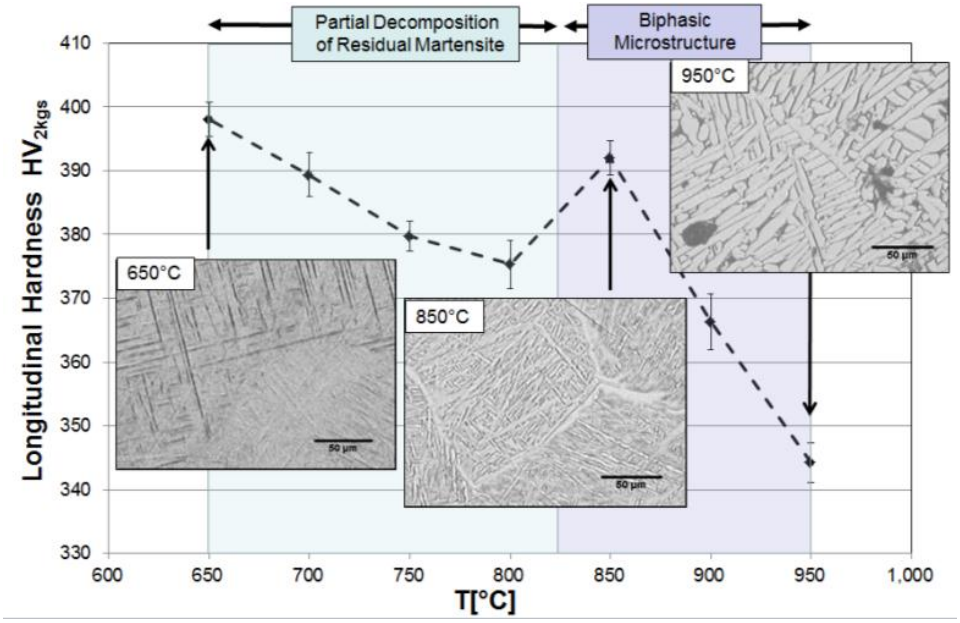

Figure 8. Microhardness measurements of STQHF samples, the attached OM presents a typical microstructure at different HT temperatures.

Microhardness measurements (**Figure 8**), characterized by a decrease of microhardness with the increasing HT temperatures (650 – 850 °C) followed by a sudden increase at 850^{0}C and a secondary decline with increasing temperatures (900 to 950 °C). A similar tendency was observed for TD microhardness measurements with no apparent statistical differences. The substantial microhardness drop observed at a HT range of 650 – 800 °C is related to the microstructure coarsening, strain relief of martensite and its partial decomposition (mentioned in the previous paragraph).

The increase of microhardness obtained at 850 °C resulted in high fracture martensite decomposition at this temperature, and subsequent formation of a bi-phasic microstructure

composed of relatively fine lamellar α+β morphology within elongated needle-like grains, as can be clearly seen in **Figures 7a** and **b**. The later decrease in microhardness (900 – 950 °C) is explained by coarsening of the bi-phasic microstructure (see inserts in **Figure 8**), and reported in [22].

Table 4. Tensile properties evaluation of STQHF.

Sample	Yield stress [MPa]	Young modulus [GPa]
800 °C	850	112
850 °C	980	115

Initial investigation to evaluate the tensile properties of STQHF samples heat treated at 800 and 850 °C was carried out and is presented in **Table 4**. The significantly higher yield stress obtained for a sample heat treated at 850 °C is in agreement with microhardness observations, which indicates variation in the mechanical properties and further confirms the assumed phase transformation taking place within the range of 800 – 850 °C. The elastic modulus of the two heat treated samples shows no significant difference.

4. Conclusions

AR SLM manufactured Ti-6Al-4V samples exhibit distinct grain morphology difference. LD samples are characterized by fine long orthogonally oriented martensitic plates with acicular morphology - α' within columnar prior β grains approximately parallel to the building direction, whereas TD is composed of similar to LD α' microstructure within aquiaxed prior β grains. Despite the morphological differences, both building directions suggest statistically similar microhardness values. Solution treatment above the β-transus modified the typical LD columnar prior β grain structure and resulted in a newly formed acicular α' within coarser aquiaxed prior β grains for both directions upon WQ.

Complementary sub-transus HT of the STQ samples were carried out, revealing microstructural changes and a non-monotonic variation of the microhardness values. HT at low temperatures (650 – 800 °C) resulted in coarsening of the martensitic phase, its partial decomposition and subsequent decline of the microhardness values. HT at 850 °C induced the transformation of metastable acicular martensite into thermodynamically stable biphasic microstructure composed of fine lamellar α+β morphology, which is located between long parallel needle-like α grains. The new fine biphasic microstructure gave rise to a sharp increase of microhardness. High temperature HT (900 – 950 °C) led to coarsening of the biphasic microstructure and a decline of microhardness.

References

1. T. Ahmed, H. J. Rack. Phase transformations during cooling in α+β titanium alloys." Mater. Sci. & Eng. A, 1998, 243, 1-2, 206-201.
2. G. Lütjering. Influence of processing on microstructure and mechanical properties of (α+β) titanium alloys. Mater. Sci. & Eng. A ,1998, 243, 1-2, 32-45.
3. M. J. Donachie. Titanium: A Technical Guide (2nd Ed.). 2000, ASM Int.
4,. G. Lütjering, J. C. Williams. Titanium. 2007, Berlin – Heidelberg: Springer.

5. S. Banerjee, P. Mukhopadhyay. 2010. Phase Transformations: Examples from Titanium and Zirconium Alloys.
6. B. Vandenbroucke, J.-P. Kruth. Selective laser melting of biocompatible metals for rapid manufacturing of medical parts. Rapid Prototyping J., 2007, 13, 4, 196-203.
7. C. K. Chua. Rapid Prototyping - Principles and Applications. 2010, John Wiley & Sons.
8. EOS E-Manufacturing Solutions. 2015. http://www.eos.info/SYSTEMS_SOLUTIONS /METAL/SYSTEMS_EQUIPMENT/EOSINT_M280
9. H. K. Rafi, N. V. Karthik, H. Gong, Th. L Starr, B. E. Stucker. Microstructures and mechanical properties of Ti6Al4V parts fabricated by selective laser melting and electron beam melting. J. Mater. Eng. & Performance 2015, 22, 12, 3872-3883.
10. M. Yan, P. Yu. An Overview of Densification, Microstructure and Mechanical Property of Additively Manufactured Ti-6Al-4V – Comparison among Selective Laser Melting, Electron Beam Melting, Laser Metal Deposition and Selective Laser Sintering, and with Conventional Po. 2015.
11. H. Matsumoto, L. Bin, S.-H. Lee, Y. Li, Y. Ono. Frequent occurrence of discontinuous dynamic recrystallization in Ti-6Al-4V alloy with α′ martensite starting microstructure. Metall. & Mater. Trans. A, 2013. 44, 7, 3245-3260.
12. H. Beladi, Q. Chao, G. S. Rohrer. "Variant Selection and Intervariant Crystallographic Planes Distribution in Martensite in a Ti–6Al–4V alloy. Acta Mater., 2014, 80,478-489.
13. M. T. Jovanović, S. Tadić, S. Zec, Z. Mišković, I. Bobić. The effect of annealing temperatures and cooling rates on microstructure and mechanical properties of investment cast Ti–6Al–4V alloy. Mater. & Design, 2006, 27, 3, 192–199.
14. T. Vilaro, C. Colin, J. D. Bartout. As-fabricated and heat-treated microstructures of the Ti-6Al-4V alloy processed by selective laser melting. Metall. & Mater. Trans. A, 2011, 42, 10, 3190-3299.
15. I. Yadroitsev, P. Krakhmalev, I. Yadroitsava. Selective laser melting of Ti6Al4V alloy for biomedical applications: temperature monitoring and microstructural evolution. J. Alloys & Comp., 2014, 583, 404-409.
16. S. Kumar, T. S. N. S. Narayanan, S. G. S. Raman, S. K. Seshadri. thermal oxidation of Ti6Al4V alloy: Microstructural and electrochemical characterization. Mater. Chem. & Phys., 2010, 119, 1-2, 337-346.
17. S. Malinov, W. Sha, Z. Guo, C. C. Tang, A. E. Long. Synchrotron X-Ray diffraction study of the phase transformations in titanium alloys. Mater. Character., 2002, 48, 4, 279-295.
18. H. Kh. Rafi, Th. L. Starr, B. E. Stucker. A comparison of the tensile, fatigue, and fracture behavior of Ti-6Al-4V and 15-5 PH stainless steel parts made by selective laser melting. Int. J. Adv. Manuf. Technol., 2013, 69, 5-8, 1299–1309.
19. M. Simonelli, Y. Y. Tse, C. Tuck. Effect of the build orientation on the mechanical properties and fracture modes of SLM Ti–6Al–4V. Mater. Sci. & Eng. A, 2014, 616, 1-11.
20. F. X. Gil Mur, D. Rodríguez, J. A. Planell. Influence of tempering temperature and time on the α′-Ti-6Al-4V martensite. J. Alloys & Comp., 1996, 234, 2, 287-289.
21. L. Facchini. Microstructure and Mechanical Properties of Biomedical Alloys Produced by Rapid Manufacturing Technologies. Ph.D Thesis, 2010.
22. B. Vrancken, L. Thijs, J.-P. Kruth, J. Van Humbeeck. Heat treatment of Ti6Al4V produced by selective laser melting: Microstructure and mechanical properties. J. of Alloys & Comp., 2012., 541, 177-185.

NANO-CRYSTALLINE DIOPSIDE SYNTHESIZED USING MECHANICAL ACTIVATION PROCESS AS A NOVEL BIOCERAMIC TO USE MEDICAL PURPOSES; PREPARATION AND CHARACTERIZATION

R. Ghasemi [1], H. Gheisari [2], E. Karamian [1], M. Abdellahi [1], N. Rafiei [3]

[1] Islamic Azad University – Najafabad Branch
Advanced Materials Research Centre
Najafabad, Isfahan, Iran
rezaowsalou@gmail.com
[2] Islamic Azad University – Lenjan Branch
Department of Mechanical & Industrial
Isfahan, Iran
[3] Islamic Azad University – Shahreza Branch
Department of Technical & Engineering
Isfahan, Iran

Accepted October 19, 2015

Abstract

Diopside ($CaMgSiO_6$) belongs to the group of silicate biomaterials which helps osteoblasts to grow and differentiate. In this research, diopside powder was synthesized by mechanical activation method as a solid state process. Samples were composed of a blend of calcite, silica and MgO powder with 26, 55.5 and 18.5 wt. %, respectively. The materials were milled by high energy ball mill using ball-to- powder ratio 20 : 1 and rotation speed of 600 rpm for 4, 8 and 10 h. The mixture mechanical activated has been heated at 1100 °C for 2 h. XRD, SEM and BET performed on the samples to characterize. According to XRD results, the patterns show that diopside phase, with crystal size of 30 – 50 nm, were appeared in the sample mechanical activated for 8 and 10 h. Energy transferred to starting materials (23.9 MJ / g), leads to the synthesis temperature reduces to 1100 °C.

1. Introduction

Orthopaedic prosthesis has become an established treatment method since their introduction over 40 years ago. Diopside and hydroxyapatite have excellent bioactivity and are osseoconductive, allowing bone cells to grow on its surface. For this reason they have been used successfully in dentistry for many years [1]. Diopside ($CaMgSiO_6$) belongs to the group of silicate biomaterials and they have the ability to release silicate ions at a definite concentration which helps osteoblasts to grow and differentiate [2]. Also $CaSiO_3$ and akermanite ($Ca_2MgSi_2O_7$) ceramics induce good in-vivo bone formation and better material degradation compared to β- tricalcium phosphate biomaterial. This suggests silicate ceramics have potential application in bone tissue regeneration [3]. Diopside is very similar to akermanite and $CaSiO_3$. Only it has relatively slower degradation rate [4]. Diopside is a mineral belonging to the pyroxene family,

in particular it is an inosilicate with a single calcium and magnesium chain, whose chemical formula is $CaMg(SiO_3)_2$. Further it has been confirmed that the diopside possess good bioactivity and excellent bending strength, fracture toughness both in-vitro and in-vivo [5]. In that respect presently bioactive ceramics like HAP and β-TCP lack adequate mechanical strength, this limits their application in load bearing area. On the other hand, calcium silicate and bio glass have relatively quick degradation rate. Considering all these, diopside could therefore be considered, to be potential biomaterial for artificial bone and orthopaedic prosthesis. The structure of diopside is mono clinic (**Figure 1**) and the cell parameters are as follows: a = 9.67, b = 8.899, and c = 5.251 Å; $\alpha = 90$, $\beta = 74.17$, and $\gamma = 90$ °.

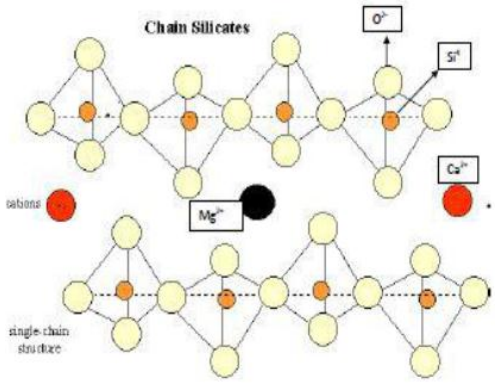

Figure 1. Structure of diopside [6].

When artificial materials are implanted into bones to improve functional impairment associated with bone defects, the materials are coated with fibrous membrane and are separated from the surrounding area. However, over the past few years, inorganic materials that come into direct contact and strongly bind with bone have seen greater application. Most of these materials are ceramics, although ceramics have low mechanical strength. diopside, a relatively strong bioactive ceramic, has recently been developed.

In the present study, the synthesis nano-crystallite structure diopside powder was prepared by mechanical activation, to use as a new biomaterials for medical purposes. In fact, energy transferred to the starting materials, causes the materials to be mechanically activated and leads to synthesis temperature reduces to low temperatures.

2 . Materials and methods

Amount of raw materials required for synthesis of 10 g diopside sample. Diopside was synthesis with talc (Merck 99 % purity), calcite (Merck 99 % purity) and silica (Merck) 4.74, 3.76, 1.50 wt. %, respectively. This compound was heated for 2 h at 1100 °C. Phase structure analysis was carried out by X-ray diffraction (XRD) (Philips X'Pert-MPD diffractometer with Cu Ka radiation (λ_1 = 0.15418 nm) over the 2θ range of 10 – 90 °). The obtained experimental patterns were compared to the standards compiled by the Joint Committee on Powder Diffraction and Standards (JCDPS) which involved card # 011-0654 for diopside phase. Diopside crystalline size of was determined using XRD patterns and modified Scherrer equation. Scanning electron microscopy (SEM) analyses evaluations were performed using a Philips XL30 to investigate the morphology. The powder prepared coated with Au by spraying, low vacuum and 25 kV accelerating voltage. Mechanical activation has been done for 4, 8 and 10 h. And BET technique has been done.

2.1. The modified Scherrer equation

The modified Scherrer equation can provide the advantage of decreasing the sum of absolute values of errors, $\sum(\pm \Delta \ln \beta)^2$, and producing a single line through the points to give a single value of intercept $\ln (K\lambda / L)$ [7].

2.2 Energy transfer

Figure 2 shows the schematic diagram of the planetary ball mill and the vial: indicating by W_P and W_v the absolute angular velocity of the plate of the mill and of one vial and by R_P and R_v the vectorial distances from the centre of the mill to the centre of the vial and from the centre of the vial to its periphery (vial radius), it can be shown the absolute velocity of one ball leaving the wall is given by:

$$V_b = [(W_p R_p)^2 + W_v^2 (R_v - d_b / 2)^2 (1 - 2W_v / W_p)]^{1/2}, \quad (1)$$

the velocity of the ball with d_b diameter, after the hits, equals that of the inner wall and can be expressed as follow:

$$V_S = [(W_p R_p)^2 + W_v^2 (R_v - d_b / 2)^2 + 2W_p W_v R_P (R_v - d_b / 2)]^{1/2} . \quad (2)$$

We have to consider now the mechanism of energy transfer. When the ball is thrown, it possesses the kinetic energy:

$$E = 1/2\, m_b V_b^2 . \quad (3)$$

After a short succession of hits, during which decreasing fractions of kinetic energy are released, the balls residual energy becomes:

$$E = 1/2\, m_b V_S^2 \quad (4)$$

and the total energy released by the ball during the series of collision events is given by:

$$\Delta E_b = E_b - E_S = -m_b [W_v^3 (R_v - d_b / 2) / W_p + W_p W_v R_p](Rv - d_b / 2). \quad (5)$$

with the assumption that the total energy transferred by the planetary mill per gram of reactant mixture and required to synthesis of nano-structure powders is a constant value, the Burgio model defines this amount of energy by the following expression:

$$E_t / g = \frac{(N_b \varphi_b f_b K_a m_b)[W_v^3 (R_v - d_b / 2) / W_p + W_P W_v R_P](R_v - d_b / 2)t}{m_{ch}} = A(J / g), \quad (6)$$

where N_b is the number of balls; K_a is a constant that accounts for the elasticity of collisions, and a value of 1 represents perfectly inelastic collisions; m_{ch} is the mass of the powder charge; and t is the synthesis time measured. φ_b is a parameter that accounts for the degree of filling of the vial; f_b is the frequency with which the balls are launched against the opposite wall of the vial.

$$\varphi_b = 1 - \left(\frac{d_b^3 N_b}{\pi R_v^2 H_v} \right)^{\varepsilon} , \quad (7)$$

$$f_b = \frac{K(W_p - W_v)}{2\pi}, \quad (8)$$

$$m_b = \frac{\pi \rho_b d_b^3}{6} . \quad (9)$$

where H_v, ρ_b are respectively the height of the vial and the density of balls? K is a proportionality constant and is approximately equal to unity and ε is a parameter called ball diameter distribution coefficient depending on the balls diameter [8].

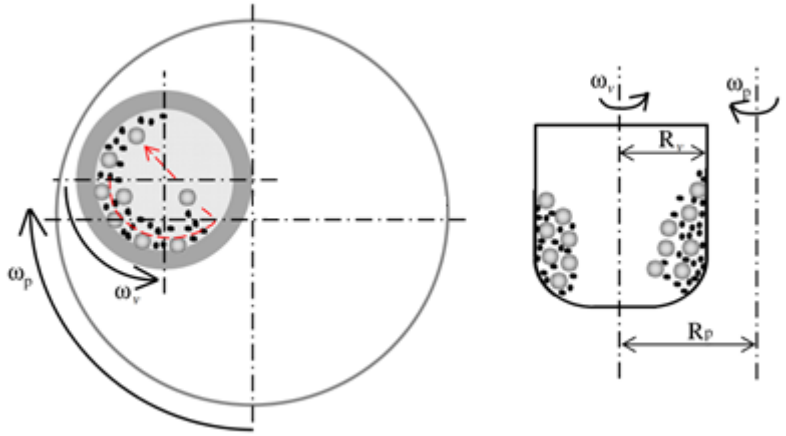

Figure 2. The schematic diagram of the planetary ball mill and the vial.

3. Results

3.1. SEM observations

Figures 3 – 5 show the SEM micrographs of the starting materials milled and heated at 1100 °C for 2 h.

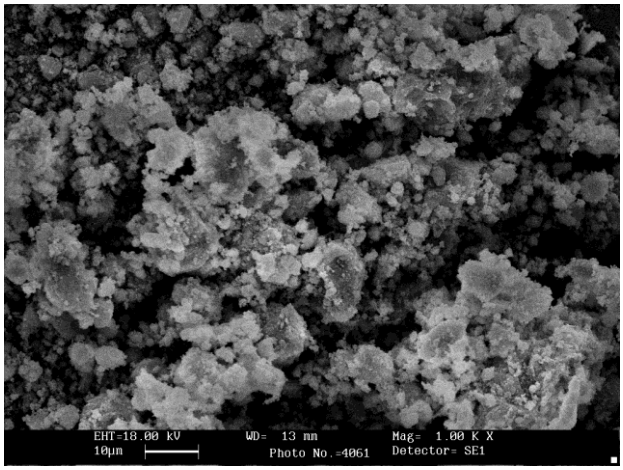

Figure 3. SEM of powder mixture milled for 4 h and heated at 1100 °C for 2 h.

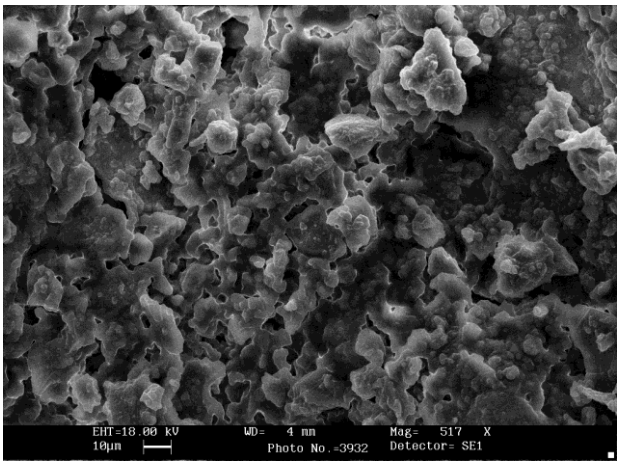

Figure 4. SEM of powder mixture milled for 8 h and heated at 1100 °C for 2 h.

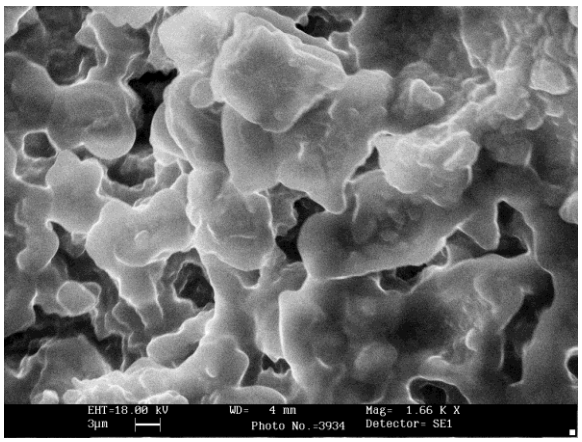

Figure 5. SEM of powder mixture milled for 10 h and heated at 1100 °C for 2 h.

3.2. XRD results

Figures 6 – **8** show XRD patterns of the samples milled for 4, 8 and 10 h and heated at 1100 °C for 2 h. According to XRD patterns (**Figures 7** and **8** – all peaks belong to diopside phase), pure diopside were synthesized in the sample milled for 8 and 10 h. In fact, diopside peaks (Standard card no. 00-011-0654) were observed in these patterns indicating the formation of pure diopside after heating in the samples milled for 8 and 10 h.

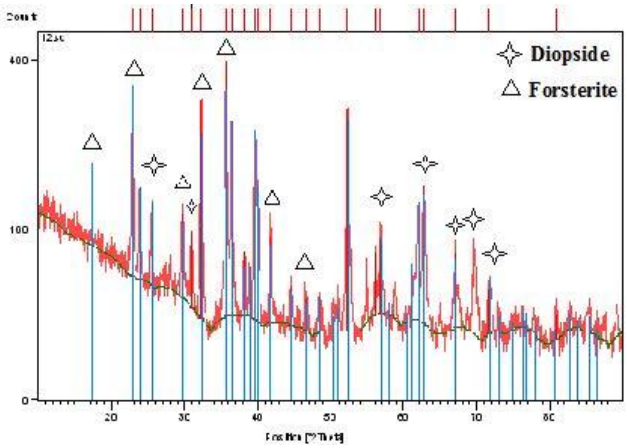

Figure 6. XRD pattern of powder mixture milled for 4 h and heated at 1100 °C for 2 h.

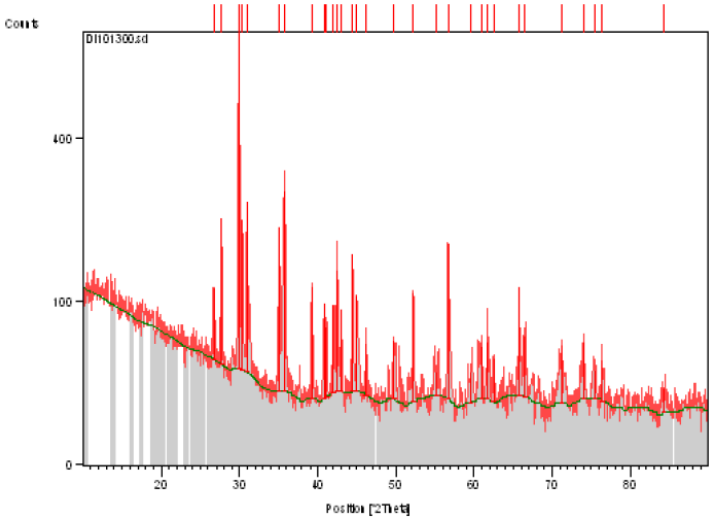

Figure 7. XRD pattern of powder mixture milled for 8 h and heated at 1100 °C for 2 h.

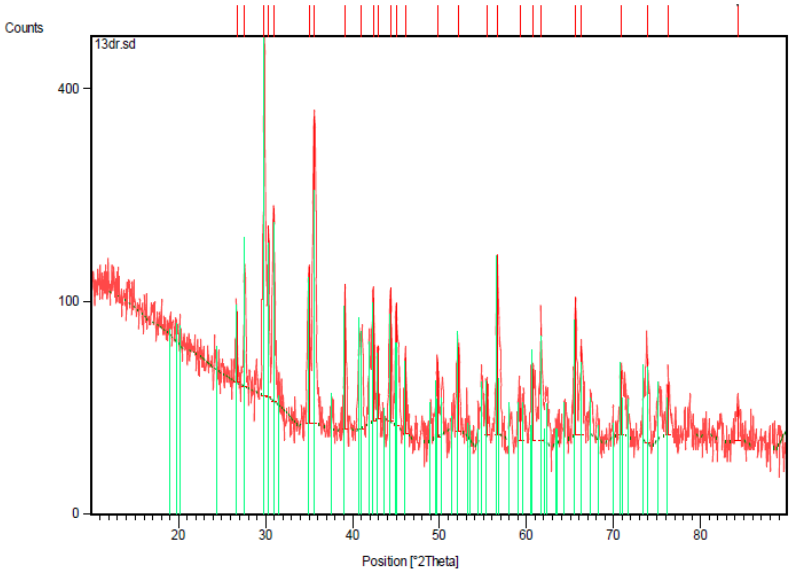

Figure 8. XRD pattern of powder mixture milled for 10 h and heated at 1100 °C for 2 h.

3.3. Estimation of crystal size

At this sample, **Figure 9**, the linear regression plot is obtained as $y = 3.6124\,x - 5.4836$. This is equivalent to Ln β = ln (1 / Cos θ) + ln ($K\lambda$ / L). From this line, the intercept is -5.4836 and $e^{-5.4836} = K\lambda / L$ and L = 330 Å = 33 nm. So, diopside crystallinity size average is 33 nm.

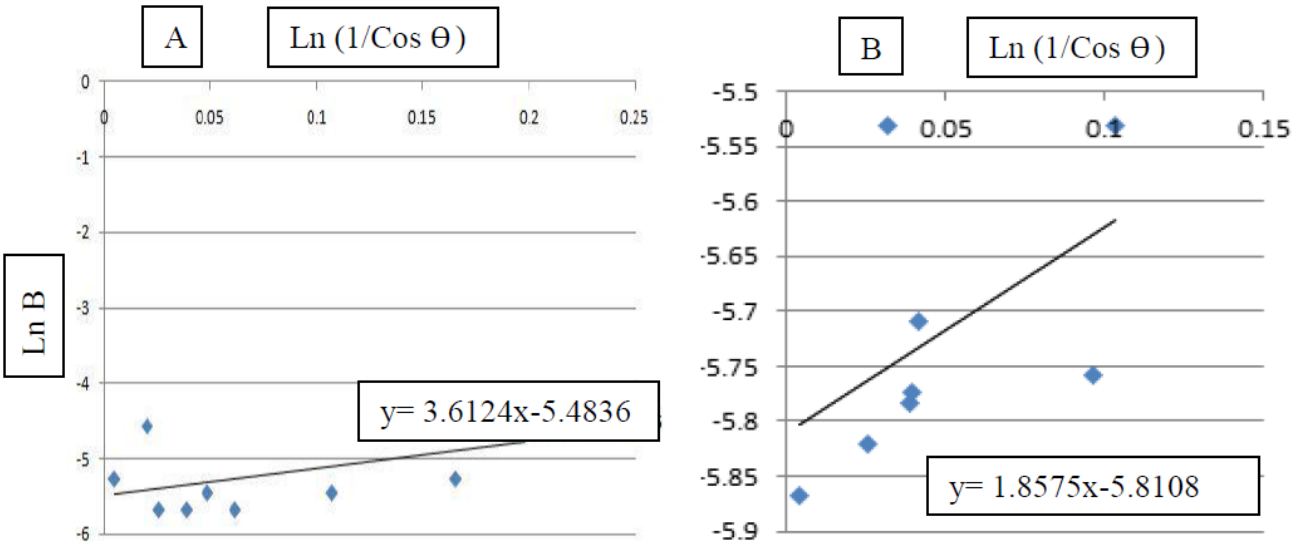

Figure 9. Plot of ln β vs. ln (1 / Cos θ) of the sample milled for 8 h (A) and for 10 h and heated at 1100 °C for 2 h (B).

Based on the same calculations for **Figure 9** – right, $y = 1.8575\,x - 5.8108$, Diopside crystal size is 46 nm. In fact, according to XRD results and modified Schererr equation it can calculate that the crystals size average of diopside synthesized are between 30 – 50 nm.

3.4 . PSA and BET results

The specific surface area of the prepared powder was calculated from the N_2 gas adsorption isotherms using the single point BET technique. The average particle size of the

prepared powder, assuming that the synthesized particle was spheroid. The particle size, D, is given by Eq. (10):

$$D = 6000 / S_{BET}\, d, \quad (10)$$

$d_{diopside} = 3$ g / cm^3, $S_{BET} = 4.76$ m^2 / g, $D = 428$ nm,

where S_{BET}, specific surface area, and d is the true density. PSA graph shows that average particle size is 589 nm. But, according to BET result, the average particle size is calculated 428 nm by Eq. (10).

The size distribution of particles was determined by PSA (**Figure 10**).

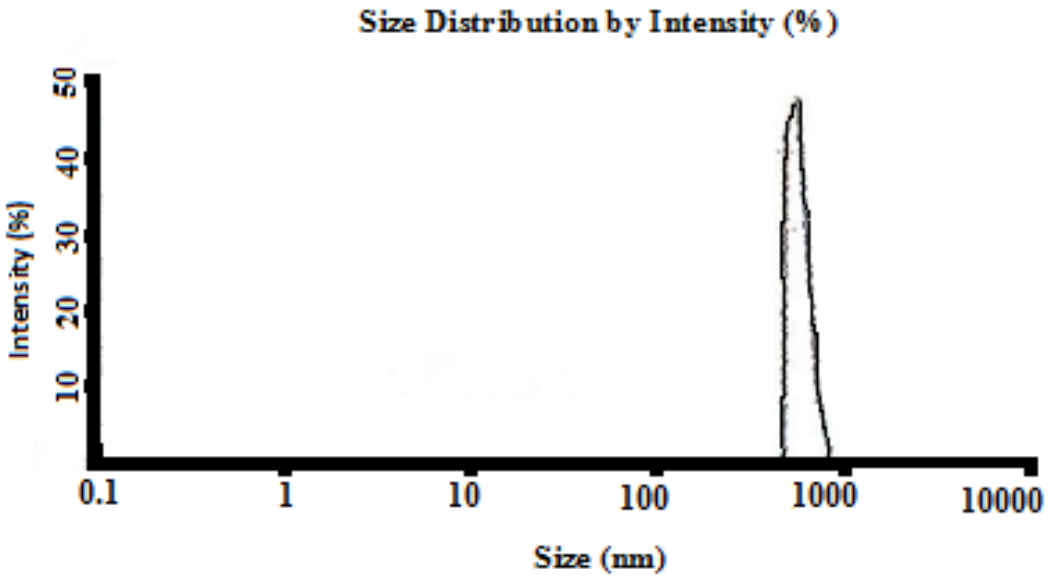

Figure 10. PSA of the starting materials milled for 10 h.

Therefore, assuming that the synthesized particles were spheroid, the BET equation result is acceptable. In fact, some of the particles are not spheroid.

3.5. Energy transfer analysis

Considering the results of optimization, **Table 1**, is presented for the object of minimum cost function, $W_v = 1.32W_p$. It means that the vial spinning rate should be higher than the plate spinning rate (in the opposite direction). On the other hand, $\varepsilon = 0.398$ which means that the ball size distribution is close to 40 %. The number of ball categories, s, is thus:

$$N_b = 4 \text{ and } \varepsilon = 0.4 \implies s = \text{Integer } (0.4 \times 4) = 1. \quad (11)$$

According to balls size and above interpretation one can wright:

$$d_b = 15,\ N_b = 4,\ S = 1 \implies (4 \times 15 \times 1) = 60). \quad (12)$$

So we can say that the size of balls used in proposed design should be 10 mm for the maximum energy transfer to the raw materials.

According to the ball mill parameters given in the Table 1 and Eq. (6), it was concluded that the energy transfer by the planetary mill per gram of the materials mixture for 8 and 10 h milling time are:

$E_{t/g} = 23.9$ MJ / g for 8 h (milling time)

and

$E_{t/g} = 29.9$ MJ / g for 10 h (milling time).

Table 1. The milling parameters optimized values in planetary ball mill.

Symbol	Milling parameters	Optimized values
N_b	Number of balls	4
d_b	Balls diameter (m)	0.015
R_v	Vial radius (m)	0.035
H_v	Vial height (m)	0.070
ε	Ball size distribution coefficient	0.398
W_p	Velocity of the plate (rad / s)	62.80
W_v	Velocity of vial (rad / s)	82.89
R_p	Distance between the center of the plate and the center of the vial (m)	20.0

4. Discussion

According to XRD patterns (**Figures 7** and **8**), pure diopside were synthesized in the sample milled for 8 and 10 h. In fact, diopside peaks (Standard card no. 00-011-0654) were observed in these patterns indicating the formation of pure diopside after heating of the samples milled for 8 and 10 h. According to XRD results and modified Scherrer equation it can calculate that the crystals size average of diopside synthesized are between 30 – 50 nm.

Based on BET result and above calculation and their comparison with PSA graph, it can conclude that particles size average of the starting materials milled for 10 h are in submicron range.

Figures 4 and **5** show the SEM micrographs of the heated powder and crystals of diopside were clearly visible. The SEM observations indicate that the samples with 8 and 10 h mechanical activation have glassy surface. These glassy zones can be belong to diopside phase, $CaMgSiO_6$, which is a kind of silicate phase containing 55.5 wt. % SiO_2 (silica).

Based on energy transfer analysis, the energy amount transferred to mixture materials are almost 23.9 and 29.9 MJ / g for 8 h and 10 h milling time, respectively. This energy amounts cause the materials to be mechanically activated. In fact, the energy transferred to the materials mixture, causes the synthesis temperature of diopside reduces to 1100 °C, whereas based on the previous studies, Diopside phase was synthesized above 1100 °C.

Most of energy transferred to particles materials save in the materials as crystal defects such as grain boundary, dislocations density and vacancy concentration. These crystal defects lead to high path atom diffusely. These high paths causes increasing and intensity of chemical reaction and improvement of Diopside phase synthesis. In fact, it causes the synthesis temperature of Diopside reduces to low temperature, 1100 °C.

According to calculation by PSA graph, BET result and SEM micrographs observation, most of the powder particles milled for 10 h are spheroid. In fact, the morphology of powder milled is spheroid and about 400 – 600 nm. In fact, the powder mixture is sub-micron size. Moreover, raw materials milled sub-micron particles size, high of specific surface area, lead to increasing of free energy. This high free energy causes driving force to react between raw

materials particles. Surface to bulk atoms ratio of particles, SBR, increases by increasing specific surface area of particles size. Regarding to surface diffusion activation energy in comparison bulk diffusion activation energy is too low amount. So, atom diffusion increases between particles and it causes to intensive reaction between raw materials and lead to Diopside phase synthesis at low temperature, low thermal energy, after milling for 10 h by high energy ball mill.

5. Conclusions

According to above discussion, we can conclude:

1. Diopside nano-crystallite has been synthesized at the samples milled for 8 and 10 h and heated at 1100 °C.
2. According to XRD results and modified Scherrer equation, Diopside crystals size average was calculated about 30 – 50 nm.
3. In fact, based on BET result and calculations and their comparison with PSA graph it can conclude that particles size average of the starting materials are in submicron range.
4. Based on energy transfer analysis, the energy amount transferred to the starting materials is almost 23.9 MJ / g for 8 h milling time. This energy causes the materials to be mechanically activated. In fact, this energy transfer is at least energy causes the synthesis temperature of Diopside reduces to 1100 °C, whereas based on the previous studies, Diopside phase was synthesized above 1100 °C.

Acknowledgments

The authors would like to extend their gratitude for the financial supporting provided by Najafabad Branches, Islamic Azad University, Isfahan, Iran.

Referances

1. C. Wu, Y. Ramaswamy. Porous diopside ($CaMgSiO_6$) scaffold: A promising bioactive material for bone tissue engineering. Acta Biomater., 2010, 6, 6, 2237-2245.
2. C. Wu, J. Chang, S. Ni, J. Wang. In vitro bioactivity of akermanite ceramics. J. Biomed. Mater. Res. A., 2006, 76,1, 73-80.
3. S. Xu, K. Lin, Z. Wang, J. Chang, L. Wang, J. Lu, C. Ning. Reconstruction of calvarial defect of rabbits using porous calcium silicate bioactive ceramics. Biomater., 2006, 29, 17, 2588-2596.
4. C. Wu, J. Chang. Degradation, bioactivity and cytocompatibility of diopside, akermanite, and bredigite ceramics. J. Biomed. MatER. Res. B, 2007, 83, 1, 153-160.
5. T. Nonami, S. Tsutsumi. Study of diopside ceramics for biomaterials. J. Mater. Sci. Mater. Med., 1999, 10, 8,475-479.
6. R. Nagar. Preparation of diopside by novel sol–gel method using rice husk ash as silica source. Tesiss. 2011, Rourkela, Natl. Inst.Technol.

7. A. Monshi, S. S. Attar. A new method to measure nano size crystals by Scherrer equation using XRD. Majlesi J. Mater. Eng., 2010, 2, 3, 154-160.
8. M. Abdallahi, M. Bahmanpour. A novel technology minimizing the synthesis time of nano structured powders in planetary mills. Mater. Res., 2014, 17, 3, 7-22.

FABRICATION OF TIO_2 NANOTUBES ON THE ULTRAFINE-GRAINED TITANIUM SUBSTRATES FOR DENTAL APPLICATION

K. Hajizadeh [1], S. H. Nemati [2], A. Hadjizadeh [2]

[1] Sahand University of Technology
Faculty of Materials Engineering
Tabriz, Iran
[2] Amirkabir University of Technology
Bio-Medical Engineering Faculty
Tehran, Iran
afra.hadjizadeh@aut.ac.ir

Accepted October 19, 2015

Abstract

Medical engineering is looking for metallic biomaterials with strong mechanical properties, high biocompatibility, ability for easy surface modification and loading drugs for the applications as the orthopaedic implants and for hard tissues engineering. Titanium (Ti) based materials, are the most appropriate choices for this purpose, because of their unique TiO_2 passive layers. However, these substrates have weak mechanical strength, osseointegration and antibacterial properties. For solving these problems one solution is to process their microstructure from coarse grain to ultrafine grain to increase both their mechanical and surface energy, and the use of surface modification techniques, in order to generate very specific surfaces with TiO_2 nanotubes. This is due to the fact that TiO_2 nanotubes in various diameters and lengths enhance bone bonding, cellular response and are good reservoirs for loading drugs and antibacterial agents. This article reports the production and characterization of nano structured titanium substrates with improved mechanical properties, followed by anodizing surface modification technique, used to produce TiO_2 nanotubes on the ultrafine grained titanium. These TiO_2 nanotubes will be loaded with appropriate drugs for dental application.

1. Introduction

Titanium and its alloys, e.g. Ti-6Al-4V have been the most selected candidate for medical implant applications. Commercially pure titanium (CP-Ti) with its original coarse-grained (CG) state is known to be biologically more compatible than Ti-6Al-4V. However, its mechanical strength is not high enough for the most orthopaedic applications. In the past decade, severe plastic deformation (SPD) techniques have been extensively used to produce metallic materials with ultrafine-grained (UFG) microstructure, exhibiting higher physical and mechanical properties than coarse-grained (CG) counterparts. Pure titanium can be processed by SPD in order to refine its grain size and as a result increase the strength. This can be achieved by the use of a technique called equal channel angular pressing (ECAP) being an appropriate method for enhancing strength of pure titanium by decreasing its grain size below

one micrometer [1]. Metals processed by the SPD methods will possess ultrafine grain size (average grain size less than 500 nm), a large fraction of high angle grain boundaries (higher than 50 %), high dislocation density, and they may also have very high vacancy concentration [2]. Therefore, these materials will have high amounts of stored energy, providing a direct strengthening effect. Moreover, the ultrafine-grained titanium has shown higher surface hydrophilicity than coarse grain titanium (66 ± 2 and 80 ± 2.3, respectively) as well as cellular behavior [3]. Although Ti products considered as a large part of the commercial dental market, their antibacterial properties are not enough for many applications and lead to infection, in this case inflammatory is one the most important problems that have to be solved [4]. Also, another common disadvantage of titanium is to be non-bioactive for strong bone bonding, so this makes a fibrous tissue around implant and causes loosening and finally a failure in the implantation process. To solve the above mentioned problems surface treatment has been proposed. The material surface should be designed to increase bone's cell responses for formation new bone [5]. There are various kinds of surface modification methods that helps to improve the osteointegration of the implant's surface, such as sand blasting, acid and alkali treatment, bioactive coating of hydroxyapatite (HA) and calcium phosphate, and electrochemical oxidation (Anodizing). Anodizing can make controllable and uniform nanotubes on the titanium oxide surface layer. In anodizing TiO_2 nanotubes (TiO_2-NTs) are open at the top and closed at the bottom, and they can be at various sizes. The diameters and lengths of TiO_2-NTs can be controlled and TiO_2-NTs with certain dimensions not only do not damage but also improve the biological properties of the Ti substrate [4].

This article reports the production and characterization of nano structure titanium substrates with improved mechanical properties, followed by anodizing surface modification technique, used to produce TiO_2 nanotubes on the ultra fine grain titanium. These TiO_2 nanotubes will be loaded with appropriate drugs for dental application in future studies.

2. Experimental procedure

2.1. Material and processing

The chemical composition (wt. %) of the CP-Ti investigated was 0.18 % O, 0.03 % N, 0.16 % Fe, 0.17 % Pd, 0.18 % Cr and balance Ti. At first, the material was annealed at 800 °C for 1h in argon atmosphere and then air cooled. With this procedure, an equiaxed microstructure having an average grain size of about 20 mm was obtained (**Figure 1A**). ECAP samples with a length of 70 mm and diameter of 14.5 mm were machined from the annealed material. A specially designed ECAP die with the channel angle of 105 ° and the corner angle of 20 was used which leads to an imposed strain of about 0.8 per pass (**Figure 1B**). The ECAP die was placed tightly inside the cylindrical steel block. The heating bars were placed vertically in the steel block for heating the die. Prior to each pass, the billets were preheated to the respective temperature of ECAP for 10 min in the die, which was maintained at the ECAP temperature. The ECAP tests were performed on a servo-hydraulic 2000 kN computerized press. The billets were successfully pressed for 10 passes at 250 °C under a constant ram speed of 1 mm s^{-1} (**Figure 1C**). A composite lubricant containing about 50 % graphite powder, 25 % MoS_2 and 25 % grease was used between the billet and the die walls in order to reduce the frictional effects.

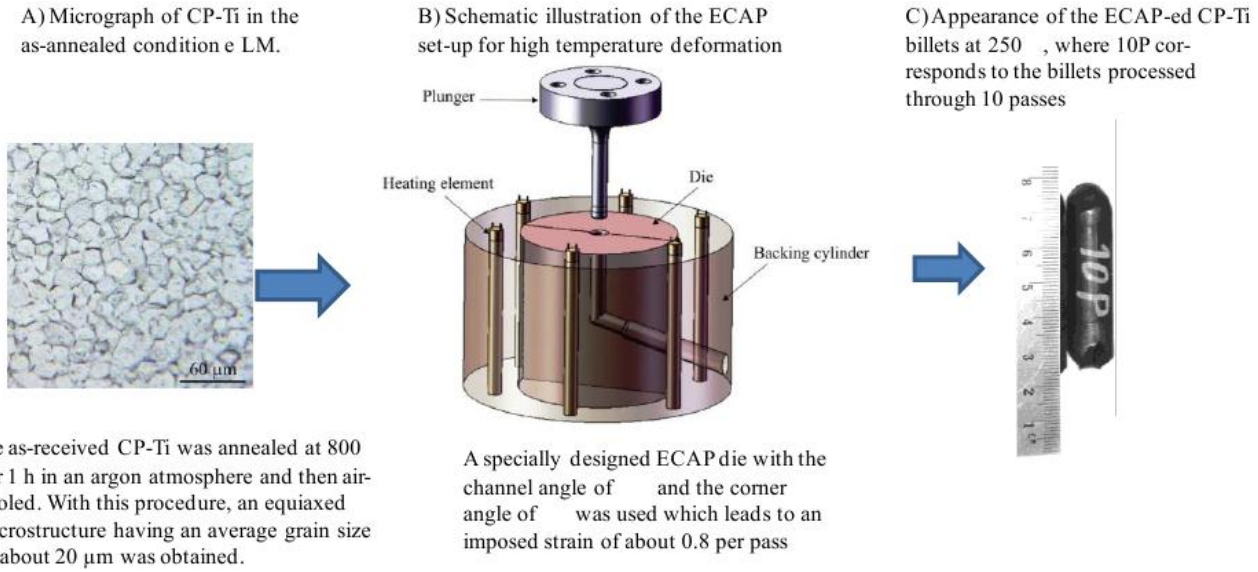

Figure 1. Equal channel angular pressing (ECAP).

2.2. Microstructure and mechanical properties characterization

Light (LM) and transmission electron microscopy (TEM) were used to investigate the microstructural changes in the processed billets. Specimens were prepared for LM in the standard manner. The studied areas were polished with 0.05 mm colloidal silica and etched in a solution containing 2 % HF, 6 % HNO_3, and 92 % H_2O_2. The TEM specimens were examined by a Philips CM 200 microscope operating at 200 kV. Specimens for TEM were cut from the middle sections of the processed billets perpendicular (cross section) to the pressing direction. Thin foils for TEM were first mechanically polished and finally electro-polished in a Tenupol 5 double jet-polishing unit in a solution. Tensile test specimens were cut from the billets according to JIS- Z2201 standard by using an electric discharge machine (EDM). Tensile tests were performed at room temperature using a MTS 810 servo-hydraulic testing machine at initial strain rates of $5 \cdot 10^{-3}$.

2.3. TiO_2 nanotube synthesis and characterization

Chemicals used for the synthesis of TiO_2 nanotubes include ethylene glycol, ammonium fluoride, which were purchased from Sigma Aldrich. In order to create TiO_2 nanotubes, a simple and cost effective electrochemical anodization technique was used.

Titanium samples were cut in dimentions of (1 cm × 1 cm × 1 mm thickness) using an electric discharge machine. Prior to anodization, the substrates were polished with sand papers (400, 600, 800, and 1000) sequentially sonicated in acetone, then rinsed with deionized water, and dried (**Figure 2A**). These samples were used as substrate to synthesize the nanotubes. The anodizing procedure was performed according to the protocol reported in the reference [6]. The electrolyte was 0.2 wt. % solution of NH4F in 49 ml ethylene glycol and 1 ml deionized water prepared with 1 h continuous mixing with magnetic stirring (**Figure 2B**). The experimental setup consisted of a two electrode arrangement, with Cu rod as the counter-electrode. The distance between the substrates and the counter-electrode was approximately 25 mm. The anodization was carried out at room temperature. A constant 60 V DC was used for

all experiments (**Figure 2C**). After anodization, the samples were rinsed with deionized water and dried. The morphological evaluation of non-detached TiO_2 nanotubes was obtained using Hitachi S-4700 FE-SEM.

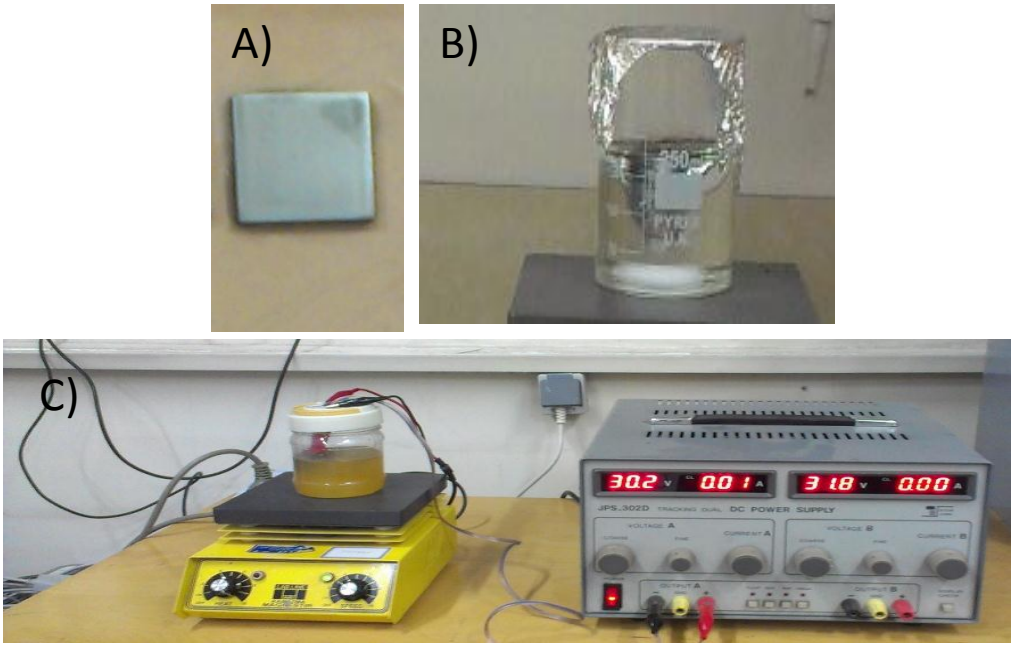

Figure 2. TiO_2 nanotube synthesis process.

3. Results and discussion

3.1. Proceeding of ultrafine-grained CP-Ti by ECAP

In order to refine the grain size of commercially pure titanium (CP-Ti) to a submicrometer range, equal channel angular pressing (ECAP) was performed at a temperature range of 200 – 300 °C. The experiments revealed that, 250 °C was the minimum temperature at which ten passes of ECAP could be performed in a 105 ° die without the cracking of billets (**Figure 1C**).

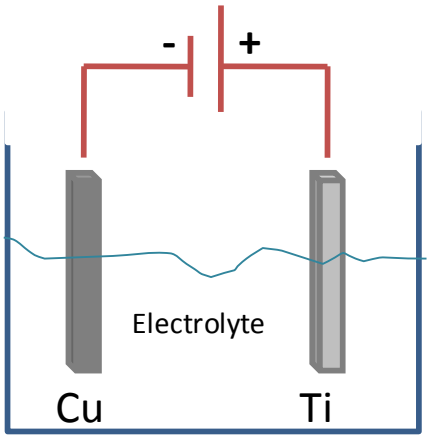

a) $2H^+ + 2e^- \longrightarrow H_2$

b) $Ti + 2\,H_2O \longrightarrow TiO_2 + 4H^+ + 4e^-$

c) $TiO_2 + 4F^- \longrightarrow [TiF_6]^{2-} + 2O_2^{2-}$

Figure 3. TiO_2 nanotube formation mechanism [7].

Figure 3A shows a typical microstructure of CP-Ti after 10 passes of ECAP taken from the cross section of a processed billet. As expected, the initial coarse-grained structure

underwent a significant refinement during ECAP and evolved to a UFG structure. The microstructure is characterized mainly by equiaxed grains. The grain size is in the range of 30-450 nm with an average value of 183 nm (**Figure 4B**). TEM observations also revealed that some grains are nearly free of lattice dislocations, while others contain a high density of dislocation. Such inhomogeneous structures are typical of SPD-processed materials.

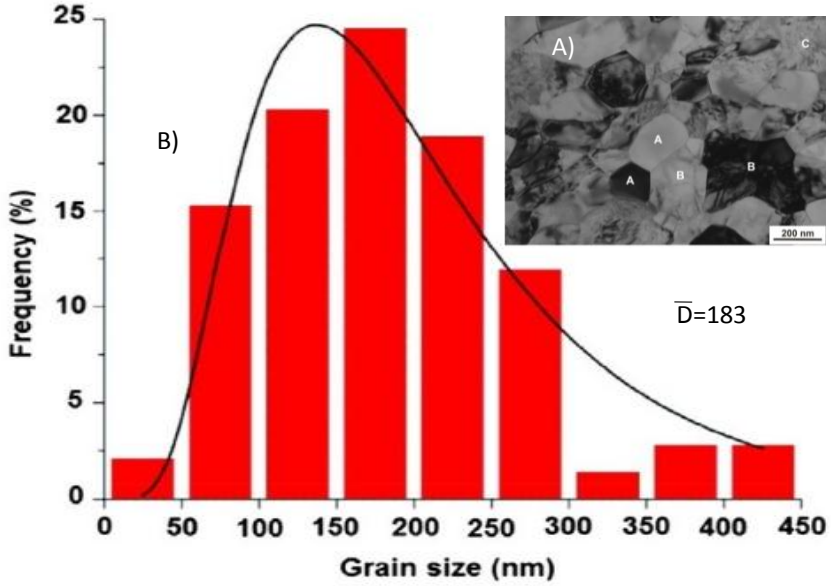

Figure 4. Bright field TEM micrographs (A), and grain size distributions (B) from cross-section of a CP-Ti billet after processing by 10 passes of ECAP at 250 °C [1].

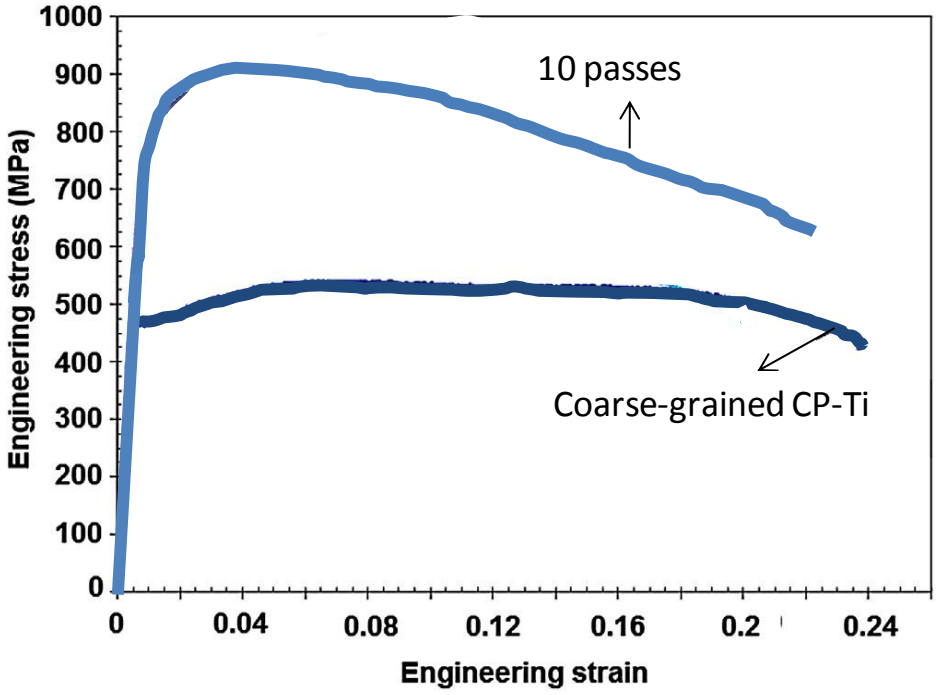

Figure 5. Tensile engineering stress-strain curves of coarse-grained and UFG CP-Ti after processing by 10 passes ECAP at 250 °C [1].

Figure 5 shows the engineering stress-strain curves obtained by tensile tests for the starting material and the ECAP processed CP-Ti specimens. It can be seen that, processing 10 passes by ECAP led to a significant increase in the values of yield strength by 62 % from 463 to 750 MPa, and ultimate tensile strength by 65 % from 540 to 892 MPa. These improvements in strength values were obtained while maintaining a sufficient ductility of 20.5 % elongation to failure as compared with 24 % in CG Ti. The enhancement of strength is explained in terms of grain refinement and dislocation density increasing. The high ductility of UFG pure Ti with the absence of strain hardening behavior is attributed to its enhanced strain rate sensitivity.

3.2. Fabrication of TiO_2 nanotubes by electrochemical anodization

Figure 6 shows typical SEM micrographs from the surface of CP-Ti samples after anodization treatment. It is clearly seen that, the anodization resulted in vertically oriented TiO2 nanotube arrays (**Figures 6B** and **C**). The length of nanotubes was measured to be in the range 7 and 10 μm (**Figure 6D**), whereas, their inner diameters were from 60 to 100 nm (**Figure 6C**).

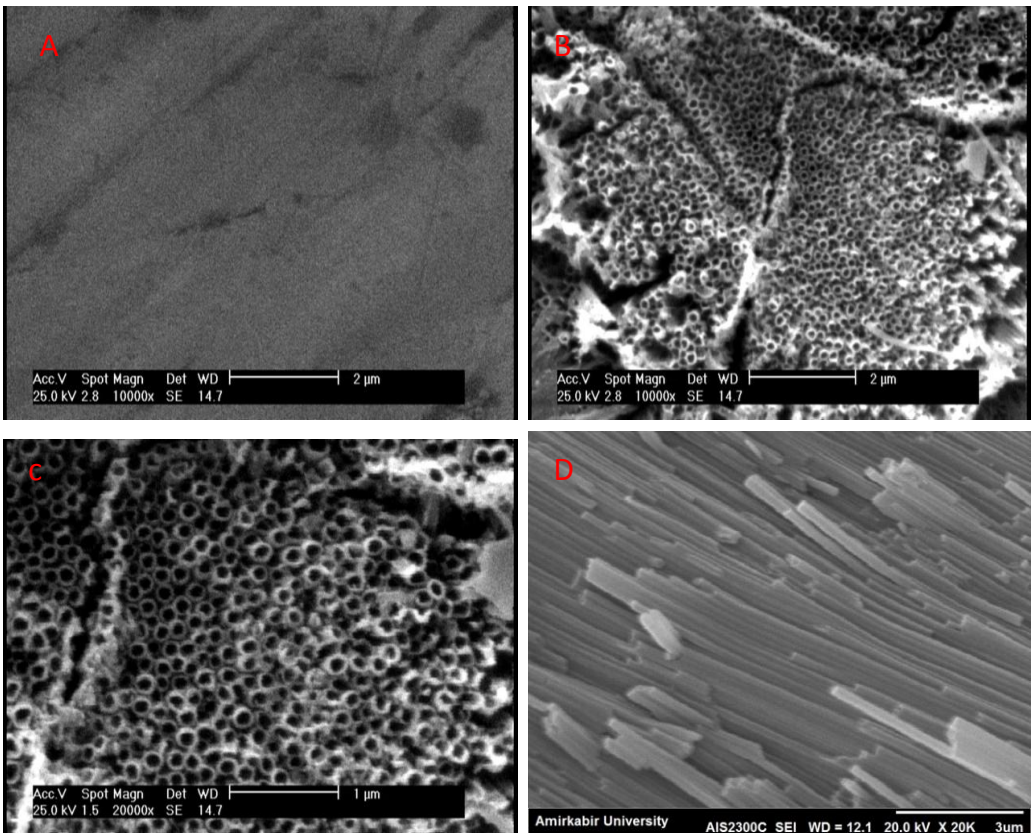

Figure 6. Typical SEM micrographs from the surface of CP-Ti samples after anodization treatment. TiO_2 nanotube formation on the ultrafine grain titanium by anodization: A) ultrafine grain titanium before anodization, B) ultrafine grain titanium after anodization, C) TiO_2 nanotube array with higher magnification, d) longitudinal observation of TiO_2 nanotubes.

According to the reported studies [8], TiO_2 nanotubes are grown by electrochemical anodization in aqueous or organic electrolytes with fluoride ions (e.g. organic electrolyte with glycerol or ethylene glycol etc). Usually anodization can be performed in a two-electrode

electrochemical cell with titanium as the anode, cupper or other metal as the cathode. A constant potential is applied using a DC power supply. In electrochemical anodization performed in organic electrolytes, the water content in the electrolyte determines the extension of nanotube array formation. Infact, water makes pore-wall splitting' in the ordered porous oxide to form nanotubes. By increasing the anodization time the transition from nanopore to nanotube occurs. By altering process parameters such as voltage, time, electrolyte type, one can change the nanotube diameter, wall thickness and length [8].

4. Conclusion

Equal channel angular pressing of CP-Ti at 250 °C results in an ultrafine-grained structure with mean grain size of 183 nm. Formation of the UFG structure in CP-Ti resulted in a significant improvement in: Yield strength by 62% from 463 to 750 MPa, Ultimate tensile strength by 65 % from 540 to 892 MPa. The UFG Ti exhibited an adequate ductility of 20.5 % elongation to failure and UFG tensile specimens fractured in a ductile manner. Post surface treatment of ultrafine-grained CP-Ti by electrochemical anodization is capable to produce arrays of amorphous TiO2 nanotubes with lengths ranging from 7 and 10 μm and inner diameters in the range of from 60 to 100 nm. These TiO_2 nanotubes will be loaded with appropriate drugs for dental application in future studies.

5. References

1. B. E. K. Hajizadeh, K. Topolskib, K. J. Kurzydlowskib. Ultra-fine grained bulk CP-Ti processed by multi-pass ECAP a warm deformation region. Mater. Chem. & Phys., 2014, 143, 3, 1032-1038.
2. S. G. A., K. Hajizadeh, B. Eghbali. Stored energy and recrystallization kinetics of ultrafine grained titanium processed by severe plastic deformation. Phys. B, 2013, 417, 33-38.
3. H. Maleki–Ghaleh, K. Hajizadeh, A. Hadjizadeh, M. S. Shakeri, S. Ghobadi Alamdari, S. Masoudfar, E. Aghaie, M. Javidi, J. Zdunek, K. J. Kurzydlowski. Electrochemical and cellular behavior of ultrafine-grained titanium in vitro. Mater. Sci. Eng. C, 2014. 39, 299-304.
4. S. Mei, H. Wang, W. Wang, L. Tong, H. Pan, C. Ruan, Q. Ma, M. Liu, H. Yang, L. Zhang, Y. Cheng, Y. Zhang, L. Zhao, P. K. Chu. Antibacterial effects and biocompatibility of titanium surfaces with graded silver incorporation in titania nanotubes. Biomater., 2014, 35, 14, 4255-4265.
5. L. M. Bjursten, L. Rasmusson, S. Oh, G. C. Smith, K. S. Brammer, S. Jin. Titanium dioxide nanotubes enhance bone bonding in vivo. J. Biomed. Mater. Res. A, 2010, 92, 3, 1218-1224.
6. T. Shokuhfar, A. Hamlekhan, J. Y. Chang, C. K. Choi, C. Sukotjo, C. Friedrich. Biophysical evaluation of cells on nanotubular surfaces: The effects of atomic ordering and chemistry. Int. J. Nanomed., 2014, 9, 3737-3748.

7. C. C. B. S. Minagar, J. Wang, E. vanova, C. Wen. A review of the application of anodization for the fabrication of nanotubes on metal implant surfaces. Acta Biomater., 2012, 8, 2875-2888.
8. M. Kulkarni, A. Mazare, E. Gongadze, S. Perutkova, V. Kralj–Iglic, I. Milosev, P. Schmuki, A. Iglic, M. Mozetic Titanium nanostructures for biomedical applications. Nanotechnol., 2015, 26, 6, 062002.

PREPARATION OF $Cu_{84}Al_{12}Ni_4$ SHAPE MEMORY ALLOYING BY HIGH ENERGY MECHANICAL MILLING

S. Mimouche, M. Azzaz

University of Sciences & Technology Houari–Boumediene
Laboratory of Science & Genius of Materials
Algeriers, Algeria
s.msofiane @gmail.com

Accepted October 19, 2015

Abstract

In the present work are shown the results obtained by high energy mechanical milling for Cu-Al-Ni shape memory alloy. the mechanical alloying powder $Cu_{84}Al_{12}Ni_4$ (wt. %) was fabricated in high energy planetary ball milling at a speed of 250 r / min for various milling times (10, 20, 30, 40, 50 and 60 h) the weight ratio of the balls of powder was 15 to 1. this mechanical alloying process is significantly modifying the characteristic of the powder, the recovered grains are ultimately compacted, after suitable heat treatment the shape memory is produced. The means used to study the different evolution are SEM Scaning Electron Microscopy, Differential thermal analysis DTA, X-ray Diffraction analysis and DRX in situ.

1. Introduction

Mechanical alloying is a technique of powder metallurgy which allows the production of alloys from mixtures of pure or alloyed powder elements. The milling occurs by impingement and friction of the balls on the powder; the powder particles are flattened respectively, welded, and fractured under the effect of repeated collisions between the beads, but also the beads with the wall of the jar. This study aims to develop a shape memory alloy Cu Al Ni by high energy mechanical milling from elemental powders Cu, Al and Ni. However, the production of this alloy which makes a very high thermal stability [1, 2] by the conventional method (fusion) presents high brittleness [3], which is due to a large grain size and their large elastic anisotropies [4]. With the technique of mechanical alloying, the parameters of the grain size and the composition of the alloys can be controlled better [5, 6].

2. Experimental

In order to ensure good quality of the samples, the preparation method requires good cleaning after the use of each jar. The mill used is of type planetary ball milling, which has a speed of 250 r / min, with four jars containing 7 balls 20 mm in diameter, and the powders of Cu, Al and Ni. The weight ratio of the balls of powder was 15 to 1.

The specifics of this elementary powder are shown in **Table 1**. The weighing and preparation of the load (powders and beads), as well as the recovery of the powders were

carried out, under an argon atmosphere to reduce the risk of oxidation of the powder during milling. Several milling time ranging from 10 to 60 h, with a step of 10 h were tested, study the influence of milling time on the alloy forming condition. Using a hydraulic press, milled powders were compacted under a vacuum at a pressure of 2 GPa for 1 h in a cylinder 13 mm of diameter. After compaction, the obtained pellets are subjected to a homogenization treatment at 950°C for 1 hour followed by water quenching.

Table 1. Specification and mixture of elemental powders.

Powders	Powder of Cu	Powder of Al	Powder of Ni
Size, µm	100	100	100
Purity, %	99.99	99.7	99.7
Composition, wt. %	84	12	4

3. Results and discussions

3.1. X-Ray diffraction analysis

The diffraction profile of milled powders for different milling time is shown in Figure 1. The structural evolution of the initial powder presents diffraction peak plans {(111), (200), (220), (311), (222)} for copper (Cu-fcc) and those of aluminum and nickel {(111), (200), (220), (311)}. The lattice parameters measured, respectively of 0,360 nm for copper, 0.403 nm for aluminum and 0.353 for nickel. They perfectly match the values of copper, aluminum, and nickel.

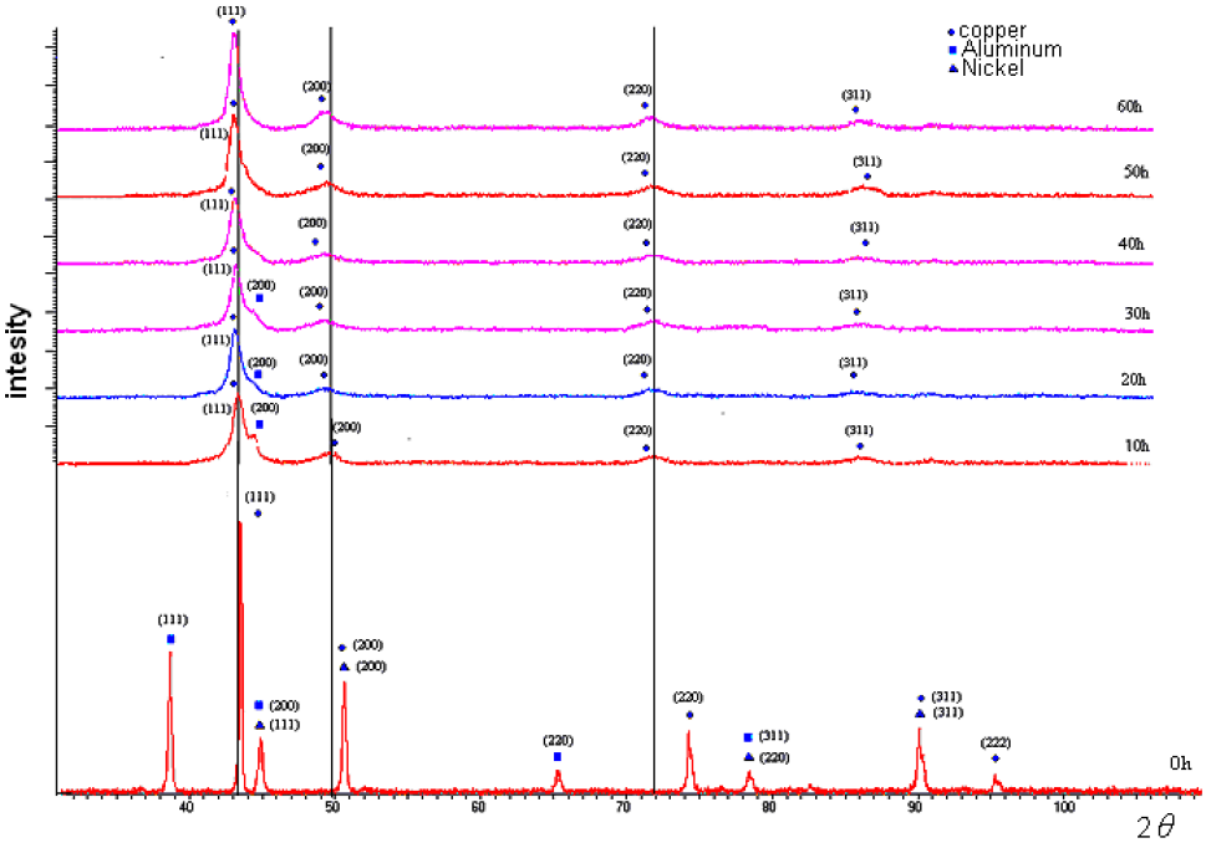

Figure 1. X-ray diffraction patterns of $Cu_{84}Al_{12}$ N_4 powder for different milling times.

Increasing milling time causes reduction in the intensity of the diffraction peaks; the peaks of Al and Ni are smaller than that of Cu because of their small amount in the overall composition. However, a shift of the peak position of copper to the small diffraction angles and their extensions are recorded. 30 h after milling, there is a complete disappearance of the peaks of aluminum and nickel: only the peaks of Cu phase are observed, this phenomenon has already been observed in the work of [7, 8].

The progressive shifting of the copper peaks is attributed to a dissolution of the aluminum atoms and nickel in copper and their enlargement is due to a reduction in the size of the diffracting areas and many constraints introduced in the lattice during the milling process.

The process of diffracting patterns can be done with xpowder software, which calculates using the formula of Williamson and Hall coherent domain size **Figure 2** and lattice parameter **Figure 3**.

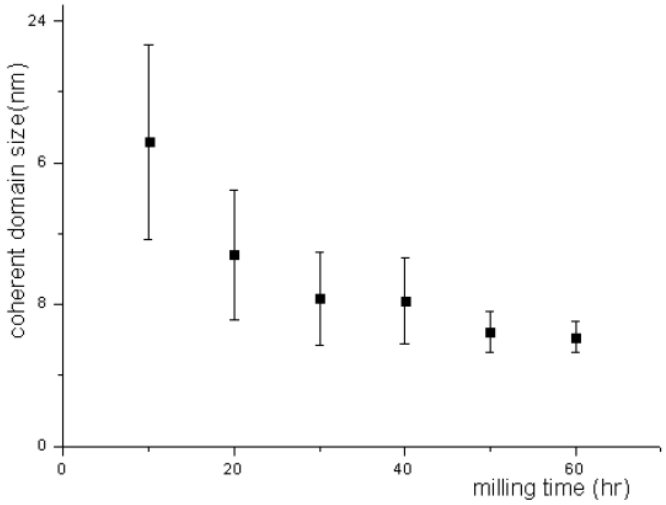

Figure 2. Evolution of coherent domaine size as a fonction of milling time.

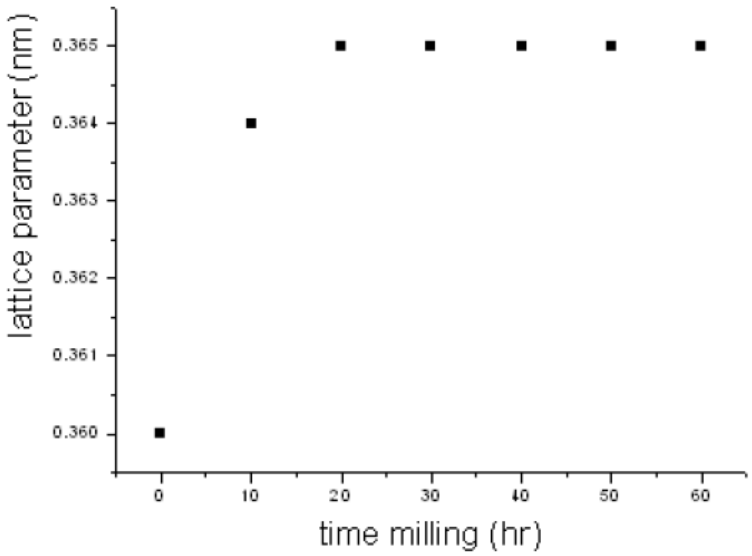

Figure 3. Lattece parameters of Cu as a fonction of milling time.

Dissolving nickel atoms and aluminum causes the increase in copper lattice parameter (Cu-fcc). This increases in the early hours of the milling process and seems to reach a stationary value.

3.2. Morphology of powder during mechanical milling

The mechanism of the formation of alloy by high energy mechanical milling basically consists of reducing the grain size by repeated impact, which leads to the phenomena of fracture and cold welding of powder particles. **Figure 4** shows that the grain formation results from an agglomeration of smaller particles.

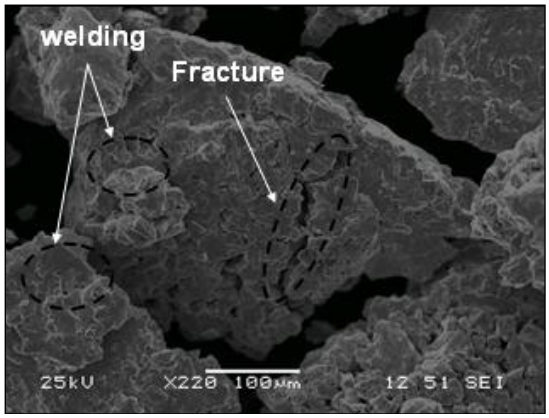

Figure 4. Scaninig electron microscopy (SEM) of $Cu_{84}Al_{12}Ni_4$ grain.

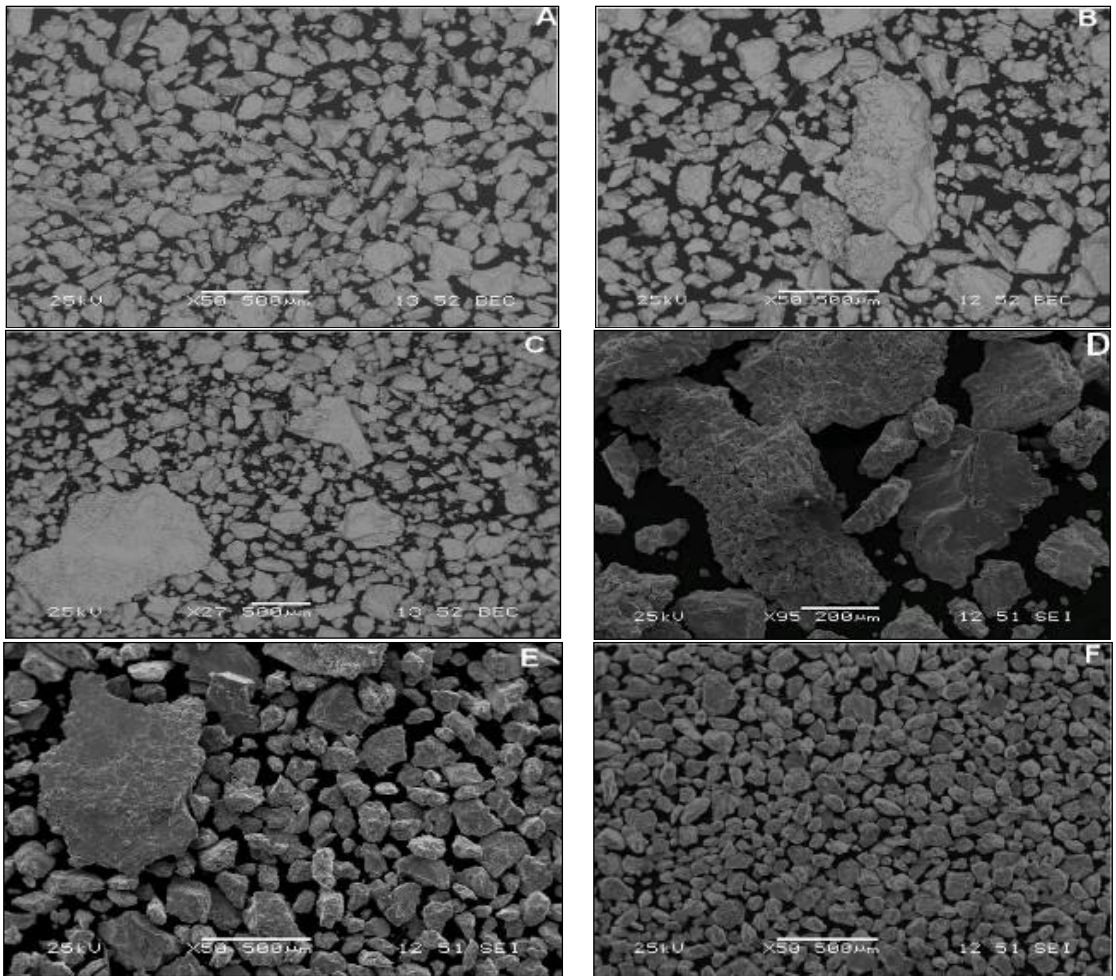

Figure 5. Morphology of powders $Cu_{84}Al_{12}Ni_4$ for different milling time: (a)10; (b) 20; (c) 30; (d) 40; (e) 50 and (f) 60h.

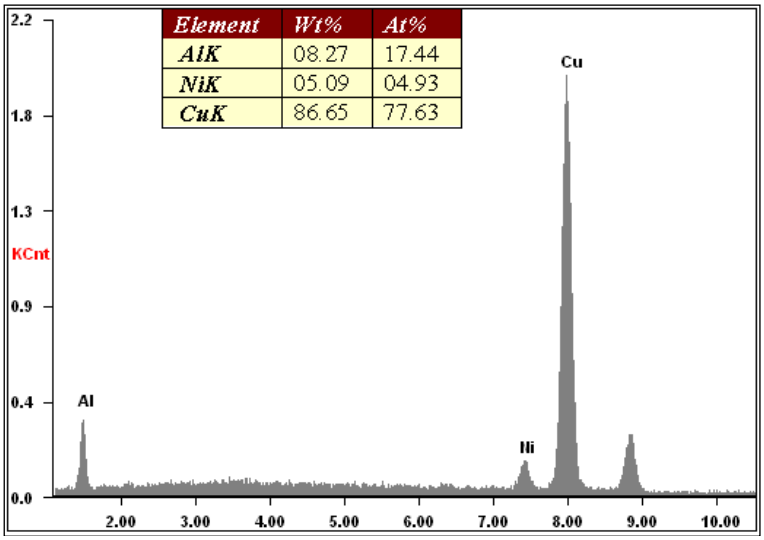

Figure 6. EDS analysis of $Cu_{84}Al_{12}Ni_4$ powder milled for 20 h.

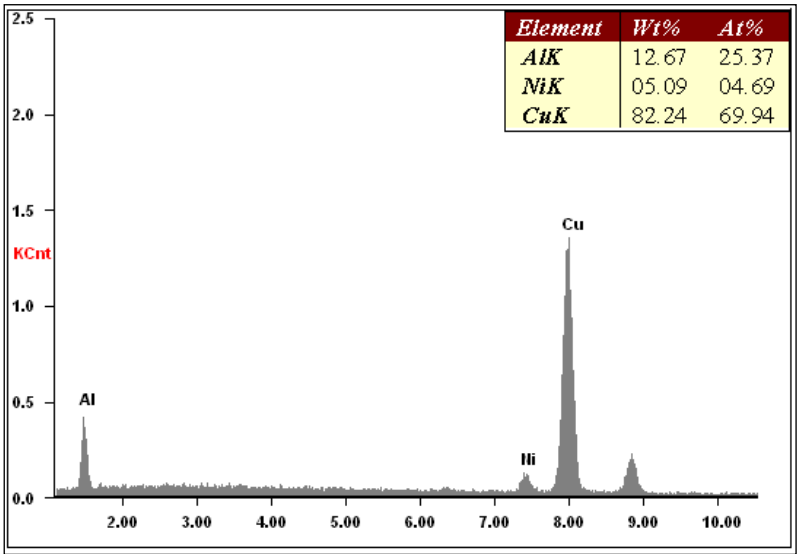

Figure 7. EDS analysis of $Cu_{84}Al_{12}Ni_4$ powder milled for 60 h.

Changes in the morphology of Cu powder, Al and Ni during mechanical milling are shown in **Figure 5**. After 10 h of millding, there is a formation of the first powders of grains. However, the agglomeration of the powder particles becomes more important to 20 h of millding, ranging in size between 400 and 1000 μm, while the distribution of the grains is not uniform. The analysis by EDS shows that the Cu content is increased and that of Al was reduced in **Figure 6**. After 30 h of milling, the grain size is smaller than the ones done within 20 h. A prolongation of milling to 60 h leads to a better uniformity of grain on **Figure 5F**, an analysis by EDS of the powder particles has mounted a concentration close to the initial concentration **Figure 7**.

3.3. Differential thermal analysis (DTA)

The transformation characteristics of milled powders were evaluated using a Differential Thermal Analysis (DTA). Powders weighing between 40 and 50 mg were tested in an argon atmosphere at a rate of 10 °C heating / cooling. **Figure 8** shows the DTA analysis of samples of initial powders and powders milled at 10, 30 and 60 h.

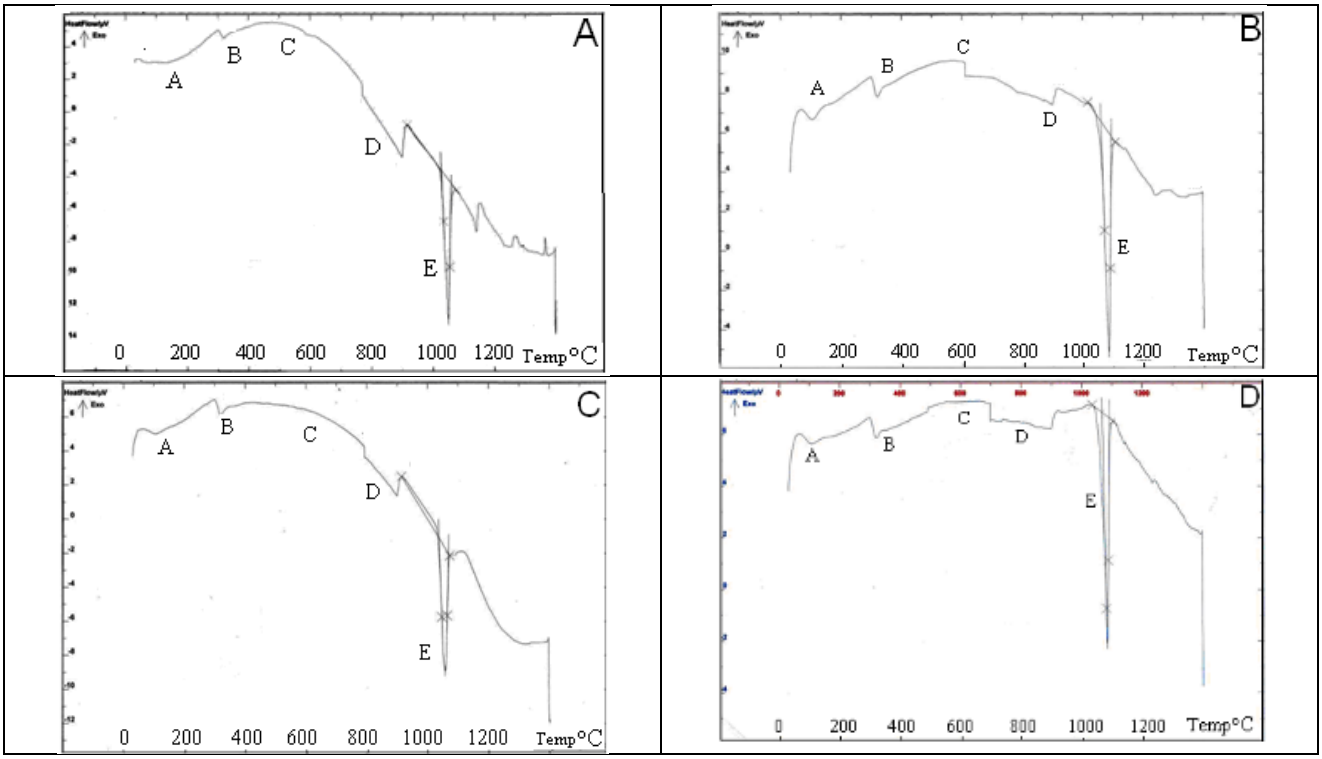

Figure 8. DTA thermograms for $Cu_{84}Al_{12}Ni_4$ powder: (A) elemental powder; (B) 10 h of milling; (C) 20 h of milling; (D) 30 h for milling.

The curve of the initial powder DTA **Figure 8A**, presents an evolution (A) between 100 and 300 °C which corresponds to the transformation of the martensite ($\beta'_1 \rightarrow \beta_1$). A second exothermic peak recorded about 350 °C corresponds to the formation of precipitation of equilibrium, whose composition is close to Cu_9Al_4, This transformation is responsible for the aging phenomena in this alloy, between 350 and 790 °C we record an evolution (**C**) very spread corresponding to the re-dissolution of precipitation coherents with the matrix. With continuous heating between 790 and 910 °C, the resulting mixture ($\alpha + \gamma_2$) dissolves to give a stable β phase evolution (**D**). The heating thermogram exhibits an exothermic peak fine of fusion between 1150 and 1090 °C. The enthalpy associated is 15.9987 μv · s / mg.

In general, the various transformations are presented in different milling time **Figures 8A – C**. However, the position of the peaks relating to the changes (**C**) and (**D**) immensely varies with the milling time.

3.4. In situ high temperature X-ray

The diffractograms of X-ray of **Figure 9**, obtained on the elemental powder Cu84Al12Ni4 annealed at 250, 340, 780 and 900 °C Highlighting the various developments encountered during the process performed in DTA. The CuAlNi alloy at room temperature shows a stoichiometric AlxNiy phase, which usually diffracts the plan (110), evenly presenting the phases of equilibrium γ_2–CuAl and α. At 250°C, there is an existence of peak on the β'_1 phase.

By increasing the annealing temperature, the peak intensity of the β'_1 phase increases and its width decreases. The peak of the α phase is refined, then shift to the small diffraction angles, by which their intensity increases. As we can see, the line on this phase corresponds to the plan (200). We also notice the disappearance of the peaks relating to the AlNi phase.

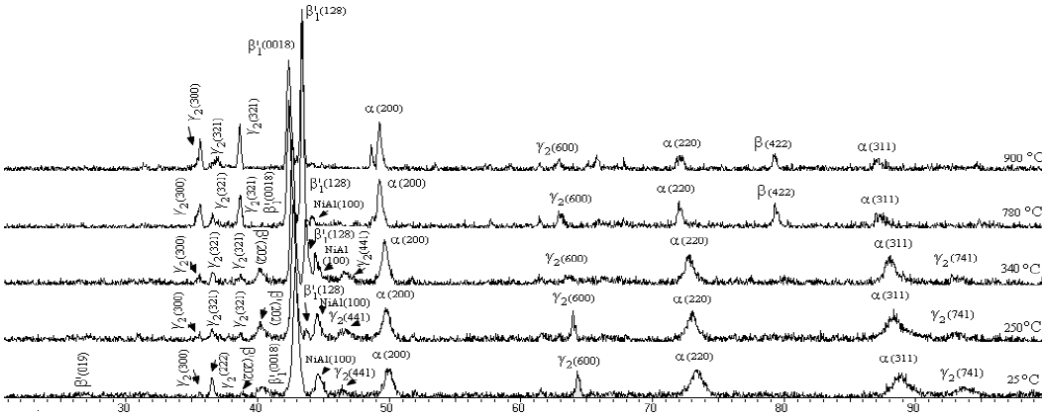

Figure 9. X-ray in situ analysis for elemental powder.

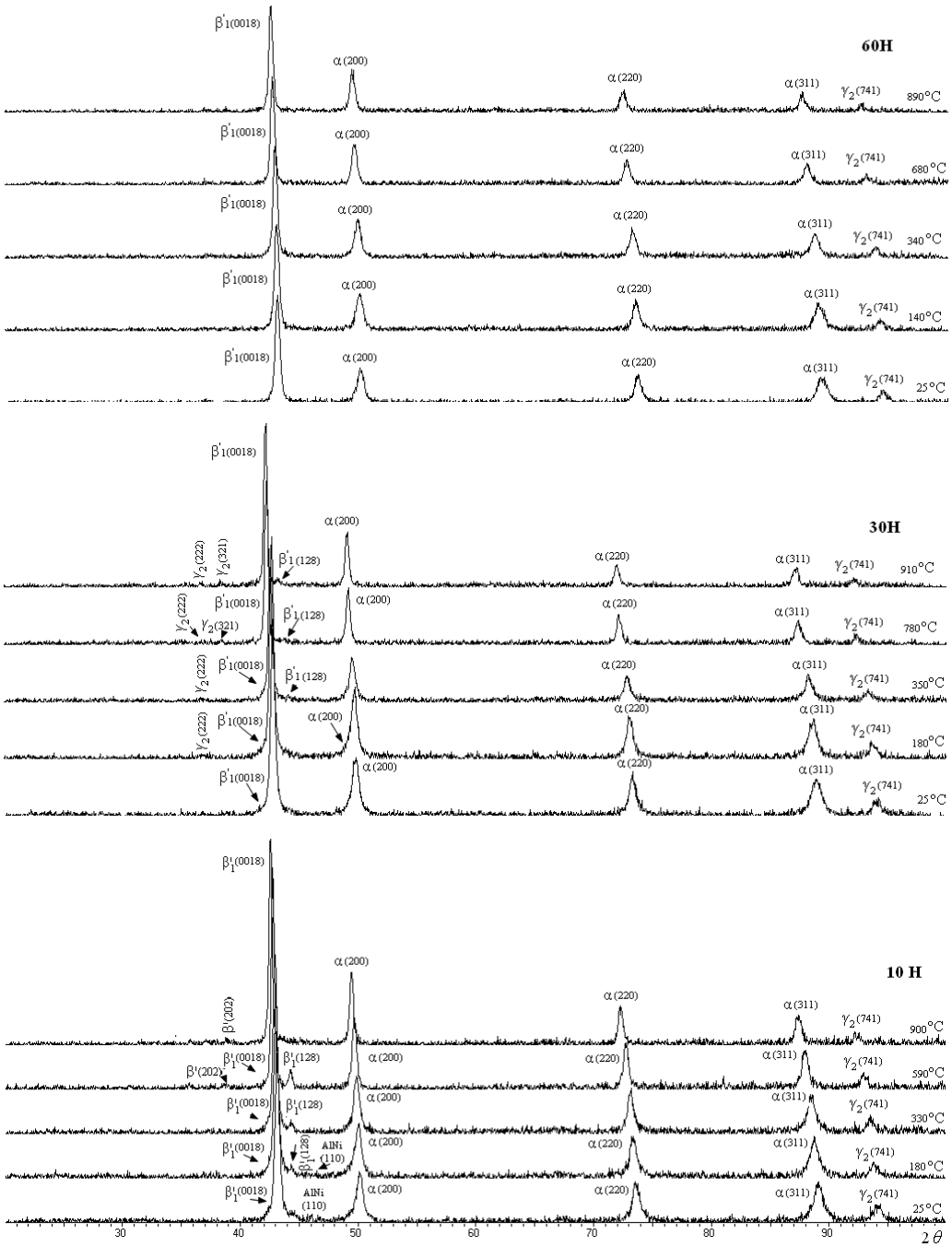

Figure 10. X-ray in situ analysis of powder milled for 10, 30 and 60 h.

The X-ray diffractograms obtained after 10 h of milling **Figure 10**, are made during a heating from ambient temperature to 900 °C. Showing the equilibrium and non-equilibrium phase formed following the annealing. One can see the presence of the AlNi phase diffracting the plan (110) at temperature 180 °C, which disappears by decomposing, the diffraction spectra also shows the presence of phase β'_1 Type 18R, which diffracts the plan (128).

By increasing the annealing temperature to 590 °C, the peak intensity β'1 increases, and the presence of phase β' 9R follows the plan (202). At 900 °C temperature, the peaks of the α phase diffracting along plans (200), (220) and (311) are refined, which then move to the small diffraction angles. We also notice the disappearance of the peak β'_1 phase (128).

The presence of β'_1 stage with the main line corresponding to the plan (0018) and the α phase shows that the affected area corresponds to a bi-phase structure consisting of α + β phases. At longer milling times of 30 and 60 h **Figure 10**, the annealed merely grow peak intensity because the compound is already obtained by milling, so the effect of annealing is only to eliminate the constraints and defects introduced by milling.

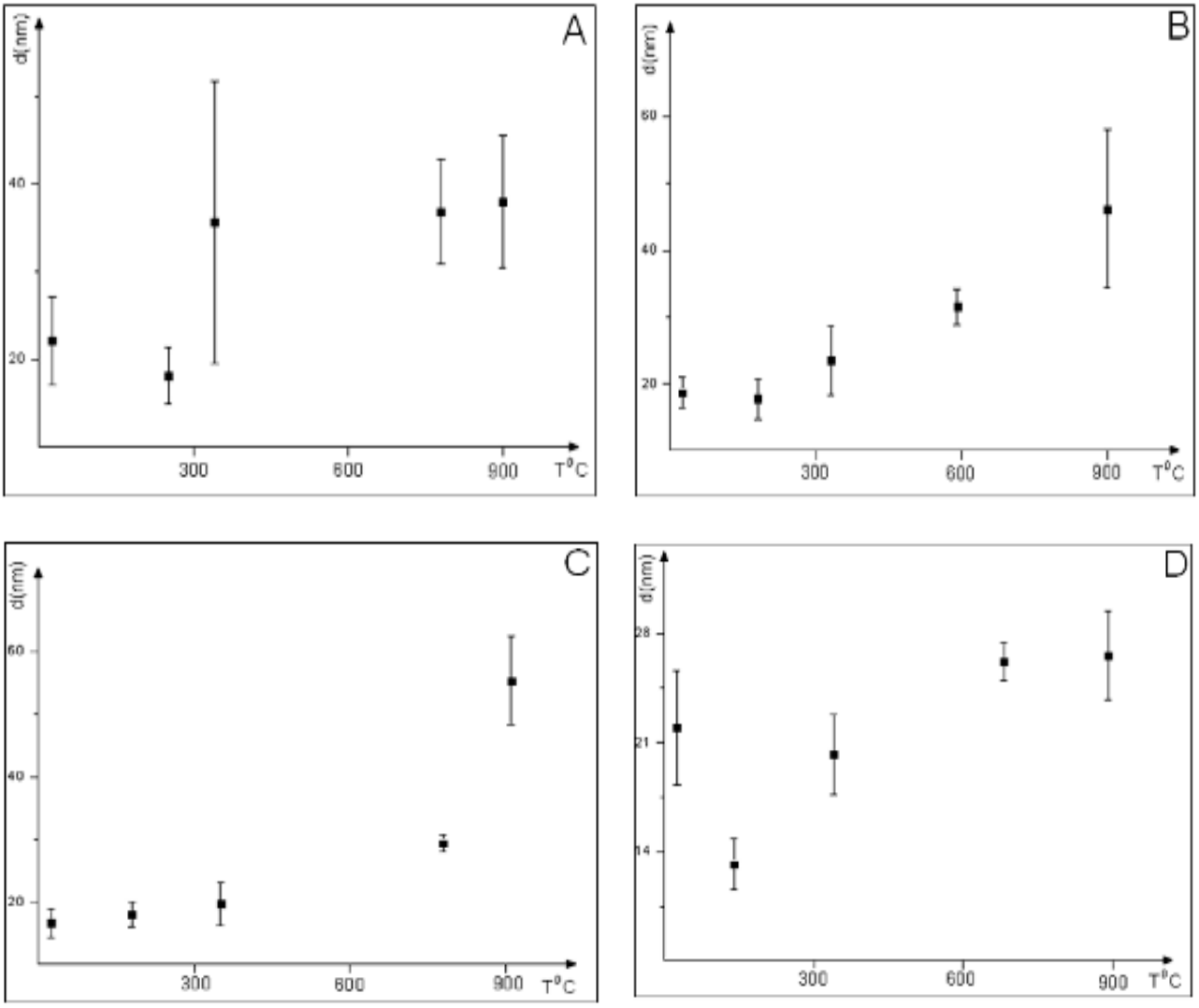

Figure 11. Evolution of coherent domaine size as a fonction of annealing temperature for (A) elemental powder; (b) 10 h for milling; (C) 20 h for milling; (D) 30 h for milling.

The X-ray diffraction shows that the structure of CuAlNi powders obtained by mechanical alloying is crystalline. The size of coherent domains such as annealing, increases quite significantly between gross millding state and annealed state. Moreover, a slight decrease of the size of the coherent domains is observed after the first annealing temperatures **Figure 11**.

4 Conclusions

1. Mechanical alloying can be used for the development of CuAlNi alloy, a single phase of FCC structure is obtained at a speed of 250 r / min after 30 h of mechanical milling and this is thanks to the miscibility of Al and Ni in Cu.

2. The chemical composition of the sample $Cu_{84}Al_{12}Ni_4$ after 60 h of milling is close to the original composition and it is generally homogenneous in the μm scale.

3. Increasing the milling time causes reduction in the size of coherent domains estimated at 6 ± 1 nm after 60 h of milling, and the increase in the lattice parameter.

4. The size of Cu crystallites increases between the gross millding state and annealed state.

References

1. G. K. Kannarpady. A. Bhattacharyya. Effect of mechanical and thermal cycling on shape memory properties of high temperature Cu-Al-Ni single crystals. J. Am. Soc. Mech. Eng., 2004, 69, 281-285.
2. V. Recarte, J. I. Perezc–Landazabal, A. Ibarra. High temperature 'h' phase decomposition process in a Cu-Al-Ni shape memory alloy. J. Materials Sci. & Eng. A, 2004, 378, 112, 238-242.
3. S. Miyazaki, K. Otsuka, H. Sakamoto, K. Shfmizu. Fracture of Cu-Al-Ni shape memory alloy. Trans. Jpn. Inst.Met., 1981, 22, 4, 244-252.
4. S. Miyazaki, K. Otsuka. Development of shape memory alloys. LSLJ Int., 1989, 29, 353-377.
5. P. P. Rodriguez, R. B. Perez–Saez, J. Perez–Landazaba, V. Recarte, O A. Ruano, M. L., N. San, J Juan. Martensitic transformation in Cu-Al-Ni shape memory alloys obtained by hall milling. J. Phys. IV, 2003, 1121: 575-578.
6. Z Y. Li, Pan, , N. Tang, Y.-B. Jiang, N. Liu, M. Fang, F. Zheng. Cu-Al-Ni-Mn shape memory alloy processed by mechanical alloying and powder metallurg. J. Materi. Sci. & Eng. A, 2006, 417, 112.225-229.

7. S. M. Tang, C. Y. Chung, W. G. Liu. Preparation of CuAlNi based shape memory alloying powder metallurgy method. J. Proc. Technology, 1997, 63, 307-312.
8. X. Zhu, L. Zhou, F. Mei, L. Ming, G. Shen, T. Ning. Structure evolution of Cu-based shape memory powder during mechanical alloying. Trans. Nonferrous Met. Soc. China, 2007, 17, 1422-1427.

UNIAXIALLY ALIGNED ELECTROSPUN NANOCOMPOSITE PREPARED THROUH A NOVEL PROCESSING TECHNIQUE

S. Karimi [1], N. Tucker [2], A. Fessard [3], N. Bunk [4], M. P. Staiger [5, 6]

[1] Canterbury Agriculture & Science Centre
The New Zealand Institute for Plant & Food Research
Lincoln, New Zealand
Samaneh.Karimi@plantandfood.co.nz
[2] University of Lincoln
School of Engineering
Lincoln, United Kingdom
[3] Université de Technologie de Belfort Montbéliard
Department of Argonom, Design & Mechanical Engineering
Sevenans, France
[4] Electrospinz Limited
Blenheim, New Zealand
[5] University of Canterbury
Department of Mechanical Engineering
Christchurch, New Zealand
[6] The MacDiarmid Institute for Advanced Materials & Nanotechnology
Wellington, New Zealand

Accepted October 19, 2015

Abstract

Uniaxially aligned poly(vinyl alcohol) fibers were electrospun using a proprietary gap spinning method. Epoxy based composite films reinforced with low volume percentage (0.13vol%) of electrospun nanofibers were prepared using two different processing routes; a conventional wet lay-up and a novel electrospraying technique. The effects of the processing method on the properties of the fabricated materials were studied using scanning electron microscopy, tensile tests, dynamic mechanical analysis and thermogravimetric analysis. The results of the mechanical and thermal studies revealed property enhancement by changing the processing route to the electrospraying technique. This is ascribed to an increased level of fiber/matrix interaction and a more efficient interfacial adhesion compared to the materials prepared through the conventional wet lay-up method. A significant boost of 7 and 2.5 folds in tensile strength and Young's modulus was observed for the specimen fabricated using electrospraying technique, compared to the neat matrix.

1. Introduction

One of the routes toward nonofiber production is based on electrospinning. Electrospinning technology enables production of continuous polymer nanofibers from polymer solutions or melts in high electric fields [1]. When the electric force on the polymer liquid overcomes surface tension, a thin polymer jet is ejected. The charged jet is elongated and accelerated by the electric field, undergoes a variety of instabilities, dries, and is deposited on a

substrate as a random nanofiber mat [2]. The process has been known since the mid-1800s, but did not enjoy commercial success until it was adopted for the production of non-woven filter materials in the late 1930s [3].

In the field of composite materials, very little has been achieved in the use of electrospun fibers as sole reinforcement. This is probably due to the emphasis of the development effort in fiber manufacturing being aimed at the production of random oriented fiber mats for filtration. In the field of nanofiber composites, however, the majority of the literature is firstly on carbon nanotube / nanofiber [4] and secondly on cellulose nanofiber reinforced composites [5]. The two well-known and major drawbacks in the production of these nanocomposites are agglomeration or inefficient dispersion of nanotubes or nanofibers and lack of control over their orientation. The electrospinning process offers the possibility to overcome these challenges as the complex process can be orchestrated in a way to provide control over the porosity and alignment of the spun nanofibrous mat.

The efficacy of randomly oriented electrospun fibers as a reinforcement has been studied [6]. A review of literature unveil that the non-woven or randomly arranged nanofiber mats, as collected to date from electrospinning, generally cannot result in a significant improvement in the mechanical properties of the composites with their reinforcement. It is widely known from composite theory and practice that to maximize the mechanical performance of a composite material, arrangement of fibers in pre-determined directions i.e. unidirectional is required [7]. In this light, several research groups have reported fabrication of aligned electrospun nanofibers by various techniques [8]. For example aligned electrospun fibers have been produced by using a rotating drum or disk collector [9], gap spinning methods [10], and auxiliary counter electrodes [11]. However, there is very limited published research on the application of aligned electrospun nanofibers as the sole reinforcement phase in polymer matrix composites.

In this work we demonstrate potential of using uniaxially aligned PVOH nanofibers in the epoxy matrix, using two different processing techniques, namely traditional wet lay-up and electrospraying application of resin. It is worth to note that one of the key issues in manufacturing of nanocomposite materials is the effective impregnation of the fibrous mat with polymeric matrix to form a coherent and intimate interface between fiber and matrix. To date no direct correlation between mechanical performance of electrospun nanocomposites and the processing technique is developed. To fine-tune the interaction between the nanofibers and the polymeric matrix, electrospraying technique was devised to optimize thermal and mechanical properties of the outcome material. The morphology of nanofibers as well as nanocomposites was characterized by using scanning electron microscopy. Thermal and mechanical properties were accessed via thermogravimetric analysis (TGA), dynamic mechanical analysis (DMA) and tensile test, respectively. Overall, this effort is anticipated to inspire new opportunities for application of aligned electrospun nanofibers in composite materials and to unleash the special functionalities and properties of the resulting materials through a novel processing technique.

2. Experimentals

2.1. Materials

Poly(vinyl alcohol) (PVOH) was supplied by Chemiplas NZ limited, Wellington, New Zealand. The PVOH had an average molecular weight of 118000 – 124000 g / mol and degree of hydrolysis (DH) in the range of 86 – 89 %. A bisphenol-A based epoxy resin (West System 105

resin, West System 206 hardener, Nuplex Ltd., New Zealand) was used with a resin-to-hardener ratio of 5:1. Manufacturer's data for the viscosity of the unreacted resin was given as 1000 centipoise at 22 °C.

2.2. Preparation of nanofibers

An aqueous polymer solution was prepared by dissolving PVOH in distilled water for 2 h at 60 °C, by the help of a mechanical stirrer. The solution concentration was adjusted to 8 wt. %.

The electrospinning process was a proprietary gap spinning method developed by Electrospinz Ltd in cooperation with Plant and Food Research Institute scientists. Preliminary experiments were done with various spinning parameters and gap length to come up with the optimum condition for the specific requirement of this research. Finally the applied spinning voltage of 12 kV with tip to collector distance of 160 mm and gap length of 96 mm was used. During electrospinning, the environmental temperature and humidity was controlled at 20 ± 1 °C and 35 ± 1 %, respectively. Nanofibrous mat of continuous uniaxially aligned fibers of PVOH with dimension of 96 × 60 mm ($l \times w$) was collected after 90 min on pre-designed square steel plates covered with silicon release paper and were dried in a vacuum oven at 50 °C overnight.

2.3. Preparation of nanocomposite films

Firstly the nanocomposite films were prepared through wet lay-up method. 0.2 g of mixed epoxy resin / curing reagent was dripped onto the pre-dried rectangular nanofibrous mat. This small amount was enough to fully imperegnate the dimension of the nanofibrous mat and forms a thin film. Then the surface was cautiously covered with a silicone release paper and placed into an aluminium vacuum bag, evacuated and sealed using an A300/16 Multivac vacuum sealer (Sepp Haggenmüller GmbH & Co, Germany) prior to the curing cycle at 45 °C for 24 h. Then the bags were unwrapped, the nanocomposite film was peeled off from the back plate, labelled as WLNC and kept in plastic bags for four days before various characterization tests. The thickness of such prepared nanocomposite films was 0.1 ± 0.02 mm.

In the electrospraying technique all of the conditions were the same only instead of dripping the amount of epoxy / hardener mixture, the Electrospinz Laboratory ES1 machine, was used to electrospray the resin onto the nanofibrous mat. The applied voltage for electrospraying was 12 kV. The plate of nanofibrous mat was installed on a moving rail in desired distance of the spinning tip (15 cm) and was moved in distinct intervals in order to uniformly cover the mat surface with tiny resin droplets.

2.4. Characterization

Surface morphology, diameter and alignment of the obtained nanofibers as well as the topography of nanocomposites fracture surfaces were studied by JEOL Neoscope JCM-5000 scanning electron microscopy (SEM). Samples were coated with gold for 240 s by a Quorum Q150R sputter coating machine to avoid charging. Measurements of fibers dimensions on obtained micrographs were done using the Electrospinz SEM Analyser software. The results were reported as the mean values of the data for each set of measurements.

The tensile mechanical properties of fabricated nanocomposites were investigated using a universal testing machine (Instron 4444). Rectangular shaped specimens of $80\,(l) \times 6\,(w) \times 0.1(t)$ mm³ were used. The initial gap between jaws was adjusted to 25 mm.

Tests were run at room temperature according to ASTM D882. A crosshead speed of 50 mm/min and load cell of 500 N was used for this test. The average values of the modulus, tensile strength and elongation at break over at least four replicates for each sample were taken.

Dynamic mechanical measurements were performed using a DMA Q800 (TA Instruments) equipment in the rectangular tension mode at 1 Hz, in the temperature range from room temperature to 150 °C and heating rate of 5 °C / min. The dimensions of the samples were 15 $(l) \times 5\ (w) \times 0.1(t)$ mm³. The strain values were sufficiently small to assure that the mechanical response of the specimen was within the linear viscoelastic range. The storage modulus, the loss modulus, and the ratio of these two parameters, $\tan\delta$ were determined.

Thermogravimetric analysis was carried out with a TGA Q600 (TA Instruments) equipment. Data were obtained under linear temperature conditions. The temperature was swept from room temperature to 500 °C at a heating rate of 10 °C / min under a nitrogen atmosphere.

3. Results and discussion

3.1. Microstructural analysis

The average diameter of the uniaxially aligned and random PVOH fibers was 267 nm, (Figure. 1a-b). The micrographs of fracture surfaces of fabricated materials are clearly showing the degree of morphological variation by addition of fibers and the change in manufacturing process.

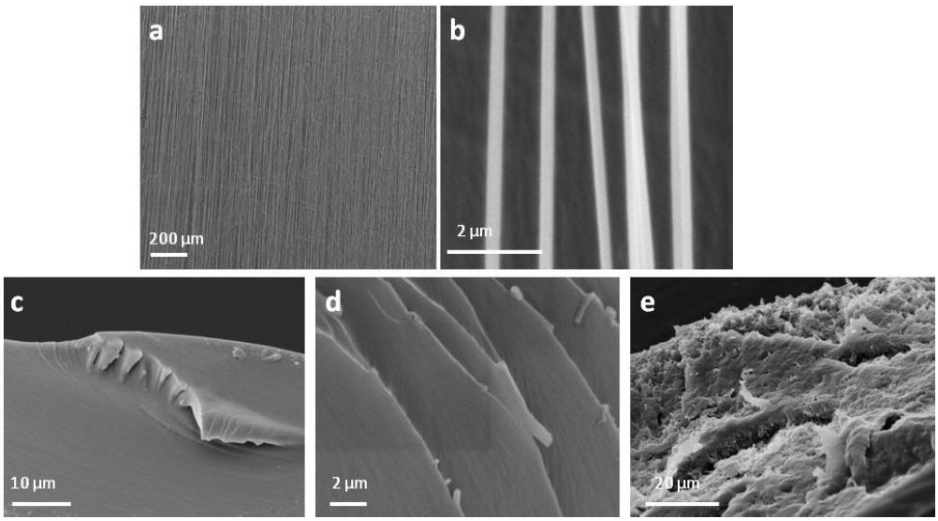

Figure 1. Scanning electron micrographs of (a, b) electrospun PVOH fibers and tensile fracture surfaces of: (c) NE, (d) WLNC, (e) ESNC.

As illustrated in **Figure 1c** the neat epoxy film (NE) has a brittle fracture behavior, characterized by large smooth areas. **Figure 1d** illustrated the SEM of failure surface of WLNC film and proved reasonable interfacial adhesion between the two phases, characterized by epoxy beads on the fiber remnants. This is attributed to the fiber / matrix compatibility and the possible hydrogen bonding interactions existing at their interface. The anhydride and the epoxy groups in the epoxy resin can react with the hydroxyl groups in the PVOH [12]. It has been stated that the PVOH ground surface, which represents the bulk, has reactive functional groups present at the outermost surfaces. As a result the PVOH polymer has more reactive functional

groups and a higher surface energy, which produces a surface with increased wettability and more possibilities for the creation of chemical bonds. ESNC films revealed a considerably different fractographic features (**Figure 1e**). The microstructure of the failure surface completely varied with that of WLNC films implying a shift in the level of the fiber/matrix interaction. The rough fracture surface and indistinct epoxy / fiber interface is evidence of efficient interfacial interaction of the two phases.

Apparently a dramatical increment in the fiber / matrix interfacial area by electrospraying the epoxy resin, rather than simple impregnation, led to such a significant shift. It is also worth to note that the fracture surface roughness observed in ESNC film helps to create a more tortuous path which requires more energy to propagate cracks and should lead to better mechanical performance [13].

3.2. Tensile properties

Recorded data for all three tensile parameters (tensile strength, Young's modulus and elongation at break) are presented in **Figure 2**.

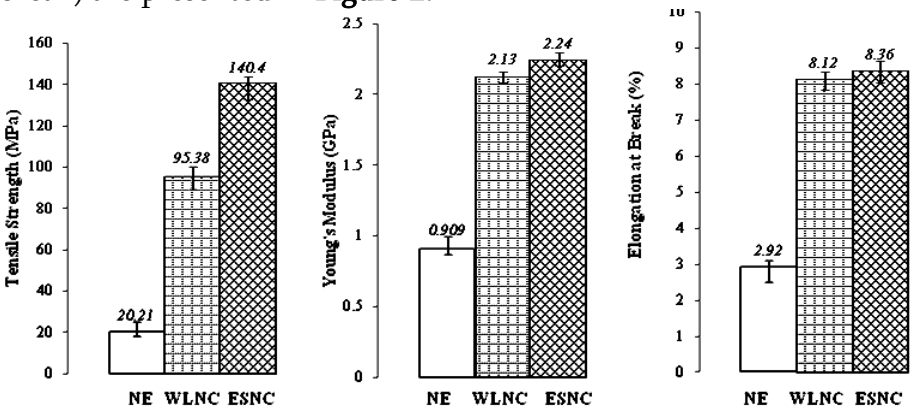

Figure 2. Tensile strength (MPa), Young's modulus (GPa) and elongation at break (%) of fabricated materials.

Significant increases in tensile strength (472 %), Young's modulus (234 %) and elongation at break (278 %) against neat matrix, were recorded for WLNC. Changing the processing technique to electrosprayed resin addition lifted these values to 695, 246 and 286 %, respectively. In the case of WLNC, it can be proposed that nanofibers bridge at the onset of matrix crack and contribute to redistribution of stresses near damage such as interfacial debonding so failure is delayed, resulting in the observed increase in mechanical performance. The significant contrast in results of the ESNC indicate that this novel processing technique improves the efficiency of fiber / matrix interactions and encourage the formation of a 3D fiber/matrix network securing the percolating nanofiber network within the matrix. The concomitant increase of elongation at break supports this proposition. The improved stiffness and ductility is a departure from the usually observed properties of nanocomposites, in which increases in modulus occur at the expense of elongation at break [14 – 16].

It is noteworthy to mention, the significant increases in mechanical properties observed in this study are believed to be mostly due to the alignment of the electrospun fibers as aligned fibers are classically more efficient reinforcements than randomly orientated fibers. In a study of epoxy reinforced electrospun cellulose nanofibrous mat, tensile strength of aligned cellulose nanofibrous mat in the longitudinal direction was increased seven fold compared to random mat [17].

3.3. Dynamic mechanical analysis

The effects of fibers addition and the variation in processing technique on the linear mechanical properties were investigated by DMA and the plots of the storage tensile modulus (E´) and loss angle tangent (tanδ) at 1 Hz as a function of temperature for the studied materials are given in **Figure 3**. The neat epoxy resin film showed a typical mechanical behaviour of an amorphous polymer material and presented the steepest slope of modulus drop with temperature compared to composite films (**Figure 3**).The modulus drop happened in the glass-rubber transition zone which is due to an energy dissipation phenomenon involving cooperative motions of long amorphous segments likely to rotate and translate [18]. With increasing temperatures the tensile modulus steadily decreases due to irreversible chain flow and disentanglement that are typical in amorphous polymers. At even higher temperatures, the modulus dropped sharply due to unrecoverable deformations of polymer matrix.

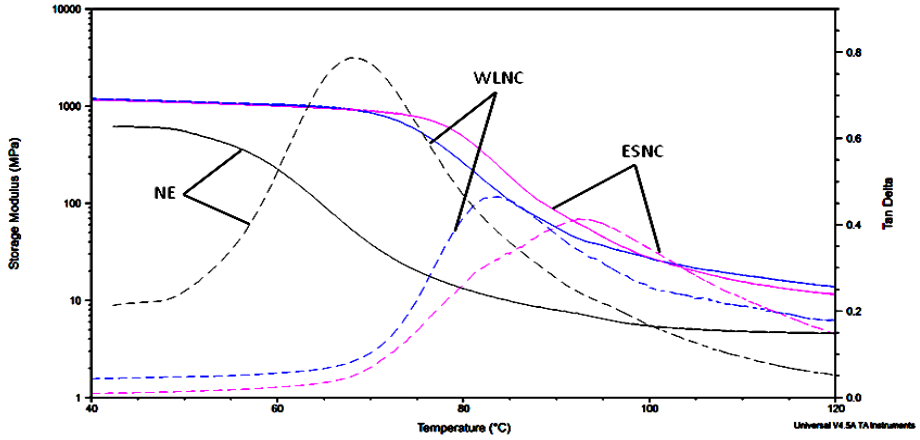

Figure 3. Evolution of logarithm of storage modulus (E') and tan δ as a function of temperature.

However results obtained from the reinforced films showed an improvement in storage modulus over the range of temperature for both WLNC and ESNC films, with predominance in the latter. For example the storage modulus of WLNC and ESNC films at 75 °C was increased by 28 and 38 times over that of the neat matrix. Moreover, as displayed in **Figure 3**, with change in processing technique, the tanδ peak shifted towards higher temperatures. Typically the higher the T_g, the higher the cross-linked density and the higher the modulus. As expected, the most prominent temperature peak shift occurred in the ESNC film which was + 23.73 °C. The height of tanδ peaks was also decreased for the fiber / epoxy nanocomposite films, suggesting that the dampening effect was reduced with the embedding of fibers into the matrix. The significant reinforcing effect observed in the ESNC film is ascribed to the intimate fiber/epoxy interfaces which cause the fibers to effectively communicate through the matrix via the percolation network held by hydrogen bonds. Thus reduce force impact and deformation thereby enhancing the storage modulus above T_g.

3.4. Thermogravimetric analysis

TGA is the most favoured technique for comparing and ranking the thermal stability of various polymeric samples. In this research in order to obtain deeper insights on the interactions between the constituent phases and the effect fibers addition and processing technique on thermal stability of fabricated films, TGA experiments carried out. Obtained thermogravimetric (TG) and derivative TG) curves are depicted in **Figure 4**.

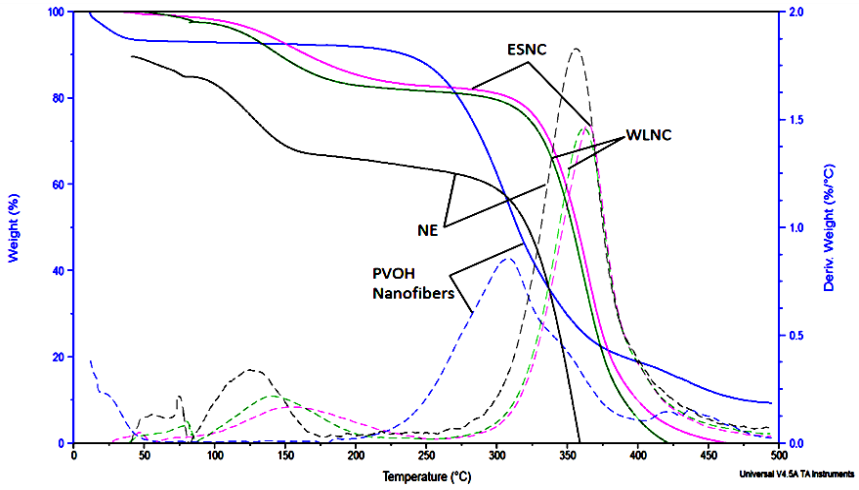

Figure 4. TG and DTG curves of PVOH nanofibers, NE, WLNC and ESNC films.

The PVOH nanofiber mats had the lowest thermal stability of the studied materials with a three-stage thermal decomposition process. The first stage presents the loss of weak physically absorbed water while second stage exhibits the decomposition of the PVOH side chains. The third stage shows the decomposition of the main chain of the PVOH [19]. The epoxy resin underwent typical thermal degradation beginning at 326 °C leading to a mass loss of 42 %. The thermal degradation profile of these materials combined into nanocomposite films showed similar effects. Overall, TGA findings were coherent with findings discussed in previous sections and followed the same trend: ESNC > WLNC > NE > PVOH. This again corroborated the good interaction between fibers and the matrix phase.

4. Conclusions

The findings of this research demonstrated that by using uniaxially aligned nanofibers, it is possible to make a considerable shift in thermal and mechanical performance of nanocomposite materials. The significant increase in mechanical properties at low levels of fiber addition indicates that the presence of aligned nanofibers made by electrospinning, with evident good interfacial adhesion between matrix and filler, are efficient reinforcements for composite articles. The novel electrospraying technique further improved the properties of the nanocomposites, and is a robust manufacturing technique with a ready potential for scale-up. It is worth noting that conventional composite manufacturing techniques may not be suitable for use with electrospun fibers due to the risk of fiber wash and poor impregnation. Electrospraying protects the nanofibers from handling damage, and importantly, does not affect fiber alignment.

Acknowledgements

Plant and Food Research Institute and mechanical engineering department at University of Canterbury are acknowledged for support of this research. Electrospinz Ltd, Blenheim kindly acknowledged for sincere cooperation and loaning certain pieces of equipment.

References

1. D. H. Reneker, A. L. Yarin. Electrospinning jets and polymer nanofibers. Polymer, 2008, 49, 10, 2387-2425.
2. W. Teo, S. Ramakrishna. A review on electrospinning design and nanofibre assemblies. Nanotechnol., 2006, 17, 14, R89.

3. N. Tucker, J. J. Stanger, M. P. Staiger, H. Razzaq, K. Hofman. The history of the science and technology of electrospinning from 1600 to 1995. J. Eng. Fabrics & Fibers, 2012, 7, 3, 63-73.
4. Y. Liu, S. Kumar. Polymer / carbon nanotube nano composite fibers – A review. ACS Appl. Mater. & Interfaces, 2014, 6, 9, 6069-6087.
5. K.-Y. Lee, Y. Aitomäki, L. A. Berglund, K. Oksman, A. Bismarck. On the use of nanocellulose as reinforcement in polymer matrix composites. Composites Sci. & Technolo, 2014, 105, 15-27.
6. Z.-M. Huang, Y.-Z. Zhang, M. Kotaki, S. Ramakrishna. A review on polymer nanofibers by electrospinning and their applications in nanocomposites. Composites Sci. & Technol., 2003, 63, 15, 2223-2253.
7. A. Kelly. Concise Encyclopedia of Composite Materials. 2012, Elsevier.
8. Y.-Z. Long, B. Sun, H.-D. Zhang, J.-L. Duvail, C.-Z. Gu, H.-L. Yin. Fabrication and applications of aligned nanofibers by electrospinning. Nanotechnol. Res. J., 2014, 7, 2, 155-160.
9. P. Katta, M. Alessandro, R. Ramsier, G. Chase. Continuous electrospinning of aligned polymer nanofibers onto a wire drum collector. Nano Lett., 2004, 4, 11, 2215-2218.
10. D. Li, Y. Wang, Y. Xia. Electrospinning nanofibers as uniaxially aligned arrays and layer-by-layer stacked films. Adv. Mater., 2004, 16, 4, 361-366.
11. A. Nurfaizey, J. Stanger, N. Tucker, N. Buunk, A. Wallace, M. Staiger. Manipulation of electrospun fibres in flight: the principle of superposition of electric fields as a control method. J. Mater. Sci., 2012, 47, 3, 1156-1163.
12. T. Chihani, P. Flodin, T. Hjertberg. Modification of epoxy surfaces with different polyvinylalcohol polymers. J. Appl. Polymer Sci., 1993, 50, 8, 1343-1350.
13. C. L. Wu, M. Q. Zhang, M. Z. Rong, K. Friedrich. Tensile performance improvement of low nanoparticles filled-polypropylene composites. Composites Sci. & Technol., 2002, 62, 10, 1327-1340.
14. S. I. Marras, K. P. Kladi, I. Tsivintzelis, I. Zuburtikudis, C. Panayiotou. Biodegradable polymer nanocomposites: the role of nanoclays on the thermomechanical characteristics and the electrospun fibrous structure. Acta Biomater., 2008, 4, 3, 756-765.
15. V. Causin, B.-X. Yang, C. Marega, S. H. Goh, A. Marigo. Nucleation, structure and lamellar morphology of isotactic polypropylene filled with polypropylene-grafted multiwalled carbon nanotubes. Eur. Polymer J., 2009 ,45, 8, 2155-2163.
16. S. Karimi, P. M. Tahir, A. Dufresne, A. Karimi, A. Abdulkhani. A comparative study on characteristics of nanocellulose reinforced thermoplastic starch biofilms prepared with different techniques. Nordic Pulp & Paper Res. J., 2014, 29, 1, 41-45.
17. H. Liao, Y. Wu, M. Wu, X. Zhan, H. Liu. Aligned electrospun cellulose fibers reinforced epoxy resin composite films with high visible light transmittance. Cellulose, 2012. 19, 1, 111-119.
18. A. P. Mathew, W. Thielemans, A. Dufresne. Mechanical properties of nanocomposites from sorbitol plasticized starch and tunicin whiskers. J. Appl. Polymer Sci., 2008, 109, 6, 4065-4074.
19. N. Othman, N. A. Azahari, H. Ismail. Thermal properties of polyvinyl alcohol (PVOH) / corn starch blend film. Malaysian Polymer J., 2011, 6, 6, 147-154.

ON MORPHOLOGY OF INDIUM PHOSPHIDE BASED NANOWIRES

D. Jishiashvili, Z. Shiolashvili, N. Makhatadze,
A. Jishiashvili, B. Buadze, L. Chkhartishvili

Georgian Technical University
Department of Engineering Physics
Tbilisi, Georgia
d_jishiashvili@gtu.ge

Accepted October 19, 2015

Abstract

The InP based nanowires were produced by direct annealing of crystalline InP sources in hydrazine (N_2H_4) vapor and subsequent condensation of volatile spices onto the substrates. The morphology and sizes of nanowires showed strong dependence on the growth temperature. In the temperature range of 440 – 540 °C, the morphology of InP nanostructures were changed from true nanowires with minimum diameters of ca. 25 nm formed at 440 °C, to faceted, several μm size large crystalline blocks of InP growing at 540 °C simultaneously with the rhombus decorated zigzag shaped InP nanowires with extended surfaces. The nanowires growth mechanism also varied with the temperature. In the range of 440 – 500 °C they were growing through the Vapor–Solid mechanism. At 540 °C the Vapor–Solid and Vapor–Liquid–Solid mechanisms coexisted forming large elongated blocks of indium phosphide together with zigzag shaped InP nanowires.

1. Introduction

The bulk Indium Phosphide (InP) is an important semiconductor due to its unique electronic and optical properties [1, 2]. These outstanding features are even more pronounced in one dimensional InP nanowires (NWs) because in such nanomaterials the properties are strongly influenced by the increased surface-to-volume atomic ratio and different size-depended quantum effects [1, 3 – 7]. III–V semiconductor nanowires have been considered as the most promising materials for next generation optoelectronic devices including light emitting diodes, opto-transistors, lasers, photodetectors, and solar cells [8, 9]. Recently the great interest was attracted to the photovoltaic and photodetectors application of InP nanowires and InP nanowire areas. The reason for this lies in the very high optical absorption in InP nanowire areas that may exceed 90 % [4, 9, 10].

The bulk InP has the zinc blend (ZB) structure, while InP nanowires may easily adopt the unusual wurtzite (WZ) structure together with ZB one. In some cases both structures may coexist and the interband transitions in the mixed-phase regions of nanowires may increase the efficiency of photodetectors or solar cells [11]. The morphology can also change the properties of InP nanowires. For example, the zigzag-shaped InP nanowires exhibit unique novel optical properties which may find applications in optoelectronic devices [2, 12, 13].

The purpose of this study was to investigate the temperature dependence of the morphology of InP nanowires produced by pyrolytic method in the presence of hydrazine (N_2H_4) vapor.

2. Experimental

Nanowires were grown in the vertical quartz reactor, which was first evacuated down to $5.3 \cdot 10^{-3}$ Pa and then filled with N_2H_4 vapor, which was containing 3 mol. % H_2O. The reactor was then isolated from the vacuum system and the saturated pressure of N_2H_4 (~$1.3 \cdot 10^{-3}$ Pa) was established in the chamber at the room temperature. The source material in the form of unpolished 2 – 3 mm thick single crystalline InP disc was placed at the flat bottom of the reactor (the hot zone) and the substrates (polished Si and glass) were placed on a tubular quartz spacer at 0.5 – 2.0 cm above the source (the cold zone). The external furnace was attached to the bottom of the reactor. The source was annealed in the temperature range of 400 – 580 °C. The substrate was subsequently heated due to radiate and convective heating from below, and its temperature was determined by the source temperature and the distance from the source. The typical growth process lasted for 40 – 60 min.

The morphology and structure of NWs were studied using FEI Quanta FEG 600 Scanning Electron Microscope (SEM) and FEI Tecnai F30 (FEG) equipped with energy dispersive X-ray (EDX) and a high-angle annular dark-field (HAADF) detector. XRD data were taken on a Shimadzu XRD–6000 diffractometer.

3. Results and discussion

InP nanowires were grown on the substrates heated at three different temperatures – 440, 500 and 540 °C. The first step in the InP nanowire growth process was the thermal decomposition of crystalline InP source. As a result, the gaseous phosphorus ambient and In precursors were formed. Simultaneously, at elevated temperatures due to the pyrolytic decomposition of hydrazine the active chemical species were produced. They include H_2 and atomic hydrogen (as an intermediate product), together with NH, NH_2, NH_3, molecular and atomic nitrogen.

As it was found in [14], in the presence of hydrogen the InP dissociation temperature can be significantly decreased. For example, the energy of activation of dissociation reaction is reduced from 154.5 down to 38.9 kJ mol^{-1}, and InP dissociates at 297 °C in the presence of atomic hydrogen. The most important is that the phosphine (PH_3) appears in the gaseous phase together with P_4, and the pressure of diphosphorus (P_2) increases up to 10^{-5} Torr, providing phosphors precursors for the growth of InP NWs.

The transportation of In to the Si substrate surface needs the formation of volatile molecules. The only volatile species that could perform this task are In suboxides (In_2O). The water molecules diluted in hydrazine and some residual oxygen in the reactor are considered to be the only sources for producing indium suboxides. In_2O served as a precursor in deferent technologies that were developed for the growth of InP nanowires. The solid powder of In_2O_3 is usually used for producing indium suboxides. This is accomplished by annealing of a mixture of In_2O_3 and pure In, or using carbon powder with In_2O_3. In both cases, due to the absence of oxygen, the heat treatment causes the transformation of stabile In III oxides into the volatile

indium suboxide or CO_2. In our technology In_2O was produced after thermal dissociation of InP, formation of indium droplets onto the surface of source InP and interaction with water vapor. The water content in hydrazine was quite low (3 mol. %) for producing stabile In_2O_3, but its concentration was sufficient to form volatile suboxides which then served as precursors for the synthesis and growth of nanowires.

Figure 1 represents the XRD pattern of InP nanowires synthesized at 440 °C on Si substrate. Only the diffraction peaks of zinc bland type InP are observed. All nanowires synthesized in the temperature range of 440 – 550 °C have the same zinc bland structure. It should be noted, that in our previous work [15] using the same technology but Ga + InP source, we have obtained core-shell nanowires with wurtzite InP core and amorphous Ga_2O_3 shell. The formation of WZ InP can be attributed to the presence of Ga in the source material.

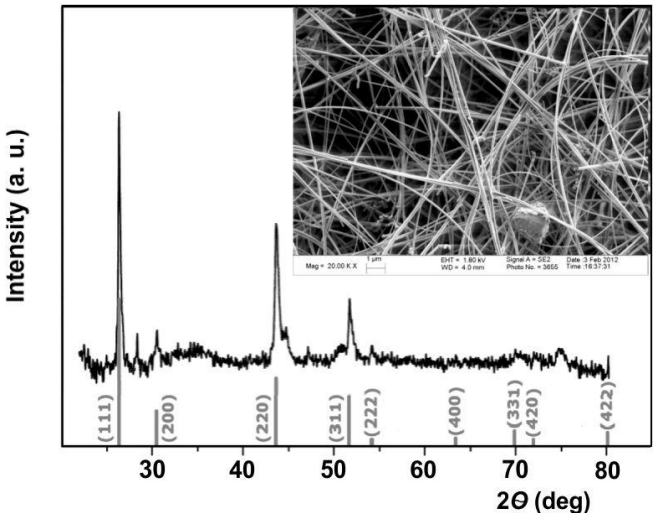

Figure 1. XRD pattern of InP nanowires grown on Si substrate at 440 °C. Inset shows the SEM image of the same nanowires.

At lower temperatures the nanowires have smaller diameters and circular cross-sections. The grown nanowire "mat" is shown in the inset of **Figure 1**. No evidence of tapering was observed in InP nanowires. The aspect ratios of nanowires were sufficiently high as the lengths of some NWs in the inset of **Figure 1** exceeded 30 μm and the minimum thickness was less than 25 nm. The large deviation in NW diameters is a drawback of the developed technology together with the deposition of side products at the early stage of the NW growth. Unevenly distributed side product may change the local temperatures at the NW nucleation sites causing the large deviation in NW diameters.

The absence of catalyst droplets at the NW tips indicates that the growth was performed through the oxide-assisted Vapor–Solid (VS) method.

TEM investigation of grown product reveals that two types of NWs were formed on the Si substrate at T_s = 440 °C. Both of them are presented in **Figures 2a** and **b**. The first one has a uniform diameter and its side-wall appears as a straight line in the TEM image (**Figure 2a**). Its body has less dark spots and lines in HAAD STEM (**Figure 2b**) indicating more or less uniform distribution of density and strains. The electron diffraction patterns (not shown in **Figure 2**) confirmed that both NWs had ZB structure and they were growing along the [111] direction with d-spacing of 0.34 nm that corresponds to interplane distance in ZB InP.

The (111) surfaces of ZB III/V semiconductors have the lowest surface free energy. Due to the low stacking fault energy of (111) InP, this crystal easily forms twins which are

frequently observed in InP NWs [16]. These so-called rotational twins may cause the blue shift of Photoluminescence and an unexpectedly large photovoltaic effect [17, 18]. This type of twinning was also observed in our InP nanowires. **Figure 2c** represents one of the randomly twinned InP nanowires. The growth direction is again [111] but the electron diffraction pattern (not shown in **Figure 2**) presents the striation of spots that are characterizing the intensive twinning. Insertion of a twin plane into the zinc-blende crystal changes the stacking order creating a small segment of wurtzite between two zinc-blende domains. Each time the twin is formed the wall of NW changes the direction by 39 degrees causing the irregular side-wall profile shown in the TEM image (**Figure 2d**). The morphology of these NWs exactly coincides with typical shapes of twinned III / V semiconductors reported by other authors [19].

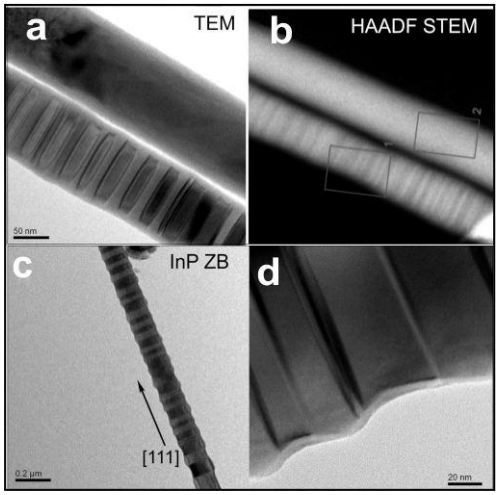

Figure 2. TEM images of zinc blend InP NWs without and with rotational twins grown at 440 °C (a); HAADF STEM image of same NWs (b); randomly twinned NW (c) and the image of its sidewall (d).

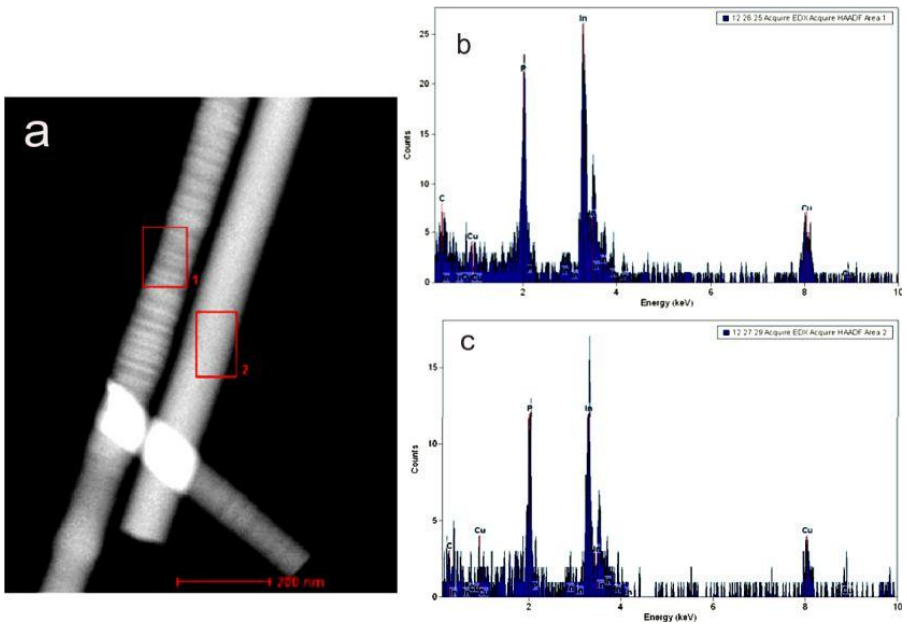

Figure 3. HAAD STEM image of InP nanowire (grown at 440 °C) with regular zinc blend structure and with rotational twins (a) and corresponding EDX spectra of NWs taken from the rectangular areas marked by 1 and 2 in a (b, c).

The composition of NWs was analyzed using the high-angle annular dark-field (HAADF) scanning transmission electron microscopy (STEM). This method is based on the *z*-contrast effect and the material with high mean atomic number appears in the image as a bright area. Two neighboring nanowires were chosen for analyzes. The first was containing large amount of twins and the second was nearly uniform with much less twins. **Figure 3a** presents the HAADF STEM image of both NWs with their characteristic features. In the twinned NW the deviation of NW diameter along the growth direction can be clearly detected. Note that the color of untwined nanowire is uniform displaying the uniform distribution of material all over the wire. It means that the dark spots on the ZB nanowire without twins presented in **Figure 2a** are caused solely by local strains and charges. The image of a left nanowire in **Fig.ure 3a** shows non-uniform distribution of density caused by twinning and insertion of wurtzite segments.

The composition was determined using EDX method and the analyzed framed square areas are shown in **Figures 3b** and **c**. As can be seen both nanowires have the same composition close to stoichiometric InP. The carbon and Cu signals are caused by TEM grid and partly by hydrocarbon contaminants which were adsorbed during the air exposure of NWs. The most important result is that even in the presence of oxygen and nitrogen precursors in the hydrazine decomposition products, both nanowires do not contain oxygen or nitrogen. One possible explanation is that the growth temperature (T_s = 440 °C) is insufficient to produce indium nitride, while oxides are reduced in the presence of hydrogen.

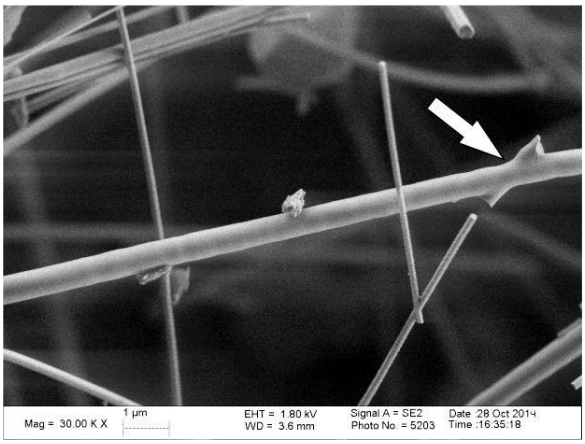

Figure 4. Zinc-blend InP nanowires produced at 500 °C.

The increase of growth temperature up to 500 °C caused the formation of mostly untwined InP nanowires. However, the diameters of NWs were also increased reaching the maximum value of ca. 600 nm (**Figure 4**). Again, no catalysts were found at NW tips and the growth was performed by VS method. At this temperature the secondary nucleation and brunching was taking place as it is indicated by a white arrow in **Figure 4**.

The dramatic changes in the morphology of NWs were observed when the growth temperature was raised to 540 °C. **Figure 5** illustrates the morphologies of materials produced at this temperature. Two types of materials can be defined in **Figures 5a** and **b**. One represents large, several micrometers wide and faceted blocks of crystalline InP with catalyst ball tip. Their widths reach several micrometers and lengths – tens of μm. It should be noted that the amount of products grown on Si substrate at 540 °C exceeds by 3 – 4 times that of NWs produced at lower temperatures.

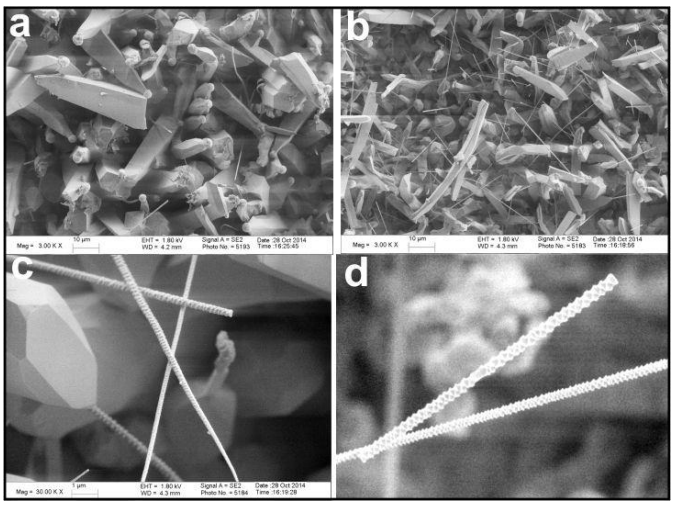

Figure 5. SEM images of two types of InP NWs formed on Si substrate at 540 °C (a, b); Increased view of zigzag shaped nanowires.

The presence of catalysts is clear evidence that NWs were growing through the VLS method. This method needs low energy budget and hence may take place at low temperatures. However, the situation is reverse in our experiments as at low temperatures the NWs are grown by VS mechanism which is then changed to VLS at elevated temperatures. XRD patterns show no evidence of the presence of crystalline In or any other crystalline material in catalyst tips. We suppose, that at high temperatures, close to 540 °C, after intensive adsorption of In_2O molecules, a part of them was reduced by hydrogen to metallic In, which then coalesced into large molten In droplets providing catalysts for VLS growth. The process involved permanent dissolution of phosphorus and indium precursors in molten catalyst, oversaturation and segregation of solid InP. After the furnace was switched off and the process was stopped, the solidification of cooled catalyst proceeded at a high concentration of impurities which prevented the crystallization of catalyst droplets. The porous appearance of some catalyst surfaces also confirms this assumption. In contrast to VLS growth at 540 °C, at lower temperatures (440 – 500 °C) the intensity of In_2O sublimation and adsorption was significantly lower and adsorbed molecules were consumed solely for the VS growth of InP nanowires.

The second type of NWs is also clearly seen in **Figures 3a** and **b**. These are straight NWs wit uniform diameters in the range of 50 – 200 nm. They are scattered all over the surface covered with large InP blocks. SEM images of these NWs are shown in **Figures 5c** and **d**. The absence of catalyst tips indicates that in contrast to large InP blocks, this type of NWs was growing through the VS mechanism.

The same types of NWs were obtained in [12, 13]. They were produced in the quartz tube heated up to 1200 °C. This temperature is by 660 °C exceeding the growth temperature in our processes. The authors call them the periodic-rhombus-decorated single-crystal InP and explained their formation by the presence of ZnSe promoter in the reaction chamber. These twinned NWs were characterized by unique structural and optical properties which were making them interesting for the device applications. Our experimental setup does not use ZnSe. It can be suggested that formation of this unusual structure is caused and promoted by the presence of active hydrazine decomposition products together with a high growth rate at elevated temperatures which leads to intensive twinning, and results in the formation of NWs with observed morphology.

4. Conclusions

InP nanowires were grown by annealing crystalline InP sources in the vapor of hydrazine diluted with 3 mol. % H_2O. In_2O and phosphorus formed after thermal dissociation of InP served as precursors for the synthesis of NWs. In the temperature range of 440 – 500 °C the zinc blend type InP nanowires with regular structure and twinned nanowires were produced. They were growing through the Vapor–Solid mechanism. NWs produced at 440 °C had smaller diameters (20 – 100 nm) then those, synthesized at 500 °C. At 540 °C two types of nanowires were simultaneously observed: elongated large InP crystalline blocks with several micrometer cross sections grown by In catalyzed Vapor–Liquid–Solid mechanism and zigzag shaped, twinned, straight InP NWs with diameters in the range of 50 – 200 nm. Formation of zigzag InP NWs is explained by the high activity of hydrazine decomposition products and intensive twinning that take place at 540 °C.

Acknowledgements

The authors are thankful to Prof. Dr. Greta R. Patzke and Dr. Roman Kontic (University of Zurich, Institute of Inorganic Chemistry, Zurich, Switzerland) for permanent help in experimental work.

References

1. M. T. Borgström, J. Wallentin, M. Heurlin, S. Fält, P. Wickert, J. Leene, M. H. Magnusson, K. Deppert, L. Samuelson. Nanowires with promise for photovoltaics. IEEE J. Selec. Topics Quan. Electr., 2011, 17, 4, 1050-1061.
2. H. J. Joyce, Q. Gao, H. H. Tan, C. Jagadish, Y. Kim, J. Zou, L. M. Smith, H. E. Jackson, J. M. Yarrison–Rice, P. Parkinson, M. B. Johnston. III–V semiconductor nanowires for optoelectronic device applications. Prog. Quant. Electr., 2011, 35, 2-3, 23-75.
3. M. Heurlin, P. Wickert, S. Fält, M. T. Borgström, K. Deppert, L. Samuelson, M. H. Magnusson. Axial InP nanowire tandem junction grown on a Si substrate. Nano Lett., 2011, 11, 5, 2028-2031.
4. M. Chen, E. Nakai, K. Tomioka, T. Fukui. Application of free-standing InP nanowire arrays and their optical properties for resource-saving solar cells. Appl. Phys. Express, 2015, 8, 012301, 1-3.
5. J. Wallentin, N. Anttu, D. Asoli, M. Huffman, I. Åberg, M. H. Magnusson, G. Siefer, P. Fuss–Kailuweit, F. Dimroth, B. Witzigmann, H. Q. Xu, L. Samuelson, K. Deppert, M. T. Borgström. InP nanowire array solar cells achieving 13.8 % efficiency by exceeding the ray optics limit. Science, 2013, 339, 6123, 1057-1060.
6. H. Kamimura, C. J. Dalmaschio, S. C. Carrocine, A. D. Rodrigues1, R. C. Gouveia, E. R. Leite, A. J. Chiquito. Optoelectronic characteristics of single InP nanowire grown from solid source. Mater. Res. Express, 2015, 2, 045012, 1-4.
7. M. De Luca, A. Zilli, H. A. Fonseka, S. Mokkapati, A. Miriametro, H. H. Tan, L. M. Smith, Ch. Jagadish, M. Capizzi, A. Polimeni. Polarized light absorption in wurtzite InP nanowire ensembles. Nano Lett., 2015, 15, 2, 998-1005.

8. J. Xiang. Semiconductor Nanowires. 2014, Cambridge: Royal Soc. Chem. – Thomas Graham Publ. House.
9. L. Cao, J. S. White, J.-Sh. Park, J. A. Schuller, B. M. Clemens, M. L. Brongersma. (2009) Engineering light absorption in semiconductor nanowire devices. Nat. Mater. 8(8):643-647.
10. A. Hosseinnia, N. Anttu. Absorption through a coupled optical resonance in a horizontal InP nanowire array. Photon. Res., 2015, 3, 4, 125-128.
11. J. Vishal. Study of photocurrent generation in InP nanowire-based p^+–i–n^+ photodetectors. Nano Res., 2015, 7, 4, 544-552.
12. G. Shen, Y. Bando, B. Liu, Ch. Tang, D. Golberg. Unconventional zigzag indium phosphide single-crystalline and twinned nanowires. J. Phys. Chem. B, 2006, 110, 41, 20129-20132.
13. H. Tsuzuki, D. F. Cesar, M. R. S. Dias, G. E. Marques. Tailoring electronic transparency of twin-plane 1D superlattices. ACS Nano, 2011, 11, 5, 5519-5525.
14. V. I. Gorbenko, A. N. Gorban. Thermal decomposition of indium phosphide in vacuum and atomic hydrogen environment. Radio Electr. , 2012, 1, 26, 7-10.
15. D. Jishiashvili, Z. Shiolashvili, N. Makhatadze, A. Jishiashvili, V. Gobronidze, D. Sukhanov. Vapor–Solid growth of InP and Ga_2O_3 based composite nanowires. Eur. Chem. Bull., 2015, 4, 1-3, 24-29.
16. R. L. Woo, R. Xiao, Y. Kobayashi, L. Gao, N. Goe, M. K. Hudait, Th. E. Mallouk, R. F. Hicks. Effect of twinning on the photoluminescence and photoelectrochemical properties of indium phosphide nanowires grown on silicon (111). Nano Lett., 2008, 8, 2, 4664-46692.
17. J. Bao, D. C. Bell, F. Capasso, J. B. Wagner, Th. Mårtensson, J. Trägårdh, L. Samuelson. Optical properties of rotationally twinned InP nanowire heterostructures. Nano Lett., 2008, 8, 3, 836-841.
18. J. Wallentin, M. Ek, L. R. Wallenberg, L. Samuelson, M. T. Borgström. Electron trapping in InP nanowire FETs with stacking faults. Nano Lett., 2012, 12, 1, 151-155.
19. Q. Xiong, J. Wang, P. C. Eklund. Coherent twinning phenomena: towards twinning superlattices in III–V semiconducting nanowires. Nano Lett., 2006, 6, 12, 2736-2742.

ASSESSMENT OF POLYSULFONE MEMBRANES EMBEDDED WITH CARBON NANOTUBES AND POLYESTER NON-WOVEN FABRIC SUPPORT FOR THE TREATMENT OF OIL AND GAS PRODUCED WASTEWATER

O.-A. Kwame [1], D. B. Nkazi [1], J. Mulopo [1], S. E. Iyuke [1], S. D. Mhlanga [2]

[1] University of the Witwatersrand
School of Chemical & Metallurgical Engineering
Johannesburg, South Africa
oakwame57@gmail.com
[2] University of Johannesburg
Department of Applied Chemistry
Johannesburg, South Africa

Accepted October 19, 2015

Abstract

This paper considers the use of modified Polysulfone membranes for the treatment of wastewater produced in the oil and gas industry. The micro-porous anisotropic membranes were prepared using the Phase Inversion (PI) method and embedded with carbon nanotubes (CNTs) and / or not supported on a polyester non-woven fabric. The membranes were characterized using the Scanning Electron Microscopy (SEM), atomic force microscopy (AFM), Fourier Transform Infrared Spectroscopy (FTIR), and tensile strength analysis. The pore sizes ranged from 1.598 μm for the membranes with the fabric support to 0.191 mm for the CNT imbedded membranes without a fabric support. The results showed that the functionalized CNTs interacted with the hydrophobic membranes to enhance its physical, chemical and mechanical properties. The addition of a fabric support decreased the pore sizes of the PI membranes. The membranes were tested for performance and it was shown that increasing pressure increased permeates flux and CNTs increased permeate flux while controlling fouling via pore blockage. The fabric influenced the flux decline by providing further resistance to the flow of permeates through the membrane. Permeates were collected and tested for oil concentrations. The results showed oil rejections ranging between 78 and 90 % with the mixed matrix phase inversion membrane supported on a polyester non-woven fabric having the highest oil rejections.

Introduction

Produced oil wastewater is the largest waste stream from oil and gas exploration and production processes [1] and as a rule of thumb the quantity of produced oil wastewater from offshore and onshore activities is approximately three times that of the oil that is refined.

Produced oil wastewater is generated when underground saline water, which is denser than crude oil settled in reservoir rocks, comes out with some oil and gas during the drilling process or when formation water, injected into the oil wells during exploration comes to the surface with the oil and saline water mixture. Produced oil wastewater contains various organic

and inorganic impurities dissolved in the dispersed oil or in water [2] and these impurities cannot be discharged directly to the environment. Typical concentration of oil in produced water ranges from 50 to 1000 mg / L or more, depending on the oilfield [3, 4]]. Contaminants in dispersed oil include carcinogens polycyclic aromatic hydrocarbons (PAHs) and heavy alkyl phenols, dissolved minerals that contains trace amounts of heavy metals and normally occurring radioactive materials such as radium 226 and 228 [5].

Different physical and chemical treatment methods have been considered for the treatment of produced oil wastewater [2, 6]. However; the challenge has been that most of these technologies are not suitable for produced oil wastewater for offshore processes due mainly to space limitations and to the cost and additional toxicity of chemicals often required in these processes [2]. Biological treatments have been also considered and although they are less costly and better at removing dissolved and suspended compounds from the wastewater, they still face the challenge of limited space on offshore platforms [2].

To circumvent the above problem of space limitations, membrane treatment processes have been considered for medium to large offshore platforms as well as the onshore treatment of produced oil wastewater. Membrane processes have proven to have low capital cost, makes no use of toxic chemicals and can treat large flows of wastewater to produce high quality permeates [7]. However; the major challenge with the application of membrane processes has been the occurrence of fouling [8] which significantly affect the membrane performance and increases the overall cost of wastewater treatment. There have been suggestions that the membrane fouling can be controlled through modification with materials such as carbon nanotubes (CNTs) or polyvinyl alcohol [9, 10). This is the context behind this paper which seeks to assess the performance of modified membranes with carbon nanotubes and a polyester non- woven fabric.

Material and methods

Materials

Crude oil from NATREF Laboratory in Sasolburg, South Africa was used in the production of synthetic oil water. All chemicals were analytical grade chemicals from Sigma-Aldrich, unless otherwise stated. Polysulfone beads (mol wt. 35 000Da), 1-methyl-2-pyrrolidinone (NMP, ≥ 99 %), calcium carbonate ($CaCO_3$), iron (III) nitrate nonahydrate ($Fe(NO_3)_3.9H_2O$, ≥ 98 %), cobalt (II) nitrate hexahydrate ($Co(NO_3)_2.6H_2O$, 98 + %) and 55 % nitric acid (HNO_3 of 55 % concentration) were all bought from Sigma-Aldrich. Technical grade nitrogen and acetylene gas were bought from Afrox South Africa. Sojitz Corp., Japan donated the polyester non-woven fabric.

Equipment and methods

A 1000 mg / L oil water mixture was prepared using millipore water. This was sonicated for 30 min until the oil was adequately dispersed in the water. This solution was left untouched in ambient conditions for a month to ensure the dispersed oil did not naturally separate into the different phases.

The CVD method was used in the production and functionalization of CNTs with acetylene as the carbon source and the produced metallic alloy as the catalyst as described by Phao [11]. The setup is illustrated in **Figure 1**. Nitrogen was used as the inert gas to purge the

system of any unwanted material and reduce the amount of impurities in the CNTs. One gram of the catalyst was measured onto a quartz boat and placed at the center of the horizontal furnace. The furnace was set to 700 °C and inert nitrogen gas passed through the quartz tube at 180 ml / min for 110 min. After the purge time, acetylene gas (along with nitrogen gas) was allowed through the system at a rate of 90 ml / min for 1 h to initiate the CNT growth.

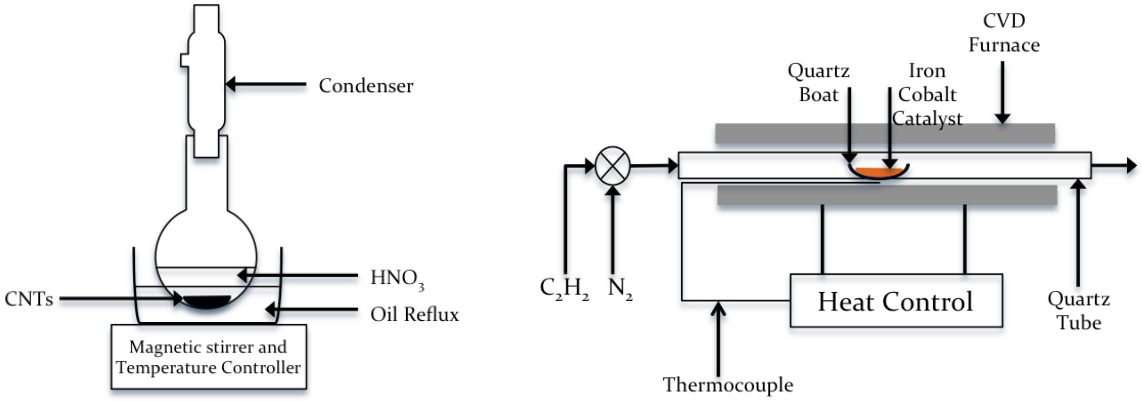

Figure 1. (a) CVD set up for CNT synthesis (b) Acid treatment of synthesized CNTs.

The as grown CNTs were soaked in 100 ml of HNO_3. This was then refluxed at 110 °C for 4 h. The mixture was allowed to cool and poured into a 5000 ml beaker of distilled water to allow the functionalized CNTs (fCNTs) to settle. The fCNTs were thoroughly washed with distilled water until a neutral pH was attained and then dried at 120 °C prior characterization.

The phase inversion method was used in the preparation of the polymeric membranes. A 20 % w/w casting solution was prepared using polysulfone (PSF) as the polymer and (NMP) as the solvent. The PSF beads were dissolved in the solvent by magnetic stirring for 24 hours, until a homogenous solution was obtained [11]. For the fCNT/PSF blended membranes, a 0.04 wt. % concentration of CNTs was dispersed in the solvent and mixed *via* ultrasonication until a homogenous solution was obtained before the PSF beads were added. The NMP was used to top up the solution to its initial level to ensure that a 20 % w/w solution was maintained. The solution was then cast using a casting blade set to 250 μm. The casting solution was cast on a glass plate, with the polyester non-woven fabric firmly supported onto the glass. The cast solution was then immersed into a bath of distilled water for the phase separation step. The membrane was further washed with distilled water and stored in another water bath for 24 h to ensure the complete liquid-liquid transfer of the liquid and solvent.

The Sterlitech™ membrane test cell system was used for the membrane filtration tests. **Figure 2** presents the flow diagram of the system. The system allowed for 4 membranes to be tested simultaneously. This made it easier to repeat the experiment and reduce the standard deviation. To compact the membranes, distilled water was passed through each membrane at 689.475 kPa for a minimum of 4 h. Pure water fluxes were calculated at four different pressures for each membrane: 172.37, 241.32, 310.26 and 379.21 kPa. The prepared synthetic produced oil was then passed through the membranes and the permeate fluxes determined at the same pressures. The fluxes were calculated using Eq. (1):

$$J_p = \frac{V}{A\,\Delta t}, \quad (1)$$

where, J_p is the permeate flux (for both water and oil fluxes) obtained and is measured in (l / m h), V is the volume of the collected permeate, A is the effective membrane area (0.0042 m^2 for this system) and Δt is running time during which permeate was collected.

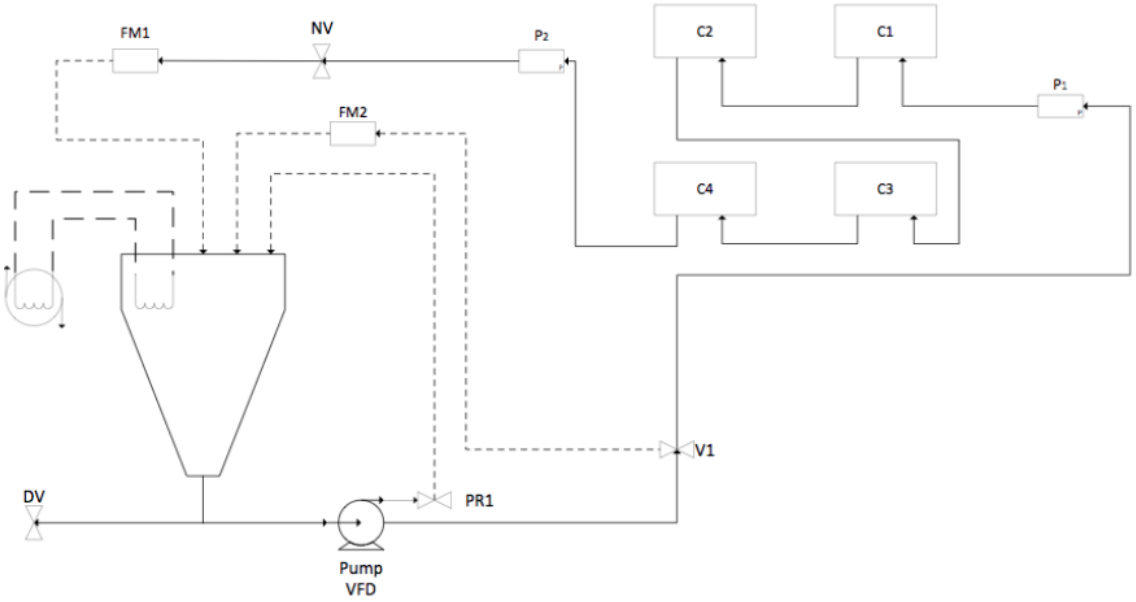

Figure 2. The Sterlitech™ membrane test cell system.

Displayed text	Description
P1	Inlet pressure sensor in psi / bar
P2	Outlet pressure sensor in psi / bar
VFD	Variable frequency drive
PR1	Pressure relief valve in 150 psi
DV	Tank drain valve
V1	Bypass needle valve
NV	Control valve
FM 1& 2	Flow sensor 1 and 2
C1, C2, C3 & C4	Membrane cells

The same experiment was conducted at a constant pressure of 45 psi for 2 h to determine the flux variation with time. The volume after every 15min was measured and used to calculate the relative flux (J_r), which is given as

$$J_r = \frac{J_t}{J_o}, \quad (2)$$

where, J_t is the flux after every 15 min and J_o is the initial flux. The flux decline (FD_t) was then calculated using the following equation

$$FD_t = \left(1 - \frac{J_t}{J_o}\right) \times 100 \quad (3)$$

The efficiencies of the membranes were determined by calculating the percentage oil rejection (R) by the following equation

$$R = \left(1 - \frac{C_p}{C_f}\right) \times 100, \quad (4)$$

where, C_f in mg / L is the concentration of the prepared synthetic produced oil (1000 mg / L) and C_p is that of the oil in the permeate. The concentrations were measured using a UV–Vis photo-spectrometer.

Analysis

Transmission Electron Microscopy (TEM) analysis was used to confirm the existence of CNTs and Raman spectroscopy combined with Fourier Transform Infrared Spectroscopy (FTIR) were used to confirm the presence of functional groups in the CNTs walls. An Energy

Dispersive Spectroscopy (EDS) analysis was used to investigate the purity and composition of the synthesized nanotube. The synthetic produced oil wastewater was passed through the prepared membranes and the permeate fluxes were collected and recorded at the same pressures. These permeates were then characterized for oil rejections using the UV-Vis photo-spectrometer. The variation of flux with time was also recorded to study the effects of fouling on the membrane.

Results and discussions

The properties of the Phase Inversion (PI) membranes prepared were analyzed and the effects of the addition or not of CNTs and the fabric on the physical, chemical and mechanical properties of the membranes were investigated. **Table 1** summarizes the pore and fracture sizes. It was found that the top surface of the PI CNT membrane is very similar that of the PI bare membrane except the surface pores are slightly larger with an average diameter of 0.191 mm, compared with 0.164 mm of the PI bare membranes. The fractures in the cross section are also slightly larger in the PI CNT membranes with an average size of 1.587 μm, compared to the 0.659 μm of the PI bare membranes The pores size are 1.192 and 1.592 μm for the PI bare on fabric and PI CNT on fabric respectively. The pore and fracture sizes increases after CNTs are imbedded into the membrane. The membranes cast on fabric have smaller surface pore and larger fracture sizes than those without the fabric support. This is due to the interaction between the casting solution and the fabric, which seems to enhance the rate of the liquid-liquid exchange between the water and the NMP solvent and in turn increases the pore sizes of the membrane. These pores and fracture sizes are consistent with micro porous anisotropic membranes as reported in the literature [12].

Table 1. Pore and fracture sizes synthesized membranes.

	Top surface pore size	Cross sectional fracture size
PI bare	0.164 μm	0.659 μm
PI CNT	0.191 μm	1.587 μm
PI bare on fabric	1.192 μm	1.727 μm
PI CNT on fabric	1.598 μm	3.417 μm

The Veeco Di3100 atomic force microscope was used to evaluate the topographic images of the membrane surfaces. A contact mode (or tapping mode) AFM was employed. In this mode, a laser beam is deflected off the back of a cantilever and the deviation signals are read and illustrated as the topographic images. The pore distribution was qualitatively analyzed and surface roughness presented. The surface roughness of a membrane is directly related to the gas permeability of the membrane [13]. In the 3D images, the nodules (or peaks) represent the bright spots, while the pores (or valleys) represent the dark spots. **Figure 3** presents the AFM images for the PI bare and PI CNT membranes. **Figure 3b** has a higher distribution of dark and light spots (nodules and pores) for the same area. This is translated to an increase in the Roughness R_a from 62.387 to 328.33 nm. This agrees with what is expected i.e. the modification of the membrane with CNT should translate to an increase in the permeability of the membrane.

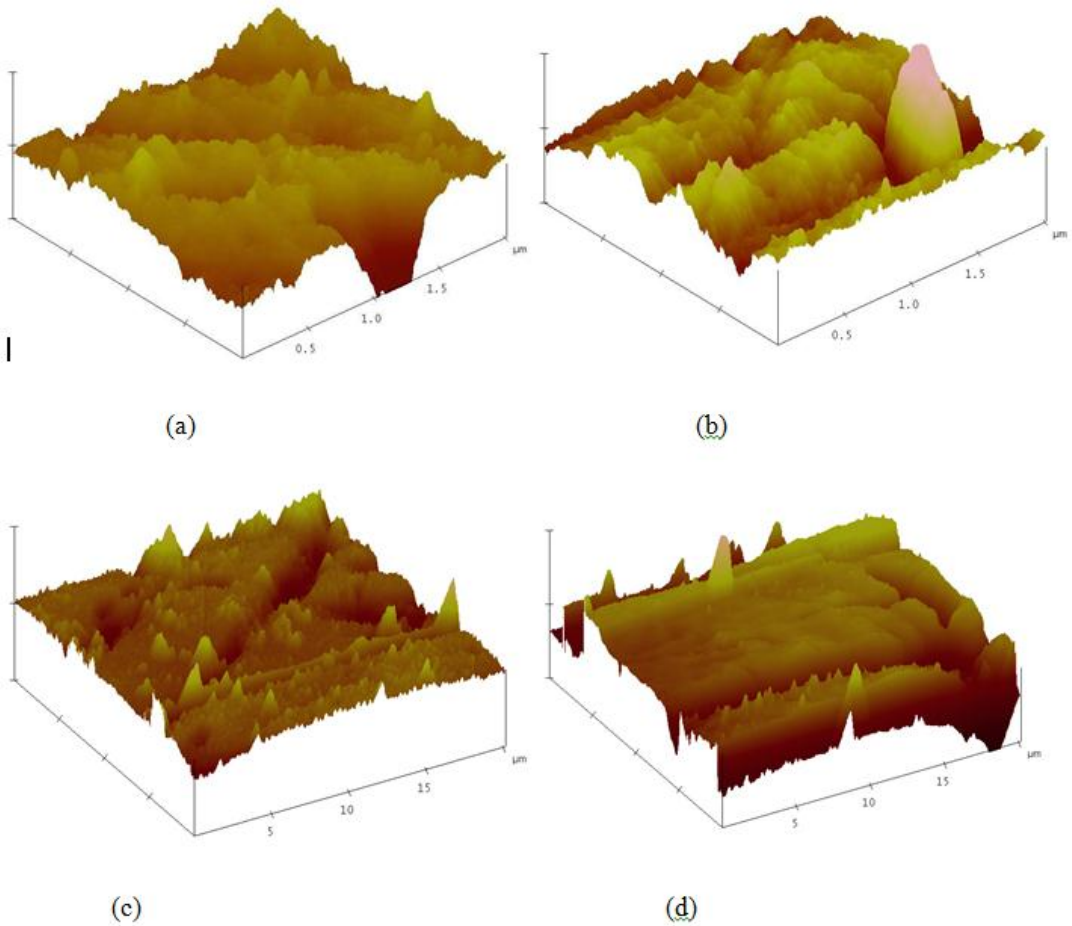

Figure 3. (a) AFM image of PI bare; (b) AFM image of PI CNT; (c) AFM image of PI bare on fabric; (d) AFM image of PI CNT on fabric.

A sessile drop experiment was performed to determine the water contact angles of the membranes and the contact angles measured for the two membranes also agree with the expected decreasing trends: 79.832 and 72.158° for the PI bare and PI CNT membranes respectively.

Table 2. Contact angle and roughness results for fabric-supported membranes.

	Contact angles	Roughness (R_a)
PI Bare	79.83°	62.39 nm
PI CNT	72.16°	328.33 nm
PI bare fabric	80.73°	92.91 nm
PI CNT fabric	77.93°	154.77 nm

These results follow the existing trend where the introduction of CNT increases the pore and nodule distribution on the membrane surface. The Roughness R_a for the PI bare and PI CNT membrane on a fabric support are 92.911 and 154.77 nm, respectively. The contact angles in turn decrease from 80.730 to 77.929° for the fabric-supported PI bare and PI CNT membranes respectively. Comparing the membranes without the support with those with a support reveals that the introduction of the fabric support increases the surface roughness and

the contact angles of the PI membrane (**Table 2**). This makes the membranes more permeable to gases but slightly less hydrophilic. **Table 2** summarizes the AFM and contact angle results for all the synthesized membranes.

The FTIR analyses were performed to assess if the CNT were properly blended and dispersed onto the membrane structure and **Figure 4** shows the spectra for the PI bare, PI CNT membrane and the PI membranes with and without a fabric supported.

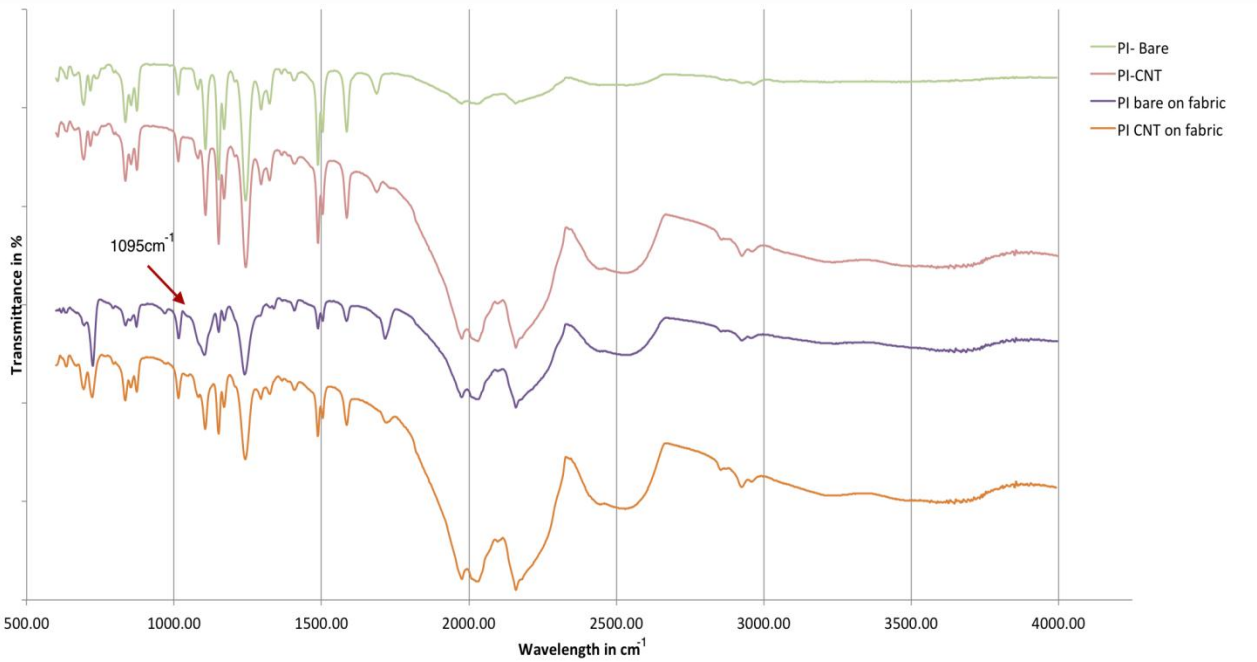

Figure 4. FTIR spectra for PI bare, PI CNT membranes, and PI membranes with and without a fabric supported.

The spectra of PI bare and PI CNT membranes have the characteristic peaks for a polysulfone (PSF) membrane [14]. The spectra for PI CNT however contain an extra band from 3400 to 3480 cm^{-1}, characteristic for hydrogen bonds [15]. The presence of this band confirms the presences of the fCNTs interacting with the PSF structure and explains the increased pore sizes, permeability and hydrophilicity **Figure 4** shows that there is no significant change in the bond structure with the addition of the fabric support. One slight difference however is the reduction of the peak at 1095 cm^{-1}. This peak reduces and merges with the peak at 1109 cm^{-1} in the membranes supported on a fabric. This peak may be associated with the stretching and bending of the sulfonated group. This could indicate some interaction between the polymer layer and the non-woven fabric support.

Tensile strength

The TA.XT Plus Texture Analyzer was used for the tensile strength analysis to assess the mechanical properties of each membrane Membranes with higher tensile stress are able to withstand higher cross flow pressures and thus less susceptible to breaking during the filtration process. Membranes with higher UTS are regarded as rigid. The Young's modulus or the modulus of elasticity is also presented to give an indication of the stiffness of the membrane. **Table 3** summarizes the tensile strength and Young's modulus information for the membranes imbedded with CNTs.

Table 3. Effect of CNTs and the fabric on the mechanical properties of the membrane.

	Tensile stress in kPa	Young's modulus in N / m²
PI bare	13.55	433.78
PI CNT	16.24	421.14
PI bare on fabric	64.77	1000.00
PI CNT on fabric	75.92	913.57

The addition of CNT increases the tensile strength of the membrane but also reduces the rigidity of the PI membrane. This could be due to the interaction between the CNTs and the polymer structures of both membranes. The FTIR in **Figure 4** has shown a significant interaction between the CNTs and the PI membranes with the introduction of the O–H bond. The reduced rigidity maybe attributed to this interaction. The tensile stresses expressed here are smaller than what the actual membranes is subjected to during the filtration tests. This is because the membrane samples used here are significantly smaller (force per 11 cm) than those used in the filtration tests (force per 35 mm). The results however give an accurate representation of the stresses the membranes can handle. Table 3 shows a significant increase in the tensile strength and Young's moduli for the membrane cast on a fabric support.

Filtration tests

Figure 5 presents the oil fluxes at various pressures for the different prepared PI membranes.it is seen that the permeate fluxes increase with pressure for all the membranes. Increasing pressure increases the driving force applied across the membrane which in turn increases the flux. **Figure 5** shows that the PI bare membrane has the highest permeate flux while the addition of CNTs decreases the fluxes through the membrane. This is probably due to the interaction between the oil droplets and the CNTs.

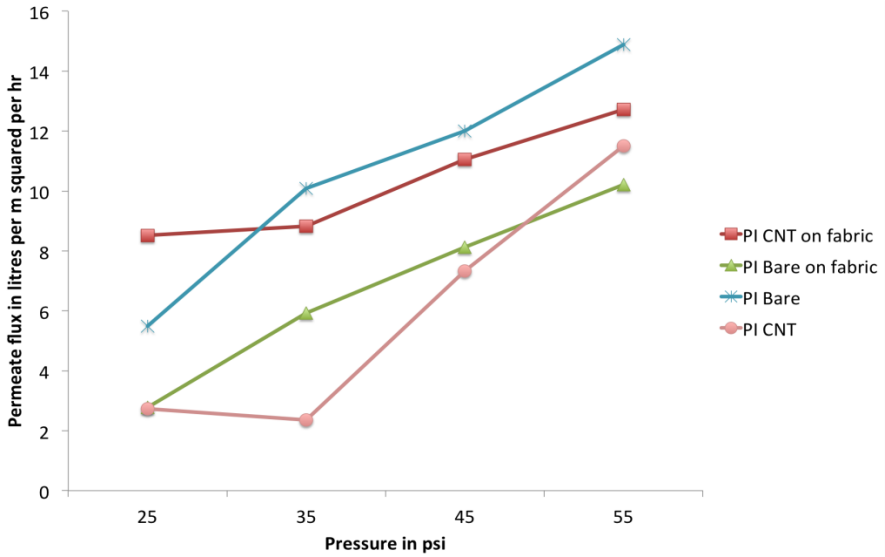

Figure 5. Permeate fluxes at various pressures; initial oil concentration 1000 mg / L.

The increase in flux with pressure is nonlinear in all the cases presented above. This is because the membranes present resistances to flow during the filtration process [16]. The effect of flow resistance is better understood by varying the time.

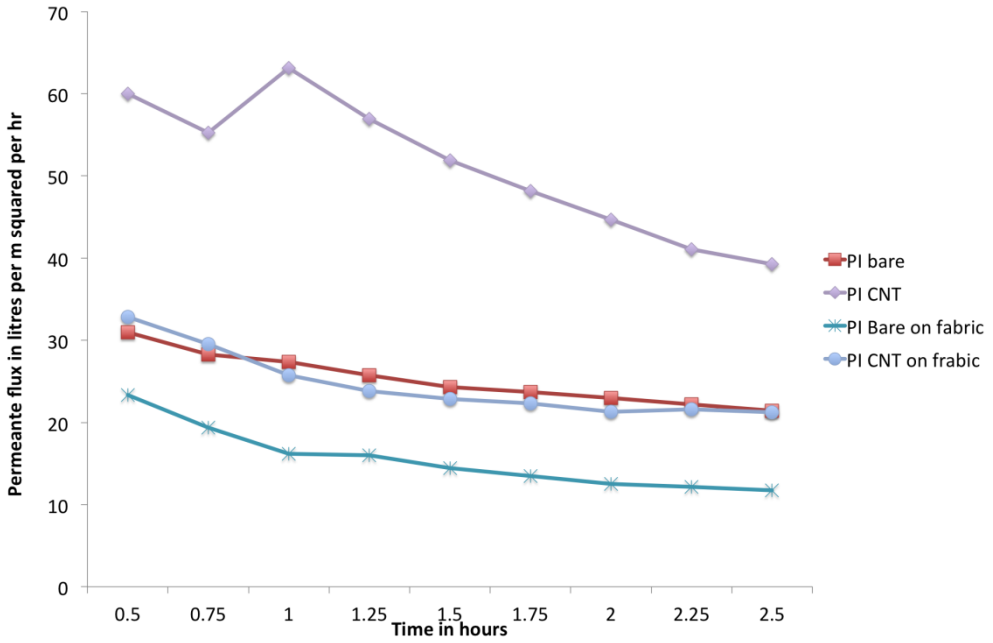

Figure 6. Flux variation with time at a constant pressure of 45psi.

The variation of fluxes with time is presented in **Figure 6**. This experiment was conducted at a constant pressure of 45 psi. The plots show a similar trend of reduction in flux with time. This can be attributed to two main phenomena; pore blockage and resistance due to concentration polarization [16]. Some oil particles get locked up in the pores of the membranes and hinder flow across the membranes. Oil droplets also collide with each other as they are being forced through the membrane. With time, larger droplets of oil are formed that can no longer pass through the pore structures of the membrane. This is probably the cause of the decline in flux over time. From **Figure 6** one may see that the addition of CNTs help control flux decline by controlling fouling of the membrane [17].

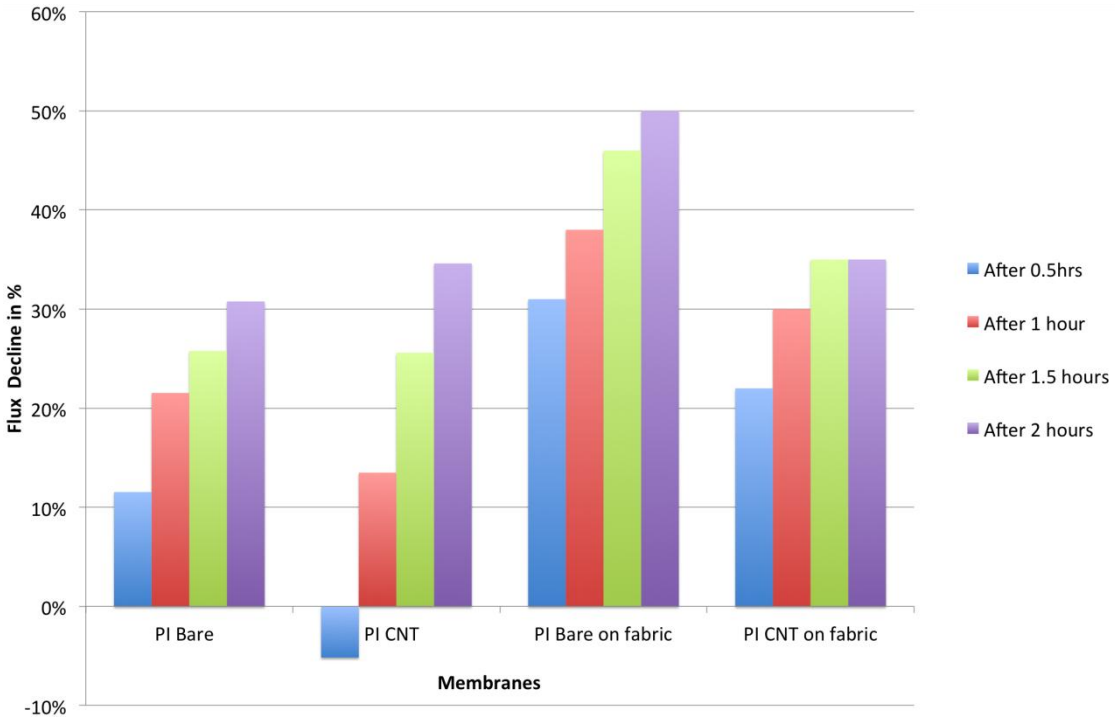

Figure 7. Flux decline of the membranes at a constant pressure of 45psi.

Figure 7 shows the flux decline for the 4 types of membranes over the 2 h period and that the PI bare on fabric membrane has the highest flux decline and this flux decline decreases with the addition of CNTs. The point at which flux decline shoots up the most between the second half hour for the PI bare and PI CNT on fabric membranes and between the third half hour for the PI CNT and PI bare on fabric membranes. Flux decline stays the same for the last half hour in the PI CNT on fabric membrane and this could be due to buildup of the oil layer on the membrane surface.

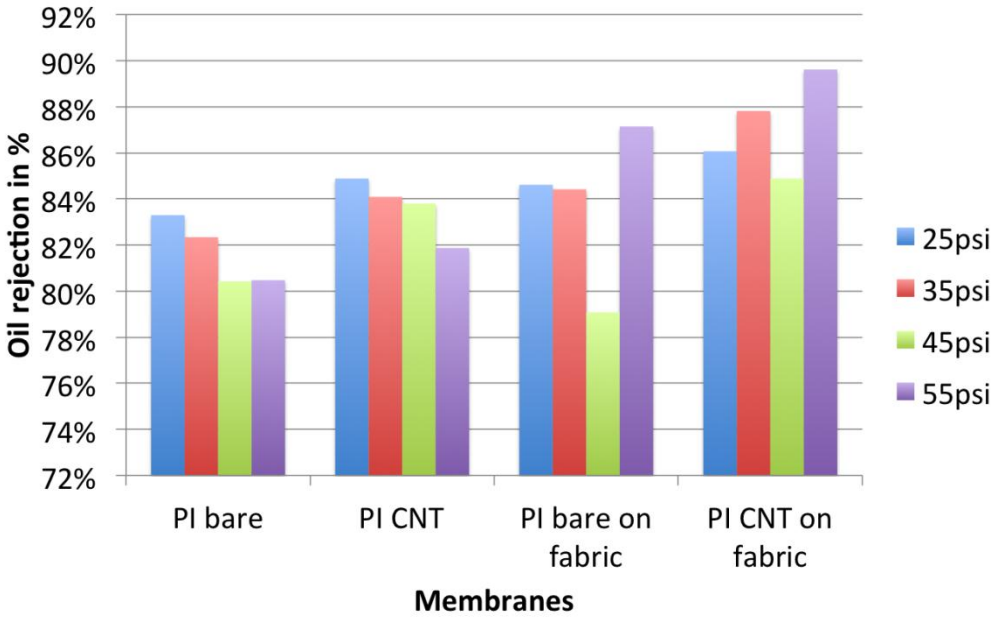

Figure 8. Oil rejections for the various pressures.

The Cary 300 Bio UV–Vis spectrophotometer was used to analyze the oil permeates in order to determine the oil rejections. **Figure 8** shows that all the rejections range between 78 and 90 %, with the fabric-supported membranes having higher rejections compared to the membranes without the fabric support. The oil rejections seem to decline with the increase in pressure. This may be explained by the fact that increasing cross membrane pressure forces the oil through the membrane pores and in turn reduces its rejection values. The membranes supported on a fabric require larger cross membrane pressures to overcome the extra resistance provided by the fabric. It is also seen from **Figure 8** that the addition of CNTs to the membranes increases the oil rejections. The interaction between the CNTs and the membrane makes the membrane hydrophilic and thus allows for more water and less oil to pass through the membrane.

Conclusions

This paper has assessed the performance of modified membranes in the treatment of produced oil wastewater. The phase inversion method was employed in synthesizing the membranes. The membranes were modified with CNTs and a polyester non-woven fabric. It was observed that carbon nanotubes improve the porosity, permeability, hydrophilicity, and tensile strength of the membrane. Polyester non-woven fabric increased the roughness and permeability of the membrane. The membranes supported on a fabric and imbedded with CNTs have higher tensile strength.

Filtration tests have shown that that the increase in the filtration pressure increased the permeate flux across the membranes. The permeate flux through the membrane also decreased with time. The addition of CNTs helped reduce this flux decline. The use of the fabric was found to make the membrane more susceptible to fouling *via* pore blockage because it significantly reduced the pore sizes.

The membranes were found to be effective in removing the oil particles from the produced water with oil rejections ranging between 78 and 90 %. Though these rejections are high, the oil concentrations are still above the allowable discharge limits of 50 mg / L and thus would require further treatment before disposal to the environment. The membranes developed in this work can however be used for recycling water within Enhanced Oil Recovery (EOR) processes.

Acknowledgements

The authors would like to acknowledge CHIETA and the University of Witwatersrand for the funding and facilities provided for this research.

References

1. L. Muehlenbachs, M. A. Cohen, T. Gerarden. The impact of water depth on safety and environmental performance in offshore oil and gas production. Energy Policy, 2013, 55, 699-705.
2. M. Ebrahimi, D. Willershausen, K. S. Ashaghi, L. Engel, L. Placido, P. Mund, P. Bolduan, P. Czermak. Investigations on the use of different ceramic membranes for efficient oil-field produced water treatment. Desalination, 2010, 250, 3, 991-996.
3. B. Chakrabarty, A. K. Ghoshal, M. K. Purkait. Effect of molecular weight of PEG on membrane morphology and transport properties. J. Membrane Sci., 2008, 309, 1-2, 209-221.
4. A. Fakhru'l–Razi, A. Pendashteh, L. C. Abdullah, D. R. A. Biak, S. S. Madaeni, Z. Z. Abidin. Review of technologies for oil and gas produced water treatment. J. Hazardous Mater., 2009, 170, 2-3, 530-551.
5. T. Bakke, J. Klungsøyr, S. Sanni. Environmental impacts of produced water and drilling waste discharges from the norwegian offshore petroleum industry. Marine Environ.l Res., 2013, 92, 154-169.
6. K. S. L. de Figueredo, C. A. Martínez–Huitle, A. B. R. Teixeira, A. L. S. de Pinho, C. A. Vivacqua, D. R. da Silva. Study of produced water using hydrochemistry and multivariate statistics in different production zones of mature fields in the potiguar basin – Brazil. J. Petroleum Sci. & Eng., 2014, 116, 109-114.
7. A. B. Koĺtuniewicz, R. W. Field. Process factors during removal of oil-in-water emulsions with cross-flow microfiltration. Desalination, 1996, 105, 1-2, 79-89.
8. C. Wu, A. Li, L. Li, L. Zhang, H. Wang, X. Qi, Q. Zhang,. Treatment of oily water by a poly(vinyl alcohol) ultrafiltration membrane. Desalination, 2008, 225, 1-3, 312-321.
9. G.-D. Kang, Y.-M. Cao. Development of antifouling reverse osmosis membranes for water treatment: A review. Water Res., 2012, 46, 3, 584-600.

10. S. Maphutha, K. Moothi, M. Meyyappan, S. E. Iyuke. A carbon nanotube-infused polysulfone membrane with polyvinyl alcohol layer for treating oil-containing waste water. Sci. Rep., 2013, **3**, Article number: 1509.
11. N. Phao, E. N. Nxumalo, B. B. Mamba, S. D. Mhlanga, A nitrogen-doped carbon nanotube enhanced polyethersulfone membrane system for water treatment, Phys. & Chem. Earth A/B/C, 2013, 66, 148-156.
12. J.-H. Choi, J. Jegal, W.-N. Kim. Fabrication and characterization of multi-walled carbon nanotubes/polymer blend membranes. J. Membrane Sci., 2006, 284, 1-2, 406-415.
13. M. Khayet, K. C. Khulbe, T. Matsuura. Characterization of membranes for membrane distillation by atomic force microscopy and estimation of their water vapor transfer coefficients in vacuum membrane distillation process. J. Membrane Sci., 2004, 238, 1-2, 199-211.
14. N. Ghaemi, S. S. Madaeni, A. Alizadeh, P. Daraei, M. M. S. Badieh, M. Falsafi, V. Vatanpour. Fabrication and modification of polysulfone nanofiltration membrane using organic acids: Morphology, characterization and performance in removal of xenobiotics. Separation & Purification Technol., 2012, 96, 214-228.
15. K. C. Khulbe, T. Matsuura. Characterization of synthetic membranes by raman spectroscopy, electron spin resonance, and atomic force microscopy; A review. Polymer, 2000, 41, 5, 1917-1935.
16. B. Chakrabarty, A. K. Ghoshal, M. K. Purkait. Ultrafiltration of stable oil-in-water emulsion by polysulfone membrane, J. Membrane Sci., 2008, 325, 1, 427-437.
17. Y. S. Li, L. Yan, C. B. Xiang, L. J. Hong. Treatment of oily wastewater by organic–inorganic composite tubular ultrafiltration (UF) membranes. Desalination, 2006, 196, 1-3, 76-83.

CONTROL OF THE FORBIDDEN GAP WIDTH BY VARYING THE COMPOSITION OR THE THICKNESS OF THE LAYERS OF IV–VI SEMICONDUCTORS

A. M. Pashaev [1], O. I. Davarashvili [2], M. I. Enukashvili [2], Z. G Akhvlediani [2, 3], L. P. Bychkova [2], V. P. Zlomanov [4]

[1] National Aviation Academy
Baku, Azerbaijan
[2] I. Javakhishvili Tbilisi State University
Tbilisi, Georgia
omardavar@yahoo.com
[2] I. Javakhishvili Tbilisi State University
E. Andronikashvili Institute of Physics
Tbilisi, Georgia
[4] M. Lomonosov Moscow State University
Moscow, Russia

Accepted May 25, 2015

Abstract

The paper deals with investigation of the lattice constants of solid solutions $Pb_{1-x}Sn_xTe$ and $PbS_{1-x}Se_x$ and strained semiconductors PbTe and PbSe, and of their optical transmission spectra. The objective of the investigation is to reveal possible spectral overlap of the forbidden gap width in the layers of solid solutions of different compositions and of strained semiconductors. By the lattice constants, compositions x of solid solutions and deformation $\varepsilon = (a - a_s)/a_s$ in strained layers were determined. The forbidden gap width of the layers under study was determined by straightening the squared absorption coefficients obtained by the analysis of transmission spectra. It is shown, that with compression of the PbTe layers 60 nm in thickness grown on BaF_2 substrates, at $T = 300$ K the forbidden gap width coincides with that for the solid solution $Pb_{1-x}Sn_xTe$ of composition $x \approx 0.11$. For the PbSe layer 66 nm thick grown on the KCl substrate, with tension of the layer, the forbidden gap width exceeds, that for the PbS layer. If we grow the strained PbS layers with tension on substrates BaF_2 or KCl, and the PbTe layer on the BaTe substrate, it will be possible to overlap the spectral region from 1 to 3 μm in the strained layers. At the same time, if we grow solid solutions $Pb_{1-x}Sn_xTe$ of different compositions on the BaF_2 substrate with compression of the layer, it is possible to progress along the spectrum to the region 7 – 11 μm. These spectral regions are important for studying the absorption of molecular gases such as CO, CO_2, SO_2, CH_4, HNO_3, N_2O and others.

Recently we have offered to use thin lead selenide layers grown on KCl substrates with a greater lattice constant and doped with chromium for formation of the dielectric state [1]. Under these conditions, effective "negative" pressure is realized in the epitaxial layers [2], the forbidden gap width increases, and the chromium impurity level shifts into the forbidden gap, the compensation of electrically active defects and impurities takes place, and the dielectric state forms.

As the thickness of the layers decreases, the forbidden gap width increases, and the layers can be used for designing the high-sensitive IR photodetectors over a wide spectral range. For instance, if we grow a layer of variable thickness on the same substrate, it will be possible to attain the maximum sensitivity over a specified spectral range and in the specified area of the layer.

At the same time, with the transition to epitaxial technology [3], the heterostructures with active layers based on solid solutions were fabricated. The complex layers of this kind that are active layers for lasers and photodetectors in the IR region of the spectrum have the optimal thickness ~ 1 μm, i.e. they are unstrained. At such thickness, the relaxation of strain takes place, and they have to fabricate separate heterostructures for specified wavelength.

The advantages of the strained layers grown on dielectric substrates are obvious, and it is of importance to find out in which cases the strained layers can replace the structures with solid solutions.

We grew the epitaxial layers of solid solutions $Pb_{1-x}Sn_xTe$ and $PbS_{1-x}Se_x$ > 1 μm in thickness, and layers PbTe and PbSe over a wide thickness range, even a nanorange. The layers were grown by molecular epitaxy with a "hot" wall. The layers $Pb_{1-x}Sn_xTe$, $PbS_{1-x}Se_x$ and PbTe were grown on the BaF_2 (111) substrates, whereas the PbSe layers – on the KCl(I00) substrates. The polycrystalline alloys of appropriate composition with consideration of congruent evaporation of these semiconductors were used as the sources of epitaxy. The temperature of the sources of epitaxy varied from 500 to 530 °C, and that of substrates from 240 to 360 °C. For solid solutions $Pb_{1-x}Sn_xTe$, the composition x was determined by the measurement of the lattice constant from the relation $a = 6.126 - 0.133\,x$, for the system $PbS_{1-x}Se_x$ – from the relation $a = 5.940 - 0.186\,x$.

The thickness of the layers and the lattice constants were determined by recording the X-ray diffraction lines of reflection from crysllographic planes (111), (333), (200), (400) and (600) [4]. The accuracy of determination of the thickness of layers made up 10 %, and that of the determination of the lattice constant – 0.005 % ($\Delta a = 0.0003$ Å).

The forbidden gap width was determined by straightening the squared absorption coefficients the values of which were obtained by processing the transmission spectra recorded with the help of spectrophotometer SPECORD–75IR [5].

Tables 1 and **2** give the data on a few selected layers evidently manifesting the characteristic feature of both groups of layers. From the **Tables 1** and **2**, it is obvious that, with compression of the PbTe layers ($a = 6.460$ Å) 60 nm thick on the BaF_2 substrates ($a = 6.200$ Å), the forbidden gap width made up $E_g = 0.248$ eV, which is close to the value of E_g for the solid solution $Pb_{1-x}Sn_xTe$ at $x \approx 0.11$. At the same time, at $x \approx 0.6$ and $T = 300$ K, E_g in this system reduces to zero [6], i.e. the forbidden gap width in the limit of these compositions could vary by ~ 0.3 eV.

Table 1. Characteristics of the layers of solid solutions $Pb_{1-x}Sn_xTe$ and $PbS_{1-x}Se_x$ on the BaF_2 (111) substrate.

#	Layer	Solid solution	Thickness of layer, μm	Lattice constant, Å	Fraction, x	Forbidden gap width, eV
1	SL–582	$Pb_{1-x}Sn_xTe$	1.2	0.254	0.113	0.254
2	SL–584	$Pb_{1-x}Sn_xTe$	1.4	0.268	0.105	0.268
3	SL–523	$PbS_{1-x}Se_x$	1.6	0.291	0.958	0.291
4	SL–428	$PbS_{1-x}Se_x$	4.0	0.354	0.481	0.354

Table 2. Characteristics of the layers PbTe and PbSe.

#	Layer	Substrate	Compound	Thickness of layer, nm	Lattice constant, Å	Deformation $\varepsilon = (a - a_s)/a_s$	Forbidden gap width, eV
1	SL–408	BaF_2 (111)	PbTe	2500	6.459	0	0.309
2	SL–410	BaF_2 (111)	PbTe	60	6.431	0.0043	0.248
3	SL–69	KCl (100)	PbSe	1810	6.126	0	0.286
4	SL–578	KCl (100)	PbSe	180	6.149	0.0037	0.334
5	SL–555	KCl (100)	PbSe	66	6.177	0.0083	0.448

The forbidden gap width of the PbSe layer ($a = 6.177$ Å) 66 nm thick with tension on the KCl substrate ($a = 6.290$ Å) makes up 0.448eV, which exceeds that of the PbS layer (E_g = 0.410 eV).

It is obvious that, at the thickness of layers less than 200 nm, residual deformation is observed in the layers, and the forbidden gap width decreases with compression of the layer, whereas with tension its value could exceed that in the solid solution as it occurs in the system $PbS_{1-x}Se_x$.

It is possible that, in the case of PbTe, the BaF_2 substrate plays a part of component SnTe, while for the PbSe the KCl substrate plays a part of component PbS.

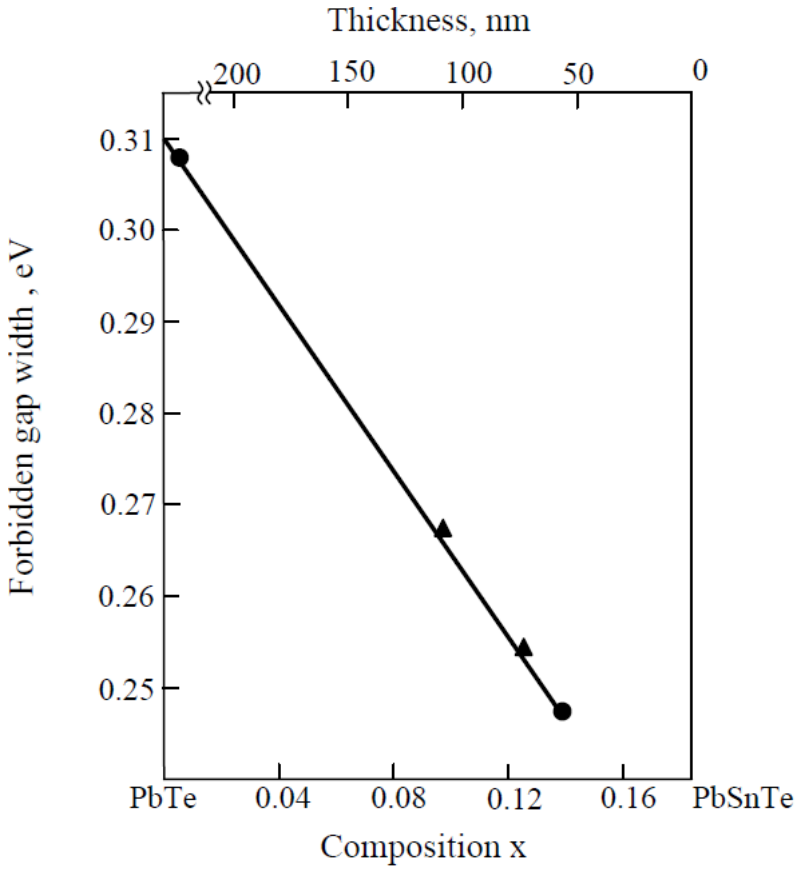

Figure 1. Composition and thickness dependence of the forbidden gap width of epitaxial layers: (●) binary compounds PbTe and (▲) solid solution $Pb_{1-x}Sn_xTe$.

By and large, in the considered cases, the layers PbTe and PbSe span the spectral range from 2.8 to 5.0 μm (0.45 – 0.25 eV) (**Figures 1** and **2**). It is noteworthy that, when the PbTe layers are grown on the BaTe substrate ($a = 6.700$ Å) and the PbS layer- on the BaF_2 and KCl substrates, the above mentioned range can be extended to the interval 1 – 3 μm, while by growing the layers $Pb_{1-x}Sn_xTe$ on the BaF_2 substrates, we can cover the interval 7 – 11 μm. This will extend the possibilities for designing the optical-excited lasers and photodetectors for detection of molecular gases: CO, HCl, CH_4, HF, H_2S, N_2O, CO_2 and SO_2, which is of importance from the standpoint of technology and environment protection.

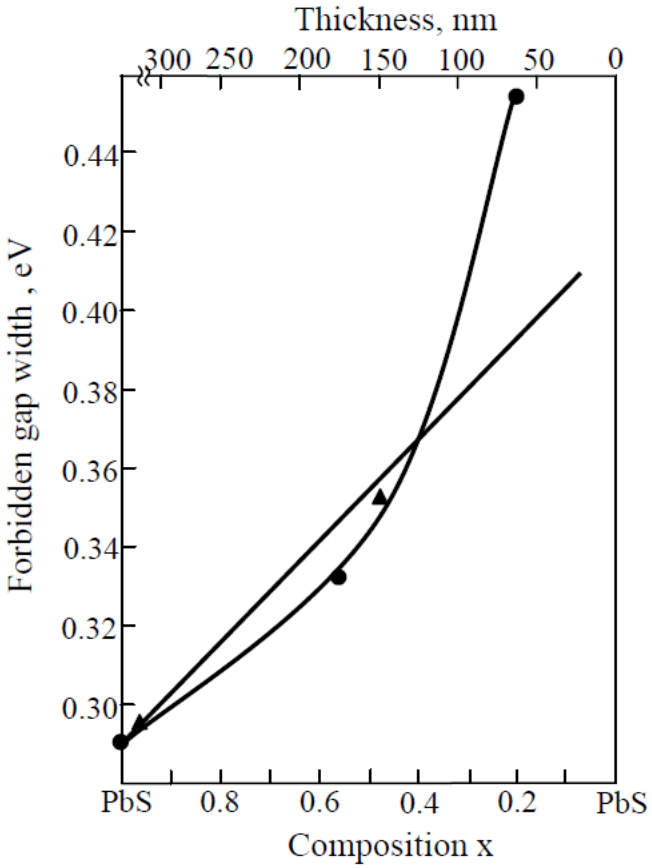

Figure 2. Composition and thickness dependence of the forbidden gap width of epitaxial layers: (●) binary compounds PbSe and (▲) solid solution $Pb_{1-x}Sn_xTe$.

How reliable the devices based on the strained layers will be in operation and how they will undergo deterioration depends on that whether we would manage to retard the movement of dislocations in the layers, on which the elastic energy of the layers could relax.

One of the methods is to grow the layers through dielectric coatings – the dislocations bend on the coating, and their number in the layers decreases. In essence, at low temperature of epitaxy, such a superlattice will allow to prolong considerably the service life of the device.

Less than a dozen selected layers appeared to be enough for revealing the possibility of controlling the forbidden gap width of the IV–VI semiconductors, and the investigation of strained nanolayers holds much promise for designing the IR lasers and photodetectors.

References

1. A. M. Pashaev, O. I. Davarashvili, V. A. Aliyev, M. I. Enukashvili, V. P. Zlomanov. The regular relation between simultaneous stabilization of the Fermi level and transformation of elastic properties in narrow-band IV–VI semiconductors, and their transformation into the dielectric state. Scientific Discovery Certificate # 340. 2008, Moscow: Int. Acad. & Assoc. Auth. Sci. Discov, 51-54.

2. A. M. Pashaev, O. I. Davarashvili, M. I. Enukashvili, Z. G. Akhvlediani, L. P. Bychkova, M. A. Dzagania. Study on the forbidden gap width of strained epitaxial lead selenide layers. J. Mater. Sci. & Eng., 2012, 2, 2, 142-150.
3. A. P. Shotov. Molecular epitaxy with a "hot wall" – efficient technology of complex and multilayered semiconductor structures. Preprint FIAN, 1986, No. 136.
4. A. M. Pashaev, O. I. Davarashvili, M. I. Enukashvili, L. P. Bychkova, R. G. Gulyaev, M. A. Dzagania, V. P. Zlomanov. The lattice constant as an indicator of the technology and properties of IV–VI semiconductors. Bull. Natl. Acad. Sci. Georgia, 2014, 40. 2-3. 11-17.
5. A. M. Pashaev, O. I. Davarashvili, M. I. Enukashvili, Z. G. Akhvlediani, L. P. Bychkova, V. P. Zlomanov. Analysis of the optical transmissin of epitaxial lead selenide layers. Trans. Natl. Aviation Acad. Azerbaijan, 2011,13, 3, 3-12.
6. Y. I. Ravich, B. A. Efimova, I. A. Smirnov. The methods of investigation of semiconductors as applied to lead chalcogenides PbTe, PbSe, PbS. 1968, Moscow: Nauka.

INFLUENCE OF A REAL SURFACE ON PHYSICAL-MECHANICAL PROPERTIES OF POLYCRYSTALLINE β-RHOMBOHEDRAL BORON

M. Darchiashvili [1], O. Tsagareishvili [1], I. Kurashvili [2],
A. Sichinava [2], I. Tabatadze [2], L. Chkhartishvili [1], G. Darsavelidze [2]

[1] Ferdinand Tavadze Institute of Metallurgy & Materials Science
Laboratory for Boron & Powdered Composite Materials
Tbilisi, Georgia
darchiashvilimaguli@gmail.com
[2] Ilia Vekua Sukhumi Institute of Physics & Technology
Laboratory of Semiconducting Materials Science
Tbilisi, Georgia

Accepted June 30, 2015

Abstract

The microstructure, dynamic Vickers microhardness and indentation modulus, temperature dependences of electrical resistivity, thermal expansion and shear modulus of β-rhombohedral boron obtained by melting in boron nitride crucibles have been investigated. In the boron microstructure, the coarse-crystalline state with a wide range of the grains sizes (0.5 – 500 μm) has been revealed. In internal structure of grains the swirl-defects, individual growing twins and accumulation of thin twins have been found. Tendency to increase dynamic microhardness and indentation modulus with improve polishing degree of the sample surface has been revealed as well. It is shown that, dynamic shear modulus measured by torsion oscillations frequencies registration method practically doesn't depend on the polishing degree. The deviation from linear temperature dependence of resistivity, relative elongation, and dynamical shear modulus in temperature interval of 200 – 600 °C with heating rates 1 – 5 °C / min have been detected. Contributions of various superficial and volume defects and local distortions of interatomic bonds in physical-mechanical properties of boron crystals are discussed.

1. Introduction

High mechanical properties, radiation resistance, specific electrophysical, optical and thermal properties stipulate real application possibilities of β-rhombohedral boron (β-boron) in composition materials, semiconducting devices and various radiation-resistant structures. For practical realization of mentioned applications it is very important to reveal correlation connections between structural states, dynamic and energetic characteristics of structural defects and structure-sensitive physical-mechanical properties of β-boron and then establish their predicting and controlling possibilities.

The β-boron bulk crystals are characterized by dislocation origin defects such as twins and stacking faults in the {100} crystallographic systems [1, 2]. These types of dislocation origin planar defects together with point defects give possibilities of modification of β-boron physical

characteristics in the wide range. Concentration of these defects is higher in the filaments formed from gas-phase state and in bulk samples received by quenching from the melt [3].

At present, the mechanisms of influence of the determined types of structural defects on the structure-sensitive physical-mechanical properties of β-boron obtained in different conditions have not been studied. There is no information about complex researches of structural states and physical properties of β-boron profiled samples too.

Present work deals with the investigations of microstructure, electrophysical characteristics, thermal expansion, microhardness, shear modulus and mechanical oscillations energy scattering processes of profiled samples of polycrystalline β-boron.

2. Experimental

The β-boron bulk crystals were obtained by melting in boron nitride crucible in Ar atmosphere. As raw material for melting microcrystalline boron of 99.8 wt. % purity was used.

The profiled samples were prepared from the bulk crystals by consistent use of cutting, mechanical grinding and polishing methods. To reveal microstructure 20 % KOH + 40% $K_3Fe(CN)_6$ + 40 % H_2O chemical solution was used. At the last stage of mechanical and chemical treatment purification of the test samples surfaces was conducted in the ultrasonic cleaner CD–1800. Microstructure was investigated by the optical microscope NMM–80RF/TRF.

Electrophysical characteristics were determined with Ecopia HMS–3000 device in the constant magnetic field with induction of 0.5 T by the Hall-effect measurements. Temperature dependence of electrical resistivity of β-boron samples prepared by cutting with diamond disk and polishing with diamond paste (grain size of 0.25 μm) was obtained by compensation method. Measurements were conducted with the heating velocity of 2 °C / min in Ar atmosphere. Temperature dependence of the relative elongation was studied by quartz dilatometer with capacity sensors. Controlling of the experiment and reading of the information were conducted by digital ports and results development has been performed by special computer software.

Study of Vickers dynamic hardness and elastic modulus of β-boron polished with various grain size diamond pastes were carried out on Shimadzu Ultra Micro Hardness Tester DUH 211S. Testing was performed at load–unload mode according to ISO–14557 standard [4]. Definition of dynamic hardness of the samples during loading was conducted by software of the tester. Static microhardness was determined by measuring the diagonals of imprints with an optical microscope. A reduced elastic modulus was obtained by calculation of stiffness on the upper point of unloading curve with application of well-known relations [5].

Investigations of internal friction and relative shear modulus were carried out on the laboratory device by registration of torsion oscillations damping logarithmic decrement and frequency in the temperature interval of 20 – 750 °C in 10^{-4} Torr vacuum. The absolute value of shear modulus is determined at the room temperatures by comparing the standard (polycrystalline vanadium) and test specimens:

$$G = G_0 \frac{f^2}{f_0^2},$$

where G_0 and f_0 are shear modulus and oscillation frequency of the standard specimens, while G and f that of the test specimens.

3. Results

The β-boron samples polished with 1 μm and 0.25 μm diamond pastes are polycrystalline and characterized by variety of defects (**Figure 1**). Grain sizes changes in wide range of 0.5 – 5 μm. Grains inner structure consists of non-homogeneously distributed etch pits of various sizes (0.5 – 1 μm). Most of them are porous with pores of different sizes. Distorted and linear curves of slipping deformation have been also revealed. Some of them are decorated by small-sized inclusions. There are numerous single twins and their clusters of different sizes. There are also etch-pits with lower concentration in samples polished with 0.25 μm diamond paste. In many cases, twins distributed in parallel orientation have been found.

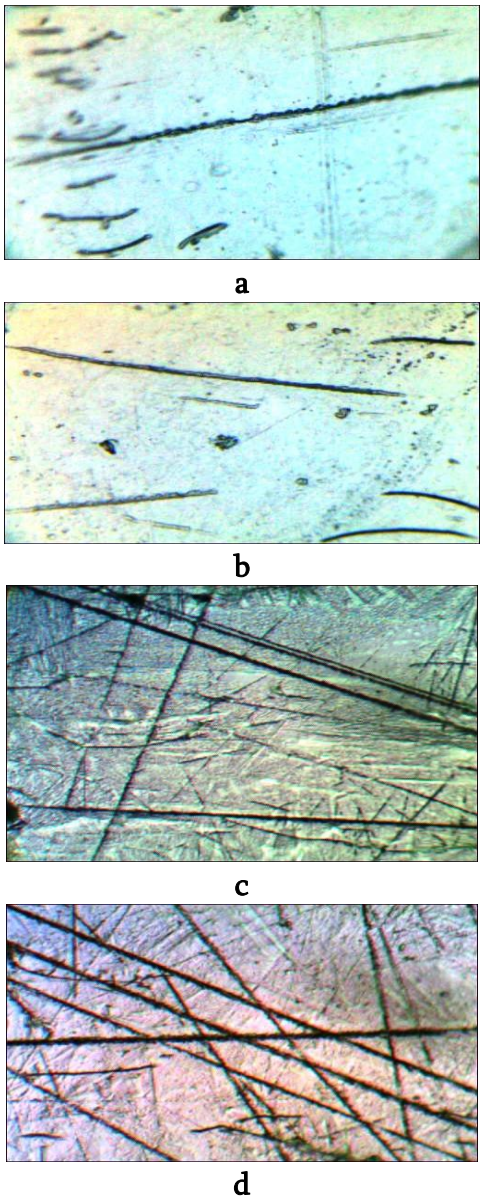

Figure 1. Metallographic images of β-rhombohedral boron polished with 0.25 μm diamond paste: a – deformation lines decorated with dispersive inclusions, b – etch pits and deformation lines with various form and length, c – single and grouped twins, and d – set of intercrossed twins.

Improving of surface mechanical treatment degree leads to decrease of current carriers' concentration and increases their mobility. In the samples cut with diamond disk, current carriers' concentrations are raised. Annealing at temperature of 300 °C for 1 h stipulates reduction of current carriers' concentration (**Table 1**).

Table 1. Influence of surface treatment quality on electrophysical characteristics of β-rhombohedral boron.

Electrical characteristics / Surface treatment quality	Resistivity, Ohm · cm	Current carrier concentration, cm^{-3}	Current carrier mobility, $cm^2 \cdot V^{-1} \cdot s^{-1}$
Cutting with diamond disk	$0.6 \cdot 10^4$	$5 \cdot 10^{14}$	2.0
Polished with 1 μm diamond paste	$1.25 \cdot 10^4$	$2 \cdot 10^{14}$	2.5
Polished with 0.25 μm diamond paste	$3 \cdot 10^4$	$4 \cdot 10^{13}$	4.5

Mechanical treatment of the surfaces influences on temperature dependence of electrical resistivity. On the electrical resistivity temperature dependence of the samples cut with diamond disk, it forms a kink within temperature interval 250 – 300 °C. It is thermally stable, because it does not weaken during annealing at temperature of 300 °C for 1 h. Anomalous changes of resistivity practically completely disappear in samples polished with 0.25 μm diamond paste (**Figure 2**).

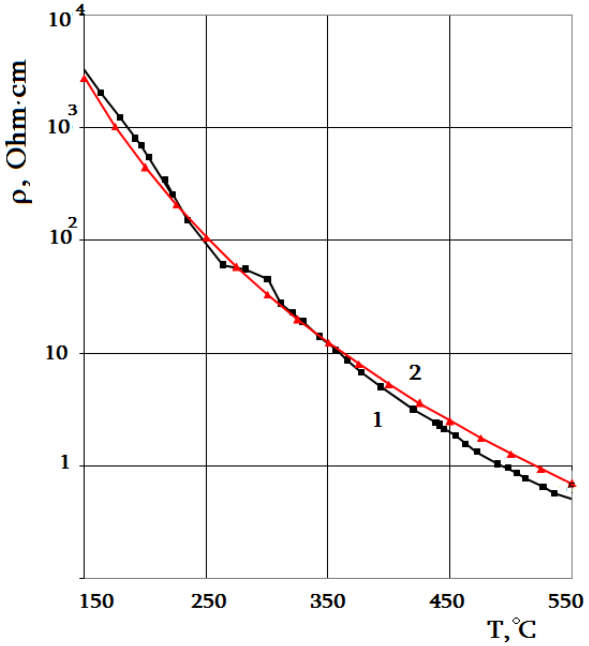

Figure 2. Electrical resistivity temperature dependence of β-rhombohedral boron: 1 – after cutting with diamond disk, and 2 – after polishing with 0.25 μm diamond paste.

Temperature dependence of relative elongation is characterized by deviations from linearity in the temperature interval 200 – 500 °C. It is most clearly revealed in the β-boron

sample treated by cutting on diamond disk. **Figure 3** shows slight difference between relative elongation curves fixed in heating and cooling processes. Raising mechanical treatment level leads to the weakening of deviations of relative elongation in the temperature interval 200 – 500 °C and suppresses the difference between temperature dependence of relative elongation in heating and cooling processes. Annealing at 300 °C for 1 h of samples mechanically treated at different levels causes weakening of the relative elongation deviations in the temperature interval 200 – 500 °C.

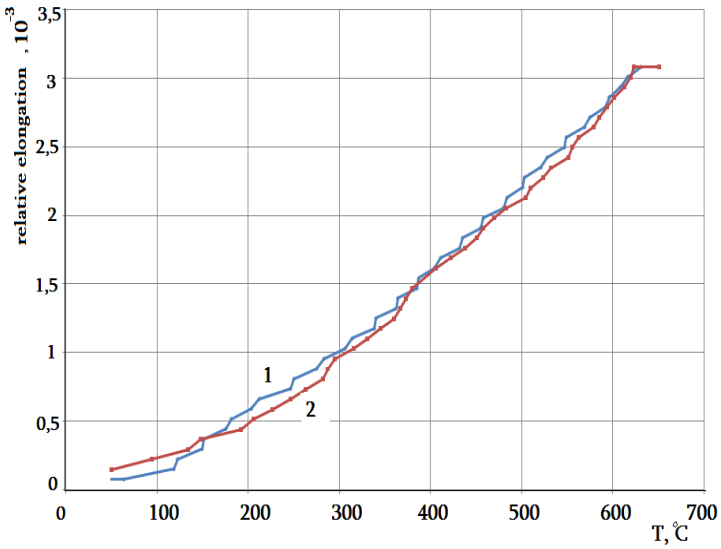

Figure 3. Relative elongation vs temperature of β-rhombohedral boron polished with 0.25 μm diamond paste: 1 – heating and 2 – cooling with rates of 2 °C / min.

Figure 4 represents dependence of Vickers dynamic microhardness of β-boron polished with various diamond pastes vs. penetration depth. Non-monotonic change of dynamic microhardness during indentation is clearly seen from **Figure 1**. At 0.30 – 0.36 μm depth levels microhardness reaches the maximum value and then decreases slowly. Such a behavior is known as reverse indentation size effect [6]. A small plateau is visible on both charts at 0.10 – 0.25 μm depths. The degree of samples surface treatment determines a clear increase of microhardness.

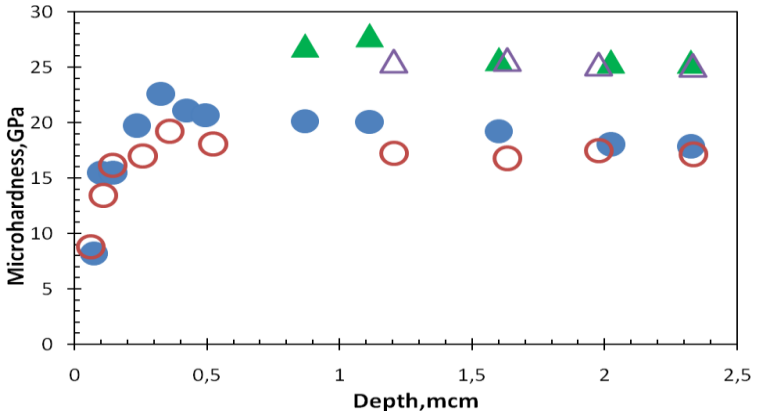

Fig.ure 4. The β-rhombohedral boron microhardness vs. penetration depth. Dynamic microhardness of samples polished with diamond pastes: ● – 0.25 and ○ – 1 μm, and static microhardness of samples polished with diamond pastes: ▲ – 0.25 and Δ – 1 μm.

Indentation modulus of β-boron polished with various grain size diamond pastes changes non-monotonically with penetration depth and has two maxima at small depths. Both maxima are displaced deep into the specimen for surfaces treated with 0.25 μm diamond pastes. Static hardness values and their changes versus penetration depth for surfaces treated with different diamond pastes differs insignificantly (**Figure 5**).

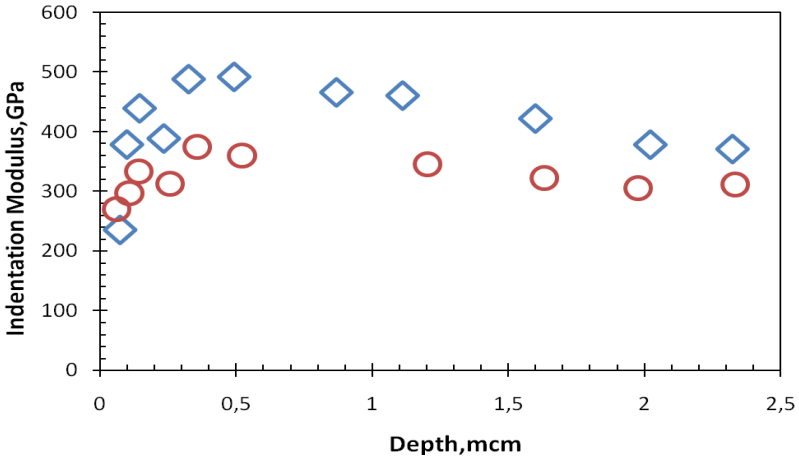

Figure 5. The β-rhombohedral boron indentation modulus vs. Penetration depth for samples treated with diamond pastes: ◊ – 0.25 and ○ – 1 μm.

The values of oscillations frequency of β-boron and standard (vanadium) samples of identical sizes $0.5 \times 0.5 \times 20$ mm^3 were determined at the room temperature in vacuum ~ 10^{-4} Torr, and based on them, the absolute values of shear modulus were calculated. Slight increase in shear modulus was revealed by raising treatment level of the samples surfaces. Samples obtained by cutting on the diamond disk are characterized by comparatively low value of shear modulus. Samples polished by 0.25 μm diamond paste are characterized by high values of shear modulus (**Table 2**).

Table 2. Physical-mechanical characteristics of β-rhombohedral boron specimens.

Mechanical treatment	Shear modulus, Kg / mm^2	Relaxation processes activation parameters		
		Temperature, °C	Activation energy, eV	Frequency factor, s^{-1}
Cutting on diamond disk	17500	235	1.10	$8.5 \cdot 10^{11}$
		400	1.70	$2 \cdot 10^{13}$
Polishing by diamond paste 1 μm	18000	250	1.25	$8 \cdot 10^{12}$
		410	1.85	$2.5 \cdot 10^{14}$
Polishing by diamond paste 0.25 μm	19000	260	1.30	$1 \cdot 10^{13}$
		420	1.90	$5 \cdot 10^{14}$

Annealing at 300 °C in vacuum practically does not influence on shear modulus of the sample after cutting. Slight increase of shear modulus of the sample polished by 1 μm paste has been observed. This trend is more clearly shown in the samples polished by 0.25 μm diamond

paste. The values of shear modulus are slightly lower than known literature data. Probably these differences are related with high concentration of point and dislocation origin defects.

Treatment level of samples surfaces does not have substantial effect on temperature spectra of internal friction and shear modulus. Internal friction spectra of all three kinds of samples are represented by maxima at temperatures of 230 – 260, 300 – 320, and 400 – 420 °C, respectively (**Figure 6**).

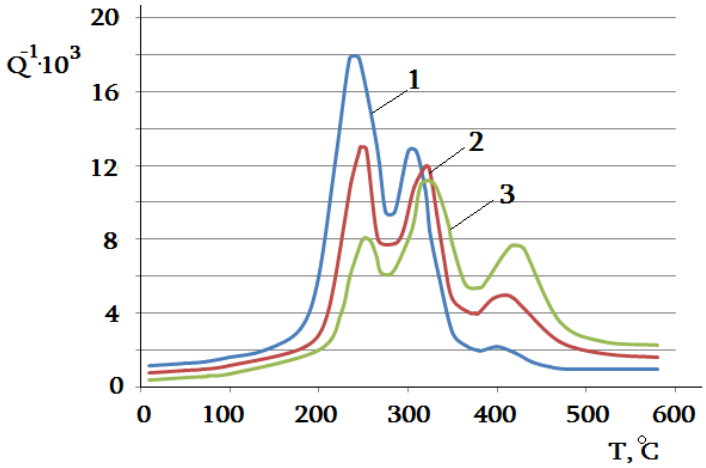

Figure 6. The β-rhombohedral boron internal friction temperature dependence: 1 – after cutting with diamond disk, f_0 =1.5 s^{-1}, 2 – after polishing with 1 μm diamond paste, f_0 =1.3 s^{-1}, and 3 – after polishing with 0.25 μm diamond paste, f_0 =1.2 s^{-1}.

Clear changes are revealed on the curves of shear modulus in the vicinity of internal friction maxima (**Figure 7**).

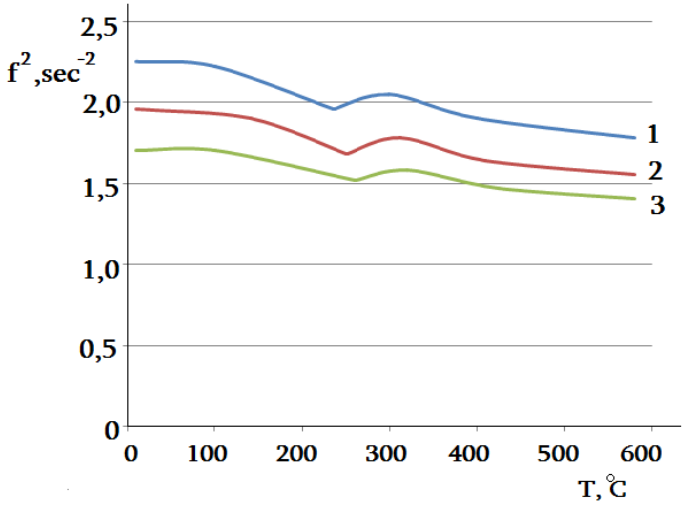

Fig.ure 7. The β-rhombohedral boron shear modulus temperature dependence: 1 – after cutting with diamond disk, f_0 =1.5 s^{-1}, 2 – after polishing with 1 μm diamond paste, f_0 =1.3 s^{-1}, and 3 – after polishing with 0.25 μm diamond paste, f_0 =1.2 s^{-1}.

Internal friction relaxation maxima differ from each other in temperatures, intensities and activation characteristics. Internal friction maxima in 300 – 320 °C temperature range are non-relaxation origin: the temperature does not depend on oscillations frequency, whereas

intensities sharply increase by raising oscillation amplitude. In the vicinity of non-relaxation maximum, increment of shear modulus is revealed. According to the theory, similar maxima of internal friction are related to the phase transformation type processes in solids [7]. By raising polishing level, values of all relaxation processes' activation energies and frequency-factors increases.

It has been experimentally established, that by raising mechanical treatment level, the intensity of internal friction relaxation maxima in the temperature range 230 – 260 °C significantly decreases, whereas at temperatures of 400 – 420 °C intensity of internal friction maximum sharply increases. Activation characteristics of the relaxation maxima of the samples treated on the diamond disk are minimal in comparison with analogous maxima of polished samples.

4. Discussion

Conducted metallographic investigations revealed nonhomogeneous distribution of planar defects in polished β-boron samples. Planar defects of β-boron bulk crystals in the form of twins and stacking faults were previously investigated in [1, 2, 8]. It should be noted that, revealing of complete dislocations in boron crystallographic modifications rarely take place and at present their crystallographic characteristics practically have not been established.

The investigated experimental samples are high resistive p-type semiconductors. According to the theory, low concentration of electrons or holes does not influence on dislocation origin defects mobility and structural-sensitive mechanical properties of semiconducting materials [9]. In the present work, it is real to assume presence of strong interaction and inter-blocking of the numerous defects existed in the superficial structure and defects existed in bulk. They can stipulate changing in physical-mechanical properties in the wide ranges. The blocking and unblocking processes of defects can stipulate anomalous changes of structure-sensitive physical-mechanical properties of β-boron in the interval 200 – 500 °C.

Specific changes of electrical resistivity, thermal expansion, internal friction and shear modulus spectra of samples treated with diamond disk are close to monocrystalline β-boron characteristics [10 – 14]. Electrophysical, thermal and mechanical properties of mechanically polished β-boron samples are practically identical to the characteristics of vapor-deposited [15] and quenched from the melted state β-boron samples [16].

In all kind mechanically treated β-boron samples in the temperature range of 200 – 500 °C temperature spectra of resistivity, thermal expansion, shear modulus and internal friction showed phase transformation-type processes. Possibilities of phase transformation type processes in β- boron crystals are confirmed in work [17].

Experiments showed that, saturation of microhardness and indentation modulus begin from near depth ~ 1 – 2 μm. From this it can be conclude that influence of polishing by 0.25 μm and 1 μm diamond pastes of β-boron samples on the investigated structure-sensitive properties expands to the depth: ~ 2 μm.

In the superficial layers, it is possible significant changes of various defects mobility, phase transformation conditions and generation of impurity and vacancy atmospheres in dislocations and planar defects cores. These structural changes may stipulate increase of mechanical characteristics and activation energy of relaxation processes and also decrease of anomalous changes of electrical resistivity and thermal expansion.

5. Conclusions

Improving of the degree of β-boron crystals surfaces treatment leads to increase of electrical resistivity and decreases current carriers' concentration. It is shown, that in polished samples microhardness and indentation modulus increases in a wide range of indenter penetration depth.

With raising surfaces treatment level, anomalous changes of electrical resistivity and relative elongation are weakened in 200 – 500 °C temperature interval. Improving the polishing degree of β-boron crystals surfaces stipulates intensive internal friction relaxation maximum and shear modulus defect in the region 400 – 420 °C mobility of dislocation origin defects formed in polishing processes is weakened. For this reason at temperatures of 230 – 260 °C, intensity of internal friction maxima and shear modulus defect significantly decrease.

References

1. K. Kleinhenz, P. Runow. Herstellung dunner Bor Folien und elektronenmikroskopische Beobachtung inter Baufehler. Phys. Stat. Sol., 1968, 29, 627-637.
2. M. J. mc Kelvy, R. Rae Smith, L. Eyring. High-resolution electron microscopy analysis of [100] twining in β-rhombohedral boron. J. Solid State Chem., 1982, 44, 374-381.
3. G. Darsavelidze, G. Tsagareishvili, E. Kutelia, A. Zhigach, A. Tsirlin, E. Schetilina. The influence of heat treatment on the structure of boron filaments. Less-Comm. Met., 1981, 82, 89-92.
4. BS EN ISO 14577–1: Metallic Materials-Instrumented Indentation Test for Hardness and Materials Parameters, 2002.
5. W. C. Oliver, G. M. Pharr. An improved technique for determining hardness and elastic modulus using load and displacement sensing indentation. J. Mater. Res., 1992, 7, 1564-1583.
6. K. Sangwal. On the reverse indentation size effect and microhardness measurement of solids. Materials Chem. & Phys., 2000, 63, 145-152.
7. M. S. Blanter, I. S. Golovin, H. Neuhauser, H.-R. Sinning. Internal Friction in Metallic materials. A Handbook Series: Springer Series in Materials Science 90. 2007, 520 pp.
8. F. Tavadze, G. Tsagareishvili, N. Zoidze, M. Antadze. Structural peculiarities of zone-melted boron. In: Boron – Preparation and properties, 3. 1970, Warszawa, 127-132.
9. U. Jenderich, P. Haasen. Internal friction due to kink motion and kink pair formation in intrinsic and n-doped germanium. Phys. Stat. Sol. A, 1988, 108, 553-568.
10. G. V. Tsagareishvili, F. N. Tavadze, A. G. Khvedelidze, D. L. Gabunia. Study on some electrophysical properties of β-rhombohedral boron. In: Boron – Preparation and properties, 3. 1970, Warszawa, 295-299.
11. G. Darsavelidze, O. Tsagareishvili, T. Eterashvili, V. Metreveli, D. Khomeriki. Defects and physic-mechanical properties of polycrystalline β-rhombohedral boron. J. Less-Comm. Met., 1986, 117, 189-193.
12. G. Darsavelidze, D. Gabunia, N. Zoidze, D. Lezhava, I. Kurashvili. Inelastic properties Ni-doped boron. Bull. Acad. Sci. Georgia, 1997, 160, 103-106.

13. G. Darsavelidze, O. Tsagareishvili, D. Gabunia, N. Zoidze, L. Gabunia. Physical-mechanical properties of Ni-doped boron. In: Proc. 1st Int. Boron Symp. 2002, Kutahya, Dumlupinar Univ. Press, 55-59.
14. G. Darsavelidze, D. Gabunia, O. Tsagareishvili, Z. Zoidze, M. Antadze, J. Tsikaridze, E. Kutelia. Physical-mechanical properties of Zr(Re)-doped β-rhombohedral boron. J. Solid State Chem., 2004, 177, 605-608.
15. G. Darsavelidze, G. Tsagareishvili, A. Tsirlin, J. Nikuradze, O. Tsagareishvili, A. Zhigach, F. Tavadze. The dependence of the internal friction of boron fibers on amplitude. Less-Comm. Met., 1979, 67, 471-476.
16. G. Darsavelidze, G. Tsagareishvili, M. Antadze, O. Tsagareishvili, A. Khvedelidze, F. Tavadze. Real structure and internal friction of boron doped with zirconium. In: Proc. Mater. Sci. Res. Soc. Symp., 1987, 97, 139-144.
17. S. Hoffmann, H. Werheit. Phase transition in β-rhombohedral boron at 550 K. Solid State Sci., 2012, 14, 1572-1577.

СВЯЗЬ ПОВЕРХНОСТНОГО НАТЯЖЕНИЯ ЖИДКИХ МЕТАЛЛОВ С ЭНЕРГИЕЙ ИХ АТОМИЗАЦИИ

А. А. Капанадзе, Г. Д. Табатадзе, М. С. Тактакишвили

Грузинский технический университет
Департамент инженерной физики
Тбилиси, Грузия

Принята 24 июля 2015 года

Аннотация

Исследована связь поверхностного натяжения жидких металлов Bi и Hg с энергией их атомизации. Сделаны наблюдения по введению металлов в одномерных каналах цеолита Na*M*. Показано, что термин ‘поверхностное натяжение’ пригоден даже в том случае, когда атомы вводят по одному. Следовательно, в первом приближении поверхностная энергия есть энергия поверхности свободного атома. Однако это верно лишь для атомов со внешними электронными оболочками конфигураций сферической симметрии. Эти атомы проявляют прямую связь между поверхностным натяжением и теплотой испарения.

Представления о поверхностном натяжении и смачиваемости для жидких металлов сохраняют свои количественные характеристики вплоть до размеров металлических капель в 3 – 4 атомных диаметра [1]. Это следовало из применимости порометрической формулы для вычисления критических давлений, при которых различные металлы входят в каналы атомных размеров различных цеолитов.

Еще более очевидным становится «микроскопический» смысл величины поверхностного натяжения при рассмотрении опытов по созданию одноатомных цепочек в цеолите Na*M*. В этом случае можно, по-видимому, установить прямую зависимость между поверхностным натяжением металлов и энергией их атомизации. Действительно, пользуясь данными **Таблицы 1**, на основе опытных данных, можно вычислить энергию, необходимую для разбиения 1 см^3 жидкого металла на одноатомные цепочки.

Для висмута она будет равна 200 Кг м, для ртути – 290 Кг м. В пересчете на 1 г атом в обоих случаях это составляет примерно 10 ккал / г атом. Полученное значение можно сравнивать с теплотой атомизации металла – теплотой испарения Q. Для висмута Q = 41.0 ккал / г атом, для ртути Q = 14.6 ккал / г атом (температура кипения висмута 1833 К, ф ртути – 630 К).

При испарении происходит разбиение металла на отдельные атомы. Отдельные атомы можно получить также, разбивая одноатомные цепочки. Полная затраченная энергия в этом случае будет складываться из приведенной выше энергии для создания такой цепочки и энергии по разбиению ее на отдельные атомы. Если считать, что связи атомов друг с другом одинаковы во всех направлениях, для разрыва одноатомной цепочки на отдельные атомы требуется еще половина от энергии, затраченной на создание цепочки, т.е. затраты еще 5 ккал / г атом.

Таблица 1.

Тип цеолита	Вводимый металл	Расчетное критическое давление $P_{кр.}$, кбар	Экспериментальное критическое давление $P_{кр.}$, кбар	Энергия разбиения металла на одноатомные цепочки E, Кг м
Na*M*	Bi	22.8	20	200
Na*M*	Hg	28.2	29	290

Полная энергия атомизации, полученная таким образом, составляет 15 ккал / г атом, как для ртути, так и для висмута. Найденное значение очень близко к теплоте испарения ртути, но сильно отличается от теплоты испарения висмута. Из этого следует, что для висмута предположение об эквивалентности всех связей не верно.

Вывод о характере химических связей ртути и висмута, полученные нами путем сопоставления теплоты испарения и энергии атомизации этих металлов путем их предварительного разбиения на одноатомные уепочки, является хорошо известным фактом. Структура ртути и висмута в твердом состоянии, а также конфигурации электронных орбит свидетельствуют о симметрии химических связей у ртути и об асимметрии связей в случае висмута.

Полученный результат можно было предвидеть, поскольку энергия образования одноатомных цепочек (предельная степень дробления металла при вдавливании) путем преодоления сил поверхностного натяжения, определяется величиной поверхностного натяжения, которое почти одно и то же у висмута и ртути (376 дин / см и 465 дин / см соответственно), а теплоты испарения, по правилу Трутона, пропорциональны температуре кипения (для висмута Q = 41.0 ккал / г атом, $T_{кип.}$ = 1833 К; а для ртути Q = 14.6 ккал / г атом, $T_{кип.}$ = 630 К). Физически, конечно, процесы атомизации в обоих случаях должны быть похожи.

При испарении отдельный атом вырывается наружу с поверхности жидкости и рвет все связи сразу. При вдавливании в каналы одно-направление связи остается неразорванным (наиболее прочная связь). В обоих случаях совершается работа против сил поверхностного натяжения, которое есть результат взаимодействия между отдельными атомами.

С этой точки зрения, энергия связи в цепочке атомов висмута примерно равна 31 ккал / г атом, а в цепочке атомов ртути – 5 ккад / г атом, т.е. в обоих случаях не меньше, чем в массивном металле. Это позволяет надеяться, что такие цепочки могут проводить ток и будут подходящими объектами для поиска квазиодномерной сверхпроводимости [2].

Можно оценить значение поверхностной энергии, рассматривая поверхность отдельного испаренного атома и полагая, что распределение энергии сферически симметрично (Hg, Cd, Zn). После испарения, например, одного грамм-атома ртути, на что требуется 14.6 ккал, образуется $6.02 \cdot 10^{23}$ частиц с общей поверхностью $\pi d^2 \times 6.02 \cdot 10^{23}$, где d есть эффективный размер атома. Энергия, приходящаяся на единицу поверхности каждого атома, будет при этом 355 эрг / см^2, если за d принять атомный диаметр 3.0 Å. Эта величина энергии только на 13 % меньше обычного «макроскопического» поверхностного натяжения для ртути при температуре кипения (400 эрг / см^2) [2].

Для других атомов с внешними *s*-электронами получается аналогичная картина. Так, для кадмия, поверхностная энергия испаренного атома 590 эрг / см^2, тогда как поверхностное натяжение при $T_{кип.}$ равна 577 эрг / см^2; для цинка, соответственно, 850 эрг / см^2 и 750 эрг / см^2.

«Микроскопический» подход к вычислению поверхностного натяжения обсуждается в литературе уже давно [3], где внимание было обращено на связь теплот испарения с поверхностным натяжением. Описанные в настоящей работе опыты являются, по-видимому, прямым подтверждением такой точки зрения. Они, как и проведенные расчеты, также отчетливо выявляют анизотропию сил связи в атомах с *p*-оболочками, для которых «макроскопическое» поверхностное натяжение прямо не определяется теплотой испарения, хотя, по-видимому, и связано с ней. Расплавы таких металлов скорее должны быть похожи на жидкие кристаллы.

Таким образом, анализ результатов при вдавливании ртути и висмута в одномерные каналы Na*M* показывает, что понятие поверхностного натяжения хорошо применяется не только вплоть до диаметров до 10 Å, а даже тогда, когда речь идет о введении отдельных атомов металла в каналы одноатомного размера.

Отсюда следует, что обычное поверхностное натяжение имеет прямое микроскопическое происхождение и есть в первом приближении поверхностная энергия свободного атома для атомов со сферически симметричной конфигурацией внешних электронных оболочек (Hg, Cd, Zn). Только для таких атомов имеет место давно обсуждаемая в литературе прямая связь поверхностного натяжения и теплоты испарения.

Для атомов, например, с внешними *p*-оболочками: Bi, Ga, Zn и т.д., имеется асимметрия сил связи, и прямого соотношения между поверхностным натяжением жидкости и теплотой ее испарения нет. Такие расплавы могут походить на жидкие кристаллы.

Ссылки

1. А. А. Капанадзе, Г. В. Ртвелиашвили, Г. Д. Табатадзе. Nano Studies, 2013, 7, 207.
2. В. К. Семенченко. В сб.: Поверхностные явления в расплавах и возникающих из них твердых фазах. 1965, Нальчик.
3. Д. В. Гиббс. Термодинамические работы. 1950, Москва–Ленинград, Гостехизда.

THE EFFECT OF CHEMICAL COMPOSITION OF ACIDIC ACTIVATORS CONTACTING WITH CARBON STEEL ON DEVELOPMENT OF LAYERED DOUBLE HYDROXIDES ON ITS SURFACE

O. M. Lavrynenko [1], B. G. Shabalin [2], Yu. S. Shchukin [1], O. Yu. Pavlenko [1]

[1] National Academy of Science of Ukraine
F. D. Ovcharenko Institute of Bio-Colloid Chemistry
Kyiv, Ukraine
alena-lavry@yandex.ru
[2] National Academy of Science of Ukraine
Institute of Environmental Geochemistry
Kyiv, Ukraine
igns@i.com.ua

Accepted September 7, 2015

Abstract

The effect of acidic activator solutions on the formation of Fe(II)–Fe(III) layered double hydroxides and their phase transformation on the carbon steel surface was studied applying a complex physical investigation including an X-ray diffraction method, thermal analytical measurements and scanning electron microscopy (SEM). According to experimental data the main product of the phase transformation process in H_2SO_4 system was magnetite with an insignificant admixture of ferric oxyhydroxides, but the usage of HCl, HNO_3, and CH_3COOH acids led to predominant obtaining of lepidocrocite with relatively small amount of magnetite. Whereas the hydroxysulfate Green Rust II was determined as a primary mineral phase in the first case (H_2SO_4), only hydroxycarbonate Green Rust I structures were present in SEM images in the second case (HCl, HNO_3, and CH_3COOH). For the purposeful obtaining of GR(Cl^-), GR(NO_3^-), GR(CH_3COO^-) structures on the carbon steel surface the phase formation process must be carried out in an inert atmosphere.

Introduction

Fe(II)–Fe(III) layered double hydroxides (LDH) or Green Rust (GR) are commonly present as a metastable nucleus phase on the surface of iron-bearing alloys and carbon steel under various physical-chemical conditions, thus, they play an important role in wet and dry corrosion processes [1, 2]. Whereas the LDH structures are electrochemically formed on the surface of iron or steel electrodes under potentiostatic and galvanostatic conditions [3 – 5] as well as on the surface of inert electrodes (gold, silver, platinum) contacting with aerated ferrous salt solutions or both ferric and ferrous salt solutions in an inert atmosphere [6 - 8]. For example, thin layers of iron corrosion products were electrochemically deposited via the changing of the local pH value or the oxidation state of soluble precursor species [9].

At the same time, LDH structures usually appear as an intermediate phase when nanosized iron oxides, 3*d*-metal spinel ferrites and oxyhydroxides are formed on the surface of iron electrodes via chemical or electrochemical route [6, 10]. The purposeful obtaining of iron–oxygen mineral nanoparticles under the rotation-corrosion dispergation conditions (the RCD) shows the presence of Green Rust phases among the spectrum of nanostructures formed on the steel surface within 1-3 h of the phase formation process [11]. The numerous reviews [12 – 14] are devoted to investigation of chemical and colloid-chemical mechanisms of the Fe(II)–Fe(III) LDH formation, their structure, properties and practical usage for technical, medical and biological purposes. The other aspect of the LDH formation is closely connected with *red-ox* processes in the environment where Green Rusts play a role of strong reducing agent in respect to various oxidized chemical species [15].

It is well known, that the shape of anion determines the type of Green Rust lattice: whereas spherical and planar anions (Cl^-, CO_3^{2-}) coordinate the iron hydroxide layers in the Green Rust I, the three-dimensional anions (SO_4^{2-}) cause the formation of Green Rust II structure [16, 17]. The simultaneous presence of two and more anions in the dispersion medium leads to their competition in the LDH interlayer galleries [3]. But, depending on the concentration in the solution two anions can coexist in the structure of the LDH, for example, incorporation of both CO_3^{2-} and Cl^- ions into Green Rust I lattice was considered in work [18]. The carrying out of the phase formation process in the open-air system promotes free entrance of oxygen as well as carbon dioxide species into the steel surface, and so the access of carbonate ion from the CO_2 of air gives the reason to the priority formation of the (hydroxy)carbonate Green Rust [19].

The purpose of the present work is to determine the effect of the chemical composition of activator solutions on thermal behavior, phase composition and morphology of the layered double hydroxides and their oxidized products formed on the carbon steel surface under the RCD conditions in the open-air system.

Objects and methods of the research

The rotating disk electrode made of steel 3 was used for the formation of the surface iron–oxygen mineral phases according to the RCD method described in our previous work [11]. The phase formation process was carried out in the open-air system that provided an alternating contact of the steel surface with oxygen, carbon dioxide and water dispersion medium. The steel surface was exposed to mechanical treatment and the following activation using mineral or organic acids. We chose concentrated sulfuric, nitric, hydrochloric and acetic acids as activator solutions to determine the principle influence of the anion composition of the dispersion medium on the formation of Fe(II)–Fe(III) layered double hydroxides on the steel surface. The activated disk electrode was repeatedly rinsed in distilled water and onwards it was placed into the water dispersion medium (distilled water). The formation of disperse nanostructures on the steel surface lasted 24 h at around T = 20 °C. The temperature conditions were set using TS–1/80–SPU thermostat.

A complex physical investigation including an X-ray diffraction (XRD) method, thermal analytical measurements (TG / DTG, DTA) and scanning electron microscopy (SEM) was applied to study the phase composition of the surface nanostructures, their phase transformation and thermal behavior, morphology, and coherent scattering region (CSR).

The phase composition of the surface structures was conducted using computer-aided X-ray diffractometer (DRON–UM1) equipped with two Soller's slits and Ni-filtered radiation of cobalt anode CoK_α. The rate of recording got 1° / min, and the interfacial Woolf–Bragg's angle made up 80 – 90 degrees. The coherent scattering region characterizing the size of the primary particles or crystallites was calculated according to the standard Debye–Scherrer's formula.

A simultaneous study of thermogravimetric and differential thermal properties (TG–DTA) of the LDH structures was performed in the static air atmosphere by derivatigraph Q–1500D (Hungary). The record was made using computer data registration. The parameters of the pattern recording were the following: the samples 35.2 – 102.6 mg were heated at the rate 10 °C / min from 20 to 1000 °C; the sensitivity was 20 mg; TG–500, DTG–500, and DTA–250. The samples were placed into corundum crucible and covered by quartz beaker to create the equal temperature field. A scanning electron microscopy was curried out using JOEL–6700 microscope equipped with an energy-dispersive and cathode-luminescence attachment.

Results and discussion

The analysis of the surface mineral phases that had formed within 24 h after finishing activation procedure was performed using X-ray diffraction method (**Figure 1**). We can see the reflexes corresponding to the following mineral phases: lepidocrocite γ-FeOOH (JCPDS file No 08–0098), magnetite Fe_3O_4 (JCPDS file No 19–0629), goethite α-FeOOH (JCPDS file No 17–536) and Green Rust I (JCPDS file No 40–0127). According to the XRD data lepidocrocite as well as magnetite were formed on the steel surface when it was activated by HCl solution. The trace peaks of goethite and Green Rust I, probably hydroxycarbonate or mixed hydroxycarbonate-hydroxychloride, are present in the pattern (**Figure 1a**). On the contrary, only lepidocrocite belongs to the main mineral phase when the steel surface was activated by HNO_3 and CH_3COOH acids (**Figures 1b** and **c**). At that the relative quantity (XRD peak intensity) of magnetite is insignificant and goethite reflexes are seen only as a trace peaks. But magnetite is the main mineral phase after 24 h contact of the steel surface with distilled water when we used sulfuric acid as the activator solutions (**Figure 1d**). Other mineral phases such as lepidocrocite and goethite are present only as the admixtures.

Also, magnetite particles (H_2SO_4), equal quantities of magnetite and lepidocrocite phases (HCl), and mainly lepidocrocite with magnetite as an admixture (HNO_3, CH_3COOH) can be formed on its surface depending on the chemical composition of the activator solutions and the subsequent contact of the steel with distilled water within 24 h.

Table 1. The semiquantitative distribution of the mineral phases (relative units) formed on the steel surface depending on the chemical composition of the activator solutions.

Activator solutions	Distribution of mineral phases formed on steel surface within 24 h, relative units		
	γ-FeOOH	α-FeOOH	Fe_3O_4
HNO_3	0.83	0.58	0.10
HCl	0.94	0.51	0.18
H_2SO_4	0.14	1.00	1.00
CH_3COOOH	1.00	0.81	0.11

The semiquantitative distribution of every surface mineral phase calculated in relative units is present in **Table 1**. The lepidocrocite maximum (020) is determined for CH_3COOH system and its minimum is calculated for H_2SO_4 system. Goethite (110) and magnetite (311) maxima fall on H_2SO_4 system whereas magnetite minimum corresponds to both HNO_3 and CH_3COOH systems.

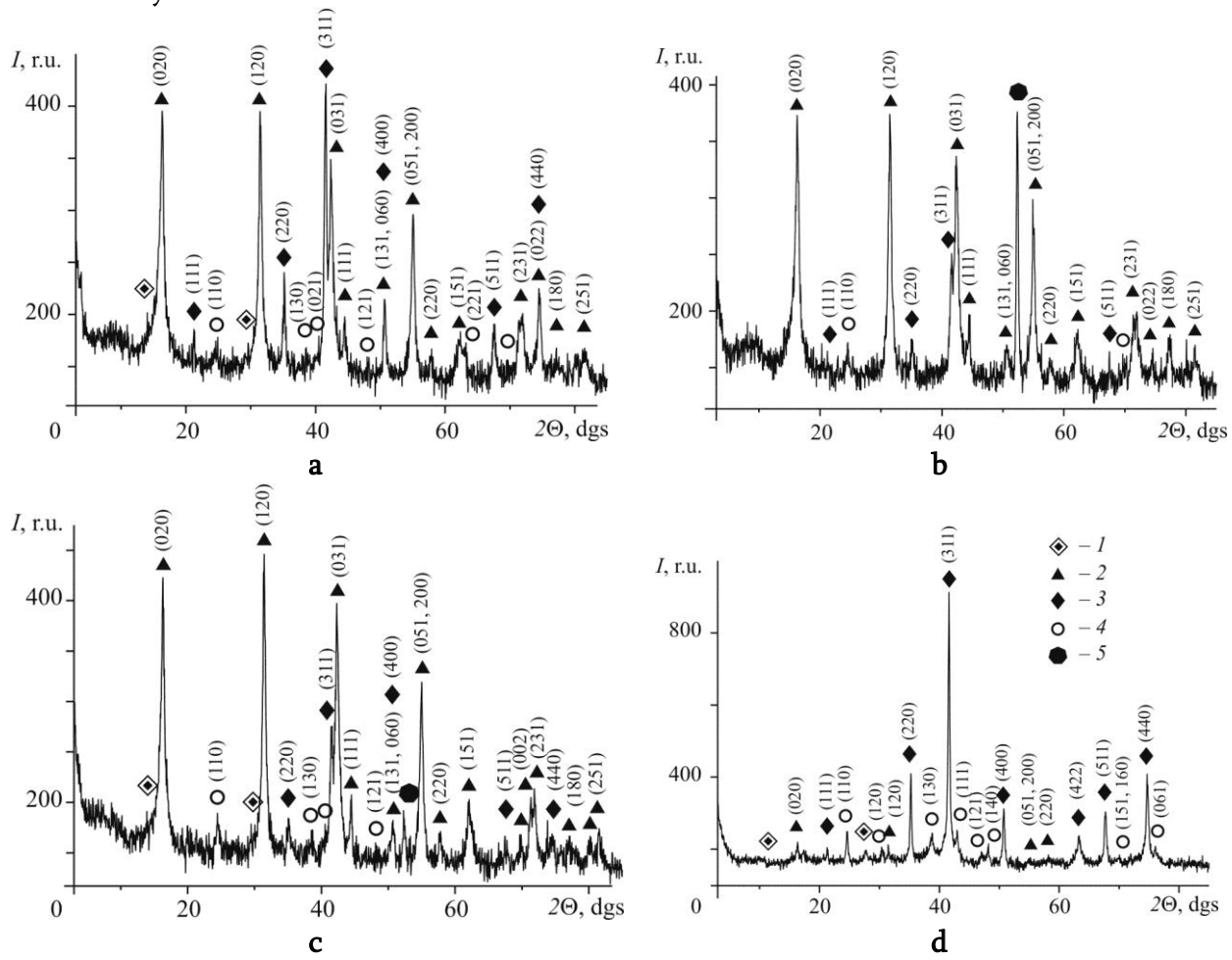

Figure 1. The mineral phases formed on the steel surface when it was activated by the following acids: a – HCl, b – HNO_3, c – CH_3COOH, d – H_2SO_4. Numbers correspond to: 1 – Green Rust I, 2 – γ-FeOOH, 3 – Fe_3O_4, 4 – α-FeOOH, 5 – Fe^0.

Table 2. The lattice parameters and crystallite size of the surface mineral phases depending on chemical composition of the activator solutions.

Activator solutions	Lattice parameters and primary particle size (CSR) of the surface mineral phases, nm										
	Magnetite			Lepidocrocite				Goethite			
	a	*V*	*d*	*a*	*b*	*c*	*d*	*a*	*b*	*c*	*d*
H_2SO_4	8.3711	586.6	24.68	–	–	–	–	–	–	–	–
HCl	8.3857	589.7	21.94	3.8755	12.5982	3.0640	10.36	4.6660	9.8765	3.0070	17.2
HNO_3	8.3722	586.8	9.87	3.8683	12.6410	3.0602	11.65	4.6489	9.8947	3.0096	15.8
CH_3COOH	8.3833	589.2	9.88	3.8790	12.6338	3.0664	13.32	4.649	9,895	3.0100	12.6

The crystal lattice parameters and the primary particle size (CSR) are present in **Table 2**. Whereas the parameter *a* of magnetite lattice does not depend on the chemical composition of the activator solution, the crystallite size of Fe_3O_4 is closely connected with the chemical

conditions on the steel surface. Also the biggest particles are formed in sulfate-containing system (~ 24 nm) and we obtain the smaller magnetite particles (~ 10 nm) in nitric and acetic systems. The lattice parameters of iron oxyhydroxides in all systems are the same but the crystallite size is insignificantly distinguished depending on the composition of the activator solution and equals 10 – 13 nm for lepidocrocite and 13 – 17 nm for goethite.

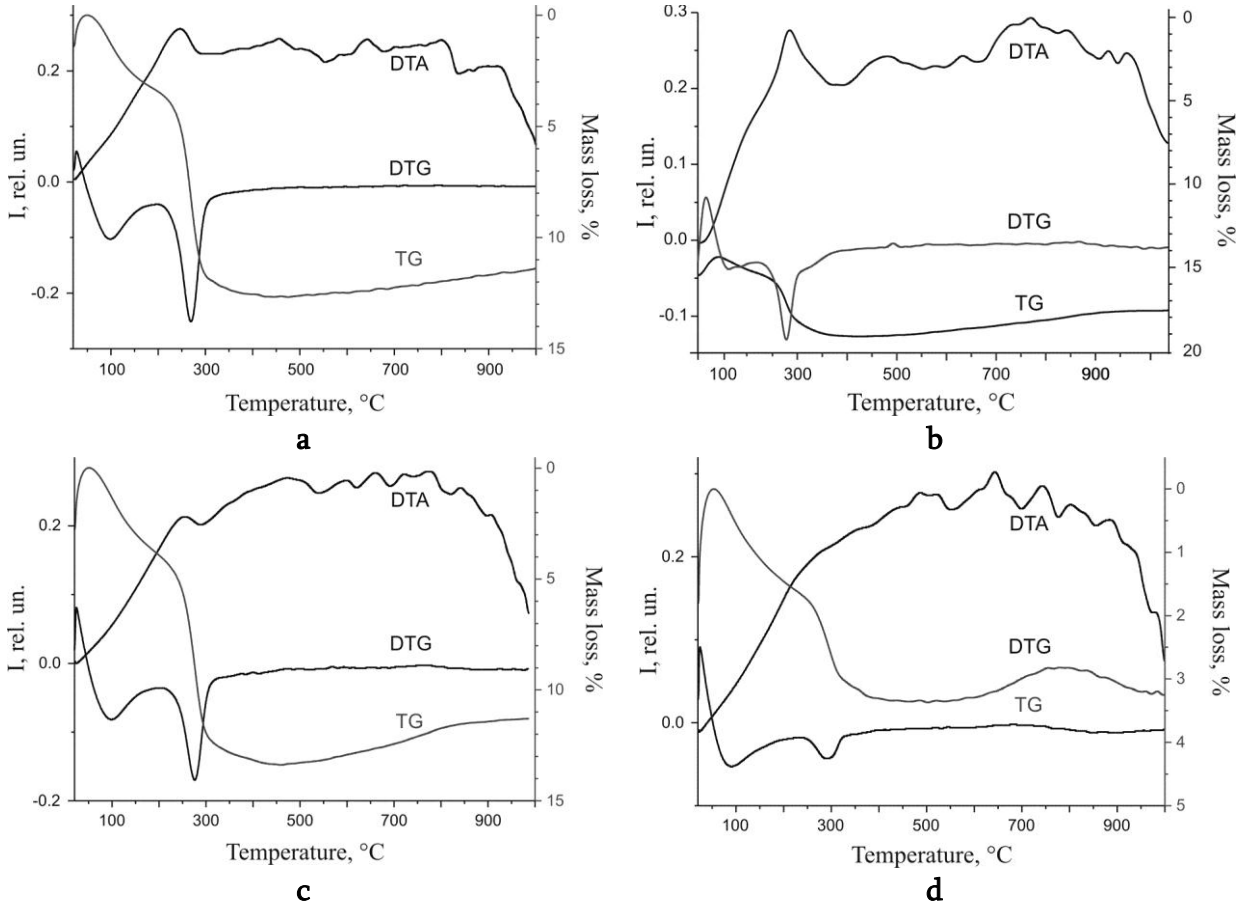

Figure 2. The TG–DTA curves for mineral phases formed on the steel surface when it was activated by the following acids: a – HCl, b – HNO_3, c – CH_3COOH, d – H_2SO_4.

The results of the thermal behavior study of the surface structures are present in **Fig.ure 2**. The analysis of the obtained data shows the appearance of two endoeffects in all DTG curves where the first minimum in the range of 90 – 100 °C corresponds to loss of the adsorbed water, and the second one in the range of 270 – 295 °C is related to the hydroxylation of oxyhydroxide lattice (**Table 3**). Whereas only single phase of iron oxyhydroxide (lepidocrocite) was formed on the steel surface when it was activated using HCl, HNO_3 and CH_3COOH acids, we suppose that the removal of the structural water from the lepidocrocite structure and its transformation into maghemite took place within a narrow temperature rang from ~ 270 to 280 °C. But two iron oxyhydroxide phases were present simultaneously (lepidocrocite and goethite) in the sample obtained on the steel surface when it was activated by H_2SO_4 acid, and a broad peak in the range 246 – 321 °C confirmed the distinction in the temperatures of their transformation into iron oxides. According to literature sources the T of the phase transformation of α-FeOOH mineral is higher than γ-FeOOH mineral and it gets ~ 350 °C in the first case and 350 – 390 °C in the second case, respectively [20]. But it is well known that thermal effects strongly depend on the particle size and nanoparticles of iron oxyhydroxides

can transform within the temperature range 260 – 320 °C [21]. Also our results agree with the data that are typical for nanostructures. The characteristic temperature of the magnetite phase conversion into maghemite equals 220 °C but it is insignificantly lower ~ 200 – 208 °C for our samples excepting H_2SO_4 system where such exoeffect is seen at T = 239 °C. And the last exoeffect corresponds to transformation of maghemite into hematite. With the exception of the H_2SO_4 system (323 °C) it lies in the range from 300 to 315 °C and such result is significantly lower in comparison with bulk mineral phases where it is higher than 500 °C [20].

Table 3. Characteristic of the thermal effects of the mineral phases formed on the steel surface that had been activated by acidic activators.

Activator solution	Thermal effects, °C				Mass loss, %
	Endoeffects		Exoeffects		
	Removing adsorbed water	Dehydroxylation of ferric oxyhydroxides	Transformation of magnetite into maghemite	Transformation of maghemite into hematite	
HCl	98	268	200	307	12.0
HNO_3	90	280	200	301	11.1
CH_3COOH	97	276	208	316	11.1
H_2SO_4	87	294	239	323	3.1

Whereas the mass loss of the samples obtained in the HCl, HNO_3 and CH_3COOH systems, according to the TG data (**Table 3**), gets 11 – 12 %, the value of such parameter for H_2SO_4 system is 3 %. That result well correlates with XRD data and can be explained by the difference in the relative quantities of iron oxyhydroxides in the phase composition of the surface structures.

The morphology of the iron–oxygen mineral phases formed on the steel surface after activation procedure is shown in **Figure 3**. The general view of the steel surface activated by HCl is present in **Figure 3a**. Primary Fe(II)–Fe(III) layered double hydroxide structures, probably mixed hydroxycarbonate-hydroxychloride Green Rust I, are seen in **Figure 3b** and **c** and magnetite particles formed on the steel surface in the HCl system are present in **Figures 3d**. The LDH structures obtained on the steel when it was activated using hydrochloric acid formed relatively big (microsized) aggregates (**Figure 3b**) that consisted of the randomly oriented plate and rods (**Figure 3c**). Magnetite particles formed the spherical aggregates that had smaller size in comparison with the LDH structures.

When we used nitric acid as the activator solution the morphology of the structures obtained on the steel surface is different from previous samples. The individual hexahedral plates (**Figure 3e**) and aggregates of hydroxycarbonate Green Rust (**Figure 3f**) are randomly oriented and lepidocrocite as the product of their solid-state transformation holds the shape and morphology of the initial structures (**Figure 3g**). Spherical magnetite particles are homogenous and well crystallized (**Figure 3h**).

The LGH aggregates formed in the corrosion pitting (defect) on the steel surface when it was activated by CH_3COOH are present in **Figure 3i**. Their enlarged images are seen in **Figures 3j** and **k**. The primary rod- and needle-like particles as it were shown in the previous cases formed the randomly oriented aggregates. The rod-like lepidocrocite particles and spherical magnetite aggregates obtained in the CH_3COOH system are shown in **Figure 3l**.

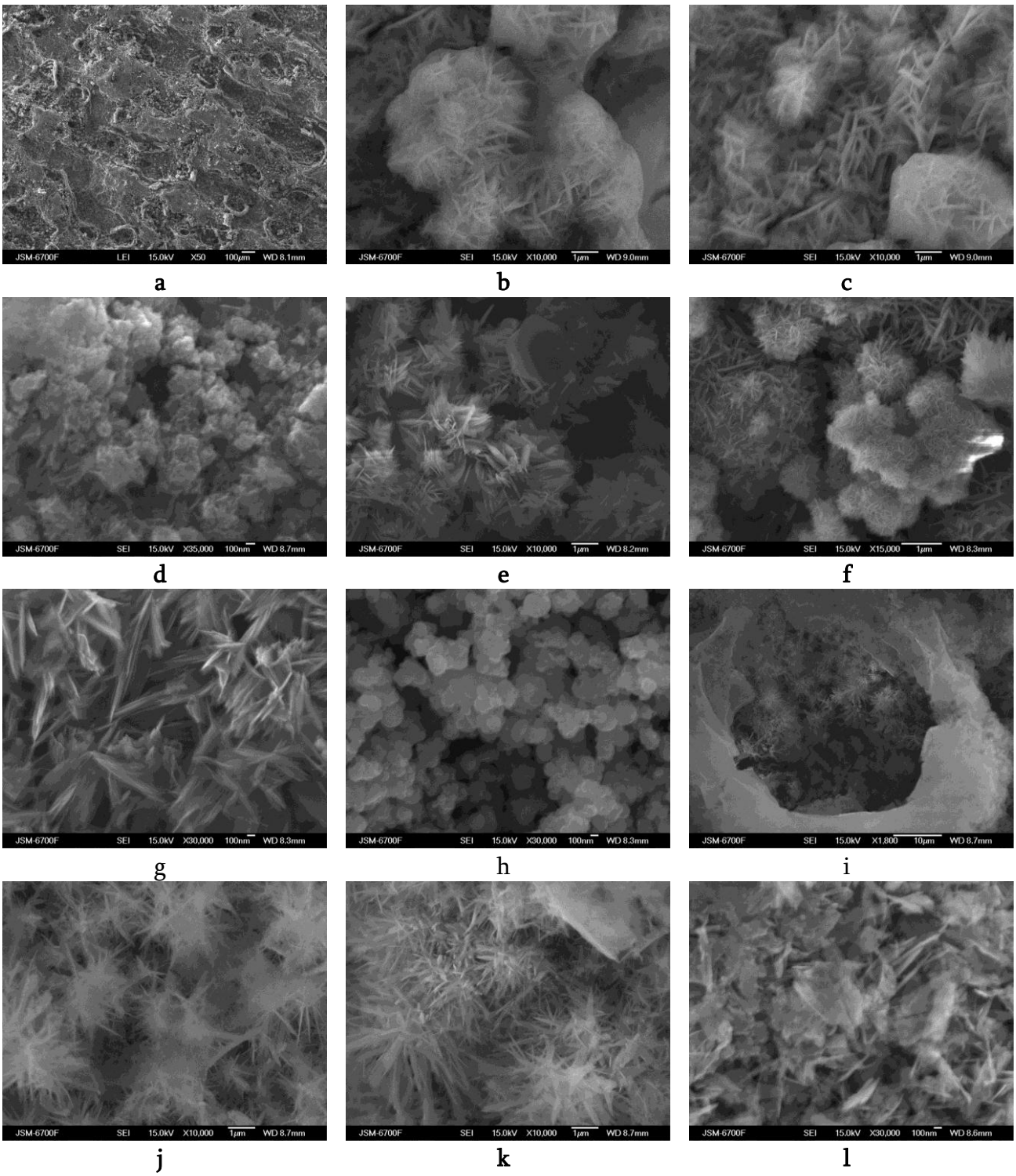

Figure 3. The SEM-images of the mineral phases formed on the steel surface activated by the following acids. HCl: a – the steel surface, b, c – Green Rust I aggregates, d – magnetite; HNO_3: e, f – Green Rust I aggregates, g – lepidocrocite, h – magnetite; CH_3COOH: i – LGH aggregates in the corrosion pitting, j, k – Green Rust I aggregates, l – lepidocrocite and magnetite particles.

In our previous work [22] we in detail described the morphology of the iron–oxygen nanoparticles formed on the surface of steel electrode activated using H_2SO_4 and afterwards placed into distilled water as well as ferric and ferrous sulfate solutions within 24 – 25 h. Also we do not repeat the SEM images of the surface structures obtained in the sulfate-containing system.

Hence, the usage of HCl, HNO_3 and CH_3COOH acids leads to formation of the randomly-oriented aggregates of Fe(II)–Fe(III) layered double hydroxides consisting of the rod- and plate-like particles on the steel surface. Iron-containing LDH structures do not keep stability in the open-air systems and they quickly transform on the steel surface according to the solid-state mechanism into ex-Green Rust (Fe(III)–GR) or lepidocrocite [23] or according to dissolution-re-precipitation mechanism into magnetite [24]. All LDH structures obtained on the surface of iron-bearing alloy (steel) when there is free air access into the system belong to the first type of Green Rust and contain CO_3^{2-} in their interlayer space due to the existence of the competition between carbon dioxide from the air and other anions from the solution.

Discussion

The formation of Fe(II)–Fe(III) layered double hydroxides or Green Rust as primary mineral phases on the surface of iron-bearing alloys has been considered to an important question of the corrosion study for many years. The various Green Rusts appearing at the beginning of aqueous corrosion processes relate to the most active iron dissolution stage [25]. Ferric oxyhydroxides resulting from the solid-state oxidation of Green Rust are determined as promoters of the iron corrosion as an electron acceptor towards metallic iron [9].

In spite of the fact that the enhanced analysis of the surface mineral phases using the latest physical-chemical methods of investigation is applied in the majority of works, the electrode surface is usually considered as a homogenous system. At that the phase formation process is described as a layer-by-layer growth of iron–oxygen structures whose mineralogical specificity is determined by the row of physical-chemical parameters, including pH value, *red-ox* condition, temperature, chemical composition of the solution contacting with electrode surface, the presence of surfactants and other chemical-active components etc. [26, 27]. But due to a such simplified approach the information about the metastable products of the phase formation process, their development in the local anodic and catodic areas of heterogeneous surface, its structural defects as well as in the corrosion pittings is being lost. At the same time the heterogeneity of carbon steels, the presence of various structural elements (ferrites, graphite, cementite) leads to occurrence of a great number of microgalvanic elements (couples) characterized by the spatially separated anodic and catodic areas. Whereas the flow of electrochemical reactions in anodal and catodal zones provides the change of the local pH values and saturate the near-electrode layer by ferric and ferrous aquahydroxoforms, hydroxyl or protons those interact with each other as well as air oxygen and oxygen-containing carbon species under open-air conditions. The acceleration of the corrosion process takes place in the crevices, cavities, pittings, and channels where pH value gradually increases from acid (at the bottom) to slightly alkali (at the top, on the surface).

Work [25] was aimed the study of a galvanic coupling between metal iron and the products of its oxidation corresponding to an electron transfer from iron (anodic site) to ferric products found in corrosion layers (cathodic site) when the various anions (carbonate, sulfate or chloride) were added into slight alkaline solutions. In particular, the oxidized Green Rust (Fe(III)–GR) will have a tendency to be consumed, due to its easy galvanic coupling with iron, whereas lepidocrocite and, especially, goethite will be able to be accumulated. In work [27], the corrosion process is considered in the view of the reaction of metal anodic dissolution balanced

by the cathodic reaction of the ferric and ferrous ion reduction and re-oxidation in water medium.

Whereas galvanostatic test shows that the presence of structural defects on the iron surface leads to localization of the corrosion process under rusts where the autocatalytic effect promotes increasing concentration of Fe^{2+}, Cl^-, and SO_4^{2-}, and as a result it causes the local acidification within the crevices, cavities, pittings, and channels [28]. The chemical changes in the surface holes are closely connected with the anodal process: accumulation and hydrolysis of Fe^{2+} cations result in the local acidification within the occluded zones. The lack of negatively charged species causes the appearance of a concentration gradient and anion flow into cavities (pittings). Such dissolved components interact with each other and the nucleation process takes place in the holes on the iron surface. So the authors [28] make a point of the formation of $Fe_x(OH)_{(1-x)}Cl$ species and akaganeite (β-FeOOH) when chloride anions are added into the solution contacting with the iron surface.

Recently we have estimated the formation of mineral phases on the steel surface activated by sulfuric acid and afterwards contacting with distilled water and ferric and ferrous sulfate water solutions according to two mechanisms carried out in the local catodal and anodal areas [22]. We supposed the solid-state oxidation of hydroxysulfate Green Rust to Fe(III)–GR and lepidocrocite in cathodal areas and dissolution–re-precipitation of ferric oxyhydroxides catalyzed by dissolved Fe^{2+} in anodal areas. Development of the iron–oxygen mineral phases in pittings includes accumulation of SO_4^{2-} anions and depolarization of hydrogen that, in general, leads to the formation of the primary metastable structure of schwertmannite $Fe_8O_8(OH)_{8-2x}(SO_4)_x$, where $1 \le x \le 1.75$. The gradual increase in the pH value in the middle of the pitting promotes schwertmannite dissolution and nanosized goethite precipitation, but the following increase in pH value to weak alkaline medium causes its re-precipitation into $GR(SO_4^{2-})$ on the steel surface.

In the present work four various acids are chosen as the activator solutions and some properties of the surface mineral phases obtained when an activated and rinsed steel electrode was carried into the water medium are underlined. Within the given study context there is an anion competition in LDH interlayer galleries and the possibility of a simultaneous coordination of a few anions in the LGH lattice when the steel electrode contacts with anions present in acids and carbon dioxide entering from air.

Whereas the existence of hydroxychloride [29], hydroxycarbonate [18] and hydroxysulphate [2] Green Rusts is not questioned, the number of literature sources devoted to studying other anionic Green Rust forms is significantly less. Despite of the fact that the various types of Green Rusts as corrosion products of iron are found via electrochemical way [3, 29 – 32] the inclusion of CH_3COO^- and NO_3^- anions into Fe(II)-Fe(III) LGH interlayer gallery is doubtful. In such a way the existence of Fe(II)-Fe(III) LDH structures coordinating the iron hydroxide layers via various families of anions including halides (Cl^-), non-metal oxoanions (CO_3^{2-}, NO_3^-, SO_4^{2-}), and organic anions (CH_3COO^-) is considered in [33]. By analogy with the study [34] where the replacement of carbonate by nitrate anions in similar to GRs pyroaurite structure, the replacement of some CO_3^{2-} by NO_3^- in the hydroxycarbonate Green Rust was suggested by the authors [19]. Also, they indirectly evidenced the occurrence of (hydroxy)nitrate Green Rust. As a matter of fact, the first Mössbauer spectra of GRs ever published were mineral phases formed on iron in 44 % NH_4NO_3 solutions at 30 °C [35]. But the preparation of the Green Rust by oxidation of $Fe(OH)_2$ in the presence of NO_3^-, according to [4],

has never given a successful result. Generally, most of the up-to-day articles are devoted to the interaction of natural Green Rusts with various nitrogen-containing species, which results in oxidation of Green Rust into ferric oxyhydroxides and reduction of NO_3^- to less oxidized forms [36] but not to the formation of GR(NO_3^-) mineral phase.

Due to calculations of equilibrium constants of various exchange reactions in LDH lattice the comparative list for monovalent and divalent anion selectivity was proposed by [37]. It may be written as: $OH^- > F^- > Cl^- > Br^- > NO_3^- > I^-$ and $CO_3^{2-} > C_{10}H_4N_2O_8S^{2-} > SO_4^{2-}$, respectively. Because the selectivity of divalent anions was higher than that of the monovalent anions, nitrate- and chloride-containing LDHs were related to the best precursors for ion-exchange reactions.

A high chemical activity of carbon dioxide from air or a high affinity of carbonate ions (CO_3^{2-}) with the hydrotalcite-like compounds or LDHs with respect to other anions entered from water solutions, e.g. chlorides, was studied in [38]. The difficulty in deintercalation of carbonate ions from LDH lattice was overcome by protonation of carbonate ions in the interlayer space and supplying the successive ion exchange with a large access of Cl^- anions.

The following investigation [3] clarified the competition of the anionic species in Green Rusts in iron-containing aqueous corrosion products and confirmed the affinity of pyroaurite-type layered hydroxides such as GRs with CO_3^{2-} anions, among any other types. In addition GRI(Cl^-) is oxidized into GRII(SO_4^{2-}) or GRI(CO_3^{2-}) when corresponding anions are present in the water medium. The preference for divalent anions over monovalent anions as well as the preference of CO_3^{2-} to other anions for intercalation into Green Rust lattice was postulated by [39].

Generally the formation of hydroxycarbonate Green Rust via the potential-dependent dissolution and oxidation of iron in bicarbonate-containing solutions is accompanied by the appearance of Fe(II)-complexes such as $FeHCO_3^+$, $Fe(HCO_3)_2$ or $Fe(CO_3)_2^{2+}$ [40 – 42], and $Fe^{II}(OH^-)_x(HCO_3^-/CO_3^{2-})$ is found as a primary ferrous-bearing species generated by corrosion process [43] The buffering properties of carbonate-containing solutions were mentioned by [6] when the Green Rust films were synthesized via electrochemical oxidation of soluble Fe(II) species in the solutions containing the corresponding anions. At that CO_3^{2-} anions within the solid Green Rust phase become HCO_3^- ions by consuming protons from the solutions that leads to pH decrease [4].

Because of a great affinity iron hydroxide layers with CO_3^{2-} anions, the formation of GR(CO_3^{2-}) was fixed when a hydrogenocarbonate solutions were added to $FeCl_2$ and NaOH medium [44], and its following oxidation caused the obtaining of goethite [45]. Probably, goethite is the product of the lepidocrocite phase transformation [46]. At the same time the work [47] determined the role of carbon dioxide in the formation of goethite versus lepidocrocite in solutions.

The precipitation of the hydroxysulfate Green Rust is possible even when the concentration of SO_4^{2-} anions is relatively small because the process acts as a sulfate pump, but the oxidation of GR into ferric oxyhydroxide is accompanied by SO_4^{2-} removal from interlayer galleries and the sulfate pump works in a reverse direction [2] Sulfate anions are accumulated on the GR(SO_4^{2-}) / γ-FeOOH interface under oxidative conditions [48]. The corrosion investigation [49] shows that the formation of goethite α-FeOOH may be enhanced in the presence of SO_4^{2-} anions, whereas akaganeite β-FeOOH gets stability in the chloride-containing medium. At that hydroxysulfate Green Rust is formed even when CO_3^{2-} anions are produced in

the system because its layered structure is more stable in comparison with hydroxycarbonate Green Rust [50].

The possibility of the incorporation of two anions CO_3^{2-} and Cl^- in the Green Rust structure was not viewed as a rule in work [18] The experimental electrochemical study of the competition between GR(Cl^-) and GR(SO_4^{2-}) shows the occurrence of three consistent reaction stages: 1. the formation of GR(Cl^-) from the initial precipitate, 2. the oxidation of GR(Cl^-) into GR(SO_4^{2-}), and 3. the oxidation of GR(SO_4^{2-}) into γ-FeOOH [50]. And it was proposed that the exchange reaction where chlorides were changed to sulfate in Green Rust structure took place in the system resulting in the formation of the more stable mineral phase than the one obtained in the presence of chloride anions.

Also, on the assumption of our experimental data as well as numerous studies referred above we may suppose the formation of two types of Green Rust structure on the steel surface depending on the chemical composition of activator solutions. Hence, the usage of sulfuric acid for activation led to the formation of hydroxysulfate Green Rust II on the steel surface and it conversed into magnetite with an insignificant admixture of lepidocrocite and goethite even in the open-air system. The TG / DTA experiments, with the TG and DTA curves confirmed the presence of relatively small amount of iron oxyhydroxides in the sample and pointed to the thermal conversion of magnetite.

However, the phase composition of the surface structures formed on the steel surface that was activated by nitric, hydrochloric and acetic acids, its crystal lattice parameters, crystallite size and thermal behavior not significantly differ depending on the chemical composition of activator solutions. The preference of CO_3^{2-} anions to other anions for intercalation into Green Rust lattice as well as free access of carbon dioxide from the air creates favorable conditions for the predominant formation of the hydroxycarbonate Green Rust. Moreover, the estimation of anion competition between CO_3^{2-} and Cl^-, CO_3^{2-} and NO_3^-, as well as CO_3^{2-} and CH_3COO^-, sends us back to the high selectivity of divalent anions with respect to the monovalent anions. Also, very likely LDHs, obtained when HCl, HNO_3 and CH_3COOH acids were used for steel activation, belong to hydroxycarbonate Green Rust I. Our data coincide with an opinion [19] regarding the phase transformation of hydroxycarbonate Green Rust into lepidocrocite. The presence of relatively small quantity of goethite may be corresponded to the following transformation of lepidocrocite. But the possibility to obtain the pure hydroxychloride, hydroxynitrate, and, probably, hydroxyacetate Green Rusts on the steel surface in the inert atmosphere will be studied in our next work.

Conclusions

1. Whereas the geometrical shape of anions determine the type of Green Rust lattice, the usage of various acidic activators gives the reason to obtain a few Fe(II)–Fe(III) layered double hydroxide structures. So, when the electrode made of carbon steel was activated by sulfuric acid the hydroxysulfate Green Rust II was formed as a primary mineral phase on its surface. Due to relatively high stability of GR(SO_4^{2-}) structure against oxidation the main product of its transformation via dissolution–re-precipitation mechanism was magnetite. The presence of ferric oxyhydroxides such as lepidocrocite and goethite may

be related to solid-state conversion of Green Rust as well as to its dissolution–re-precipitation.

2. In theory, the contact of the steel surface with nitric, hydrochloric and acetic acids may lead to the formation of the corresponding Green Rust I structures, but free access of oxygen and carbon dioxide from air causes the formation of single layered double hydroxide phase – hydroxycarbonate Green Rust I. The thermal behavior and phase composition of the products of GR(CO_3^{2-}) transformation does not strongly depend on the anion composition of the acids; as the main products of GR(CO_3^{2-}) transformation is lepidocrocite □-FeOOH. Magnetite Fe_3O_4 belongs to the second mineral phase obtained under oxidative conditions in the studied systems.
3. The existence of hydroxychloride, hydroxynitrate, and, hydroxyacetate Green Rusts on the steel surface is not excluding within short time after finishing of the activation procedure, but high chemical affinity of iron hydroxide layers with carbonate anions and free access of CO_2 from air into the open-air system causes the formation of other LDH structure – hydroxycarbonate Green Rust. The possibility of the obtaining of GR(Cl^-), GR(NO_3^-), GR(CH_3COO^-) on the carbon steel surface may be proved when the phase formation process is carried out in an inert (anoxic) atmosphere and that study will be the aim of our future work.

Acknowledgments

We express our gratitude to PhD O. A. Vishnevskij from M. P. Semenenko Institute of Geochemistry, Mineralogy & Ore Formation of NAS of Ukraine for preparing the SEM photos.

References

1. Y. Washeda, S. Suzuki. Characterization of Corrosion Products on Steel Surface. 2005, Springer.
2. P. Refait, J.-B. Memet, C. Bon, R. Sabot, J.-M. R. Génin. Corros. Sci., 2003, 45, 833.
3. Ph. Refait, S. H. Drissi, J. Pytkiewicz, J.-M. R. Génin. Corros. Sci., 1997, 39, 1699.
4. J.-M. R. Génin, Ch. Ruby, A. Géhin, Ph. Refait. C. R. Geoscience, 2006, 338, 433.
5. J. M. R. Génin., Ch. Ruby. Solid State Sci., 2008, 10, 244.
6. S. L. Legrand, H. Antony, A. Chaussé. Electrochem. Comm., 2003, 5, 208.
7. H. Antony, S. Peulon, L. Legrand, A. Chaussé. Electrochim. Acta, 2004, 50, 1015.
8. L. Legrand, R. Maksoub, G. Sagon, S. Lecomte, J. P. Dallas, A. Chaussé. J. Electrochem. Soc. A, 2003, 150, 45.
9. S. Peulon, H. Antony, L. Legrand, A. Chaussé. Electrochim. Acta, 2004, 49, 2891.
10. L. Legrand, G. Sagon, S. Lecomte, A. Chaussé, R. Messina. Corros. Sci., 2001, 43, 1739.
11. O. M. Lavrynenko, V. I. Kovalchuk, S. V. Netreba, Z. R. Ulberg. Nano Studies, 2013, 7, 295.
12. P. Nalawade, B. Aware, V. J. Kadam, R. S. Hirlekar. J. Sci. & Ind. Res., 2009, 68, 267.
13. O. M. Lavrynenko. Mater. Sci. Nanostruc., 2009, 3, 15. – *in Russian*
14. O. M. Lavrynenko. Mater. Sci. Nanostruc., 2009, 4, 16. – *in Russian*

15. J.-M. R. Génin, Ph. Refait, G. Bourrie, M. Abdelmoula, F. Trolard. Appl. Geochem., 2001, 16, 559.
16. J. D. Bernal, D. R. Dasgupta, A. L. Masckay. Glay Miner. Bull., 1959, 4, 15.
17. V. Rives. Layered Double Hydroxides: Present and Future. 2001, New York, Nova Sci. Publ.
18. L. Legrand, M. Abdelmoula, A. Géhin, A. Chaussé, J.-M. R. Génin. Electrochim. Acta., 2001, 46, 1815.
19. Y. Hamlaoui, F. Pedraza, L. Tifouti. Corros. Sci., 2008, 50, 2182.
20. W. A. Deer, R. A. Howie, J. Zussman. Rock Forming Minerals, Non-Silicates. 1962, London, Longmans.
21. R. M. Cornell, U. Schwertmann. The Iron Oxides: Structure, Properties, Reactions, Occurrence and Uses. 2003, Weinheim, Wiley–VCH.
22. O. M. Lavrynenko. The spatially separated process of the formation of nanosized iron–oxygen structures on the steel surface contacting with water dispersion medium. Nano Studies, 2015, 11, 177-190.
23. L. Legrand, L. Mazerolles, A. Chaussé. Geochim. & Cosmochim. Acta, 2004, 68, 3497.
24. A. Sumoondur, S. Shaw, I. Ahmed, L. G. Benning. Mineralog. Mag., 2008, 72, 201.
25. V. Lair, H. Antony, L. Legrand, A. Chaussé. Corros. Sci., 2006, 48, 2050.
26. L. Bousselmi, C. Fiaud, B. Tribollet, E. Triki. Electrochim. Acta, 1999, 44, 4357.
27. Sh. Suzuki, E. Matsubara, T. Komatsu, Y. Okamoto, K. Kanie, A. Muramatsu, H. Konishi, J. Mizuki, Y. Waseda. Corros. Sci., 2007, 49, 1081.
28. Z. Wang, Ch. Xu, X. Dong. Chinese J. Chem. Eng., 2008, 16, 299.
29. Ph. Refait, M. Abdelmoula, J.-M. R. Génin. Corros. Sci., 1998, 40, 1547.
30. Ph. Refait, J.-M. R. Génin. Corros. Sci., 1993, 34, 797.
31. J.-M. R. Génin, A. A. Olowe, Ph. Refait, L. Simon. Corros. Sci., 1996, 38, 1751.
32. Ph. Refait, A. Géhin, M. Abdelmoula, J.-M. R. Génin. Corros. Sci., 2003, 45, 659.
33. M. Sipiczki. Functional Materials – Syntheses, Characterization and Catalytic Applications. PhD Disser. 2013, Szeged, Univ. Szeged.
34. H. C. B. Hansen, R. M. Taylor. Clay Miner., 1991, 26, 311.
35. J. R. Gancedo, M. L. Martinez, J. M. Oton. J. Phys. Colloq. C, 1976, 6, 297.
36. H. C. B. Hansen, S. Guldberg, M. Erbs, C. B. Koch. Appl. Clay Sci., 2001, 18, 81.
37. S. Miyata. Clays Clay Miner., 1983, 31, 305.
38. N. Iyi, T. Matsumoto, Y. Kaneko, K. Kitamura. Chem. Mater., 2004, 16, 2926.
39. J. M.-R. Génin, G. Bourrié, F. Trolard, M. Abdelmoula, A. Jaffrezic, Ph. Refait, V. Maitre, B. Humbert, A. Herbillon. Environ. Sci. & Technol., 1998, 32, 1058.
40. D. H. Davies, G. T. Burstein. Corrosion NACE, 1980, 36, 416.
41. C. R. Valentini, C. A. Moira, J. R. Vilche, A. J. Arvia. Corros. Sci., 1895, 25, 985.
42. E. B. Castro, J. R. Vilche, A. J. Arvia. Electrochim. Acta, 1991, 36, 117.
43. S. Savoye, L. Legrand, G. Sagon, S. Lecomte, A. Chaussé, R. Messina, P. Toulhoat. Corros. Sci., 2001, 43, 2049.
44. O. Benali, M. Abdelmoula, Ph. Refait, J.-M. R. Génin. Geochim. & Cosmochim. Acta, 2001, 65, 1715.
45. M. Reffass, R. Sabot, C. Savall, M. Jeannin, J. Creus, Ph. Refait. Corros. Sci., 2006, 48, 709.
46. U. Schwertmann, R. M. Taylor. Clays & Clay Miner., 1972, 20, 151.

47. L. Carlson, U. Schwertmann. Clay Miner., 1990, 25, 65.
48. S. Pineau, R. Sabot, L. Quillet, M. Jeannin, Ch. Caplat, I. Dupont–Morral, Ph. Refait. Corros. Sci., 2008, 50, 1099.
49. M. Yamashita, H. Konishi, T. Kozakura, J. Mizuki, H. Uchida. Corros. Sci., 2005, 47, 2492.
50. Ph. Refait, M. Abdelmoula, J.-M. R. Génin, R. Sabot. C. R. Geoscience, 2006, 338, 476.

კონცენტრატორების ეფექტური გამოყენების ზოგიერთი ასპექტი A^3B^5 მასალებზე დამზადებულ მზის ენერგიის ფოტოელექტრულ გარდამქმნელებში

თ. ი. ხაჩიძე, ი. მ. ავალიანი, დ. მ. შალამბერიძე

საქართველოს ტექნიკური უნივერსიტეტი
ინსტიტუტი "ოპტიკა"
თბილისი, საქართველო
txachidz@gmail.com

მიღებულია 2015 წლის 8 სექტემბერს

ანოტაცია

კვლევის ძირითად მიზანს წარმოადგენს A^3B^5 ტიპის ნახევარგამტარული მზის ფოტოექტრული გარდამქმნელებისათვის ეფექტური ლინზა-კონცენტრატორების დამუშავება. ეფექტურობაში იგულისხმება ის, რომ ფოტოელექტრული გარდაქმნისას მზის ენერგია, რომელიც ეცემა ლინზა-კონცენტრატორს, მინიმალური დანაკარგებით გავიდეს მასში და მიეწოდოს ნახევარადგამტარულ ფოტოელემენტს. სფერული და ფრენელის ლინზები, რომლებიც გამოიყენება კონცენტრატორებად, ხასიათდება საკმაოდ დიდი ოპტიკური დანკარგებით, რაც ძირითადად გამოწვეულია ქრომატული და გეომეტიული აბერაციებით, არეკვლით ზედაპირიდან და დიდი კონცენტრაციისას (დიდი ლინზების გამოყენებისას) ფოკუსირებული სინათლის დიდი ზომებით (ფოკუსირებული სინათლე აჭარბებს ფოტოელემენტის ზომებს და არ ხდება მისი სრულად გამოყენება). ქრომატული და გეომეტრიული აბერაციების და ფოკუსირებული სინათლის ზომების შესამცირებლად ჩვენ მიზანშეწონილად ჩავთვალეთ მზის ენერგიის ფოტოელექტრული გარდამქმნელებისათვის დამუშავდეს და დამზადდეს ოპტიკური ლინზა-კონცენტრატორები ასფერული ზედაპირებით, ხოლო ზედაპირიდან სინათლის არეკვლის შესამცირებლად ლინზის ზედაპირი დაიფაროს განმაშუქებელი საფარით.

დღეს მსოფლიოში ყველაზე მეტად გავრცელებულია სილიციუმის ფოტოელემენტები (მონო- და პოლიკრისტალური), მათი ხვედრითი წილი მზის ენერგიის ფოტოელექტრული გარდამქმნელების ბაზარზე 86 % აღემატება. მიუხედავად იმისა, რომ მესამე და მეხუთე ჯგუფის ელემენტებისაგან შემდგარ A^3B^5 ტიპის ფოტოელემენტებს მაღალი მქკ ახასიათებთ, ძალიან მოკრძალებულია მათი გამოყენება. ეს ძირითადად გამოწვეულია ამ ელემენტების მაღალი ფასით (განსაკუთრებით ორ- და სამკასკადიანი ელემენტებისა), რაც, თავის მხრივ, განპირობებულია იმ კრისტალური სტრუქტურის ღირებულებით, რომლითაც ისინი მზადდება. სამაგიეროდ, სილიციუმის ელემენტებისაგან განსხვავებით, მათ შეუძლიათ დანაკარგების გარეშე გარდაქმნან მზის გამოსხივების კონცენტრირებული ენერგია კონცენტრაციის საკმაოდ მაღალი ხარისხით (100-ზე მეტი). ანუ ფოტოელემენტის მცირე ფართობს მიეწოდება ბევრად მეტი მზის ენერგია და მიიღება მისი პროპორციული ელექტრული ენერგია. ეს, თავის მხრივ, მასალის (სტრუქტურის) ფართობის ეკონომიის საშუალებას იძლევა და, შესაბამისად, მცირდება ფოტოელემენტის ფასიც ყოველ გამომუშავებულ ვატზე [1].

მზის ენერგიის კონცენტრირებისათვის ძირითადად გამოიყენება სხვადასხვა ტიპის (სფერული, ფრენელის და სხვ.) ლინზები და სარკეები. თავისთავად მზის ენერგიის ელექტრულ ენერგიად გარდაქმნისას პირველ რიგში მინიმალური უნდა იყოს

დანაკარგები მისი კონცენტრირებისას. ანუ რაც შეიძლება მეტმა სხივურმა ენერგიამ უნდა მიაღწიოს ფოტოელემენტამდე. ამ ამოცანის გადასაჭრელად საჭიროა კვლევების ჩატარება ახალი ეფექტური კონცენტრატორების დასამუშავებლად.

აქედან გამომდინარე, ჩვენი სამუშაოს ძირითად მიზანს წარმოადგენდა, კვლევების ჩატარება ოპტიკური კონცენტრატორების გამოყენების ეფექტურობის გასაზრდელად მენდელეევის ქიმიურ ელემენტთა პერიოდული სისტემის მესამე და მეხუთე ჯგუფის ელემენტებისაგან შემდგარი – A^3B^5-ტიპის ნახევარგამტარული ფოტოელემენტებისათვის. ექსპერიმენტისათვის ძირითადად გამოყენებული იქნება GaInP / GaAs / Ge სტრუქტურის მქონე ფოტოელემენტი, აქტიური ზედაპირის ფართობით 1×1 სმ^2. კვლევების ჩატარება პირველ რიგში მოითხოვს ოპტიკური კონცენტრატორებისათვის მასალის შერჩევას და შემდგომ ამ მასალით კონცეტრატორების კონსტრუქციისა და დამზადების ტექნოლოგიის დამუშავებას.

კონცენტრატორად შესაძლებელია გამოყენებული იქნას, როგორც ლინზები ასევე სარკეები. მათ დასამზადებლად იყენებენ მინას ან ოპტიკურად გამჭვირვალე ორგანულ მასალებს. მასალის შერჩევისას ძირითადი კრიტერიუმებია მისი სპექტრალური გამჭვირვალობისა და ფოტოელემენტის სპექტრალური მგრძნობიარობის თანხვედრა და დამზადების ტექნოლოგიის სიმარტივე (სიიაფე).

მასალებიდან ერთ-ერთი ხელმისაწვდომია პოლიმეთილაკრილატი ПММА. ამ პოლიმერულ მასალას გააჩნია კარგი ოპტიკური მახასიათებლები (გამჭვირვალობა). **ნახაზზე 1** მოცემულია გამჭვირვალობის (პროცენტებში) დამოკიდებულება მზის ენერგიის ტალღის სიგრძეზე (ნანომეტრებში).

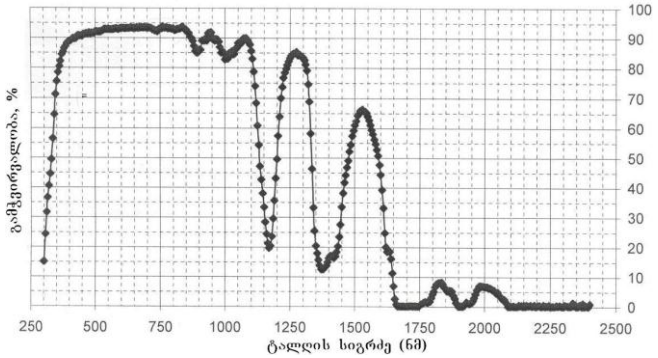

ნახაზი 1. გამჭვირვალობის (%) დამოკიდებულება მზის ენერგიის ტალღის სიგრძეზე.

როგორც ვხედავთ, ამ მასალას გააჩნია საკმაოდ მაღალი გამჭვირვალობა სპექტრის ხილულ არეში. ამ მახასითებლებიდან, აგრეთვე, ჩანს, რომ პოლიმეთილაკრილატის გამჭვირვალობის სპექტრის მაქსიმუმი სრულად მოიცავს A^3B^5 სტრუქტურის მქონე ფოტოელემენტების მგრძნობიარობის სპექტრს. გამომდინარე აქედან, შეგვიძლია დავასკვნათ, რომ პოლიმეთილაკრილატისაგან დამზადებული კონცენტრატორების გამოყენება GaInP / GaAs / Ge სტრუქტურის ფოტოელემენტებთან საკმაოდ ეფექტური იქნება.

ეფექტური მუშაობისათვის კონცენტრატორებს უნდა გააჩნდეთ კარგი ოპტიკური მახასიათებლები. ამიტომ დიდი მნიშვნელობა აქვს ასეთი მახასიათებლების მქონე ლინზების გათვლისა და დამზადების იაფი და საიმედო ტექნოლოგიის შექმნას.

ტექნიკური მოთხოვნებიდან გამომდინარე, ლინზა-კონცენტრატორის დამუშავებამდე საჭიროა განისაზღვროს მისი ტიპი. დღეისათვის მზის

ფოტოელექტრულ გარდამქმნელებში ლინზა-კონცენტრატორებად ფართოდ გამოიყენება ფრენელის ლინზები. მათი ძირითადი უპირატესობა მცირე სისქეა, მაგრამ მათ კონსტრუქციაში მაღალია სინათლის პარაზიტული გაბნევა კონცენტრირებული წრეების გადასასვლელებზე, რაც იწვევს ამ ტიპის ლინზის მიერ კონცენტრირებული სხივური ენერგიის საკმაოდ მაღალ დანაკარგებს. გამომდინარე აქედან, ჩვენ უპირატესობა მივანიჭეთ ისეთ ლინზებს და სარკეებს რომლებშიც ნაკლებია სხივური ენერგიის დანაკარგები. ასეთებია სფერული, ასფერული და ხაზოვანი ფოკუსის ლინზები და პარაბოლური სარკეები.

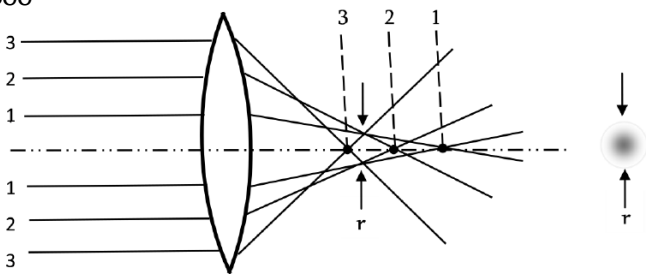

ნახაზი 2. სხივთა სვლა სფერულ ლინზაში.

სფერული ლინზები (**ნახაზი 2**) საკმაოდ გავრცელებულია, მაგრამ ამ ტიპის ლინზების ნაკლოვანებას წარმოადგენს სფერული აბერაცია ანუ მათი ოპტიკური ძალა ნაპირებზე ცენტრთან შედარებით გაცილებით მეტია. შესაბამისად, ლინზის სხვადასხვა უბანს სხვადასხვა ფოკუსური მანძილი აქვს და სხივთა პარალელური ნაკადის ზუსტად ერთ წერტილში დაფოკუსირება შეუძლებელია. როგორც **ნახაზიდან 2** ჩანს, 1, 2 და 3 სხივები ლინზის სხვადასხვა უბანს ეცემა და ლინზის ზედაპირთან დაცემის კუთხეც სხვადასხვა აქვთ. შესაბამისად, ლინზაში გავლის შემდეგ ისინი სხვადასხვა წერტილში იკრიბებიან და დაფოკუსირებულ სინათლის ლაქას გარკვეული r რადიუსი გააჩნია და ამ ლაქაში სინათლის ინტენსივობა არათანაბრადაა განაწილებული. დიდი დიამეტრის ($d > 200$ მმ) ლინზების შემთხვევაში $r > 10$ მმ. ეს კი იმას ნიშნავს, რომ მცირე ზომის ფოტოელემენტებისათვის კონცენტრირებული სინათლის ნაწილი გავა ელემენტის საზღვრებს გარეთ და, რადგანაც სწორედ კიდეებზე კონცენტრირდება სინათლის დიდი ნაწილი, გვექნება სხივური ენერგიის საგრძნობი დანაკარგები. გარდა ამისა, კონცენტრირებისას სხივური ენერგიის არათანაბარი განაწილება ფოტოელემენტზე იწვევს მის არასტაბილურ მუშაობას, რადგან შესაძლებელია მისი კიდეები უფრო გადაცხელდეს, ვიდრე ცენტრალური ნაწილი.

სფერული ლინზის აღნიშნული ნაკლოვანებები თითქმის სრულად აღმოიფხვრება ასფერული ლინზების შემთხვევაში. ასფერული ლინზის სიმრუდის რადიუსი ზედაპირის სხვადასხვა წერტილში განსხვავებულია და ისეა შერჩეული, რომ მის ზედაპირზე პარალელური სხივები (კონკრეტული ტალღის სიგრძისათვის) ერთ ფოკუსში იკვეთებიან ანუ სინათლის დაფოკუსირება შესაძლებელია ერთ წერტილში.

მიუხედავად იმისა, რომ ასფერული ლინზის გამოყენებით პრაქტიკულად იხსნება სფერული აბერაციის პრობლემა და სხივები უნდა ფოკუსირდებოდეს ერთ წერტილში, რეალურ პირობებში ფოკუსირებულ სინათლეს მაინც აქვს გარკვეული ზომები, რაც ქრომატული აბერაციითაა გამოწვეული ანუ სხვადასხვა ტალღის სიგრძის სხივები სხვადასხვა კუთხით გარდატყდება და სხვადასხვა ფოკუსში იკრიბება.

ასფერული ლინზების უპირატესობის შესამოწმებლად დამზადდა და GaInP / GaAs / Ge სტრუქტურის ფოტოელემენტთან გამოიცადა ერთი და იგივე დიამეტრის სფერული და ასფერული ლინზები (**ცხრილი 1**).

ცხრილი 1.

ლინზის ზომები, მმ	ლინზის ზედაპირი	კონცენტრირებული სინათლის ლაქის მინიმალური დიამეტრი, მმ	ფოტოელემენტის ფართობი, მმ	კონცენტრაციის ხარისხი, F_1 / F_2	მიღებული ელექტრული სიმძლავრე, ვტ
∅ 195	სფერული	11	10 × 10	298	6.1
∅ 195	ასფერული	8	10 × 10	298	6.4

ცხრილში 1 მოყვანილი ლინზების დიამეტრი და, შესაბამისად, კონცენტრაციის ხარისხი შეირჩა, როგორც მაქსიმალურსდ შესაძლებელი, იმ პირობიდან გამომდინარე, რომ ფოტოელემენტის ტემპერატურა არ აცილებოდა 60 °C სპეციალური გაცივების სისტემების გარეშე (ფოტოელემენტი განთავსებული იყო 300 სმ^2 ზედაპირის ფართობის ალუმინის რადიატორზე). ცხრილიდან ჩანს, რომ კონცენტრირებული სინათლის ლაქის მინიმალური დიამეტრი ასფერულ ლინზას საგრძნობლად ნაკლები აქვს, რაც საშუალებას იძლევა კონცენტრირებული სინათლის ნაკადი ფოტოელემენტის ზედაპირზე ჩავტიოთ და არ დავკარგოთ, რაც, თავის მხვრივ, აისახა მიღებული ელექტრული სიმძლავრის სიდიდეზე. რითაც დასტურდება ასფერული ზედაპირის ლინზების უპირატესობა სფერულთან შედარებით.

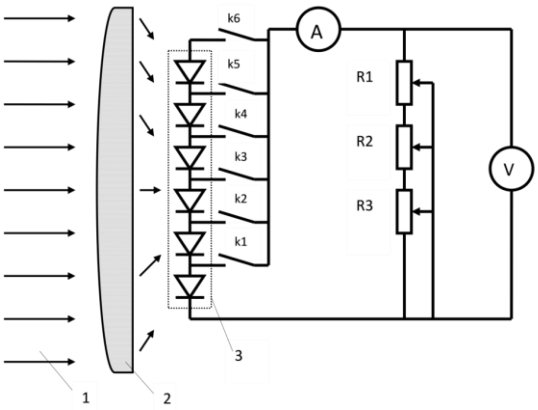

ნახაზი 3. ხაზოვანი ფოკუსის მქონე კონცენტრატორის ერთ ხაზზე განლაგებული ფოტოელემენტების გამოსაკვლევი სტენდის სქემა.
1 – მზის გამოსხივება, 2 – ხაზოვანი ფოკუსის მქონე კონცენტრატორი და 3 – ერთ ხაზზე განლაგებული ფოტოელემენტების მატრიცა.

შემდგომი კვლევები დაეთმო ცილინდრული ასფერული ლინზის კონცენტრატორად გამოყენებას. ასეთი ლინზების ფოკუსურ ლაქას ხაზი წარმოადგენს, რომლის სიგრძეც ლინზის სიგანის ტოლია. გამოკვლეული იქნა ხაზოვან ფოკუსში მოთავსებული ფოტოელემენტის მიერ გამომუშავებული ელექტროენერგიის სიდიდის შეფასება გრძივ ფოკუსში ერთ ხაზზე დალაგებულ ფოტოელემენტებთან. უნდა აღვნიშნოთ, რომ ასეთი სქემით ჩატარებული ექსპერიმენტის შედეგები ტექნიკურ ლიტერატურაში ვერ იქნა მოძიებული. ამასთან ასეთი სქემა იძლევა რიგ დადებით შედეგებს. უპირველეს ყოვლისა ფოტოვოლტური ბლოკი ბევრად მარტივდება. მარტვდება ასევე ელექტრული წრედის სქემის მუშაობაც და ამასთან აშკარად იაფდება, რადგანაც ლინზა კონცენტრატორების რაოდენობა ბევრად მცირდება. ჩატარებული ცდების სქემა მოცემულია **ნახაზზე 3** [2].

როგორც ვხედავთ, ამ ერთი ლინზის ხაზოვანი ფოკუსის ქვეშ გვერდი გვერდ მიერთებულია ექვსი ფოტოელემენტი. ცდების შედეგად დადგინდა, რომ გამომუშავებული ელექტრული ენერგია ერთ ხაზზე დალაგებული ელემენტების რაოდენობის პროპორციულად იზრდებოდა (იხ. **ცხრილი 2**). აქედან შეიძლება დავასკვნათ, რომ ელემენტების რაოდენობა შეზღუდული არ არის. ის დამოკიდებულია მხოლოდ ლინზის სიგანეზე და, თუ საჭიროა ფოტოელემენტების გრძელი ზოლი, რომელიც აღემატება მოცემული ლინზა-კონცენტრატორის სიგანეს, მაშინ შესაძლებელი გვერდზე მიდგმით – მეორე ხაზოვანი ფოკუსის მქონე ანალოგიური პარამეტრების მქონე ლინზის დამატებით.

ცხრილი 2.

ფოტოელემენტების რაოდენობა	კონცენტრატორის გარეშე			კონცენტრატორით (კონცენტრაცია = 17)		
	ძაბვა, ვ	დენის ძალა, მა	ელექტრული სიმძლავრე, მვტ	ძაბვა, ვ	დენის ძალა, მა	ელექტრული სიმძლავრე, მვტ
ერთი ელემენტი	0.7	0.81	0.567	0.7	13.6	9.52
ორი ელემენტი	1.4	0.81	1.134	1.4	13.5	18.40
სამი ელემენტი	2.1	0.82	1.722	2.1	13.5	28.35
ოთხი ელემენტი	2.8	0,82	2.296	2.8	13.5	37.80
ხუთი ელემენტი	3.5	0.81	2.835	3.5	13.4	46,90
ექვსი ელემენტი	4.2	0.81	3.400	4.2	13.5	56.70

ხაზოვავანი ფოკუსის ლინზების გამოყენება საგრძნობლად ამცირებს კონცენტრატორების რაოდენობას (ერთი კონცენტრატორი სჭირდება ელემენტებს ზოლს და არა თითოეულ ელემენტს), ამარტივებს ფოტოვოლტური ბლოკის აწყობას, ზრდის მის საიმედოობას და ამცირებს მის ფასს. ამჟამად ჩვენს მიერ წარმოებს სამუშაოები ხაზოვანი ფოკუსის სარკეების გამოყენებაზე კონცენტრატორებად. სარკეების შესაძლო უპირატესობაა ნაკლები დანაკარგები ქრომატულ აბერაციაზე.

მაგრამ, როდესაც მზის სხივები ეცემა ფოტოელექტრული გარდამქმნელის ოპტიკურ ლინზა-კონცენტრატორს, ჰაერიდან მყარ გარემოში გადასვლისას მისი დიდი ნაწილი გარდატყდება და აღწევს ფოტოელექტრულ გარდამქმნელამდე, ნაწილი კი იმის გამო, რომ დიდია სხვაობა ჰაერისა და ლინზა-კონცენტრატორის გარატეხის მაჩვენებლებს შორის აირეკლება კონცენტრატორის როგორც ზედა, ასევე – ქვედა ზედაპირიდან. არეკვლის პროცენტული სიდიდე დამოკიდებულია კონცენტრატორის მასალაზე. ჩვენს მიერ დამუშავებული და PMMA მასალაზე დამზადებული ლინზა-კონცენტრატორები ზედაპირებიდან აირეკლავენ მზიდან მოსული ენერგიის 10 % მეტს. უფრო მაღალია არეკვლაზე დანაკარგები მინის ლინზა-კონცენტრატორების გამოყენების შემთხვევაში. ეს კი იმას ნიშნავს, რომ მზის ენერგიის საკმაოდ დიდი ნაწილი ვერ აღწევს ფოტოელექტრულ გარდამქმნელამდე და, შესაბამისად, მცირდება მზის ენერგიის ელექტრულ ენერგიად გარდაქმნის ეფექტურობა. იმისათვის, რომ ლინზა-კონცენტრატორების ეს ნაკლოვანება გამოვასწოროთ, საჭიროა შევამციროთ ლინზიდან არეკვლილი სინათლე იმ სპექტრარულ დიაპაზონში, რომლის მიმართადაც აქვს მაქსიმალური მგრძნობიაროობა მზის ენერგიის ფოტოელექტრულ გარდამქმნელს.

თანამედროვე ოპტიკაში ობიექტივების დამზადებისას ეს ნაკლოვანება საგრძნობლად სწორდება ლინზების განშუქოვნებით, რითაც იზრდება ობიექტივების შუქძალა. მზის ფოტოენერგეტიკაში ჩვენს მიერ მოძიებული მასალებიდან გამომდინარე მზის კონცენტრატორების შუქძალის გაზრდის შესახებ ინფორმაცია არ არსებობს. სტატიებში და პატენტებში საუბარია მხოლოდ ფოტოელემენტის შთანთქმის კოეფიციენტის გაზრდაზე. ჩვენი აზრით, ლინზა-კონცენტრატორების განშუქოვნება ისევე, როგორც ობიექტივების ლინზების შემთხვევაში, საკმაოდ გაზრდის მათ შუქძალას და, შესაბამისად, ფოტოვოლტური ბლოკის ეფექტურობას.

ლინზის განშუქოვნება, გულისხმობს მის ზედაპირზე თხელი ფირის ან რამდენიმე ფირის დაფენას. გამომდინარე ფირის მასალიდან, სისქიდან და რაოდენობიდან, შესაძლებელია შეირჩეს სინათლის ტალღის სიგრძის ის დიაპაზონი რომლისათვისაც არეკვლა იქნება მინიმალური. განშუქოვნებით ლინზიდან არეკვლის შემცირება ემყარება ინტერფერენციის მოვლენას. როდესაც მყარ ოპტიკურ ზედაპირზე დაფენილია n_1 გარდატეხის მაჩვენებლის მქონე თხელი ფირი (მაგალითად, სილიციუმის ორჟანგი), თუ ფირის სისქე დაცემული სხივის ტალღის სიგრძის მეოთხედია, მაშინ ფირის ზედა და ქვედა ზედაპირებიდან არეკვლილი სხივების ინტერფერენციის გამო (რადგან ისინი სხვადასხვა ფაზაშია) ერთმანეთს ჩააქრობენ და მათი ჯამური ინტენსივობა ნულის ტოლი გახდება.

აღნიშნულის განსახორციელებლად მინის ლინზებზე, გარდატეხის მაჩვენებლით $n = 1.5$, ჩვენს მიერ დაფენილი იქნა სამი ფენისაგან $SiO_2 – ZrO_2 – SiO_2$ შემდგარი განმაშუქებელი საფარი. მიღებული განშუქოვნებული ლინზა-კონცენტრატორი გამოიცადა ფოტოვოლტურ ბლოკში. ექსპერიმენტმა გვიჩვენა, რომ განშუქოვნებული ლინზა-კონცენტრატორების გამოყენებისას მიღებული ელექტრული სიმძლავრის ნაზრდი მნიშვნელოვანია და ის რამდენიმე პროცენტს აღწევს. აღნიშნული კვლევები ჩატარებული იქნა მინის ლინზაზე. ასევე მიმდინარეობს სამუშაოები ორგანული მინისაგან დამზადებული ლინზების განშუქოვნებისათვის, რისთვისაც საჭირო შეიქმნა ფირების ვაკუუმური დაფენის დანადგარის შემდგომი მოდერნიზაცია. რაც მალე დასრულდება და, სავარაუდოდ, გვექნება ორგანული მინისაგან დამზადებული განშუქოვნებული ლინზა კონცენტრატორები [3].

ჩვენს მიერ ჩატარებული კვლევების შედეგები საშუალებას იძლევა ფოტოვოლტური ბლოკისთვის კონცენტრატორის პროექტირებისას მინიმუმამდე იქნას დაყვანილი იმ სხივური ენერგიის დანაკარგები რომელიც კონცენტრატორის გავლით ეცემა ფოტოელემენტს.

დამოწმებანი

1. Ж. И. Алфёров, В. М. Андреев, В. Д. Румянцев. Тенденции и перспективы развития солнечной фотоэнергетики. ФТП,. 2004, 38, 8, 937-948.
2. ჯ. ავალიანი, თ. ხაჩიძე. ფოტოვოლტაჟის ბლოკი ახალი სქემით, სადაც ფოტოელემენტები განლაგებულია ერთ ღერძზე, ოპტიკური კონცენტრატორების ხაზოვან ფოკუსში. ენერგია, 2009, 1 (49), 27-29.
3. ი. ავალიანი, რ. ჩიქოვანი, თ. ხაჩიძე, ზ. ბერიშვილი. განშუქოვნებული ლინზა-კონცენტრატორების დამუშავება და დამზადება ფოტოვოლტაიკური ბლოკის ენერგოეფექტურობის გასაზრდელად. Georg. Eng. News, 2014, 1, 27-31.

INFLUENCE OF A MAGNETIC FIELD ON ELECTRICAL EFFECTS IN LiF CRYSTALS

M. V. Galustashvili, M. G. Abramishvili, F. Kh. Akopov,
D. G. Driaev, V. G. Kvatchadze, S. D. Tsakadze

I. Javakhishvili Tbilisi State University
E. Andronikashvili Institute of Physics
Tbilisi, Georgia
maxsvet@yahoo.com

Accepted September 9, 2015

Abstract

The study belongs to a new direction in the physics of plasticity, namely, spin micromechanics that studies microscopic spin-dependent processes which influence the mechanical properties of solids. There is studied the effect of a weak magnetic field ($B = 0.9$ T) on the processes related to the existence of charges on point and linear defects in alkali halide crystals, namely, on the polarization and depolarization of a LiF crystal upon local deformation (indentation). The phenomena observed, namely, the increase in the dislocation mobility and dislocation charge and high degree of polarization, which are dependent on the state of magnetically sensitive impurity, show that magnetic field causes the decomposition of impurity–vacancy complexes slowing-down a dislocation.

1. Introduction

The effect of a weak magnetic field on the real structure and the plasticity of nonmagnetic crystals (so called magnetoplastic effect (MPE)) is extensively studied beginning from 1980s [1 – 4]. The results appeared to be paradox, since additional energy $U_M = \mu_\beta B$ transferred by magnetic field (MF) to a paramagnetic defect in a diamagnetic material is negligible low (10^{-4} eV) as compared to the energy of thermal fluctuations $U_T \sim kT \sim 10^{-2}$ eV (μ_β is the Bohr magneton, B is the magnetic field induction, k is the Boltzmann constant, and T is the absolute temperature). The studies of independent research groups show that the physic-mechanical characteristics of diamagnetic materials such as the microhardness, the yield strength, the internal friction etc., are changed under action of a weak magnetic field. All the characteristics are determined by the amount and the state of the crystal defect structure and, first of all, the dislocation mobility.

An analysis of the results on MPE selected two groups of phenomena:

1) The in situ effects which are manifested in the plasticization (or hardening) of a crystal immediately during its exposure to a magnetic field. This phenomenon is due to a

change in the interaction between a moving dislocation and stoppers as a result of a spin-dependent transformation of the structure of impurity centers in the dislocation--stopper system.

This effect is clearly illustrated in **Figure 1** that presents our results on the deformation (compression) of a LiF single crystal in magnetic field $B = 0.7$ T.

2) The "magnetic memory" effects which take place after exposure to a magnetic field and are due to the spin-dependent evolution of the local structure of impurity defects (their aggregation or dispersion); in this case, the proportions of individual defects, their pairs, threes, and clusters are changed. The new state of the impurity system is retained during some time interval after the magnetic treatment and is observed as a change in the plastic (and other) properties of the material during subsequent tests (**Figure 2**).

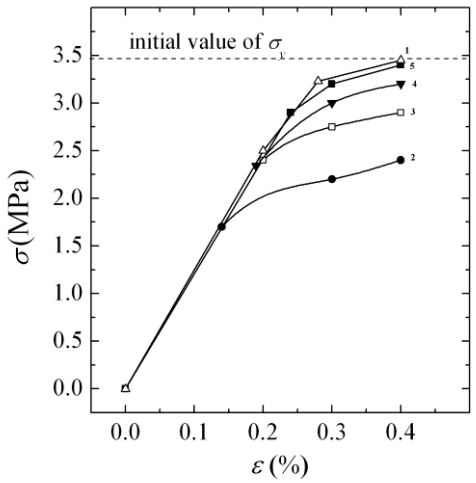

Figure 1. Stress–strain dependences of the LiF crystal measured at deformation (1) without MF and (2) in MF.

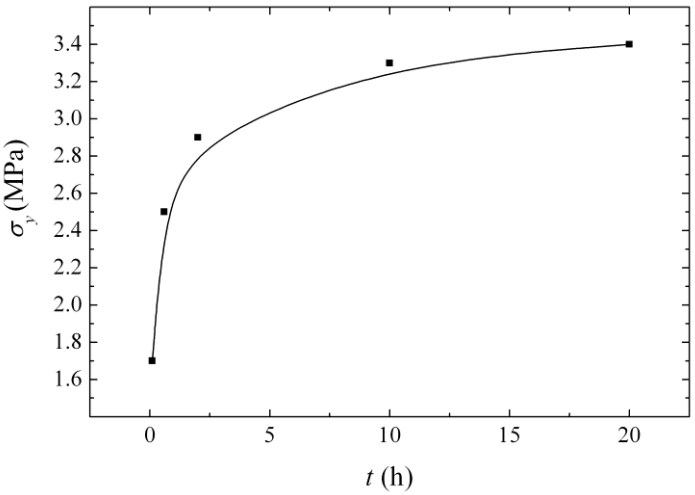

Figure 2. Recovery of yield strength σ_y as a function of time t after deformation in MF.

Our results for this group of the effects are given in **Table 1**.

Table 1.

	Yield stress σ_y, MPa	U_{max}, mV	Diagonal of indentation d, 10^{-6} m	Microhardness H, MPa
Reference sample	3.5	60	80.0	1390
After exposition in dc MF ($B = 0.9$ T)	1.6	126	86.5	1189

In alkali-halide crystals (AHC), defects, among them are dislocations, carry an electric charge. The charge influences the character of the motion and interaction of dislocations and leads, in particular, to polarization of the sample when applying a mechanical load (the Stepanov effect [5, 6]). The charge in AHC is transferred by edge dislocations and it is, mainly, due to an excess of vacancies of one sign in dislocation cores. The sign and the magnitude of the dislocation charge are determined not only by the impurity type and concentration, but also the

actions which can change its state. For example, it can be a preliminary exposure of a sample to a magnetic field.

This work is devoted to the study of the second-group effects which are immediately related to charged dislocations. Since both the process of charging dislocations and the process of establishing the charge equilibrium, namely, the screening of the dislocation charge by a shell of point defects of opposite sign (Debye–Huckel shell) are related to the impurity ion state, it can be suggested that the modification of the magnetically sensitive complexes under action of a magnetic field can influence these processes and be observed as a magnetic memory.

2. Experimental technique

According to the spectral analysis data, the LiF crystals under study contained an impurity of bivalent metal Mg^{++} ($1 \cdot 10^{-2}$ wt. %) and also other impurities (Fe, Ni, Al, Pb) in the concentration not higher than $\sim 10^{-4}$ wt. %; the samples have a relatively high ionic conductivity ($4 \cdot 10^{-16}$ Ohm^{-1} cm^{-1} at room temperature) and low concentration of hydroxyl ions OH^- (0.03 mol. %) that was found using the absorption infrared spectra. Both the factors demonstrate a higher concentration of cation vacancies which, as is known, provide a negative dislocation charge. Before each series of the measurements, the samples were annealed at 970 K for 2 h; then, they were quenched from this temperature in air and held at room temperature for 2 days. This treatment regime is most preferable to generate magnetically sensitive impurity-vacancy complexes which form during slow diffusion aggregation. All the measurements were carried out at room temperature.

The dislocation pictures of the initial sample and the sample subjected to various actions (indentation, exposure to magnetic and electric fields) were revealed by repeated chemical etching.

To measure the potential difference induced during indentation, the current silver-film current-removal electrodes were deposited on the opposite wide faces of the $5 \times 5 \times 1$ mm sample. A diamond Vickers pyramid was indented in the upper wide (001) face of the sample. The block scheme of the unit is shown in **Figure 3**.

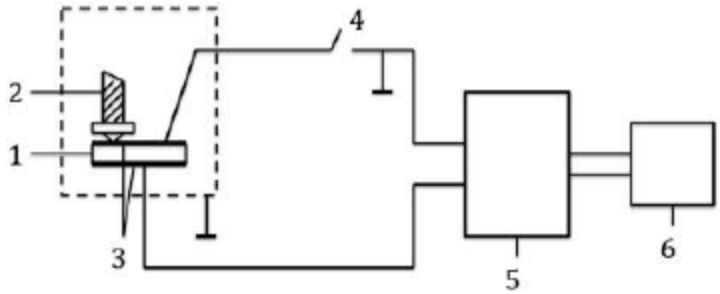

Figure 3. Block scheme of the unit for the measurement of the potential difference U during indentation: 1- sample, 2 – indenter, 3 – electrodes, 4 – switch, 5 – electrometric amplifier, and 6 – nanovoltmeter.

The magnetic treatment was the exposure of the samples to a dc magnetic field ($B = 0.9$ T) induced by a set of $SmCo_5$ plates for 30 min.

As is shown in [7], the magnetic plasticity of alkali-halide crystals is extremely sensitive to the parallel action of a weak electric field: the MPE intensity (in particular, the free path of

edge dislocations) increases exponentially with the electric field strength. Because of this, in a number of the experiments, an electric field to 1 kV / m was applied parallel to the magnetic field.

The response of the impurity structure to the magnetic field action was observed by changes in the indentation diameter d, microhardness H, the dislocation rosette rays length l, the electric signal U amplitude, and the yield strength σ of the sample. All results presented are average values of no less than 10 measurements of the above-mentioned parameters. The measurement error of potential difference U was less than 5 % and that of microhardness H was 3 %.

3. Experimental results and discussion

a) Electric stimulation of the magnetoplastic effect in LiF crystals by the "internal" electric field induced by one-directional displacement of charged dislocations

Figure 4 depicts the system of easy-glide planes in AHC and the scheme of arrangement of dislocation half-loops which form during indentation of the LiF crystal [8].

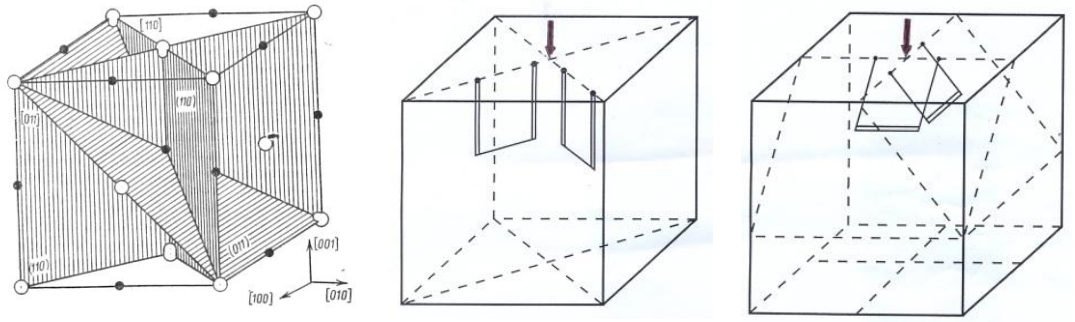

(a) (b) (c)

Figure 4. (a) {110} dislocation easy-glide planes in AHC; (b) and (c) dislocation loops in the planes oriented at angles of 90 and 45 °, respectively, to the indented upper (001) face (the arrow is an indenter and double line is the loop edge component).

In the case of simultaneous action of the magnetic $\vec{B}$ and the electric $\vec{E}_0$ fields, the fields were applied along a normal to the (001) face and parallel to one another ($\vec{B} \uparrow\uparrow \vec{E}_0$).

Along with the external electric field, there is an "internal" electric field induced by the charge transferred by dislocations which move from the indenter deep to the crystal (**Figure 5**).

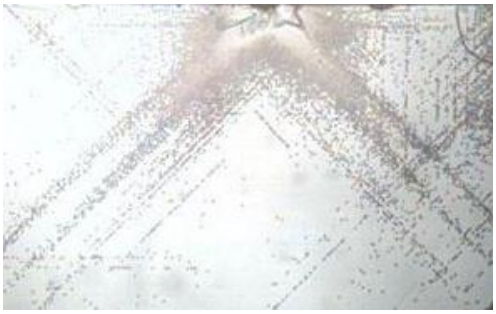

Figure 5. Dislocation "whiskers" transferring a charge in the sample volume in planes {110}[45].

Figure 6a shows the etching picture of the indented face of the initial sample. Short dislocation rosette rays l_1 (along <100>) and diagonal rays l_2 (along <110>) are the emergences of dislocation half-loops in slip planes $\{110\}_{90}$ (**Figure 4b**) and $\{110\}_{45}$ (**Figure 4c**), respectively.

The exposure only in MF insignificantly increases the dislocation mobility in planes $\{110\}_{45}$, and short rays length increases (**Figure 6b**). When the magnetic and electric fields are applied simultaneously, we can observe both the electric stimulation of the magnetoplastic effect and almost complete its suppression.

It turned out that the effect is determined by the polarity of "internal" field $\vec{E}$.

If $\vec{E}$ coincides with the polarity of external electric field $\vec{E}_0$ ($\vec{E}_0 \uparrow\uparrow \vec{E}$), we observe a sharp elongation of arms l_1, their broadening and curvature (**Figure 6c**), which demonstrates the intensification of the transverse slip in the "softened" crystal; i.e., resulting electric field $E' = E_0 + E$ stimulates the magnetoplastic effect. The electric field is assumed to increase the number of magnetically active pinning centers [7].

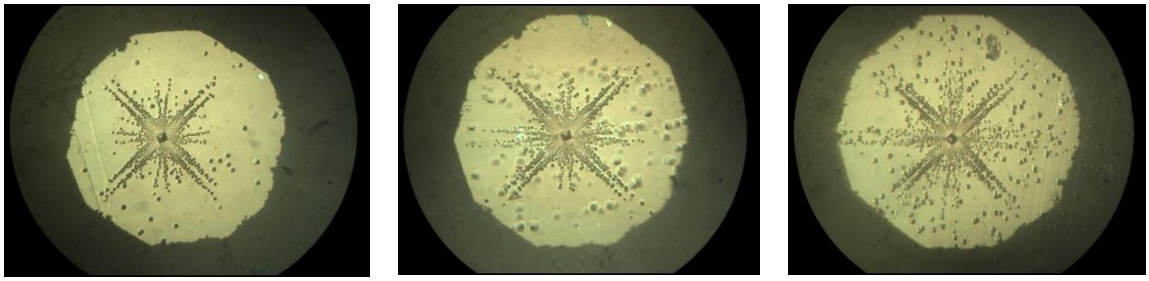

(a) (b) (c)

Fig.ure 6. Dislocation rosettes at the (001) face of LiF crystals: (a) reference ample, (b) after exposure to the magnetic field, (c) after the joint action of the magnetic and electric fields ($B = 0.9$ T and $E_0 = 0.5$ kV / m).

In the case when $\vec{E}_0 \uparrow\downarrow \vec{E}$ and resulting electric field $E' = E_0 - E$ in the sample is low (or approaches zero), the changes in the dislocation rosette are insignificant; i.e., the magnetoplasticity is suppressed by the external electric field that compensates the "internal" electric field completely or partially. This picture is observed at E_0 from ~ 0.3 to 0.7 kV / m. Hence, it can be concluded that, under conditions of this experiment, "internal" electric field E has a value within this interval (~ 0.5 kV / m).

A set of the experimental data made it possible to relate the linear density of dislocation charge q to the strength of "internal" electric field E using the method proposed in [5]: $q = E\varepsilon_0\varepsilon Sb/hL$, where ε_0 is the electric constant; ε is the permittivity; S is the indented face area; h is the indentation depth, b is the Burgers vector, and L is the length of the edge portion of the dislocation loop. The obtained value of q ($\sim 5 \cdot 10^{-13}$ C / m) agrees well with the available data on the real dislocation charge in AHC [5, 6].

b) Effect of magnetic field on the polarization of LiF crystals during microindentation

The crystal polarization during the local deformation proceeds for two stage (**Figure 7**): during indentation, the potential difference U increases sharply (stage I); thereafter, the signal continues slowly increase (stage II). Then, the depolarization takes place (right wings of the curves).

The crystal exposed to magnetic field has U_{max} almost twice as high as that observed in the initial (reference) sample. In addition, in the exposed sample, the stage II time is significantly larger and the stage is clearer.

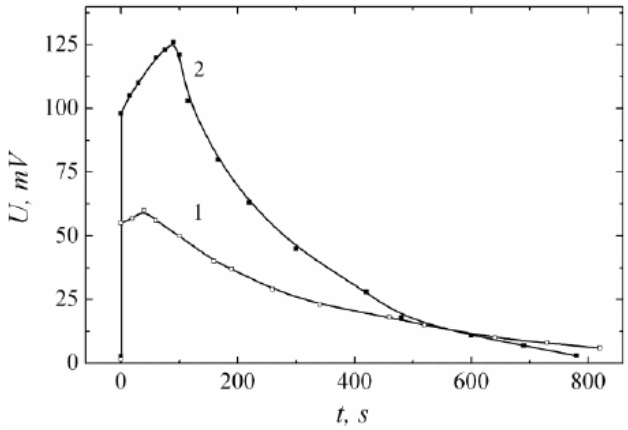

Figure 7. Dependence of potentials difference U on the time t after indentation: 1 - initial sample, 2 – exposed in dc MF ($B = 0.9$ T for 30 min).

As noted above, during impression of an indenter into face (001) of the sample, an electric charge (in our case, a negative charge) is transferred deep into the sample by the loop edge components $\{110\}_{45}$ (**Figure 5**), initiating nonequilibrium distribution of the charge and, correspondingly, potential difference U between the indented and the opposite faces. As the loops penetrate deep into the crystal, the signal increases and becomes maximal when the dislocation reaches the opposite face. The charge transfer is performed by sweeping-up of vacancies which are in the dislocation way in the slip plane and which migrate to the dislocation from the volume [5, 6]; in this case, the sweeping-up rate and, therefore, the charge value are dependent on the dislocation rate v.

During indentation of the LiF crystal, the dislocation rosette forms for two stage [9]. During the first stage (not more than 10 ms), 70 – 80 % of the rosette form, and other 20 – 30 % form for several units – tens seconds. Assuming that fast stage I and slow stage II of increasing signal U observed in the experiment correspond to these stages, we can estimate the rate of dislocations forming the dislocation rosette. In our experiments, at a load of 4.8 N, dislocations penetrate into the crystal to ~ 0.6 mm, of which ~ 0.45 mm correspond to the fast stage, and the remainder, to the slow stage.

It follows that, at the beginning of indentation (~ 10 ms) the dislocations move at a rates of $v \sim 5 \cdot 10^{-2}$ m / s. These high rates correspond to the overbarrier dislocation motion, during which dislocations do not interact to stoppers, and the dislocation penetration depth must be the same in both the initial and the exposed samples. Therefore, the higher potential difference measured in the magnetically-treated sample at stage I (**Figure 7**) can be only due to a higher value of the charge transferred by dislocations, which dislocations take trapping isolated cation vacancies (or vacancies from impurity–vacancy dipoles) meeting in its slip plane.

In the exposed crystal, the slow stage II time is about 100 s (**Figure 7**), and the signal continuously increases in this time. This seems to be due to farther displacements of the dislocations during stage II of forming the rosette (20 – 30 %). In this case, the dislocation rate

is of $\sim 2 \cdot 10^{-6}$ m / s, as can be easily estimated using the above-mentioned data. At such low rates that are close to the migration rate of cation vacancies, the vacancies have time to migrate to the dislocation from the volume. This process leads to the increase of the charge transferred by dislocations and corresponding increase in U . In addition, as is shown in Section (a), after the exposure to MF, the path of loop edge components $\{110\}_{45}$ deep into the crystal increases; in this case, dislocations deliver the charge closer to the bottom current-removal face, which also increases U .

The easy dislocation glide and the increase in the dislocation charge in the exposed sample show that a magnetic field favors the decomposition of impurity complexes, stopping dislocations, into weaker (finer) isolated vacancies, impurity--vacancy dipoles, and small-sized clusters.

The descending wings in both dependences $U(t)$ in **Figure 7** correspond to the depolarization that takes place as a result of migration of charged particles in the dislocation electric field. An analysis of the depolarization curves shows that relaxation time τ of this process is 310 s for the initial sample and 200 s for the sample exposed to MF. According to [10], $\tau \sim 1/\sigma$, where σ is the conductivity of the sample. On the other hand, according to the Nernst–Einstein relation [11], at given temperature and charge carriers of one kind, $\sigma \sim n$, where n is the charge carrier concentrations (in our samples, cation vacancies). Thus, $\tau \sim 1/n$, and the comparison of the above-mentioned relaxation times shows that the cation vacancy concentration in the exposed sample is higher by half than that in the initial sample.

4. Conclusions

a) We observed the effect of the "internal" electric field induced by the charge transfer by dislocations moving during indentation on the magnetoplasticity of the LiF crystal. It is shown that the electric stimulation and the electric suppression of the magnetoplasticity take place in magnetic field $B = 0.9$ T in the dependence on the magnitude and the direction of an external electric field with respect to those of the "internal" electric field. Based on the experimental data, we estimated the "internal" electric field strength and calculated the linear density of the dislocation charge.

b) The time dependences of the polarization of the deformed LiF crystal made it possible to reveal the two-stage character of the process, and the stages are characterized by different rates of dislocation motion ($5 \cdot 10^{-2}$ and $2 \cdot 10^{-6}$ m / s). The dislocation rates determine the mechanism of charging dislocations and, as a result, the value of the transferred charge and the measured potential difference. An analysis of the polarization and depolarization curves of the LiF crystal made it possible to separate the role of free cation vacancies in these processes among the multitude of defects, namely, decomposition products of impurity–vacancy complexes initiated by magnetic field, and to conclude that their concentration increases by a factor of almost 1.5 under action of a dc MF ($B = 0.9$ T for $t = 30$ min).

Acknowledgment

The work was supported by Shota Rustaveli National Science Foundation (Project # FR/144/6–130/13).

References

1. V. I. Alshits, E. V. Darinskaya, M. V. Koldaeva, E. A. Petrzhik. In: Dislocations in Solids, 14 (Ed. J. P. Hirth). 2008, Amsterdam, Elsevier, 333.
2. Yu. I. Golovin. Phys. Solid State, 2004, 46, 7723.
3. R. B. Morgunov. Phys. – Uspekhi, 2004, 174 , 132.
4. A. L. Buchachenko. JETP, 2006, 129, 909.
5. R. W. Whitworth. Adv. Phys., 1975, 24, 203.
6. N. A. Tyapunina, E. P. Belozerova. Phys. – Uspekhi, 1988, 156, 683.
7. V. I. Al'shits, E. V. Darinskaya, M. V. Koldaeva, E. A. Petrzhik. JETP Lett., 2008, 88, 428.
8. Yu. S. Boyarskaya, D. Z. Grabko, M. S. Kats. Physics of Microindentation Processes. 1986, Shtiintsa.
9. Yu. I. Golovin, V. I. Ivolgin, V. V. Korenkov, A. I. Tyurin, Phys. Solid State, 1997, 39, 318.
10. A. N. Gubkin. Physics of Dielectrics. 1982, Moscow, Vysshaya shkola.
11. A. Lid'yard. Ionic Conductivity of Crystals. 1982, Moscow, Inostrannaya literature.

თუთიისა და კადმიუმის შეთვისება რძემჟავა ბაქტერიების მიერ

ნ. რჩეულიშვილი [1], ე. კაკაბაძე [1], ნ. ჭანიშვილი [1], ა. რჩეულიშვილი [2]

[1] გ. ელიავას სახელობის ბაქტერიოფაგიის,
მიკრობიოლოგიისა და ვირუსოლოგიის ინსტიტუტი
თბილისი, საქართველო
archeuli@gmail.com
[2] ე. ანდრონიკაშვილის ფიზიკის ინსტიტუტი
თბილისი, საქართველო
rcheuli@gmail.com

მიღებულია 2015 წლის 9 სექტემბერს

ანოტაცია

რძემჟავა დუღილის სასურსათო პროდუქტები ფართოდ გამოიყენება ყველა ასაკის მოსახლეობის კვებაში, განსაკუთრებით – ბავშვებში. აღნიშნული პროდუქტები მდიდარია ცილებით, ნახშირწყლებით, ცხიმებით, სასარგებლო ელემენტებით (Ca, Mg, Se და ა.შ.), ვიტამინებით (ვიტამინი B12, რიბოფლავინი და ა.შ.). აქედან გამომდინარე, ძალზე აქტუალურია მაღალი ხარისხის, რძემჟავა დუღილის სასურსათო პროდუქტების წარმოება. რძემჟავა დუღილის ბაქტერიები წარმოადგენს ძირითად რგოლს რძემჟავა პროდუქტების მიღების პროცესში. კვლევის ობიექტს წარმოადგენს რძემჟავა პროდუქტიდან გამოყოფილი რძემჟავა ბაქტერიები. კვლევის მიზანია რძემჟავა დუღილის ბაქტერიების გამოყოფა მაწვნიდან, მათი გამოზრდა, მათ მიერ ლითონების (კადმიუმი, თუთია) შთანთქმის უნარის შესწავლა და ამ ლითონების ზეგავლენის შესწავლა ლითონების იონების (20 მკგ / მლ) ურთიერთქმედება ხდებოდა სხვადასხვა დროის განმავლობაში (12, 20, 36, 44 და 68 სთ). გამოყოფილ იქნა ლაქტოზის ფერმენტაციის უნარის მქონე ბაქტერიული შტამები. ჩატარდა მათი სახეობრივი იდენტიფიკაცია და დახასიათება. ბაქტერიების მიერ მძიმე მეტალების აბსორბციის უნარის შესასწავლად შერჩეულ იქნა *Lactobacillus spp.* E11 K3 და *Streptococcus thermofiles* 2N K2 ბაქტერიული შტამები, რომლებმაც დადებითი შედეგი მოგვცა ბაქტერიოცინებზე. ანალიზები ლითონების შემცველობაზე ჩატარდა ატომურ აბსორბციული სპექტრომეტრიის გამოყენებით.

რძე შეიცავს უამრავ საკვებ ნივთიერებას, რომლებიც აკმაყოფილებს ორგანიზმის მოთხოვნას (კალციუმი, მაგნიუმი, სელენი, რიბოფლავინი, ვიტამინი B12, ვიტამინ B5). იგი საკმარისი ოდენობით არ შეიცავს რკინას და ფოლიუმის მჟავას, რომელიც მონაწილეობს ბავშვის ზრდის პროცესში [1]. მაწონი – რძემჟავა პროდუქტია, რომელიც გავრცელებულია კავკასიაში. ამზადებენ ძროხის, თხის, ცხვრის და კამეჩის რძისგან და, ასევე, მათი ნარევისგან [2].

რძემჟავა ბაქტერიები (Lactic Acid Bacteria – LAB) წარმოადგენს გრამ-დადებითი ბაქტერიების ჯგუფს, რომლებიც არ წარმოქმნიან სპორებს, წარმოადგენენ ანაერობულ ან მიკროაეროფილურ კოკებსა და ჩხირებს, რომელებიც ნახშირწყლების ფერმენტაციის შედეგად წარმოქმნიან რძემჟავას, როგორც ძირითად საბოლოო პროდუქტს. არიან მჟავატოლერანტული მირკოორგანიზმები. რძემჟავა დუღილის ბაქტერიების მოთხოვნილება საკვების მიმართ სახეობა-სპეციფიკურია. ეს განსაკუთრებით აღსანიშნავია რძემჟავა ჩხირებში. ლაქტობაცილებისთვის საჭირო საკვებ ნივთიერებებში შედის ვიტამინები, ასევე სხვადასხვა ელემენტები, განსაკუთრებით, სპილენძი, მანგანუმი, ნატრიუმი, ფოსფორი, რკინა.

რძემჟავა ბაქტერიები ნახშირწყლების რძემჟავად გარდაქმნას, ნახშიროორჟანგის და ასევე, სხვა ორგანული მჟავების წარმოქმნის პროცესს ახორციელებს ჟანგბადის მცირე რაოდენობის თანაობისას. ყველა რძემჟავა დუღილის ბაქტერია ენერგიის წყაროდ საჭიროებს ნახშირწყლოვანი სუბსტრატის კომპლექსს. მათ მიერ წარმოებული რძემჟავა ეფექტურად აინჰიბირებს სხვა ბაქტერიების ზრდას, რომლებიც სასურსათო პროდუქტის გაფუჭებას იწვევენ. ფერმენტირებულ პროდუქტებში არასასურველი მიკროფლორის ინჰიბირებას იწვევს გარემოს pH მკვეთრი დაცემა, რაც განპირობებულია რძემჟავა ბაქტერიების ცხოველქმედების შედეგად წარმოქმნილი მჟავიანობით. ზოგიერთი სხვა ბაქტერია, მაგალითად, *Leuconostoc citrovorum L. Dextranicum, Streptococcus lactis*, *S. Cremis* & *liquefaciens* and *Brevibacterium* სახეობები მნიშვნელოვან როლს ასრულებს რძის პროდუქტების ფერმენტაციის პროცესში [3].

რძეში შემავალ ნახშირწყლებს შორის, ძირითადი შემადგენელია ლაქტოზა. რძემჟავა ბაქტერიები ლაქტოზის ფერმენტაციის შედეგად წარმოქმნიან რძემჟავას, რაც ხელს უწყობს pH დაწევას და შესაბამისად პროდუქტის შემჟავებას. ეს პროცესი შედედებას უდევს საფუძვლად. რძემჟავა დუღილის ბაქტერიები (LAB) ახდენენ შაქრების ფერმენტაციას და წარმოქმნიან რძემჟავას. მათ აქვთ უნარი, შეამციროონ pH შაქრიდან მჟავას წარმოქმნით, ეს ხელს უწყობს საბოლოო პროდუქტის სტაბილურობისა და უვნებლობას, ხელს უშლის პათოგენების ზრდას. მაშასადამე, რძემჟავას წარმოქმნა გადამწყვეტ როლს თამაშობს. რძემჟავა ბაქტერიები აწარმოებენ ლაქტოზის დუღილს და სწორედ ეს პროცესია ძირითადი ბიოქიმიური საფუძველი რძემჟავა პროდუქტების მიღებისას.

რძის პროდუქტები წარმოადგენს ძალზე ხელსაყრელ საშუალებას სასარგებლო მიკროორგანიზმების მომხმარებლისათვის მიწოდებაში. ნაწლავებში ამ ორგანიზმების ოპტიმალური ბალანსი უმნიშვნელოვანესია ჯანმრთელობის შენარჩუნების ასპექტში. გარკვეული ბაქტერიები, რომლებიც დადებითად მოქმედებენ აღნიშნული ბალანსის შენარჩუნებაზე იწოდებიან, როგორც პრობიოტიკები. პრობიოტიკები, რომლებიც გამოიყენება სასქესო-საშარდე გზებში არ არის გვერდითი ეფექტების მატარებელი, განსხვავებით ანტიბიოტიკებისგან. პრობიოტიკები ქმნიან ისეთ მიკრობულ გარემოს, რომელიც უკეთ უმკლავდება პათოგენებს [4, 5].

თუთია სასიცოცხლოდ მნიშნელოვანი კვალური ელემენტია ადამიანის, ცხოველისა და მცენარისთვის. ადამიანის ორგანიზმში იგი შედის 300-ზე მეტი ენზიმის შემადგენლობაში და გადამწყვეტ როლს ასრულებს უამრავი ბიოლოგიური ფუნქციის შესრულებისას. Zn აღმოჩენილია ორგანიზმის ყველა ორგანოში, ქსოვილებში, ძვლებში, სითხეებსა და უჯრედებში. თუთია სასიცოცხლოდ მნიშნელოვანია უჯრედების ზრდისა და გაყოფისათვის. Zn განსაკუთრებით მნიშნელოვანია ორსულობის პერიოდში ნაყოფის ზრდისთვის, რომლის უჯრედებიც სწრაფად იყოფა. Zn ხელს უწყობს

თანდაყოლილი ანომალიების პრევენციას. იგი მნიშნელოვან ელემენტს წარმოადგენს ზრდის აქტივაციაში - სიმაღლე, წონა და ძვლების განვითარება ბავშვებში.

ყველა მინერალს შორის, Zn ყველაზე ეფექტურია ადამიანის იმუნური სისტემისთვის. თუთიის დაბალი შემცველობა იწვევს T-უჯრედების დასუსტებას და რაოდენობის კლებას. შესუსტებული T-ლიმფოციტები ვეღარ ამოიცნობენ და ვეღარ ებრძვიან ინფექციებს. თუთიის დონის გაზრდა ეფექტურია პნევმონიის, დიარეისა და სხვა ინფექციების წინააღმდეგ.

თუთიის მიღების რეკომენდებული რაოდენობა იცვლება ასაკთან და ფიზიოლოგიურ სტატუსთან ერთად და მერყეობს შემდეგ ფარგლებში: 5-დან 18 მგ-მდე დღეში [6].

კადმიუმი წარმოადგენს ტოქსიკანტს ცხოველებში, რაც სიმახინჯეებს და სხვა უარყოფით ეფექტებს იწვევს. ცხოველებზე კვლევებმა აჩვენა, რომ Cd ხანგრძლივი ექსპოზიციის (ინჰალაციის) შედეგად იზრდება ფილტვის სიმსივნის რისკი. US Environmental Protection Agency მოახდინა კადმიუმის კლასიფიკაცია ჯგუფში B1 – შესაძლო კანცეროგენი ადამიანისთვის.

კადმიუმი გარემოში ხვდება საწვავის წვის შედეგად, ასევე თუთიის, სპილენძისა და ტყვიის მადნის დნობის შედეგად. არამწეველებისთვის კადმიუმის ექსპოზიციის ძირითად წყაროს საკვები წარმოადგენს. სიგარეტის კვამლი კადმიუმის მნიშნელოვან წყაროს წარმოადგენს. მწეველები დაახლოებით ორჯერ მეტ კადმიუმს იღებენ, ვიდრე არამწეველები.

არსებობს უამრავი მონაცემი, რომლის მიხედვითაც Zn მოხმარების გაზრდამ შესაძლოა შეამციროს Cd-ის აკუმულაცია და ტოქსიკურობა [7].

Cd ძალზე მცირე რაოდენობაც კი დიდი ხანი რჩება ორგანიზმში, განსაკუთრებით, თირკმელებში. როდესაც ამ ორგანოში კადმიუმის კონცენტრაცია გარკვეულ დონეს მიაღწევს, თავს იჩენს პროტეინურია თირკმელებში. კადმიუმი ურთიერთქმედებს თუთიასა და სპილენძთან და უკავშირდება ცილებს, რომლებიც დაკავშირებული არიან აღნიშნულ ელემენტებთან [8].

არ არსებობს მეთოდი, რომელიც გვეხმარება საკვები პროდუქტების კადმიუმისგან "გაწმენდაში". სამწუხაროდ, კადმიუმის შემცველობა საკვებ პროდუქტებში თანდათან იზრდება. მკვლევარების მიერ შეფასებულ იქნა რძემჟავა ბაქტერიების მიერ წყალხსნარების კადმიუმისგან გაწმენდის უნარი. შედეგი საკმაოდ საყურადღებო აღმოჩნდა [9].

ჩატარებულ იქნა კვლევა *Lactobacillus plantarum* CCFM8610, რომელსაც კადმიუმის დაკავშირების უნარი აღმოაჩნდა კადმიუმით გამოწვეული მწვავე ტოქსიკურობის მქონე თაგვებში. შედეგებმა აჩვენა, რომ CCFM8610 "ნამკურნალევ" თაგვებში შემცირდა ნაწლავის მიერ კადმიუმის აბსორბცია, აკუმულაცია, შემცირდა თირკმლისა და ღვიძლის ოქსიდაციური სტრესი და გაუმჯობესდა ღვიძლის ჰისტოპათოლოგიური ცვლილებები [10].

აღმოჩნდა, რომ სპეციალური რძემჟავა ბაქტერიები მნიშვნელოვნად წმენდენ წყალს კადმიუმისა და ტყვიისაგან. ყველაზე ეფექტურად ეს პროცესი განახორციელა შემდეგმა შტამებმა: *Bifidobacterium longum* 46, *Lactobacillus fermentum ME3* და *Bifidobacterium lactis Bb12* [11].

ლაქტობაცილების კულტივაციისთვის გამოყენებული იყო MRS-ბულიონი. ნატრიუმის აცეტატი და ამონიუმის ციტრატი ინჰიბაციას უკეთებს სტრეპტოკოკების, ობისა და სხვა მიკროორგანიზმების ზრდას აღნიშნულ საკვებ არეზე. ინოკულირებული

საკვები არის ინკუბაცია რეკომენდირებულია 35 – 37 °C 18 – 72 სთ განმავლობაში [12]. ქიმიური შემადგენლობა დაწვრილებით მოცემულია წყაროებში [13]. ლაქტოკოკების კულტივაციისთვის გამოყენებული იყო M-17-ბულიონი. საკვები არეები დამზადებული იყო მწარმოებლის მიერ მოწოდებული სპეციფიკაციის მიხედვით. ქიმიური შემადგენლობა დაწვრილებით მოცემულია წყაროებში [14].

ანალიზებისათვის აღებული იყო Perkin Elmer ფირმის Zn და Cd საწყისი ხსნარები 1 მგ / მლ კონცენტრაციებით. მათგან ვამზადებდით სხვადასხვა კონცენტრაციების ეტალონურ ხსნარებს. ბაქტერიული შტამებისათვის ვამზადებდით თუთიის წყალხსნარს (1 მგ / მლ). კადმიუმი გავხსენით გლიცინის 0.4 M ხსნარში (1 მგ / მლ).

ბულიონებისა MRS და M17 ჩამოსხმა მოხდა მაკარტნის 40 მლ სინჯარებში. ლითონების საბოლოო კონცენტრაცია საკვებ ნიადაგში შეადგენდა 20 ppm. გარდა ამისა, საკონტროლოდ აღებული იყო 10 ცალი MRS-ბულიონის შემცველი (ლითონის გარეშე) სინჯარა და 10 M17-ბულიონის შემცველი (ლითონის გარეშე) სინჯარა.

შემდეგ მოხდა საკვლევი ბაქტერიული შტამების შეტანა სინჯარებში: *Lb. spp.* E11 K3 – MRS, ხოლო *S. thermophiles* 2N K2 – M17 ბულიონიან სინჯარებში. ბაქტერიული შტამების შემცველი ყველა სინჯარა მოთავსდა თერმოსტატში 37°C-ზე, სადაც ხდებოდა ბაქტერიების გამოზრდა. ბაქტერიების გამოზრდა ხდებოდა 12 სთ, 20 სთ, 36 სთ, 44 სთ, 68 სთ. დროის განმავლობაში. ამის შემდეგ ვახდენდით სინჯარებიდან ბაქტერიული მასების გამოყოფას. ინკუბირებული ბაქტერიული შტამის შემცველი მაკარტნის სინჯარები ვორტექსდებოდა (VWR ™ Mini Vortexer), შემდეგ შიგთავსი გადაიტანებოდა ცენტრიფუგის 45 მლ სინჯარებში და ხდებოდა ცენტრიფუგირება 40 წთ განმავლობაში 10000 rpm (Thermo IEC MIcromax RF). სუპერნატანტები გადაიტანებოდა საწყის ჭურჭელში და იზომებოდა მათი pH. მიღებული ნალექი ჯერ ირეცხებოდა (სტერილური გამოხდილი წყლით; ცენტრიფუგირებით 40 წთ, 10000 rpm), შემდეგ კი გადაიტანებოდა ერთჯერად პეტრის ფინჯნებზე და ბიოუსაფრთხოების კაბინაში (Labconco, model # 3601024) ხდებოდა მათი გაშრობა სტერილური ჰაერის ნაკადის ქვეშ. გაშრობის შემდეგ მოხდა ნალექების (უჯრედოვანი მასა) აწონვა და გადატანა მაკარტნის სინჯარებში.

ვახდენდით ბაქტერიული მშრალი მასების სველი დანაცრებას (გახსნა) აზოტმჟავაში. ამისათვის ნიმუშებიან სინჯარებში დავამატეთ 1 მლ HNO_3. ამგვარ მდგომარეობაში ნიმუშები დაყოვნდა 3 დღე, რის შემდეგაც მოხდა ნიმუშების გაცხელება დუღილის ტემპერატურამდე. ნიმუშების თხევად მდგომარეობაში გადაყვანის შემდეგ თითოეულ სინჯარას (ნიმუშს) დაემატა 10 მლ ბიდისტილირებული წყალი.

ანალიზები ჩატარდა თანამედროვე ატომურ-აბსორბციული სპექტრომეტრით “Analist 800” (Perkin Elmer) [15] ე. ანდრონიკაშვილის ფიზიკის ინსტიტუტში. გამოყენებული იყო აცეტილენ–ჰაერის ალი. ექსპერიმენტის შედეგად მიღებული შედეგები მოცემულია **ნახაზებზე 1 – 3**.

ნახაზზე 1 წარმოდგენილი გრაფიკიდან ჩანს, რომ აღნიშნული ბაქტერია Cd^{+2} ითვისებს გაცილებით მეტს ვიდრე Zn^{+2} (დაახლოებით 2-ჯერ მეტს). ლითონის იონების შეთვისება ინტენსიურია ბაქტერიების ზრდის პირველ საათებში. ბაქტერიების ზრდის 10 საათის შემდეგ ხდება ბაქტერიების მიერ მეტალის იონების გამოდევნა ორგანიზმიდან. ბაქტერიების ზრდის 35 საათის შემდეგ აღარ ხდება ბაქტერიების მიერ მეტალის იონების გამოდევნა ორგანიზმიდან.

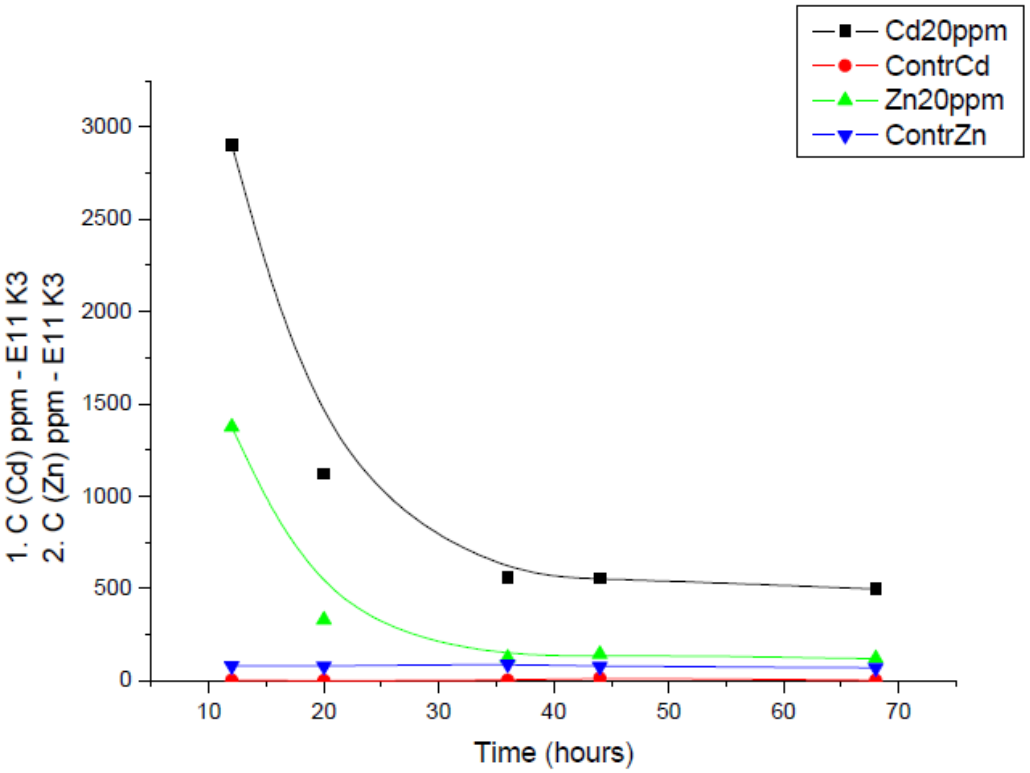

ნახაზი 1. შთანთქმული Zn^{+2} და Cd^{+2} რაოდენობა (ppm), შესაბამისად, Zn^{+2} საკვებ არესა და Cd^{+2} საკვებ არეში გაზრდილი *Lb. spp.* E11 K3-ბაქტერიების მიერ.

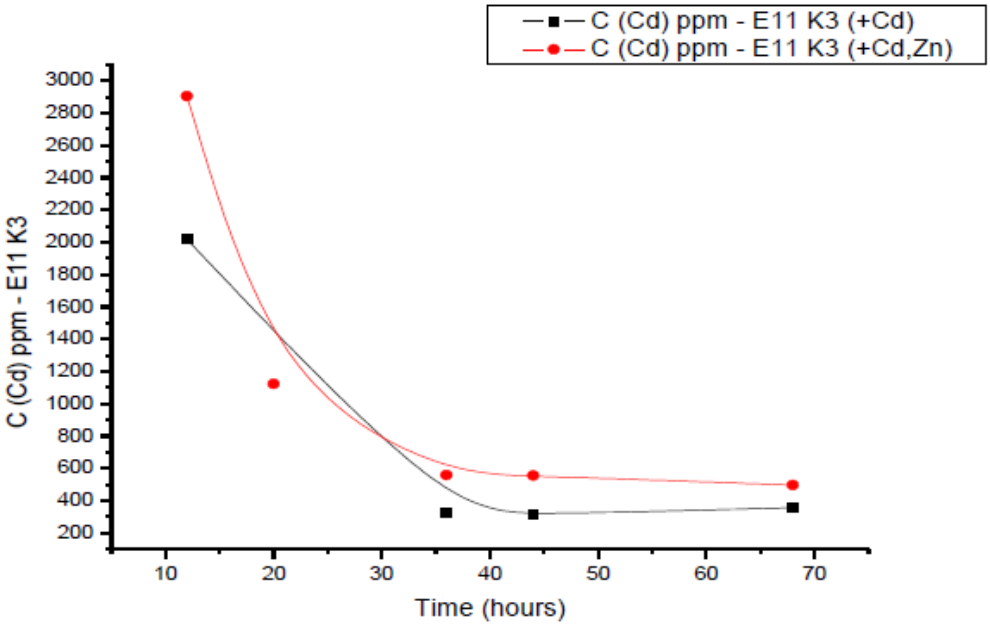

ნახაზი 2. შთანთქმული Cd^{+2} რაოდენობა (ppm) Cd^{+2} და Cd^{+2} + Zn^{+2} საკვებ არეში გაზრდილი *Lb. spp.* E11 K3-ბაქტერიების მიერ.

ნახაზზე 2 წარმოდგენილი გრაფიკიდან ჩანს, რომ საწყის ეტაპზე Cd^{+2}-ის კონცენტრაცია Cd^{+2}+Zn^{+2}-იან საკვებ არეში გაზრდილ ბაქტერიებში უფრო მეტია, ვიდრე მხოლოდ Cd^{+2}-იან საკვებ არეში კულტივირებულ ბაქტერიებში. აღნიშნული გვაფიქრებინებს, რომ **Zn^{+2}**-ის არსებობა საკვებ გარემოში ხელს უწყობს Cd^{+2}-ის შეთვისებას ბაქტერიების მიერ ბაქტერიების გამოზრდის საწყის პერიოდში. თუმცა საერთო ჯამში, განსხვავება დიდი არ არის.

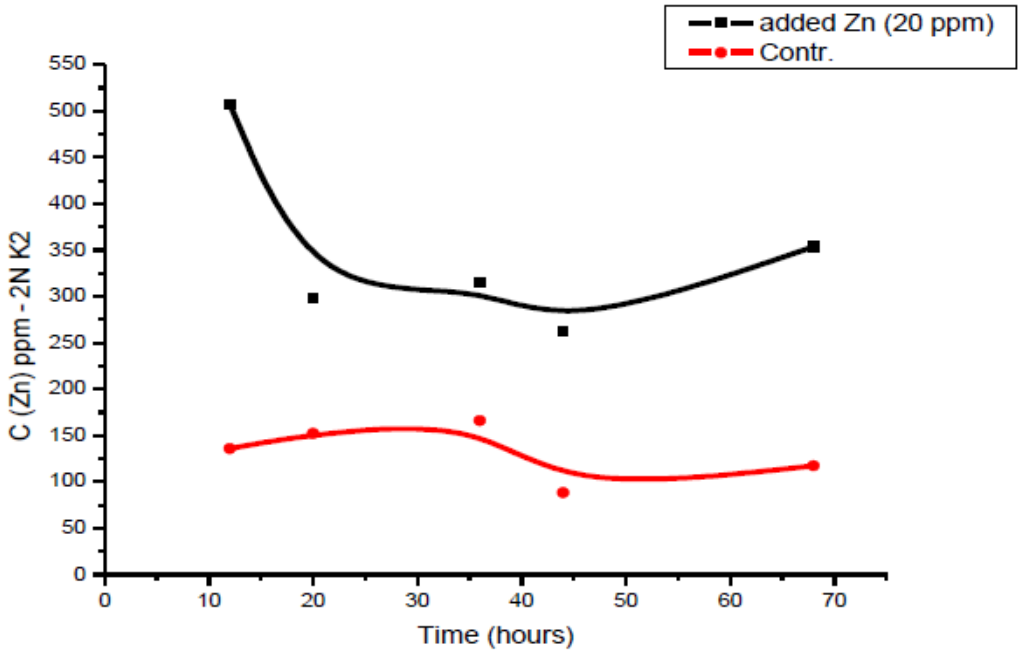

ნახაზი 3. შთანთქმული Zn^{+2} რაოდენობა (ppm)
Zn^{+2} საკვებ არეში გაზრდილ *S. Thermophiles*
2N K2 მიერ და მისი კონტროლთან შედარება.

როგორც **ნახაზიდან 3** ჩანს, შეინიშნება **Zn^{+2}** რაოდენობის კლების ტენდენცია ბაქტერიების გამოზრდის დროის გაზრდასთან ერთად. თუთიის ასეთი რაოდენობა საკონტროლო ნიმუშებში (საკვებ გარემოში არ არის შეტანილი თუთია) აიხსნება იმით, რომ (საკვები გარემო თვითონ შეიცავს თუთიას (1.56 მკგ / მლ).

შედეგებმა აჩვენა, რომ *Lb. spp.* E11 K3 ტიპის ბაქტერიებს გააჩნიათ Cd^{+2} ათვისების უკეთესი უნარი Zn^{+2} შედარებით (დაახლოებით 2-ჯერ). მეტალის იონების შეთვისება ინტენსიურია ბაქტერიების ზრდის პირველ საათებში. ბაქტერიების ზრდის 10 საათიდან 35 საათამდე შემდეგ ხდება ბაქტერიების მიერ მეტალის იონების გამოდევნა ორგანიზმიდან. 35 საათის შემდეგ მეტალების კონცენტრაცია ბაქტერიებში აღარ იცვლება.

საწყის ეტაპზე Cd^{+2} კონცენტრაცია Cd^{+2} + Zn^{+2} საკვებ არეში (საკვებ არეში დამატებული იყო როგორც Zn ასევე Cd) გაზრდილ ბაქტერიებში (*Lb. spp.* E11 K3) უფრო მეტია, ვიდრე მხოლოდ Cd^{+2} საკვებ არეში კულტივირებულ ბაქტერიებში. აღნიშნული გვაფიქრებინებს, რომ **Zn^{+2}** არსებობა საკვებ გარემოში ხელს უწყობს Cd^{+2} შეთვისებას ბაქტერიების მიერ ბაქტერიების გამოზრდის საწყის პერიოდში. თუმცა საერთო ჯამში, განსხვავება დიდი არ არის.

Cd^{+2} ტოქსიკური მოქმედება თრგუნავს ბაქტერიული შტამის *S. thermophiles* 2N K2 ზრდას.

საკვებ არეში Zn^{+2} თანაობა ხელს უწყობს *Lb. spp.* E11 K3 შტამის მიერ Cd^{+2} აბსორბციას, კერძოდ, Zn^{+2} ხელს უწყობს კადმიუმის შეთვისებას აბსორბციის საწყის ეტაპზე (12 სთ), ხოლო შემდეგ კადმიუმი გამოიდევნება უჯრედებიდან. თუმცა ნარჩუნდება იმაზე დიდი რაოდენობით (537.85 ppm), ვიდრე მხოლოდ Cd^{+2} საკვებ არეში გაზრდილ ბაქტერიებში (339.59 ppm).

Lb. spp. E11 K3-ბაქტერიისთვის საკვებ არეში შეტანილი Zn რაოდენობა არ არის ტოქსიკური კონცენტრაცია, რის გამოც კონტროლისა და Zn საკვებ არეში გაზრდილი ბაქტერიული მასები ერთმანეთის ტოლია.

როგორც ჩანს შეინიშნება Zn^{+2} რაოდენობის კლების ტენდენცია *S. thermophiles* 2N K2 ტიპის ბაქტერიების გამოზრდის დროის გაზრდასთან ერთად. თუთიის ასეთი რაოდენობა საკონტროლო ნიმუშებში (საკვებ გარემოში არ არის შეტანილი თუთია) აიხსნება იმით, რომ საკვები გარემო თვითონ შეიცავს თუთიას (4 მმკგ / გ)

დამოწმებანი

1. V. Capozzi, P. Russo, M. T. Dueñas, P. López, G. Spano. Lactic acid bacteria producing B-group vitamins: a great potential for functional cereals products. Appl. Microbiol. & Biotechnol., 2012. 96, 6, 1383.
2. ი. მალხაზოვა. მაწვნის დედოებიდან გამოყოფილი ენდემური რძემჟავა ბაქტერიების გენოტიპური და ფენოტიპური დახასიათება (ბიოლ. მეცნ. კანდ. სამეც. ხარისხის მოსაპ. წარმოდ. დისერტაცია). 2006, თბილისი, გ. ელიავას სახ. ბაქტერიოფაგ., მიკრობიოლ. და ვირუსოლ. ინსტ.
3. Food and Agriculture Organization: http://www.fao.org/docrep/x0560e/x0560e10.htm
4. G. E. Gardiner, Ch. Heinemann, M. L. Baroja, A. W. Bruce, D. Beuerman, J. Madrenas, G. Reid. Oral administration of the probiotic combination Lactobacillus rhamnosus GR-1 and L. fermentum RC-14 for human intestinal applications. Int. Dairy J., 2002, 12, 2. 191.
5. Sh. Hekmata, H. Soltania, G. Reid. Growth and survival of Lactobacillus reuteri RC-14 and Lactobacillus rhamnosus GR-1 in yogurt for use as a functional food. Innov. Food Sci. & Emerging Technol., 2009, 10, 2. 293.
6. A. Leonardi, S. Zanoni, M. de Lucia, A. Amaretti, S. Raimondi, M. Rossi. Zinc Uptake by Lactic Acid Bacteria. 2013. http://dx.doiorg./10.5402/2013/312917
7. M. M. Brzóska, J. Moniuszko–Jakoniuk. Interactions between cadmium and zinc in the organism. Food & Chem.Toxicol., 2001, 39, 10, 967.
8. D. W. Fassett. Cadmium: Biological effects and occurrence in the environment. Ann. Rev. Pharmacol., 1975, 15, 1, 425.
9. T. M. Halttunen, C. Collado, H. el-Nezami, J. Meriluoto, S. Salminen. Combining strains of lactic acid bacteria may reduce their toxin and heavy metal removal efficiency from aqueous solution. Lett. Appl. Microbiol., 2008, 46, 2, 160.
10. Q. Zhai, G. Wang, J. Zhao, X. Liu, F. Tian, H. Zhang, W. Chen. Protective effects of Lactobacillus plantarum CCFM8610 against acute cadmium toxicity in mice. Appl. & Environ. Microbiol., 2013, 79, 5, 1508.

11. T. Halttunen, S. J. Salminen, R. Tahvonen. Rapid removal of lead and cadmium from water by specific lactic acid bacteria. Int. J. Food Microbiol., 2007,114, 1, 30.
12. http://himedialabs.com/TD/M641.pdf
13. http://himedialabs.com/TD/M1164.pdf
14. http://www.himedialabs.com/TD/M1029.pdf
15. http://www.perkinelmer.com/Catalog/Product/ID/N3050417

CALCULATION OF THE BINDING ISOTHERMS FOR Zn(II)_ AND Cd(II)_ C-PHYCOCYANIN COMPLEXES BY UV / VISIBLE SPECTROSCOPY

E. Gelagutashvili

I. Javakhishvili Tbilisi State University
E. Andronikashvili Institute of Physics
Tbilisi, Georgia
eterige@gmail.com

Accepted September 14, 2015

Abstract

The interaction of Cd(II) and Zn(II) ions with C-phycocyanin (C–PC) from *Spirulina platensis* has been studied by UV / Visible spectroscopy at 10 mM ionic strength. The absorbance variation with increase of metal ions concentrations was used to construct the half-reciprocal. The logarithm of binding constants and Gibbs free energy for Cd(II)_ and Zn(II)_C-phycocyanin complexes were estimated from this plot.

Introduction

The nanoparticles can play a topmost role in the field of nanomedicine such as health care and medicine diagnostic and screening purposes, drug delivery systems, antisense and gene therapy applications, and tissue engineering and expectations of nanorobots configuration [1]. However, up to date, most microorganisms that have been reportedly used for synthesis of nanoparticles are pathogenic to either plants and / or humans [2]. So over the years, researchers have turned to nonpathogenic microorganisms. *Spirulina platensis* and *Nostoc sp.* are two blue–green microalgae (cyanobacteria), is an important representative of these microorganisms. *Spirulina* has several pharmacological activities such as antimicrobial, anticancer, metallic-protective (prevention of heavy-metal poisoning against Cd, Pb, Fe, Hg), as well as immunostimulant and antioxidant effects due to its rich content of protein, polysaccharide, lipid, essential amino and fatty acids, dietary minerals and vitamins [3].

Spirulina is multicellular filamentous blue green algae. The chemical composition of *Spirulina platensis* reflects its potential in human food and as a source of natural products. One of basic protein of *Spirulina platensis* is C-phycocyanin (C–PC), which use as fluorescent protein probe in living cells [4]. *Spirulina* biopolymers used in nanostructured scaffolds [5]. Phycocyanin, a blue pigment associated with the chlorophyll of this organism, exhibits antioxidant and anti-inflammatory properties [6]. Antibacterial and anti-inflammatory effects are critical when scaffolds are used in humans [5].

Cadmium is a potent toxicant to bacteria, algae and fungi. *Spirulina platensis* has a high tolerance to cadmium and it effectively applied to phytoremediate waste water [7]. Cd has been shown to change the binding characteristics of the SP1 transcription factor Zn-finger to DNA [8].

Inhibition of DNA repair is an important genotoxicity mechanism of Cd. This may occur when Cd(II) complete with Zn(II) for a common binding site on enzymes involved in DNA synthesis [9]. In spite of the fact, that there is significant increase in the interest on studying the effect of metals with microorganisms and their components, the mechanism of metal ions interaction with them is essentially unknown.

In this work the interaction of Cd(II) and Zn(II) ions with C-phycocyanin from *Spirulina platensis* at 10 mM ionic strength has been studied by UV / Visible spectroscopy.

Materials and methods

Stock solutions of Cd(II) and Zn(II) were prepared by dissolving $CdSO_4$ and $ZnSO_4$ in deionized water. $CdSO_4$ and $ZnSO_4$ were analytical grade. C-phycocyanin preparations were obtained by the method given in Ref. [10]. To determine the degree of purity of the samples, spectrophotometric (wavelengths 250 – 750 nm) and electrophoretic methods were used. The concentration of C–PC was determined by ultraviolet-visible spectroscopy using a value of $\varepsilon_{\lambda = 615\ nm} = 279\ 000\ M^{-1}\ cm^{-1}$ for the absorption coefficient. The purity of the protein was assessed from the ratio of absorbances at $\lambda = 615$ nm and $\lambda = 280$ nm ($A_{615} / A_{280} \geq 4$). Absorption titration was performed in the 620 nm, by adding metals solutions to C–PC and recording the spectrum after each addition. Fitting of absorption titration has been performed model, where two extinction coefficients ε_b and ε_f are used for a chromophore bound to C–PC and free in solution [11]. The intrinsic binding constant K was determined from the plot of $D / \Delta\varepsilon_{ap}$ vs D, where D is the concentration of metal, $\Delta\varepsilon_{ap} = [\varepsilon_a - \varepsilon_f]$ and $\Delta\varepsilon = [\varepsilon_b - \varepsilon_f]$. The apparent extinction coefficient ε_a, is obtained by calculating A_{obs} / [C –PC], A_{obs} optical density, ε_b and ε_f correspond to the extinction coefficient of the bound form of C–PC and the extinction coefficient of free C–PC, respectively. The data were fitted to Eq. (1), with a slope equal to $1 / \Delta\varepsilon$ and a Y intercept equal to $1 / \Delta\varepsilon K$. ε_b was determined from $\Delta\varepsilon$ and K was obtained from the ratio of the slope to the Y intercept:

$$1 / \Delta\varepsilon_{ap} = D / \Delta\varepsilon_{ap} + 1 / \Delta\varepsilon K. \quad (1)$$

For biosorption isotherms studies, the concentration of C-phycocyanin was constant, while the metal concentration in each case was varied. The initial metal concentration was varied within the range $10^{-6} – 10^{-4}$ M. The C–PC concentration was 10^{-4} M. All the experiments were carried out at 23 °C, at ionic strength 10 mM.

Results and discussions

The absorption spectra of C–PC in the presence of Cd(II) and Zn(II) ions are shown in **Figures 1A** and **B**, and in Figures **2C** and **D**, respectively. The electron absorption spectra of C–PC in the presence of increasing amounts of the metal ions showed strong reduction of the peak intensities (hypochromicity). The absorbance variation at $\lambda = 620$ nm with increase of metal ions concentrations was used to construct the half-reciprocal plot [11, 12].

The logarithm of binding constants was estimated from this plot. They are equal to: for Cd(II) $pK = 3.41$, for Zn(II) $pK = 3.24$. Correlation coefficient R is more, than 0.9 in both cases.

The binding constant K was used to calculate the Gibbs free energy $\Delta G^0 = -RT\ln K$, where R is the gas constant and T is the temperature by Kelvin. Respectively Gibbs free energy ΔG^0 for Cd(II) 4.64 kcal / mol, for Zn(II) 4.4 kcal / mol. The results of the study indicate that calculated values of ΔG^0 are characteristic for hydrogen bonds.

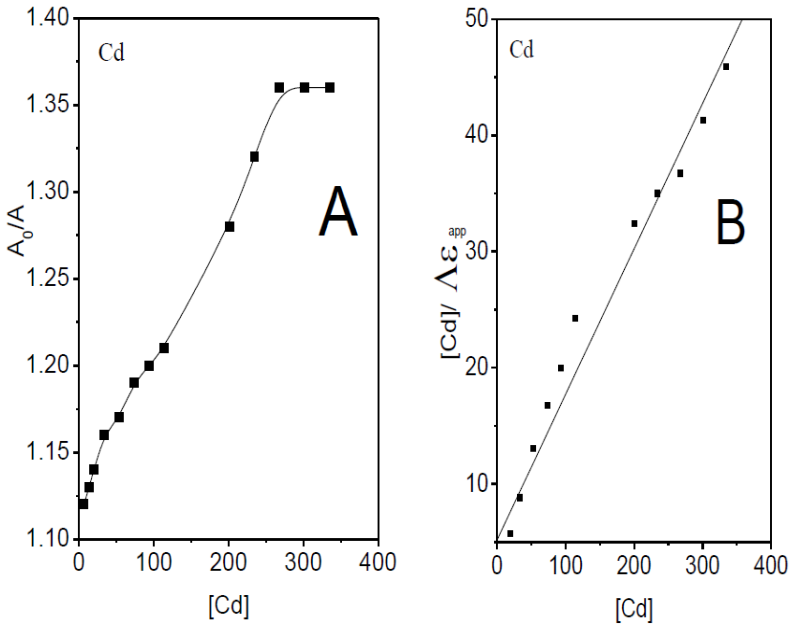

Figure 1. Plot of the absorption titration data at 620 nm, demonstrating the saturation of binding of C–PC to Cd(II) (A). Half-reciprocal plot of C–PC binding with Cd(II) ions as determined from the absorption titration data(B) ([Cd] / $\Delta\varepsilon_{ap}$ vs [Cd]).

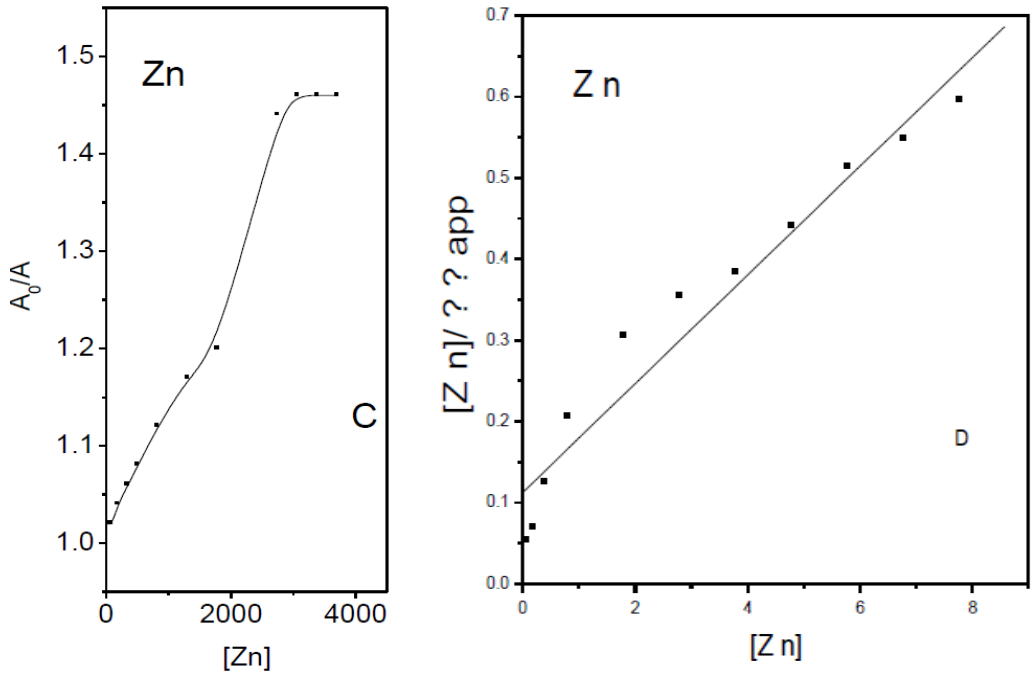

Figure 2. Plot of the absorption titration data at 620 nm, demonstrating the saturation of binding of C–PC to Zn(II) (C). Half-reciprocal plot of C–PC binding with Zn(II) ions as determined from the absorption titration data (D) ([Zn] $\Delta\varepsilon_{ap}$ vs [Zn]).

Comparison of these results for Cd(II) and Zn(II) ions shown, that Cd more effectively bound to C-phycocyanin, than Zn. These results are in good agreement with our previous data [13], where interaction of metal ions with C-phycocyanin were studied using thermodynamic methods (equilibrium dialysis) at various ionic strength (50, 20, 2 mM) and using optical methods (absorption and fluorescence titration),when C-PC was dissolved in water. Difference between binding constants using equilibrium dialysis may be explained effect of ionic strength on the metal-C-PC binding constants. In [14] was studied influence of ionic strength on Cd(II)_C-PC interaction using equilibrium dialysis and was shown also effect of ionic strength. The dependence of metal-C-PC complex stability on ionic strength of solution shows the competition of Na(I) and metal ions for binding sites.

Comparison of present data for Cd_ and Zn_C-phycocyanin complexes, with results using the same method , when C-phycocyanin is dissolved in water shown, that effect of ionic strength is insignificant. The reason may be, that the absorption titration is generally impeded because of relatively small changes in absorption upon binding of metal complexes to proteins. These changes of absorption are especially small for ligands which have less affinity for C–PC.

References

1. T. Kubik, K. Bogunia–Kubik, M. Sugisaka. Curr. Pharmaceu. Biotechnol., 2005, 6, 17-33.
2. A. Ahmad, P. Mukherjee, D. Mandal, S. Senapati, M. Khan, R. Kumar, M .Sastry.vJ. Am. Chem. Soc., 2002, 124, 12108-12109.
3. S. M. Hoseini, K. Khosravi–Darani, M. R. Mozafari. Mini Rev. Med. Chem., 2013, 13, 1231-1237.
4. A. J. Tooley, Y. A. Cai, A. N. Gleser. Proc. Natl. Acad. Sci., 2001, 98, 10560 10565.
5. M. G. de Morais, B. da Silva Vaz, E. G. de Morais, J. A. Vieira Costa. Biomed. Res. Int., 2014, Article ID 762705, 1-9 .
6. V. B. Bhat, K. M. Madyastha. Biochem. & Biophys. Res. Commun., 2001, 285, 262-266.
7. N. Rangsayatorn, E. S. Upatham, M. Kruatrachue, P. Pokethitiyook, G. R. Lanza. Environ. Pollution, 2002, 119, 45-53.
8. H. J. Thiesen, C. Bach. Biochem.& Biophys. Res. Commun., 1991, 176, 551-557.
9. T. G. Rossman, N. K. Roy, W. C. Lin. Lars. Sci. Publ., 1992, 118, 367-375.
10. F. W. J. Teale, R. E. Dale. Biochem. J., 1976, 116, 161-165.
11. H. J. Li, D. M. Crothers. J. Mol. Biol., 1969, 39, 461-477.
12. A. M. Pyle, J. P. Rehmann, C. V. Kumar, N. J. Turro, J. K. Batton. J. Am. Chem. Soc., 1989, 111, 3051-3057.
13. E. Gelagutashvili. Am. J. Biomed. & Life Sci., 2013, 1, 12-16.
14. E. Gelagutashvili, A. Khizanishvili, E. Ginturi, N. Kuchava, N. Bagdavadze, A. Rcheulishvili, L. Mosulishvili. J. Biolog. Phys. & Chem., 2007, 7, 103-106.

TRANSFORMATIONS IN MAGNETIC FLUIDS CAUSED BY ACTIVITIES OF MAGNETIC NANOPARTICLES

K. Kotetishvili, N. Kobalia, G. Chikhladze

Georgian Technical University
Department of Engineering Physics
Tbilisi, Georgia
ketinooo@hotmail.com
gurchix@gmail.com

Accepted September 18, 2015

Abstract

The paper deals with transformations fixed in magnetic fluids due to definite activities of magnetic nanoparticles inside them. It is shown that in the case of absence of fixed flux the spin velocity and components $\hat{m}_x$ and $\hat{m}_y$ are space invariant, while at the fixed flux the spin velocity together with $\hat{m}_x$ and $\hat{m}_y$ varies with varying of the width of y. It is stated as well that in magnetic fluids the magnetization increases in the spiral form, because during its rotation it itself becomes responsible for movement of the fluid with the spin velocity $\omega_z \neq 0$, which itself changes the magnetization.

Introduction

In MRI three kinds of magnetic flux density are applied: the first – strong B_0 field in z-direction, the second – B_1 transverse radio-frequency wave and the third – space-coded fields (G gradients) in z-directions as well. In the paper low (sick) fields of $0.10 - 0.35$ T are considered. In such kind of low fields the fluid is unable to reach saturation and nano-particles revolve in additional rotating magnetic field. The magnetization in magnetic fluids increases in spiral form.

Magnetization in sick fields. Basic equations

Under an action of a magnetic field the expression for relaxation of the magnetization for magnetic fluids is given as follows

$$\frac{\partial \vec{\mathrm{M}}}{\partial \mathrm{t}} + \vec{\upsilon} \cdot \nabla \vec{\mathrm{M}} - \vec{\omega} \times \vec{\mathrm{M}} + \left(\frac{1}{\tau}\right)\left(\vec{\mathrm{M}} - \vec{\mathrm{M}}_{\mathrm{sat}}\right) = 0, \quad (1)$$

which at the same time provides as the magnetization, as the re-orientation of given field. $\vec{v}$ is the vector of linear velocity of the magnetic fluid, while $\vec{\omega}$ the vector of spin velocity of the magnetic fluid and τ – its time of relaxation [1, 2].

The left-hand-side of (1) is straightly dependent on $\vec{v}$ velocity of the linear motion and on $\vec{\omega}$ angular (spin) velocity. The equation of state in the magnetic field possesses the time constant characteristic for the equilibrium magnetization, described by the following expression:

$$\frac{1}{\tau} = \frac{1}{\tau_B} + \frac{1}{\tau_N}, \tag{2}$$

τ_B and τ_N being Brown's and Neel's times of relaxation, respectively, given as follows:

$$\tau_B = \frac{3V_h\mu_C}{kT},$$

$$\tau_N = \tau_0 e^{\frac{k\alpha V_p}{kT}}, \tag{3}$$

V_h being the hydrodynamic volume of nano-particles in m^3, while μ_C – the dynamic viscosity of the given fluid (ns / m^2).

If the number of particles in a magnetic fluid is fixed (for example, being located at its surface), the only Neel's relaxation is in action, while Brown's relaxation is absent.

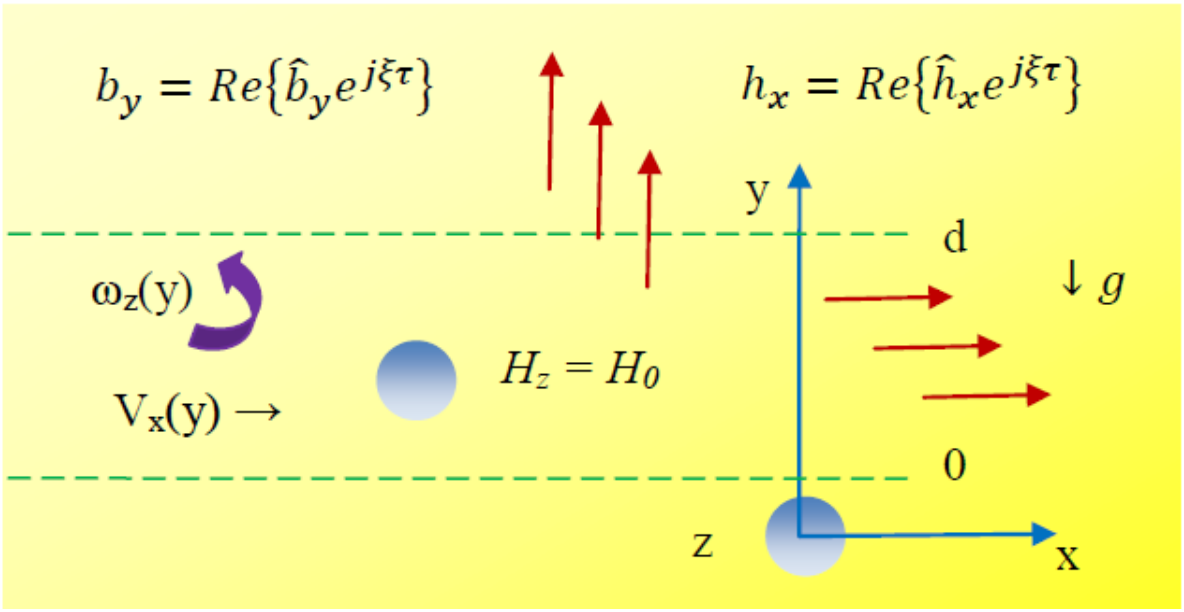

Figure 1. Flux of a magnetic field.

In **Figure 1** the flux of a magnetic fluid is presented in the fixed area *(y = 0, y = d)*. The trended flux is pumped by H_0 magnetic field acting in z direction and by *x* directed sinusoidal magnetic field of the sick signal with the complex amplitude $\hat{h}_x$ as well, as in y direction by the sinusoidal magnetic fluctuation density of the sick signal with the complex amplitude $\hat{b}_y$. In x and *y* directions the components of the magnetic field vary due to the sinusoidal law with ξ frequency. $v_x(y)$ velocity is directed along *x*-axis, while the spin velocity $\omega_z(y)$ – along *z*-axis and both are y dependent. As it is seen in **Figure 1**, the velocity of the flux bleeding is directed only along x-axis while time-average spin velocity – only along *z*-direction.

Taking into account the distribution of magnetic field strengths (densities) as they are given in figure, $\vec{\imath}_x$ and , $\vec{\imath}_z$ are space homogeneous due to corresponding zero space derivatives.

According to Ampere's law, when the conductivity is zero $\left(\vec{J}=0\right)$ or the change in current density differs from it $\left({}^{\partial\vec{D}}/_{\partial t}\neq 0\right)$, the field strength should be zero and given by (4) surely (see [3]):

$$\vec{\nabla}\times\vec{H}=\vec{J}+\frac{\partial\vec{D}}{\partial t}=0. \tag{4}$$

Gauss's law regulates densities of the fixed magnetic flux along i_y:

$$\vec{\nabla}\cdot\vec{B}=\frac{\partial b_x}{\partial x}+\frac{\partial b_y}{\partial y}+\frac{\partial(B_0)}{\partial z}=0. \tag{5}$$

Then ${}^{\partial b_y}/_{\partial y}=0$, when ${}^{\partial b_x}/_{\partial x}={}^{\partial(B_0)}/_{\partial z}=0$. Based on this survey we may conclude that b_y and h_x should be constant in space and independent on y, while h_y may be dependent on y, when y itself depends on m_y.

The density of total instantaneous magnetic fluctuations $\vec{B}$, total instantaneous magnetic field $\vec{H}$ and total instantaneous magnetization $\vec{M}$ are given as follows

$$\left.\begin{aligned}\vec{B}&=Re\left\{\left(\hat{b}_x(y)\vec{\imath}_x+\hat{b}_y\vec{\imath}_y\right)e^{j\xi t}\right\}+B_0\vec{\imath}_z,\\ \vec{H}&=Re\left\{\left(\hat{h}_x\vec{\imath}_x+\hat{h}_y(y)\vec{\imath}_y\right)e^{j\xi t}\right\}+H_0\vec{\imath}_z,\\ \vec{M}&=Re\left\{\left(\hat{m}_x(y)\vec{\imath}_x+\hat{m}_y(y)\vec{\imath}_y\right)e^{j\xi t}\right\}+M_0\vec{\imath}_z,\end{aligned}\right\} \tag{6}$$

while the relation between $\vec{B}$, $\vec{H}$ and $\vec{M}$ is given in the following way:

$$\vec{B}=\mu_0\left(\vec{H}+\vec{M}\right), \tag{7}$$

Here $\hat{m}_x$, $\hat{m}_y$ are functions of the spin velocity ω_z given by the following expressions:

$$\hat{m}_x=\frac{M_0}{H_0}\cdot\frac{\left(j\xi\tau+1+\frac{M_0}{H_0}\right)\hat{\tilde{h}}_y-(\omega_z\tau)\frac{\hat{\tilde{b}}_y}{\mu_0}}{(j\xi\tau+1)\left(j\xi\tau+1+\frac{M_0}{H_0}\right)+(\omega_z\tau)^2},$$

$$\hat{m}_x=\frac{M_0}{H_0}\cdot\frac{(\omega_z\tau)\hat{\tilde{h}}_y+(j\xi\tau+1)\frac{\hat{\tilde{b}}_y}{\mu_0}}{(j\xi\tau+1)\left(j\xi\tau+1+\frac{M_0}{H_0}\right)+(\omega_z\tau)^2}. \tag{8}$$

Conclusion

Analysis shows that in the case of absence of fixed flux the spin velocity and $\hat{m}_x$ and $\hat{m}_y$ are space invariant. When the flux is fixed the spin velocity together with $\hat{m}_x$ and $\hat{m}_y$ varies with varying of the width of y. The second term in (1) contributes nothing, as to the velocity of the flux along x and at ${}^{\partial}/_{\partial z}$ magnetization is zero. In magnetic fluids the magnetization increases in the rotating (spiral) form, as to at the rotation it itself is responsible for movement of the fluid with the spin velocity ω_z, differing from zero, which itself changes the magnetization.

References

1. D. G. Giancoli. Physics. Principles with Application. 1995, New Jersey.
2. K. M. Koch, P. B. Brown, D. L. Rothman, R. A. de Graaf. Sample specific diamagnetic and paramagnetic passive shimming. J. Magn. Reson., 2006, 182, 1, 66-74.
3. K. V. Kotetishvili, G. G. Chikhladze. Linearization of Langevin's equation in magnetic fluids. Nano Studies, 2013, 7, 225-228.

LIGHT INDUCED LINEAR POLARIZATION IN SPIROPYRAN DOPED NEMATIC LIQUID CRYSTAL MIXTURE

L. V. Devadze, Ts. I. Zurabishvili, N. O. Sepashvili, G. Sh. Petriashvili

Georgian Technical University
V. Chavchanidze Institute of Cybernetics
Tbilisi, Georgia
devadze2005@yahoo.com

Accepted September 23, 2015

Abstract

Photochromic properties of the spiropyran doped nematic composite were investigated. It was shown that when the nematic host has a high order parameter the composite exhibits a dichroic behavior which is a light controllable. High optical polarization of the composite promises the introducing of a novel optical data storage medium, which enables to record the light characteristics such as wavelength, polarization and phase, with high optical density.

Introduction

Photochromic compounds are the subject of active research due to their outstanding photosensitive properties and potential applications in the fields of optoelectronics and photonics. These applications rely on the ability of photochromic molecules to change color as well as other physical and chemical properties upon illumination. Spiropyrans (SPs) are photochromic materials that have been extensively investigated due to their potential applications in devices such as light-sensitive eyewear [1], information recording and processing, including three-dimensional recording, which is based on large section of two-photon absorption of SPs [2, 3], optical memory [4, 5], molecular devices [6, 7], nonlinear device components and optical switches [8 – 14], light activated drug delivery systems [15]. SPs can be transformed into a merocyanine (MC) state upon UV irradiation, and it also can be reversed to a SP state by irradiating with visible light or by heating. More specifically, the carbon-oxide bond of the SP is cleaved when it is transformed into an MC state upon UV irradiation. The MC state not only converts to a polar molecule, but it also turns dark purple in color. Since the interconversion between closed SPs form and their open MC form involves a large molecular rearrangement, some compounds of this class does not exhibit photochromism in a solid-state reaction [16]. To extend the range of commercial applications, SPs are typically included in polymer matrices [17 – 19] and monolayer films [20 – 23].

In this paper, we report a SP doped nematic liquid crystal composite that exhibit a light controllable spatial-temporal linear polarization. Due to the unique properties of liquid crystal materials, liquid crystal doped SP system is assumed to have many advanced optical attributes

quite different from those of isotropic liquids, semiconductors and polymer doped ones. Further, SP doped liquid crystals present additional features: an extremely high solubility of SP in the liquid crystal host, which can vary in the range 1 – 4 % (by weight) without destroying the liquid crystalline phase, a high orientation order parameter for SP molecules provided by the spatial orientation of the liquid crystal host molecules.

Results and discussions

As the initial nematic materials were utilized commercially available and certified compounds MLC–7023, ZLI–1939, ZLI–4788, BL–006, BL–036, BL–038 (all from Merck), and as the photochromic material – 1',3',3'-Trimethyl-6-nitro-1',3'-dihydrospiro[chromene-2,2'-indole] (from Sigma-Aldrich), Figure 1.

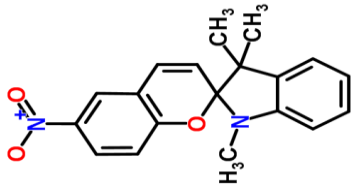

Figure 1. Schematic structure of spiropyran.

The photo switching behavior and absorption spectra of the composites were investigated with a UV / VIS Spectrometer at room temperature. For light-induced generation of the MC, the samples were irradiated at the absorption band of the SP, using a 100 W mercury lamp HG 100 AS, (Jelosil, Italy), with the 290 – 400 nm bandpass filter and for the reverse switching to the non-colored form of SP, was utilized 540 – 630 nm bandpass filter. The distance from the lamp to the sample was about 12 cm. The intensity of the light at the samples was about $I = 0.12$ mW / cm^2. In order to investigate the optical properties of the composites, we built a planar optical cell using two glass plates. The spacing between the substrates was adjusted to 20 μm by using of Mylar films. To obtain homogeneous alignment, we already coated by spin coating with polyvinyl alcohol solved in water and rubbed in one direction by a rubbing machine. After that the cell was filled with SP doped nematic mixture, by capillarity in isotropic phase. To compare the solubility of SP in the different nematic hosts and determine the maximum of the non-saturated concentration, we have prepared next mixtures: 1. X%ZLI–1939+Y% SP, 2. X%MLC–7023 +Y% SP, 3. X%ZLI–4788+Y% SP, 4. X%BL–036+Y% SP, 5. X%BL–038+Y% SP, and 6. X%BL–006+Y% SP, where X = 99 – 96 % and Y = 1 – 4 % (by wt.).

During the experiments, we found that the solubility of the SP strongly depends on the host mixture. For example, the maximum of the non-saturated solubility of SP in MLC–7023 was just 1 %, whereas in BL–036 and BL–038 it increases up-to 4 % by weight. Another interesting result we have observed was the batochromic shifting of the absorption bands of MC. The maximum of the absorption peak of mixture ZLI–1939 / MC was located at $\lambda = 552$ nm in the optical spectrum, while for the MLC–7023 / MC, this maximum corresponds to $\lambda = 656$ nm, giving the spectral shifting $\Delta\lambda = 104$ nm. To demonstrate the UV light stimulated absorption dependence on the expose time, we selected and investigated the following mixture: 96 % wt. BL–036 + 4 % wt. SP. **Figure 2** shows the conversion of the SP molecules from close to open ones, when irradiated by UV lamp with different time intervals. In this picture is demonstrated the significant, time-dependent, increasing of the absorption of MC upon UV irradiation.

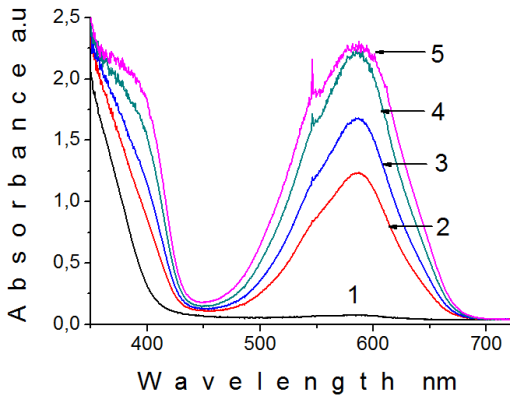

Figure 2. The effective absorption dependence on the expose time for mixture 96 % wt. BL–036 + 4 % wt. SP, upon exposure to UV lamp. Curve 1 corresponds to the absorption before irradiation. By the numbers of 2, 3, 4 and 5 are given the absorption curves with 5, 10, 20 and 40 s of exposure times, respectively.

For the calculation of light intensity (in percentages) outgoing from the optical cell with different UV exposure time, we used the general equation which gives the relationship between absorbance and transmittance:

$$A = 2 - \log_{10} \% T, \quad (1)$$

(hence $\% T = 10^{2-A}$), where A and T, respectively, are the absorbance and transmittance. The calculated conversion units between A and I% are listed in the **Table 1**.

Table 1.

Exposure time T, s	Absorbance A at λ = 585 nm	Transmittance I% at λ = 585 nm
0	0.05	89.12
5	1.23	5.89
10	1.68	2.09
20	2.22	0.60
40	2.26	0.55

As shown from **Table 1**, before the UV expose the light transmittance of the sample was equal to $I_1 = 89.12$ % and significantly drops down to $I_2 = 0.55$ %, after 40 s to the exposure. This switching behavior is reversible. After the UV exposure, the optical cell turns itself from the dark to the transparent condition during one hour, or this process can be stimulated by light or temperature. We have performed the light induced back switching by using of 540 – 630 nm band pass filter and during 12 s the sample became transparent when the light intensity of the sample was about $I = 0.34$ mW / cm^2. Next experiment we have carried out was to induce a linear dichroism (LD) in the nematic / MC composition. It is known that LD is the difference in absorption of the light linearly polarized parallel and perpendicular to an orientation axis and can be calculated using the following equation:

$$\mathrm{LD} = A_{\parallel} - A_{\perp}. \quad (2)$$

As regards the dichroic ratio this is defined by the next equation:

$$D(\lambda) = A_{\parallel} / A_{\perp}. \quad (3)$$

Where $A_{\parallel}$ and $A_{\perp}$ are the absorptions of the long dichroic axis of the anisotropic material parallel and perpendicular to the plane of polarization respectively. To demonstrate the dichroic properties of the sample, at first we irradiated optical cell with UV lamp during 2 s. After that we measured the absorption in two orthogonal orientations with respect to the polarizer. In **Figure 3**, is shown the absorbance of the sample in two orthogonal orientations, parallel and perpendicular to the transmitting axis of the polarizer. By using of Eq. (2), we calculated the linear dichroism of the composition which was equal to LD = 1.08, and according to the Eq. (3), the dichroic ratio was calculated as $D(\lambda) = 7.12$, at $\lambda = 585$ nm.

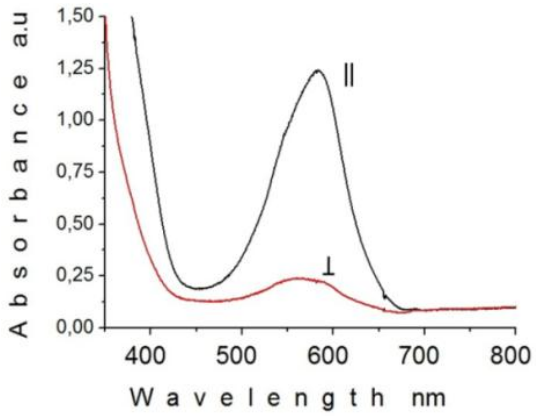

Figure 3. Linear dichroism of nematic doped MC matrix, after UV irradiation, where || is the absorption of the long dichroic axis of MC, parallel to the plane of polarization of the polarizer, and ⊥ is the absorption of the long dichroic axis of MC, perpendicular to the plane of polarization of the polarizer.

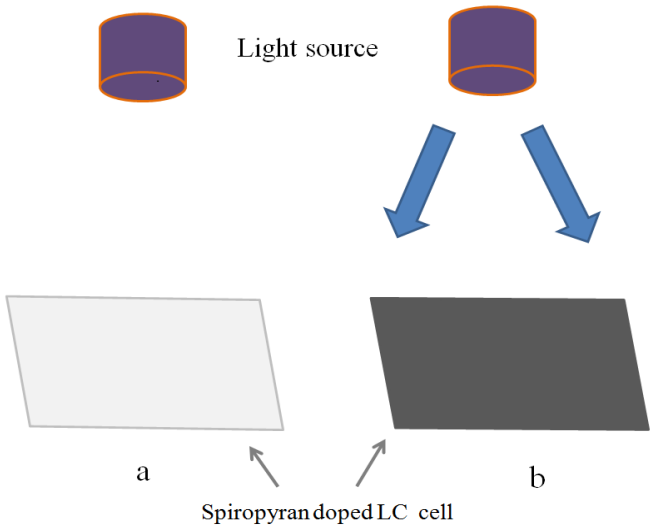

Figure 4. A scheme of the light induced modulation of the optical transparency of the SP doped cell.

We have examined the light modulation properties of the optical cell consisting of an SP doped nematic matrix. The transition time from transparent to the dark stages of optical cell, strongly depends on the exposure light intensity that can vary from milliseconds to one second. In **Figure 4**, is shown a set-up, which demonstrates a light induced modulation of the optical transparency of the SP doped cell, and in **Figure 5**, is demonstrating the optical light transmittance before and after UV exposure.

(a) (b)

Figure 5. An optical cell before (a) and after (b) UV exposure.

To obtain a light induced distribution of the linear polarization in the optical cell, we prepared a transparent plastic mask with a regular distribution of black squares (**Figure 6**). The sample cell was tightly covered with the mask and then was irradiated by UV light for 20 seconds, to obtain a regular distribution of non-irradiated areas. As a result, when irradiated by the reading light, on the screen below, we have obtained the distribution of non-polarized and linearly polarized lights, caused by the distribution of transparent and black squares on the mask, (Figure 6). It should be noted that, it is possible to use a surface covered with photosensitive layer and record optical information, modulated by the light intensity and / or by the light polarization.

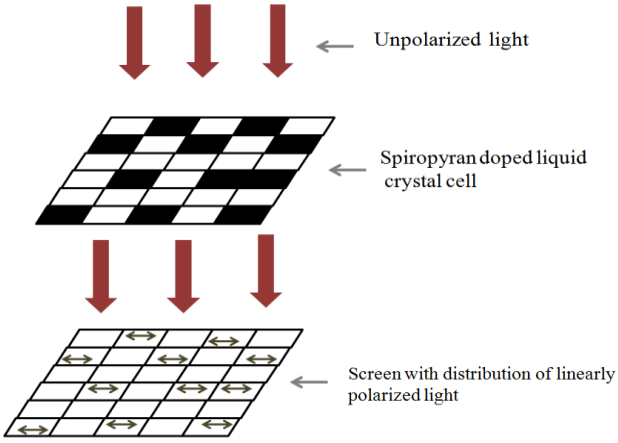

Figure 6. Experimental set-up for the recording of the spatial distribution of linear polarization in the cell filled with SP doped nematic matrix.

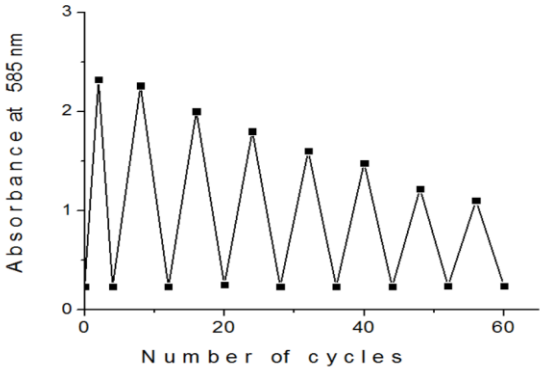

Figure 7. The number of recordings erasing cycles for a SP-doped liquid crystal mixture.

The number of recordings-erasing cycles, that a system can undergo, is a critical experimental parameter. To study the feasibility of repeated cycles, experiments on the fatigue resistance of the SP doped nematic structure upon UV and visible light irradiation were carried out. In a cycle, a system is transformed from SP configuration to MC one, and then back to the

SP form. Using visible light, we induced the switching of the MC molecules back to their initial SP form, and found that after 12 s of irradiation, the sample became transparent again. The switching between the two molecular forms can be performed efficiently for several tens of cycles, as shown in **Figure 7**.

Conclusion

To summarize, in this study, we report a SP doped nematic liquid crystal composite. Our results demonstrate that SP can be used as an efficient photo switcher and when doped in the oriented nematic matrix it acts as the linear polarizer with light controllable behavior. The use of photochromic materials in memory system is desirable, because they present several major advantages over the current optical systems, including their erasable/rewritable capability, high resolution, and high sensitivity. We envisage that the investigated composite can find versatile application in light controllable shutters, smart windows and in optical storage memory systems, where the light characteristics such as wavelength, polarization, and phase can be multiplexed to enable data storage and thus have the potential to dramatically increase the achievable memory density.

References

1. J. C. Crano, T. Flood, D. Knowles, A. Kumar, B. van Gemert. Pure & Appl. Chem., 1996, 68, 1395.
2. R. Guglielmetti. Studies Org. Chem., 1990, 40, 855.
3. D. A. Parthenopoulos, P. M. Rentzepis. Science, 1989, 245, 843.
4. K. Japaridze, L. Devadze, J. Maisuradze, G. Petriashvili, Ts. Zurabishvili, I. Mzhavanadze, N. Sepashvili. Bull. Georg. Natl. Acad. Sci., 2013, 7, 57.
5. A. S. Dvornikov, J. Malkin, P. M. Rentzepis. J. Phys. Chem., 1994, 98, 6746.
6. T. Yoshida, A. Morinaka, J. Photochem. Photobiol. A, 1994, 78, 179.
7. I. Willner, S. Rubin, R. Shatzmiller, T. Zor. J. Am. Chem. Soc., 1993, 115, 8690.
8 K. Kinashi, Y. Ono, Y. Naitoh, A. Otomo, Y. Ueda. J. Photochem. & Photobiol. A, 2011, 217, 35.
9. S. V. Paramonov, V. Lokshin, O. A. Fedorova. J. Photochem. & Photobiol. C, 2011, 12, 209.
10. S. Kumar, K. Velasco, A. Mc Curdy. J. Mol. Struc., 2010 , 968, 13.
11. N. Shao, X. Gao, H. Wang, R. Yang, W. Chan. Anal. Chim. Acta, 2009, 655, 1.
12. E. Mele, D. Pisignano, M. Varda, M. Farsari, G. Filippidis, C. Fotakis, A. Athanassiou. Appl. Phys. Lett., 2006, 88, 203124.
13. A. Athanassiou, M. Lygeraki, D. Pisignano, K. Lakiotaki, M. Varda, E. Mele, C. Fotakis, R. Cingolani, S. Anastasiadis. Langmuir, 2006, 22, 2329.
14. H. B. Laurent, H. Dürr. Pure & Appl. Chem., 2001, 73, 639.
15. R. Tong, H. D. Hemmati, R. Langer, D. S. Kohane. J. Am. Chem. Soc., 2012, 134, 8848.
16. S. Iyengar, M. C. Biewer. Cryst. Growth Des., 2005, 5, 2043.
17. A. Yamano, H. Kozuka. Thin Solid Films, 2011, 519, 1772.
18. X. Li, J. Li, Y. Wang, T. Matsuura, J. Meng. J. Photochem. & Photobiol. A, 2004, 161, 201.
19. S. H. Kim, S. Y. Park, C. J. Shin, N. S. Yoon. Dyes Pigm., 2007, 72, 299.
20. Z. S. Fu, B. B. Sun, J. Chen, L. Yuan. Dyes Pigm., 2008, 76, 515.
21. C. Elsässer, A. Vüllings, M. Karcher, P. Fumagalli. J. Phys. Chem. C, 2009, 113, 19193.
22. I. Vlassiouk, C. D. Park, S. A. Vail, D. Gust, S. Smirnov. Nano Lett., 2006, 6, 1013.
23. Y. Wu, C. Zhang, X. Qu, Z. Liu, Z. Yang. Langmuir, 2010, 26, 9442.

НЕЙТРОННЫЙ ФИЛЬТР ДЛЯ ПОГЛОЩЕНИЯ ТЕПЛОВЫХ И РЕЗОНАНСНЫХ НЕЙТРОНОВ

Н. В. Багдавадзе, Т. И. Зедгинидзе, Т. Г. Петриашвили

Тбилисский государственный университет им И. Джавахишвили
Институт физики им. Э. Андроникашвили
Тбилиси, Грузия
tamuna777petriashvili@yahoo.com

Принята 29 сентября 2015 года

Аннотация

Предложена технология нейтронного фильтра для поглощения тепловых и резонансных нейтронов на основе окиси кадмия. С целью увеличения поглощающей способности фильтра в интервале энергий нейтронов 3 – 62 кэВ используют смесь порошков окиси кадмия и металлического селена, спрессованную до плотности 4.7 – 5.0 г / см^3 и толщины 4 – 7 мм. Причем доля окиси кадмия в смеси порошков 14.0 – 25.5 мас. %, а металлического селена 75.5 – 86.0 мас. %.

Облучение образцов эпитермальными нейтронами применяется для повышения селективности метода НАА (нейтроноактивационного анализа). Этот способ основан на избирательной активации в исследуемом образце таких нуклидов у которых изменение сечения захвата нейтронов эпитермальной области не подчиняется закону $1 / V$ (V – скорость нейтрона). Оно пропорционально $E^{-1/2}$ и имеет резко выраженные резонансные максимумы, достигающие иногда сотен и десятков тысяч барн.

Облучение таких нуклидов достаточно интенсивным пучков резонансных нейтронов с энергией от 1 до 1000 эВ с небольшим энергетическим разбросом позволяет проводить избирательную активацию. В результате появляется возможность разработки для многих элементов весьма специфических методик определения.

Из-за отсутствия достаточно мощных источников монохроматических нейтронов с регулируемой энергией, в практике активационного анализа используют резонансные , получающиеся в процессе замедления быстрих. Наибольшую интенсивность потоки резонансных нейтронов имеют в атомных реакторах, в которых число нейтронов резонансной энергии изменяется по закону $1 / E$.

Зависимость потока резонансных нейтронов от энергии создает наиболее благоприятные условия для активации элементов, у которых резонансы расположены в области низких энергий, так как здесь поток резонансных нейтронов выше. В практике НАА в целях избирательной активации применяют фильтры из различных веществ или их комрозиций, обладающих, в свою очередь, большими сечениями поглощения нейтронов определенных энергий. Пропускание изотропного поля тепловых нейтронов

фильтрами из Cd, B, Au и др. изучено в работах [1, 2]. Известно, что Cd обладает свойством сильно поглощать тепловые нейтроны до резонансной энергии 0.178 эВ (8000 барн), а в области 0.4 эВ сечение резонансного поглощения $\sigma_{\text{рез.}}$ резко падает. Поэтому в первом приближении допускают, что кадмий захватывает все нейтроны с $E \leq 0.4$ эВ и пропускает надтепловые.

Активация нуклидов за кадмиевым экраном проводится преимущественно на эпитермальных и быстрых нейтронах, а наведеная активность пропорциональна величине его сечения в этой энергетической области спектра нейтронов и потоку.

Значения резонансных интегралов $I_{\text{рез.}}$ сечений активации на тепловых нейтронах $\sigma_{\text{т}}$ определяют целесообразность использования того или иного способа активации для данного элемента, она может быть установлена по отношению $I_{\text{рез}} / \sigma_{\text{т}}$.

Эффект резонансной активации данного нуклида оценивается величиной его кадмиевого отношения, которое определяется как отношение активности в результате активации в полном потоке нейтронов (без кадмиевого фильтра) к активности в кадмиевом фильтре. Представленная работа относится к прикладной ядерной физике и может быть использована в гамма-спектрометрическом варианте инструментального нейтроноактивационного анализа, в частности в резонансном нейтронном активационном анализе для избирательной активации образцов.

Работа ставила целью увеличение поглощающей способности нейтроно-поглощающего фильтра в диапазоне энергий 3 – 62 эВ, что обеспечивает преимущественную активацию радионуклида ^{203}Hg.

Использование предлагаемой композиции в качестве фильтра тепловых и резонансных нейтронов основано на том, что содержащийся в фильтре кадмий интенсивно поглощает тепловые нейтроны с энергией $E \leq 0.4$ эВ, а поглощение резонансных с $E_{\text{рез.}} = 3, 7, 21, 32, 35, 46, 52$ и 62 кэВ осуществляется благодаря наличию в нем металлического Se.

Применение окиси кадмия и металлического селена в пропорциях 1:5 или 1:10 обусловлено необходимостью подавления активации ^{75}Se соответственно в 5 и 10 раз для идентификации радионуклида ^{203}Hg в биологических материалах различного происхождения.

Важной характеристикой нейтронного экрана является его толщина, обеспечивающая содержание в материале фильтра такого количества поглощающего компонента, которое реализует необходимый эффект подавления нейтронов интересующих энергий. Расчет нейтронопоглощающих экранов по содержанию кадмия может быть проведен путем с равнения с используемыми в ядерной технике кадмиевыми фильтрами для поглощения тепловых нейтронов. Материалом известных кадмиевых фильтров служат кадмиевые фольги толщиной 0.5 см $P_{\text{Cd}} = 8.5$ г / см^3. Для таких фольг содержание кадмия на единицу площади, т.е. размером 1 см × 1 см × 0.5 см составляет 0.45 г.

Предлагаемый материал плотностью $\rho = 5$ г / см^3 состава CdO содержит на единицу площади (1 см × 1 см × 1 мм) 0.115 г кадмия. Таким образом, для обеспечения равнозначного с кадмиевым экраном эффекта поглащения тепловых нейтронов предлагаемый материал должен иметь толщину 4 мм.

Аналогично могут быть расчитаны нейтронные фильтры произвольных композиций. Например, для композиции нейтронного экрана состава CdO + 10 Se с плотностью $\rho = 4.7$ г / см^3 толщина состовляет 7 мм.

14.0 г окиси кадмия и 86.0 г порошка металлического селена перемешивают в шаровой в мельнице в течение 4 ч. Смесь увлажняют 4 % воды (4 мл), протирают через сито с числом отверстий 625 отв. / см^2 и помещают в герметичный сосуд для равномерного распределения влаги в обьеме порошка. Через 20 – 24 ч из порошка формуют под давлением 10 г / см^2 изделие в виде диска с диаметром $D = 28$ мм и высотой $h = 3 – 5$ мм или же виде балочки 10 мм × 10 мм × 20 мм. При приложении столь высоких давлений частицы металлического селена растекаются, связывая частицы кадмия в монолитное тело. Для удаления временной связки – воды изделие сушат в течение 2 ч при 110 °C.

Нейтроннопоглощающая способность предложенного фильтра исследовалась экспериментально. Исследования проводили путем сравнения активности радионуклида ^{75} Se, полученного при обучении селенсодержащих эталонов сравнения на основе фенолоформальдегидной смолы в кадмиевой фольге, и экранах из описаных нейтронопоглощающих материалов. Экраны были изготовлены в виде контейнеров цилиндрической формы с плотно насаживаемой крышкой. Облучение проводили флюенсом $1 \cdot 10^{18}$ н / см^2, содержание Se в стандартном материале $1 \cdot 10^{-7}$ г, спектрометрические измерения проводились на полупроводниковом Ge(Li)-спектрометре обьемом 55 см^3 и разрешением 2.6 кэВ для 1332 кэВ. Время измерения 15 мин. Полученные результаты позволили сделать вывод о пяти и десятикратном ослаблении потока нейтронов соотстветствующих энергий матерялами, содержащими Se и CdO в соотношениях 5:1 и 10:1.

Таким образом, предложена технология нейтронного фильтра для поглощения тепловых и резонансных нейтронов на основе окиси кадмия. С целью увеличения поглощающей способности фильтра в интервале энергий нейтронов 3 – 62 кэВ используют смесь порошков окиси кадмия и металлического селена, спрессованную до плотности 4.7 – 5.0 г / см^3 и толщины 4 – 7 мм. Причем доля окиси кадмия в смеси порошков 14.0 – 25.5 мас. %, а металлического селена 75.5 – 86.0 мас. %.

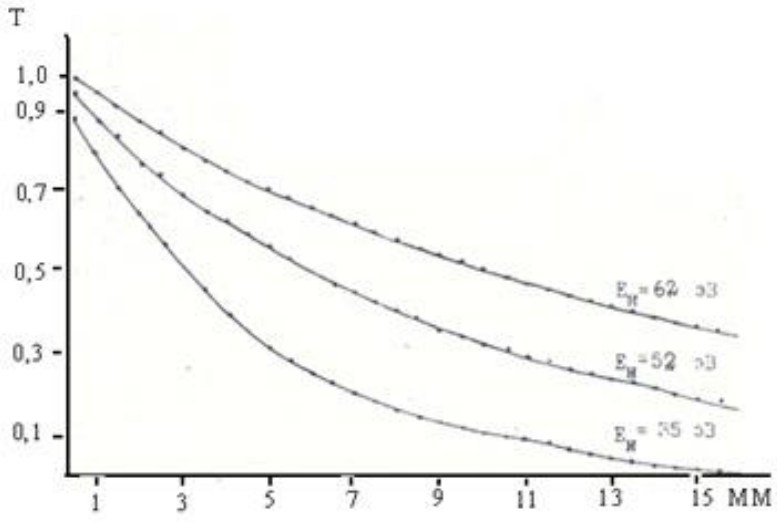

Рисунок 1. Зависимость фактора пропускания T от толщины CdO + Se экрана.

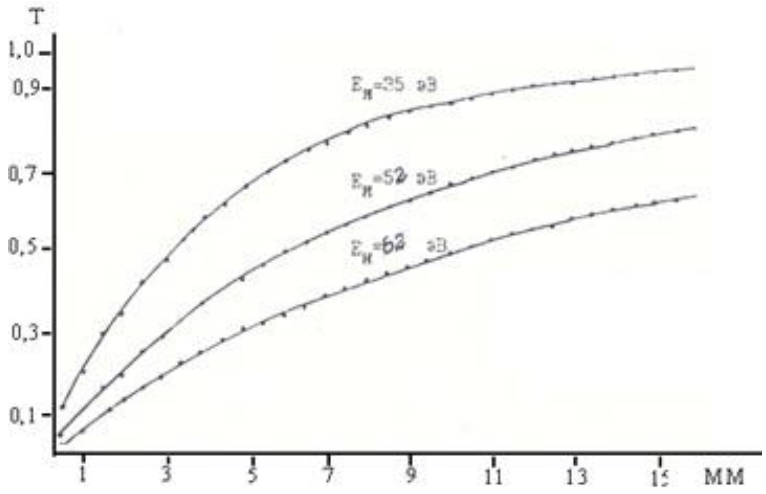

Рисунок 2. Зависимость фактора поглощения F от толщины CdO + Se экрана.

Эффективность поглощения нейтронов резонансных энергии, генерируюших активность ^{75}Se рассчитывали определением факторов пропускания T и поглошения F для нейтронов в материале экрана (**Рисунки 1** и **2**).

Ссылки

1. Н. А. Дамбург, Л. Л. Пелекис. Применение кадмиевого фильтра в активационном анализе на реакторных нейтронах. Изв. АН Латв. ССР (Сер. физ.-мат. Наук), 1970, 4, 19-26.
2. U. Kucepa. Epithermal neutron activation analysis of trace elements in biological materials. Radiochem. & Radioanal. Lett., 1979, 38, 229-246.

HYBRID PHOTOSENSITIVE SPAZ COMPOUNDS

J. Maisuradze, L. Devadze, Sh. Akhobadze,
Ts. Zurabishvili, N. Sepashvili

Georgian Technical University
V. Chavchanidze Institute of Cybernetics
Tbilisi, Georgia
devadze2005@yahoo.com

Accepted September 30, 2015

Abstract

Spiropyrans (SP) are one of the popular classes of photochromic bistable compounds that change their optical and structural properties in response to external inputs such as light, metal ions, heat, mechanical stress, etc. This "smart materials" are unique for photonics, optoelectronics, information record and storage, optical switches, different types of sensors, drug delivery, ecology, etc. Azobenzene (AZ) derivatives are of a particular interest due to their ability to reversibly undergo trans-cis isomerization followed by sharp changes in some of their properties. It is expected that the combination of photoactive AZ and photochromic SP could lead to an interesting light-controllable molecular device to control on-off switching of photoinduced processes. To extend their functional properties, we synthesized photobifunctional compounds SPAZ. Photoconversion of hybrid compound incorporated in polymer matrix takes place at a room temperature. Spectral data indicate intra-molecular total conjugation.

Spiropyrans (SP) are an interesting class of bistable photochromic compounds. Bistable molecules and molecular assemblies may exist in two different thermodynamically stable states isolated by a certain energy barrier. A transformation from one state to another is possible under the influence of external stimulators (light, heat, mechanical stress, electrical and magnetic fields, etc.).

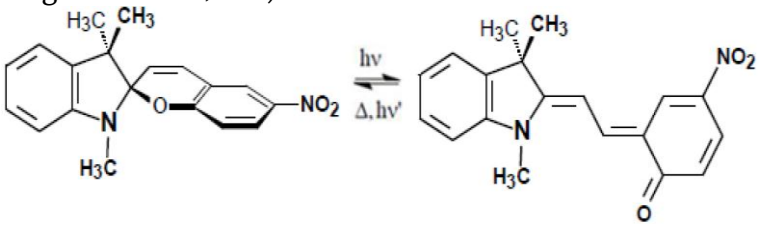

Figure 1. Spiropyran (SP) and merocyanine (MC) isomers.

An uncolored molecule of a volumetric spiropyran (SP) under the impact of the ultraviolet (UV) light is transformed into a colored, coplanar polar merocyanine (MC) form, with its physical and chemical properties changing (**Figure 1**). In practice, spiropyrans are used in such light-controlled devices, as information recorder (including three-dimensional information), storing and processing systems, non-linear optical materials, molecular computers, regulated optical density filters; they are also used in medicine to make nanocontainers to transport a medication across a human body, etc.

A closed form of SP is two orthogonal chromophores (with pyran and indoline fragments), which absorbs in a spectral UV area, while a photoisomerized planar MC form is presented as a single conjugated system, which absorbs and radiates in a visible (Vis) spectrum area. For the practical use of SP, such parameters of SP, as photosensitivity to the UV and

visible lights, position of maximum absorption of a colored form gained as a result of photoisomerization on the spectrum and its life duration (stability) associated with the speeds of transformation of the system into its initial, uncolored form, are important. It is clear that the speed of relaxation processes is determined by the environmental characteristics (solvent polarity, temperature, etc.). Photo- and thermal stability of a spiropyran-containing system is a very important feature.

Optimization of the spectral and kinetic properties of a spiropyran was done by us by varying the functional groups with different electronic properties and their positions in a photochromic molecule. The molecular skeleton was also changed – the compounds with photosensitivity to UV light greater than that of the existing analogs were gained by substituting indoline by azaindoline. In some polar solvents azaindoline spiropyrans are uncolored in terms of thermodynamic equilibrium resulting in their photo- and thermal stability. A change in a molecular skeleton done by introducing an additional fragment to the indoline part has increased the photosensitivity of the compound to the visible light [1 – 3].

By modifying the spiropyran molecules into amphiphilic molecules done by us by introducing a long alkyl radical at a nitrogen atom, the system acquired the ability of self-organization into micelles and its efficient photosensitivity increased at the expense of internal energy. A micellar structure blocks the relaxation in a spiropyran form what increases the stability of a colored MC form [4].

In addition to the above-listed parameters of spiropyrans, the position of maximum absorption is also very important. For practical use, it is desirable to be located in the area of an inexpensive diode laser radiation (780 nm) what can be done by increasing the length of the molecule conjugation. It should be noted that by substituting an oxygen atom by a sulphur atom in a spiropyran molecule, the absorption maximum shifts to almost 900 nm, but the relevant molecules are characterized by instability and high degradation.

By considering the above-mentioned, aiming at a further improvement of the properties of photochromic spiropyrans, we considered the synthesis of new hybrid bifunctional photosensitive compounds on the spiropyran basis expedient. A colored photoinduced form of hybrid compounds gained by merging spiropyran and different photochromic compounds synthesized and studied by a number of authors [5 – 9] turned out to be instable. As a result, photochromic transformations in them were mostly observed either at low temperatures, or by using femtosecond technology. Such state of affairs limits the practical use of such compounds.

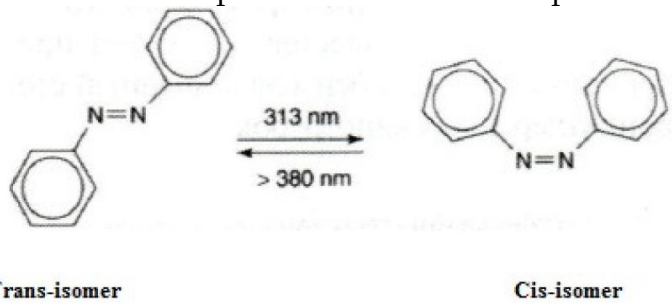

Figure 2. Azobenzene isomerization.

As the theory of conjugated chromophores suggests, by introducing a second photochromic center to a photochromic molecule, the spectral properties are improved (e.g. extinction coefficient increases) and conjugated π-system is elongated resulting in a bathochromic shift of the absorption band. By considering this fact, introduction of a photochromic azobenzene molecule to a photochromic spiropyran molecule as the second absorption center was considered expedient by us (**Figure 2**).

For this purpose, we introduced 2-hydroxide-8-nitro-5[(4'-phenyl) Diazenyl] benzaldehyde at Fisher's base analogs and gained hybrid compound 1 (**Figure 3**), with its absorption band bathochromically shifted (100 nm) in relation to the relevant spirospyran, while photochromic transformations are observed at a room temperature. This was the result of inserting group NO_2 in state 8. Such compounds as compared to those known in literature [5 – 9] are of a wider practical use.

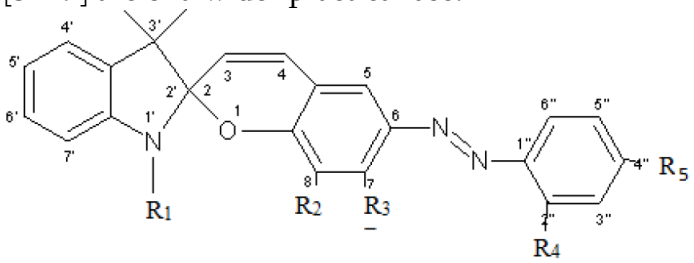

Figure 3. $R_1 = C_4H_9$, $R_2 = R_5 = NO_2$, $R_3 = R_4 = H$; R1 = CH_3, $R_2 = OCH_3$, $R_3 = H$, $R_4 = R_5 = NO_2$; and $R_1 = CH_3$, $R_2 = H$, $R_3 = OH$, $R_4 = R_5 = NO_2$.

Thus, on the base of two photochromic compounds: SP and AZ, we synthesized hybrid molecule SPAZ. By combining two photochromes: SP and electrophilic AZ, the length of the conjugation chain of a photoinduced form in one molecule increases resulting in the long-wave shift of the relevant absorption band.

Two fragments of a synthesized hybrid molecule have a common benzene ring (**Figure 3**).

Under the influence of the UV light, C–O bond is breaked and the molecule transforms into a coplanar state and a long conjugated chain is formed. So, it is expected that a hybrid molecule, under the influence of active light, may serve two functions: breaking of intramolecular bond C–O in the spiropyran part and geometrical changes – trans-cis isomerization in the azobenzene part. Bifunctionality of a hybrid molecule yields two photoproducts. The length of the conjugated chain formed under the influence of UV light, due to the presence of the azobenzene fragment, will increase and the length of the relevant absorption band will shift bathochromically. As it is known, the photochromic transformations can be observed at a room temperature by weakening C–O bond. This can be done by varying the electrical properties of the substitute and their positions in a hybrid molecule (**Figure 3**). It turned out that among the gained compounds the desirable properties were demonstrated by compound 1 (**Figure 3**). As the Diagram shows, electrophilic groups NO_2 were substituted in the state of spiropyran chromene (8) and azobenzene (4'). Such positioning of electrophilic groups weakens bond C–O and the thermal equilibrium of a compound in polar solvents shows a certain inclination to a colored form. The samples kept in the dark are colored. Under the influence of UV light (UFS 1), the color deepens gradually to reach photoequilibrium. In the dark, the thermodynamic balance reinstates. Under the influence of the visible light (SZS 1), the sample gets totally colorless. The process is observed at a room temperature.

For practical use, hybrid compound 1 was integrated with a polar polymer, polymethylmethacrylate. We studied the spectral properties of the sample as shown in **Figure 4**. A short-wave absorption band belongs to azobenzene, while a long-wave absorption band is typical to the photoinduced form of a spiropyran.

The absorption bands of a photoinduced form of a hybrid compound as compared to the absorption bands of model compounds (SP and AZ) are shifted bathochromically what must be caused by the origination a long conjugated chain of an open molecule form. The absorption spectrum corresponding to the thermodynamic equilibrium established in the dark shows that the sample is colored. Photoequilibrium established by the UV light radiation is shown in spectrum 2. The relaxation processes taking place in the dark are presented by 3, 4. The

relaxation process continues up to the establishment of thermodynamic equilibrium (1). Complete discoloration of a sample took place under the influence of such an area of the visible light, which is active for a spiropyran fragment only and which must have changed only the long-wave absorption band. As the **Figure 4** shows, the visible light influenced a short-wave absorption band as well, what is a proof of a unity of the electronic cloud of the molecule.

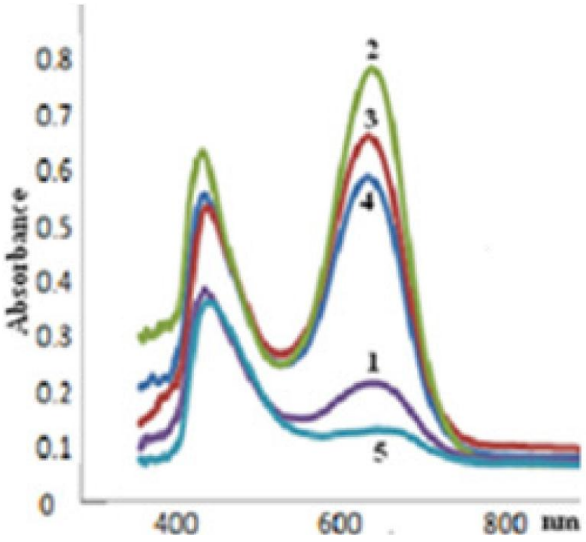

Figure 4. Absorption bands of compound 1 integrated in the polymer. 1-thermodynamic equilibrium; 2 – after radiating with UV light; 3, 4 – relaxation process taking place in the dark; 5 – after radiating with visible light (thickness of film 200 μm, concentration 2 %).

The hybrid compounds substituted by 8 – NO_2, like relevant spiropyran analogs, are subject to degradation [10], making it difficult to study their photochromic transformations in liquid solvents. Due to these circumstances, we studied the photochromic transformations of hybrid compounds in polymer films. By changing the positions of NO_2 and azo-groups the system stability is expected to increase.

Thus, on the basis of the spectral data we can conclude that before irradiation the synthesized hybrid compounds have the absorption bands typical to spiropyran and azobenzene while after irradiation a long conjugated chain is formed in a hybrid molecule.

The work is accomplished under the financing of grant project FR/395/6–420/13 of Shota Rustaveli National Science Foundation.

References

1. K. G. Japaridze. Spirochromeny. 1979, Tbilisi, Metsniereba.
2. J. P. Maisuradze, Sh. A. Akhobadze, L. V. Devadze, K. G. Japaridze. KhGS, 1982, 10, 1367.
3. J. P. Maisuradze, N. I. Makhashvili, L. V. Devadze, N. O. Sepashvili, L. P. Shishkin, K. G. Japaridze. Proc. Acad. Sci. Georg. SSR, (Chem.l Ser.), 1989, 15, 44.
4. K. Japaridze, L. Devadze, J. Maisuradze, G. Petriashvili, Ts. Zurabishvili, I. Mzhavanadze, N. Sepashvili. Bull. Georg. Natl. Acad. Sci.s, 2013, 7, 57.
5. S.-R. Keum, M.-J. Lee. Bull. Korean Chem. Soc., 1999, 20, 12.
6. K. Kinashi, K. Furuta, Y. Ueda. Chem. Lett., 2006, 35, 298.
7. K. Kinashi, Y. Ueda. Mol. Cryst. & Liquid Cryst., 2006, 445, 1.
8. R. Mardaleishvili, L. S. Koltsova, N. L. Zaichenko, A. I. Shienok, P. P. Levin, A. S. Tatikolov. High Energy Chem., 2013, 47, 205.
9. R. Mardaleishvili, L. S. Koltsova, N. L. Zaichenko, A. I. Shienok, P. P. Levin, A. S. Tatikolov. High Energy Chem., 2015, 49, 30.
10. J. Maisuradze, Bull. Georg. Natl. Acad. Sci., 2013, 2, 90.

MODERN TECHNOLOGICAL METHODS FOR FABRICATION OF HIGH PERFORMANCE SOLAR CELLS

L. Jibuti

I. Javakhishvili Tbilisi State University
Institute of Micro & Nanoelectronics
Tbilisi, Georgia
ladojibuti@gmail.com

Accepted October 4, 2015

Abstract

Photostimulated diffusion widely used in the technologies of modern electronics, finds ever-widening application in nanotechnology. Great interest in the methods of photostimulated diffusion is due to the possibility of using this highly effective method in the processes of photoinduced impurity doping. In the work, the technology of monocrystalline Si-based solar cells is given where traditional thermal diffusion processes for formation of p–n junctions and Ohmic contacts are replaced by photo-stimulated diffusion processes. This leads to the decrease in the temperature (450 °C) and duration (100 times) of the aforementioned technological processes. The increase in the efficiency of the fabricated solar cells by 7 % is observed. The ionization mechanism of crystallization in semiconductors by the method of pulsed photon irradiation is considered.

Introduction

Stages of human development require constantly increasing energy consumption, which reduces the energy reserves of the planet. Ecological processes associated with a decrease in the energy reserves and power engineering impelled scientists to create alternative energy sources.

One of the promising methods is to create current sources based on solar cells (**Figure 1**). In those places where no power supply can be provided in the usual way, the use of solar cells is very important. Currently, solar cells find rather wide application. They are placed on the roofs of houses, cars, satellites to provide electricity.

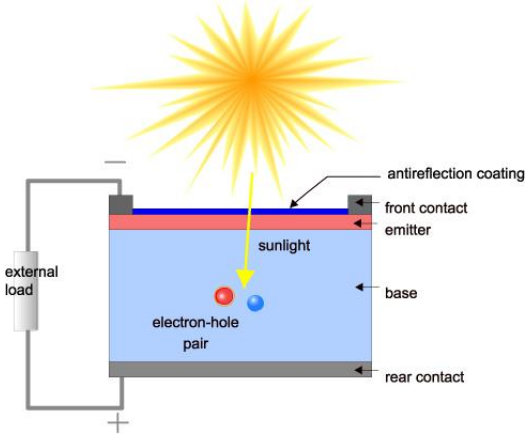

Figure 1. Solar cell.

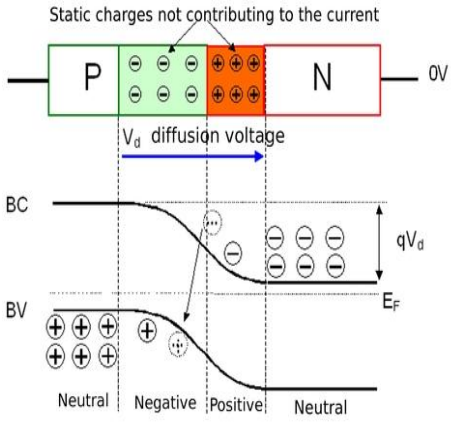

Figure 2. p–n junction.

The principle of solar cell operation (**Figure 2**): during photon absorption a p–n junction is formed. Photons falling on the p–n junction cause the rise of electron–hole pairs. Under the influence of the internal field electrons go to the n-type semiconductor, and holes go to the p-type semiconductor, and a conductor is energized. This energy can be accumulated and further used.

The aim of our work was to create a technology of high-performance solar cells, which, on the one hand, would be cheaper, but on the other hand, would increase the efficiency of the fabricated devices. We chose silicon as the object of our research as a relatively cheap material used by the well-developed microelectronic technologies. Basic technological processes for fabrication of solar cells include the creation of the p–n junction on the semiconductor substrate and the formation of Ohmic contacts in the n- and p-regions. This process is traditionally rather long-lasting (2 h) and is carried out at high (1150 °C) temperatures. As an alternative to the above technology we apply a method of pulsed photon irradiation, which greatly lowers the temperature and duration of diffusion processes [1 – 4].

Materials and methods

Technological process of solar cell fabrication

Solar cells are fabricated on the basis of monocrystalline p-Si(B) (**Figure 3**). First, chemical cleaning of a Si wafer takes place as follows (**Figure 4**): treatment in $NH_4OH + H_2O_2 + H_2O$ (1 : 1 : 4) solution at 45 °C, 10 min; washing in distilled water, 10 min; duplicating (1 : 50), 10 min; hydromechanical washing, 5 min; drying at 180 °C.

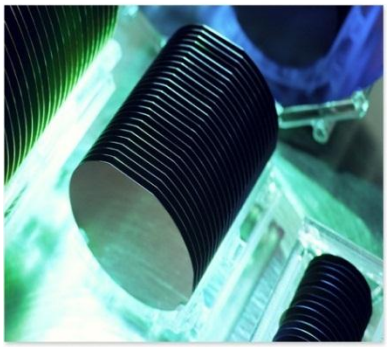

Figure 3. Monocrystalline p-Si(B).

Figure 4. Chemical cleaning of a Si wafer.

Figure 5. Dropping phosphor-silicate glass.

Figure 6. Pulse photonic irradiation equipment.

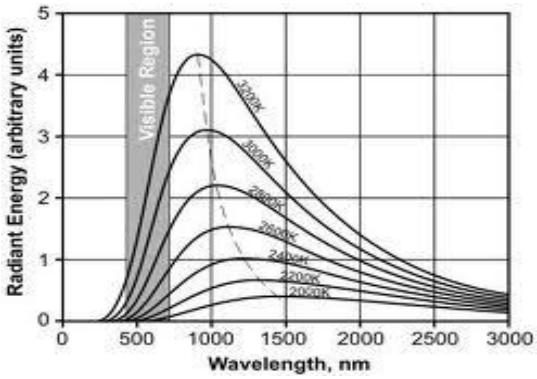

Figure 7. Radiation spectrum of halogen lamp.

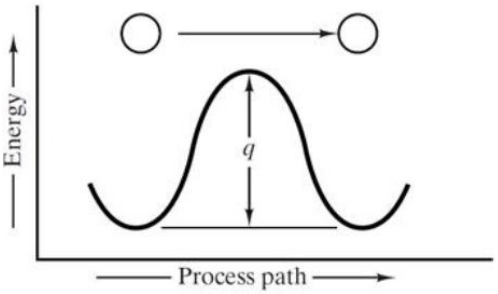

Figure 8. Process pass showing how an atom most overcome an activation energy, q, to move from one stable position to a similar adjacent position.

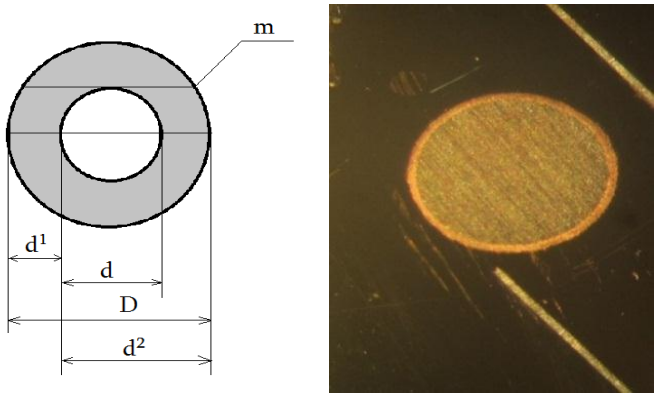

Figure 9. The depth of p–n junction.

We drop phosphor-silicate glass onto the wafer, treated in the centrifuge and spread over the whole wafer. Then we prepare the wafer for diffusion (**Figure 5**). A p–n junction is formed on the Si wafer using the photon irradiation method (**Figures 6** and **7**). As a result, phosphor diffusion in p-Si takes place to obtain the n-region. Si wafer is irradiated by photons using halogen lamps; power density of irradiation is 150 W / cm² each. Irradiation process is repeated three times, 5 s each, with 4 s intervals. The pulsed photon exposure results in the selective absorption of photons, which leads to a weakening of chemical bonds and, accordingly, to a decrease in the activation energy of diffusion processes. Thus, it becomes possible to perform activation-diffusion processes at lower temperatures and in a shorter time. As seen from the formula, $D = D_0 \exp(-E_a / kT)$ the diffusion coefficient is determined by the activation energy

(E_a, **Figure 8**) of impurities and the temperature (T) of the process. The higher the activation energy of impurities, the higher temperature is required to obtain the same diffusion coefficient. The depth (H) of the obtained p–n junction is measured by the ball grinding method (**Figure 9**): $H = m^2 / 4D = 0.3$ μm.

Figure 10. Metal coating.

Figure 11. Photolithography.

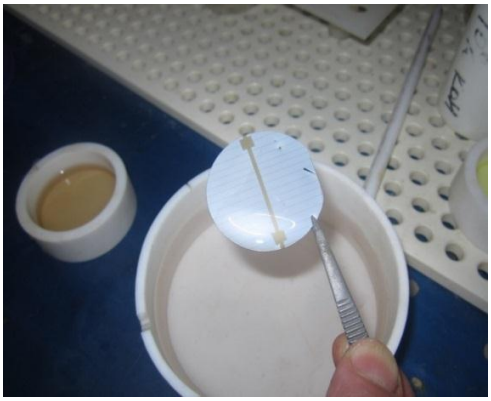

Figure 12. Development of the pattern

An aluminum layer is coated on both sides of the wafer by the vacuum method to form Ohmic contacts (**Figure 10**). Metal contacts on the lower side of the substrate are completely preserved, whereas on the upper side are formed in a grid. For this reason, we coat a photoresist on the work side of the wafer, place a photomask thereon and expose to UV light (**Figure 11**).

Afterwards, development of the pattern is performed. The exposed areas become unstable to the solution used for etching of the undesired regions (**Figure 12**). This process proceeds as follows: development in the AZ400 + H_2O (1 : 4) solution, 20 – 30 s; washing in distilled water; drying in the centrifuge; drying after visual inspection at 130 °C for 10 min; removing the photoresist in acetone; etching of aluminum in the $H3PO_4$ + HNO_3 + H_2O + CH3COOH solution; washing and drying in the centrifuge.

Then we use photo-stimulated diffusion process again to get Ohmic contacts.

Results

After completion of all the above processes, current–voltage characteristics of the solar cell are measured (**Figures 13 - 15**).

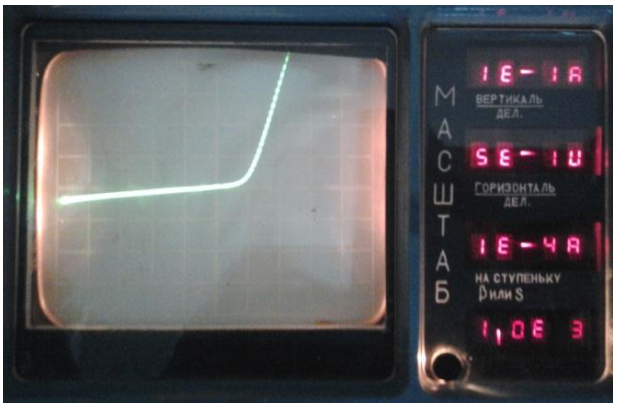

Figure 13. Typical current-voltage characteristics in the dark.

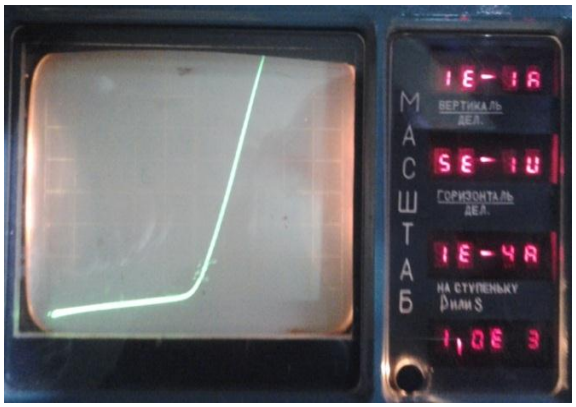

Figure 14. Changed current-voltage characteristics of the wafer during the exposure to a sun simulator (1000 W / m^2).

Figure 15. Sun simulator (ILC Technology).

Figure 16. Solar cells panel.

Table 1.

Methods	Energy density of radiation flux, W / m²	U_{oc}, V	I_{sc}, A	Current–voltage characteristics fill factor	Working area, cm²	Depth of p–n junction, μm	Efficiency, %
Photo-stimulated diffusion	1000	0.55	0.35	0.7	5.76	0.3	23
Thermal diffusion	1000	0.53	0.25	0.68	5.76	1	16

The obtained solar cells (**Table 1**) are arranged in the form of a big panel ($I = 0.35$ A, $U = 6.5$ V, efficiency 23 %) thus making it possible to charge mobile phones, radio set, accumulators, etc. (**Figure 16**).

Conclusion

The proposed solar cells technology is characterized in that the traditional, high-temperature (1150 °C), prolonged (2 h), diffusion processes are replaced by a relatively low temperature (700 °C), rapid (15 s), impulsive photon irradiation.

As a result:

The solar cell technology becomes significantly simplified and cheaper.

It becomes possible to control the depth of the resulting p–n junction. Thin (less than 1 micron) p-n junctions will be obtained, which in turn increases the efficiency of the obtained solar cells.

In the solid-phase regime, a photo-stimulated diffusion process is determined by the selective photon absorption efficiency in the reaction materials.

Acknowledgement

I thank my scientific supervisor, Associate Professor Amiran Bibilashvili for formulation task and permanent charming attention during the entire work process.

References

1. Z. V. Jibuti, N. D. Dolidze, B. E. Tsekvava. The electronic mechanism of melting of semiconductor materials. In: New Developments in Material Science. 2011, New York, Nova Sci. Publ. Inc., 43-54.
2. A. Bibilashvili, N. Dolidze, Z. Jibuti, R. Melkadze, G. Eristavi. Investigation of the photostimulated crystallization and relaxation of internal mechanical pressure in silicon on insulator epitaxial nanostructures. Nanotechnol. Percep., 2008, 4, 29-34.
3. Z. V. Jibuti, N. D. Dolidze,G. Eristavi. Photostimulated relaxation of internal mechanical stresses in epitaxial SOS–structures. Tech. Phys., 2008, 53, 808-810.
4. Z. V. Jibuti,N. D. Dolidze, G. Sh. Narsiya, G. L. Eristavi. Possible method of reducing annealing temperatures of radiation defects in ion-implanted silicon carbide. Tech. Phys. Lett., 1997, 23, 746-747.

НИЗКОТЕМПЕРАТУРНОЕ НЕЙТРОННОЕ ОБЛУЧЕНИЕ БИОЛОГИЧЕСКИХ МАТЕРИАЛОВ И ВОЗМОЖНОСТЬ ИХ МНОГОЭЛЕМЕНТНОГО АНАЛИЗА

Н. Кучава

Тбилисский государственный университет им И. Джавахишвили
Институт физики им. Э. Андроникашвили
Тбилиси, Грузия
e.kuchava@mail.ru

Принята 12 октября 2015 года

Аннотация

Обсуждаются условия правильного определения количественного содержания химических элементов как в материалах животного происхождениях, так и объектов окружающей среды, методом инструментального нейтронного активационного анализа (ИНАА). Использована низкотемпературная нейтронная активация исследуемых материалов.

Известно, что в тканях живых организмов встречаются почти все химические элементы периодической системы. Известно также, что количественное содержание элементов меняется в зависимости от многих факторов: от вида и возраста живых организмов, различных частей того или другого органа, времени года, суточного цикла, физиологического состояния организма и т.д. Выяснена физиологическая роль некоторых из них, но еще не ясна роль таких следовых элементов какими являются: Au, Cs, Rb, Sc, Hg, Ag. Возможно, что эти элементы могут выполнять определенную функцию в существовании живых организмов. В обзорной работе [1] обсужден вопрос о содержани следовых элементов в биологических тканях и жидкостях, а также об их возожной роли в жизни животных и человека. Имеющиеся в научной литературе раннего периода данные о микроэлементном составе разных органов (тканей) животных и человека (Войнар, 1960; Бабенко, 1965; Underwood, 1962, 1977; Bowen, 1966; Коломийцева, Габович, 1970; Kostik et al., 1977; Кист, 1987) часто противоречивы. Мало изучен вопрос о распределении следовых элементов в органах (тканях) человека при опухолевых заболеваниях, а также у животных при прирывываемых опухолях, что является одним из важных задач науки.

Особое значение имеют методы количественного определения содержания химических элементов в биологических материалах (БМ). С этой целью в настоящее время широко используется сравнительный метод инструментального нейтронного активационного анализа (ИНАА), который характеризуется высокой точностью, чувствительностью и с помощью которого в БМ одновременно можно определить содержание больше 14 химических элементов, по их сравнитеьно долгоживущим радионуклидам: Sc, Cr, Fe, Co, Zn, Se, Br, Rb, Ag, Sb, Ba, Au, Hg, Cs. Как известно, при использовании сравнительного метода ИНАА с рядом исследуемых образцов облучается стандарт сравнения, содержащий известное количество исследуемого элемента. В наших экспериментах использованы стандарты сравнения, приготовленные на основе фенолформальдегидной резольной смолы (ФФС).

Наши исследования по изучению элементного состава разных обьектов были проведены с помощью нейтронных потоков ядерного реактора (ЯР) и нейтронного

размножителя ПС–1 Института физики, которые представляют собой источники ионизирующих излучений альфа- и бета-частиц, протонов, нейтронов, гамма-квантов, осколков деления. Основная доля поглощенной активируемым материалом энергии приходится на нейтроны и гамма-кванты. Эта энергия переходит в кинетическую энергию атомов,что, конечном счете, приводит к его нагреву, степень которого зависит от мощности ЯР и поглощенного облучаемым материалом ядерного излучения, а также от свойств самого образца, упоковочных приспособлений, от места расположения используемого экспериментального канала в активной зоне (АЗ) ЯР. Определенную роль со своей стороны играют условия теплосъема во время облучения.

Проведению НАА БМ посвящено большое число исследований. Практически все они выполнены с облучением исследуемых образцов в обычных реакторских условиях, т. е. при наличии радиационного нагрева биоматериалов. О нагревании БМ в процессе облучения в каналах ЯР указывают авторы работ [2, 3]. В таких случаях температура облучаемых образцов может достигать нескольких сотен градусов, из- за чего возможно разрушение образца и улетучивание некоторых химических элементов, таких, как: Hg, Se, Br, I,что приводит к неконтролируемым ошибкам при количественной оценке указанных элементов. С другой стороны, изменение общей массы облучаемого образца может вызвать также ошибку при определении содержания и нелетучих элементов, содержащихся в БМ, поэтому температурный режим облучения БМ является одним из ответственных моментов при проведении НАА. Авторы работы [4] решением проблемы считают облучение БМ при низких температурах.

Сконструированный на ЯР Института физики (ИФ) охлаждаемый канал, т.н. вертикальная низкотемпературная петля (ВНТП) позволял непрерывное облучение БМ при температурах ниже 0 °С в течение 70 – 80 ч.

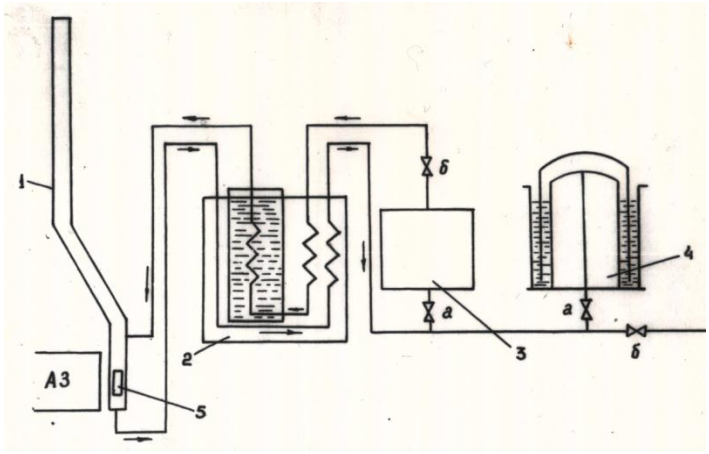

Рисунок 1. Схематическое изображение вертикальной низкотемпературной системы для охлаждения БМ во время их облучения. 1 – загрузочный канал, 2 – теплообменник, 3 – компрессор, 4 – газгольдер, 5 – облучаемый образец. а – вентиль низкого давления, б – вентиль высокого давления.

На **Рисунке 1** представлены схематические системы для охлаждения БМ, помещенных в АЗ ЯР. Технические параметры указанной системы таковы: рабочий диаметр канала составляет 20 мин, длина – 8000 мм, зона охлаждения – 600 мм. При мощности ЯР 5 МВт расход газообразного гелия 50 м^3 / ч, расход жидкого азота 60 л / ч. При данном цикле работы ЯР постоянно поддерживается разность давления $(0.2 – 0.3) \cdot 10^5$ Па.

В работе [5] был изучен нагрев БМ и стандартов сравнения в процессе их облучения в неохлаждаемом центральном сухом канале (ЦСК) и было показано, что при мощности ЯР 2 – 3 МВт температура облучаемых в ЦСК образцов достигает 250 – 300 °С. Целью работы [6] было определение влияния нагрева на изменения масс БМ и стандартов сравнения в процессе облучения в неохлаждаемых условиях и оценка связанного с этим изменения содержания химических элементов, входящих в состав БМ. В указанной работе были проведены эксперименты по облучению таблеток (< 50 мг) лиофильно высушенного цельной человеческой крови и стандартов сравнения в ВНТП и ЦСК одновременно, с непрерывным измерением температуры на поверхности облучаемых контейнеров (–140 – 150 и 260 – 270 °С, соответственно, при мощности ЯР 3 МВт). В проведенных экспериментах лиофильно высушенные таблетированные БМ при облучении в условиях низких температур сохраняют свою форму и массу, тогда, как при облучении в ЦСК образцы разбухают, разрушаются и превращаются в порошкообразную массу, которую трудно удалить из упаковочного материала, а растворение в кислотах приводит к потерям некоторых химических элементов [7]. В отличие от БМ, таблетки стандартов сравнения в этом интервале температур сохраняют свою форму. Содержание химических элементов в образцах человеческой крови, облученных в разных условиях, приведены в работе [6]. Здесь их не будем рассматривать.

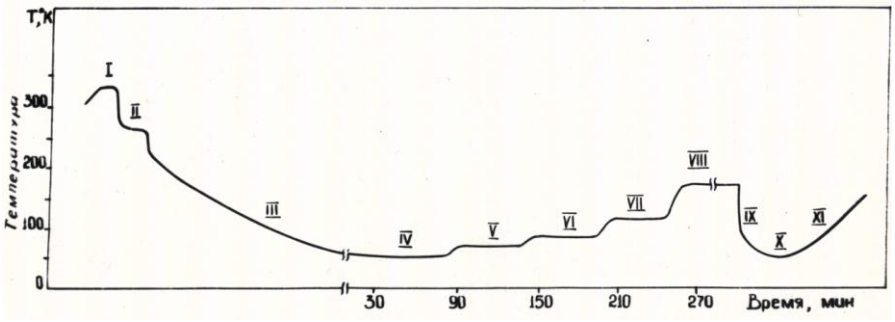

Рисунок 2. Зависимость изменения температуры на поверхности облучаемого контейнера с БМ от тепловой мощности ЯР при облучении в НТБК. I – отсутствует циркуляция газообразного гелия, ЯР не работает. II – циркуляция газообразнного гелия комнатной температуры без мощности ЯР, III – охлаждение газообразного гелия, IV – VIII – постепенное повышение мощности ЯР от 1 до 5 МВт, IX – X – откючение мощности ЯР, XI – Циркуляция неохлаждаемого газообразного гелия.

На **Рисунке 2** показана зависимость температуры БМ от режима облучения в холодном канале. Загрузку контейнера с образцами в канале проводили при " нулевой мощности" ЯР без циркуляции гелия. За этот период происходит небольшое увеличение температуры образцов (на **Рисунке 2** интервал времени 1). Далее начинается циркуляция газообразного гелия и температура начинает быстро понижаться (зона II). Через 25 – 30 мин после начала циркуляции газообразного гелия происходит быстрое снижение температуры образцов (зона III). Зона IV соответствует равновесной температуре образцов при мощности 1 МВт. Зоны V-VIII соответсвуют мощности ЯР 2, 3, 4 , 5 МВт. В зоне IX показано резкое снижение температуры образцов после перевода ЯР в «нулевую мощность». Зона X показывает циркуляцию газообразного гелия без охлаждения. Цикл облучения заканчивается перегрузкой облученных образцов из АЗ ЯР. Как видно из **Рисунка 2** с увеличением мощности ЯР при постоянном заданном расходе газообразного гелия увеличивается температура облучаемых БМ, достигая около 170 К при мощности

5 МВт. Ясно, что при облучении БМ в температурном интервале от 80 до 170 К практически исключена возможность улетучивания химических элементов.

Изменение масс БМ и стандартов сравнения, облученных в неохлаждаемых условиях в течение 70 ч сравнивали с изменением масс аналогичных образцов, отожженных в лабораторных условиях без облучения. Соответствующие данные приведены в **Таблице 1**.

Таблица 1. Изменение массы лиофильно высушенных образцов человеческой крови и стандартов сравнения при 70 ч облучении в ЦСК и отжиге в термостате.

Температура образца, °С	Уменьшение массы (%) при облучении в ЦСК		Температура отжига в термостате, °С	Уменьшение массы (%) при отжиге в термостате	
	Образца	Стандарт		образца	стандарта
190	20	3	150	13	4
260	50	14	250	47	15
300	60	37	300	57	40

Как видно из таблицы, в канале ЦСК при температуре 190 °С изменение массы БМ (в сторону уменьшения) достигает 20 %. При температуре 250 – 260 °С уменьшение масс как в канале, так и в термостате, приблизительно равны и при дальнейшем увеличении температуры до 300 °С составляет около 60 %. Уменьшение массы стандартов сравнения в интервале температур 250 – 300 °С растут, но они ниже, чем в БМ.

Анализируя таблицу можно сказать следующее: 1. Заключение о более интенсивном уменьшении массы биологического образца по сравнению со стандартным образцом до 300 °С, при их облучении в ЦСК ЯР, подтверждается результатами экспериментов без облучения; 2. Изменение масс при облучении БМ и стандартов сравнения в ЦСК ЯР и при отжиге в экспериментах без облучения близки друг другу как для БМ, так и для стандартов сравнения.

Все вышеизложенное дало возможность успешно произвестимисследования в различных областях науки и техники, а также объектов окружающей природы, среди которых, по нашему мнению, заслуживает внимание анализ некоторых минеральных вод Грузии: Боржоми, Саирме,мЗваре, Важас Цкаро и др., в которых определение содержания таких химических элементов, как Sc,мCs, Sr трудно химическими методами. В Институте физикиибылиипроведены специальныеиэкспериментыипоиизучениюиколичественного содержания некоторых химических элементов в разных объктах: в сине-зеленой водоросли цианобактерии S. Platensis, с использованием нейтронного размножителя ПС–1, с потоком тепловых нейтронов 10^6 н / $см^2$ с [8], а также быстрыми нейтронами Объединенного института ядерных исследовании г. Дубны [9]. Было изучено распределение химических элемнтов в тканях и выделенных из них субклеточных компонентах саркоматозных крыс (саркома М–1), было проведено испытание противоопухолевого препарата Оксиэтиленидендифосфоновой кислоты (ОЭДФ). Также были проведены исследования внутриклеточного распределения металлов в печени крыс при общем рентгеновском облучении животных. В наших исследованиях особое значение имеют медико-биологические исследования, связанные с медицинскими учреждениями. Назовем некоторые из них: совместно с учеными кафедры инфекционных болезней

Тбилисского медицинского института, Научно-исследовательского института генерационной функции человека им. И. Ф. Жордания и Онкологического Центра г. Тбилиси были получены заслуживающие внимания специалистов результаты [10 – 12].

Нужно отметить, что в доступной литературе мало работ, посвященных динамике содержаниия микроэлементов при индуцировании опухолей нервной системы, поэтому мы задались целью изучить этот вопрос в эксперименте. Исследования проводились на белых беспородных крысах, весом 90 – 100 г, которым еженедельно в боковую вену хвоста вводилась метилнитрозомочевина в дозе 10 мг / кг. Через каждые 30 дней забивалось по 5-10 крыс и у них бралась кровь и седалищные нервы, а с 3 – 5-го месяца и опухоли периферического нерва, для микроскопического анализа. Высушенные образцы облучались в вышеуказанных условиях интегральным потоком нейтронов 10^{19} н / см^2. Спектры гамма-излучения каждого образца измерялись через 2 – 3 недели с помощью Ge(Li) детектора типа DGL–10E. Определение количественного содержания химических элементов: Fe, Zn, Rb, Cr, Se, Co, Ba, Hg, Ag, Sb было проведено по их долгоживущими радионуклидами.

Таблица 2. Содержание химических элементов (мкг / г сухого образца) в нервной ткани крыс в динамике развития опухоли.

Элемент	Дни отбора проб							
	Контроль	30	60	90	120	150	180	210
Fe	38	94	39	68	126	206	72	73
Zn	16	24	22	116	157	165	182	152
Rb	5	8	7	24	25	31	29	19
Cr	1.3	1.4	1.8	1.8	4	2.9	1.2	2.1
Se	0.3	0.4	0.7	0.8	1.3	1.4	1.7	1.2
Co	0.09	0.5	0.1	0.1	0.5	0.6	0.2	0.1
Ba	16	21	23	13	17	24	15	9
Hg	2.1	2.1	1.25	3	2	0.65	2.8	1
Ag	0.06	0.05	0.07	0.05	0.17	0.06	0.07	0.1
Sb	0.02	0.02	0.02	0.02	0.01	0.01	0.005	0.01

Проведенные исследования показали, что содержание микроэлементов (МЭ) при индуцировании опухолей были больше выражено в нервной ткани и новообразованиях, чем в крови. В первые 1 – 2 месяца содержание МЭ в нервной ткани мало отличались от контроля. В дальнейшем, начиная с 60-го дня эксперимента, резко увеличивалось содержание некоторых определяемых элементов, как Zn, Se, Cr, Ag. Следует отметить, что при морфологическом исследовании к этому времени ни макро- ни микроскопически опухоли не обнаруживались. На 90 -ый день эксперимента было отмечено начало резкого увеличения уровня Zn, Se, Cr, Fe и Rb. Начиная с 4-го месяца микроскопически выявлялись опухоли седалищного нерва, имеющие строение доброкачественной фасцикулярной и ретикулярной нейриномы. К этому периоду в новообразованиях нервов по сравнению с контролем, резко увеличивалось содержание Zn, Se, Cr, Fe, Co, Ag. В дальнейшие сроки, как видно из **Таблицы 2**, по мере уменьшения степени зрелости в индуцированных нейрогенных опухолях – злокачественных нейриномах отмечалось нарастание содержания большинства исследуемых МЭ.

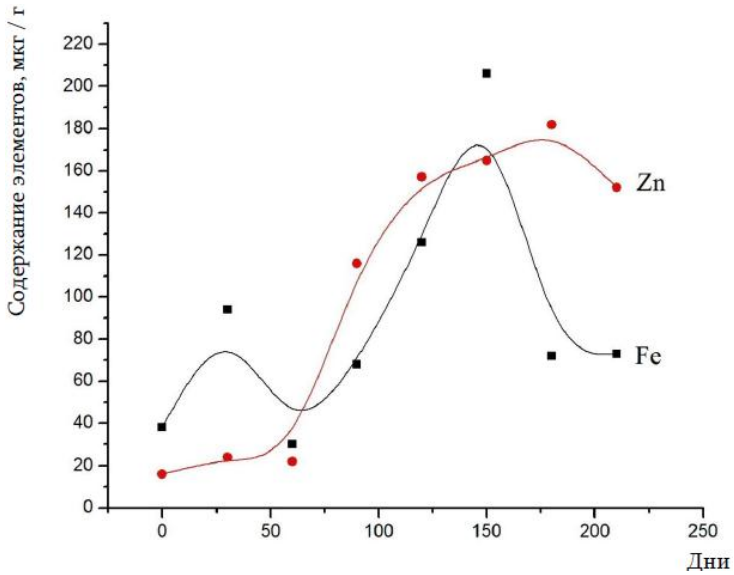

Рисунок 3. Динамика изменения количественного содержания Fe и Zn при индуцировании периферических нервов.

Как видно из **Рисунка 3**, максимальное содержание имеют химические элементы Fe и Znстогда, когда морфологически опухоль еще не выявляется, а нейтронно-активационным методом можно уже определить начало опухолевого роста, что имеет диагностическое и прогностическое значение. Таким образом, исследование содержания МЭ может служить целям дифференциальной диагностики степени анаплазии опухолей периферических нервов.

В заключении можно сказать, что вышеизложенные соображения указывают о правильном проведении ИНАА химических элементов в биологических материалах как животного происхождения, так и объектов окружающей среды.

Ссылки

1. E. Sabbioni , R. Pietra, J. Edel. J. Rad. Nucl. Chem., 1987, 110, 2, 573-581.
2. А. А. Смейлс. В сб.: Анализ следов элементов. 1961, Москва, ИЛ, 493-519.
3. D. Drune, K. Samsahl, P. Wester. Clinnica Chim. Acta, 1966, 13, 3, 285-291.
4. D. Drune, K. Jirlow. Radiochim. Acta, 1967, 8, 3, 161-164.
5. Л. М. Мосулишвили, Н. Е. Кучава. Атомная энергия, 1979, 47, 6, 392-393.
6. Н. Е. Кучава. Сообщ. АН Груз. ССР, 1988, 130, 2, 305-308.
7. А. А. Смейлс. В сб.: Анализ следовых элементов. 1961, Москва, ИЛ, 493-519.
8. N. Kuchava. Bull. Georg. Acad. Sci., 2004, 169, 3, 490-492.
9. T. L. Kalabegishvili, I. G. Murusidze, E. I. Kirkesali, A. N. Rcheulishvili, E. N. Ginturi, E. S. Gelagutashvili, N. E. Kuchava, N. B. Bagdavadze, D. G. Pataraya, M. A. Gurielidze, M. B. Frontasyeva, I. I. Zinicovscaia, S. S. Pavlov, V. T. Gristina. J. Life Sci., 2013, 7, 2, 110-122.
10. E. Sh. Botsvadze, L. M. Mosulishvili, N. E. Kuchava, E. N. Ginturi. Phys. Med. & Biol., 1969, 14, 1, 19-26.
11. L. K. Tkeshelashvili, E. V. Bochorishvili, N. E. Kuchava. J. Trace Elements Exp. Med., 1989, 2, 2/3, 178-180.
12. Э. Л. Андроникашвили, Л. К. Шарашидзе, Л. М. Мосулишвили, Д. Ш. Бениашвили, Н. Е. Кучава, Ш. Д. Маисурадзе. Сообщ. АН Груз. ССР, 1978, 89, 2, 473-476.

კოვალენტური და იონური კრისტალების დნობის პროცესის განხილვა ახლებური მიდგომით

ზ. გოგუა, მ. ჩიხლაძე, ო. კეთილაძე

საქართველოს ტექნიკური უნივერსიტეტი
საინჟინრო ფიზიკის დეპარტამენტი
თბილისი, საქართველო

მიღებულია 2015 წლის 21 ოქტომბერს

ანოტაცია

კოვალენტური კრისტალებისათვის მოცემულია დნობის ტემპერატურული პროცესის განხილვაში არსებული შეხედულებათა შორის წინააღმდეგობების გადალახვის გზები. ასევე, იონური კრისტალებისათვის შემოთავაზებულია დნობის ტემპერატურის გამოთვლა ახლებური მიდგომით.

შესავალი

ზოგადად, როგორც ცნობილია, დნობას ვუწოდებთ ნივთიერების გადასვლას მყარი აგრეგატული მდგომარეობიდან თხევად აგრეგატულ მდგომარეობაში. აქვე დავაფიქსირებთ იმასაც, რომ მყარ მდგომარეობაში ნივთიერება ინარჩუნებს ფორმას და რა თქმა უნდა, მოცულობასაც, ხოლო თხევად აგრეგატულ მდგომარეობაში კი მხოლოდ მოცულობას. დნობის საყოველთაოდ მიღებული სითბური მექანიზმი ასე ჩამოყალიბდება: ნივთიერებას გადაეცემა სითბო, რის შედეგადაც იზრდება მყარი ნივთიერების კვანძებში მყოფი ატომების რხევის ამპლიტუდა, რის გამოც ხდება ნივთიერების გაფართოება და, ამავე დროს, მისი ატომების რხევის ენერგიის ზრდის შედეგად იზრდება ნივთიერების ტემპერატურა დნობის ტემპერატურამდე. ამის შემდეგ ტემპერატურა არის უცვლელი და იწყება ნივთიერების დნობის პროცესი. ამ დროს წყდება ატომებს შორის ბმები სანამ მთელი ნივთიერება არ დადნება. ასეთია დნობის სითბური მექანიზმის მოკლე აღწერა. ამ მექანიზმს ერთი ძალზე სუსტი ადგილი აქვს. კერძოდ ის, რომ მასში დნობის პროცესად მიჩნეულია ატომებს შორის ბმების რღვევა. ეს აზრი რომ შეუსაბამოა რეალობასთან ამას ისიც მოწმობს, რომ დნობის სითბოს ბევრად აჭარბებს სუბლიმაციის სითბო. სუბლიმაციის სითბო პირდაპირ განსაზღვრავს ნივთიერების ატომებს შორის ბმის ენერგიას. გარდა ამისა, ატომებს შორის დნობის დროს ბმები რომ წყდებოდეს თხევადი ნივთიერება ვერ შეინარჩუნებდა მოცულობას. ასე, რომ თხევად მდგომარეობაში ატომებს შორის ბმები კი არ წყდება, არამედ იგი გარდაქმნილია მყარ მდგომარეობაში არსებული ბმების სახეობიდან.

ის დნობის პროცესი, რომ მხოლოდ გადაცემული სითბური ენერგიის გამო არ ხდება, ამის მაგალითებია ნივთიერების დნობის შესაძლებლობა მასზე სინათლის დასხივებით, მასში ელექტრონების ინჟექციით და სხვა. ამ დროს ნივთიერების ტემპერატურა შეიძლება საერთოდ არ შეიცვალოს ან მინიმუმ ისე არ შეიცვალოს, რომ დნობის ტემპერატურას გაუტოლდეს, როგორც ეს საჭიროა დნობის სითბური მექანიზმის შემთხვევაში.

დნობის სხვა მექანიზმების ანალიზამდე შევეხებით ნივთიერებაში ატომთა შორის ბმების თეორიის ელემენტებს.

განვიხილოთ უმარტივესი – წყალბადის მოლეკულაში ატომებს შორის განხორციელებული – ბმა LCAO მიახლოებაში. წყალბადის ეს ორი ატომი, რომლებიც მოლეკულას ქმნის, როცა დაცილებულია ერთმანეთისაგან უსასრულოდ დიდ მანძილზე, შედგება ერთი პროტონისა და მის გარშემო ორბიტაზე მოძრავი ელექტრონისაგან; რომელი იმყოფება IS კვანტურ მდგომარეობაში, რომელშიც მისი ტალღური ფუნქციებია $\Psi_1(r)$ და $\Psi_2(r)$. წყალბადის მოლეკულის ტალღური ფუნქცია LCAO მიახლოებაში არის

$$\Psi(r) = C_1\Psi_1(r) + C_2\Psi_2(r) = \sum_{i=1}^{2} C_1\Psi_1(r)$$

ენერგიის ვარიაციის შედეგად ვღებულობთ განტოლებას:

$$\delta\frac{\langle\Psi(r)|H(r)\rangle}{\langle\Psi(r)\Psi(r)\rangle} = \delta\frac{\sum_{i=1}^{2}\sum_{j=1} C_i^* C_j\langle j|H|i\rangle}{\sum_{i,j=1}^{2} C_i^* C_j} = 0\,, \qquad (1)$$

სადაც, H არის სისტემის ჰამილტონიანი. $<j|H|i>$ კი არის i კვანტური მდგომარეობიდან j კვანტურ მდგომარეობაში გადასვლის მატრიცული ელემენტი. (1) განტოლებიდან ვღებულობთ სეკულარულ განტოლებას:

$$det\left(\mathrm{H}_{ij} - \mathrm{E}\delta_{ij}\right) = 0. \quad i = 1,\ 2 \quad j = 1,\ 2, \qquad (2)$$

სადაც, $H_{ij} = \langle j|H|i\rangle$, δ_{ij} არის ერთეულოვანი მატრიცა. თუ გავითვალისწინებთ რომ $H_{11} = \langle 1|H|1\rangle = \langle 2|H|2\rangle = \varepsilon_S$ არის წყალბადის ატომის S მდგომარეობის ენერგია $H_{12} = = H_{21=}\langle 1|H|2\rangle = \langle 2|H|1\rangle = -V_K$ – ატომებს შორის კოვალენტური ბმის ენერგია, (2) სეკულარული განტოლება წყალბადის მოლეკულის ენერგიისათვის გვაძლევს შემდეგს:

$$E = \varepsilon_S \pm V_2 \qquad (3)$$

აქ $\varepsilon_S + V_2 = E_a$ არის ანტიმბელ მდგომარეობის ენერგია, ხოლო $\varepsilon_S - V_2 = E_b$ კი – მბელი მდგომარეობის ენერგიაა.

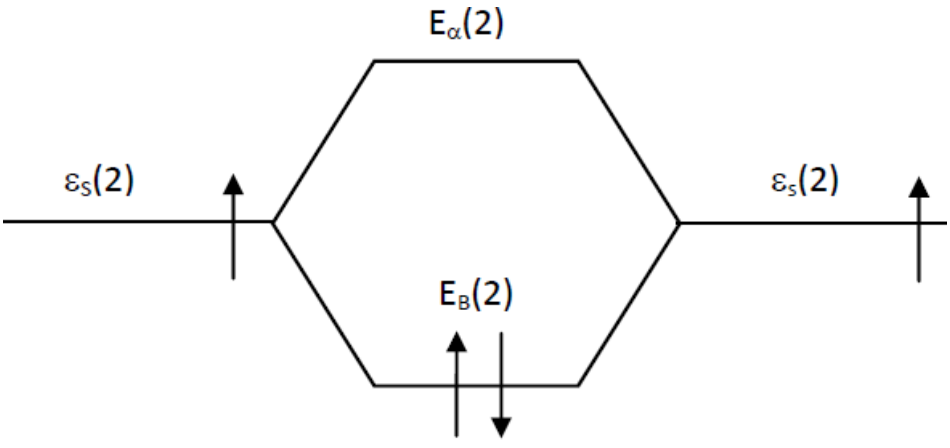

ნახაზი 1.

სქემატურად წყალბადის მოლეკულის შექმნის LCAO მოდელისეული სურათი მოიცემა ისე, როგორც ეს არის **ნახაზზე 1**

იზოლირებულ წყალბადის ატომებს აქვთ ერთი ენერგეტიკული მდგომარეობა ε_S რომელზეც 2–2 ადგილია, მაგრამ მათზე იმყოფება 1–1 ელექტრონი. ატომების ერთმანეთთან მიახლოებისას ურთიერთქმედების შედეგად ε_S მდგომარეობის ენერგია იხლიჩება ორ ენერგეტიკულ დონედ: ქვედა მბმელ და ზედა ანტიმბმელ დონეებად. თითოეულ მათგანზე არის 2-2 ადგილი. ენერგიის მინიმუმის პრინციპის თანახმად, ორივე ატომის ორივე ელექტრონი დაიკავებს ქვედა დონეს. ზედა დონე კი იქნება თავისუფალი. თუ ჩვენ ერთ ელექტრონს მოვაცილებთ მოლეკულას, ბმის ენერგია 4.3 ევ ნაცვლად გახდება 2.1 ევ. ე.ი. შემცირდება. მაშასადამე, წყალბადის მოლეკულაში ელექტრონის ვაკანსიის გაჩენა ანუ მასთან "ხვრელის" მოსვლა ბმას ამცირებს, ხოლო თუ ჩვენ წყალბადის მოლეკულას მივუერთებთ ერთ ელექტრონს, იგი დაიკავებს ანტიმბმელ დონეზეს, პაულის პრინციპის შესაბამისად. ამ შემთხვევაში წყალბადის უკვე უარყოფითად დამუხტული მოლეკულის H_2^--ის ბმის ენერგიიდან, 0.18 ევ, გამოდის მეტად საინტერესო დასკვნა, რომ "ხვრელი" ნაკლებად ამცირებს მოლეკულის ბმის ენერგიას, ვიდრე ანტიმბმელი ელექტრონი. ასევე ცნობილია ისიც, რომ თუ ერთ-ერთ ელექტრონს გადავიყვანთ მბმელი დონიდან ანტიმბმელ დონეზე, მოლეკულა იშლება.

კოვალენტურკრისტალთა დნობის შესახებ

ეს მიდგომა განზოგადოებულია ბევრად უფრო რთული მოლეკულებისათვის და სხვათა შორის, მყარი სხეულისათვისაც. მყარი სხეული ამ დროს წარმოდგენილია როგორც დიდი მოლეკულა.

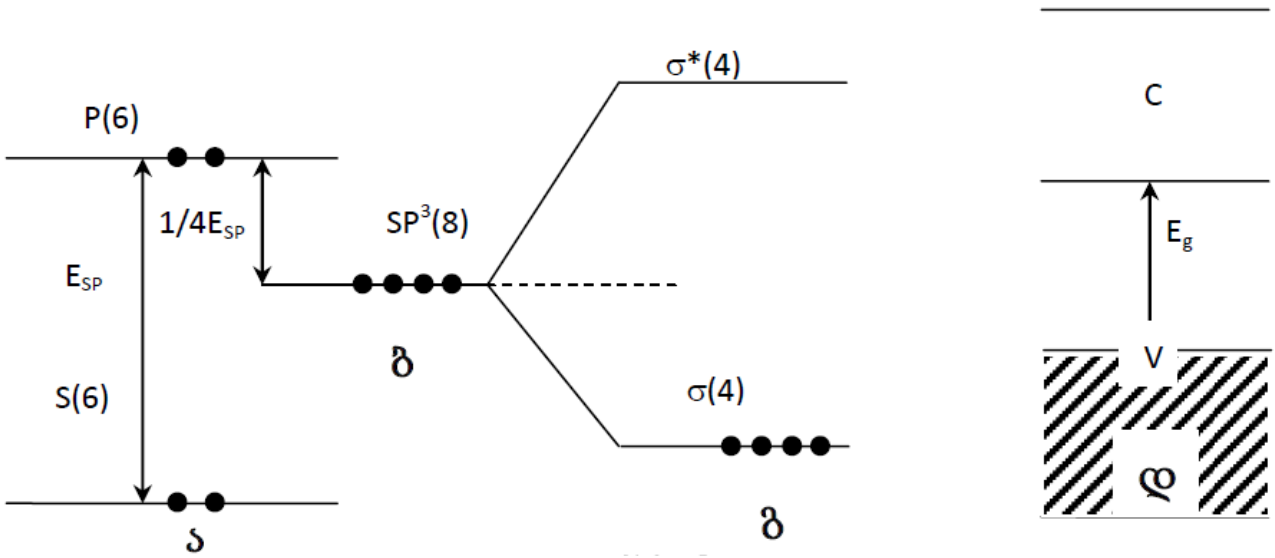

ნახაზი 2.

ნახაზზე 2ა მოცემულია მენდელეევის პერიოდული სისტემის IV ჯგუფის ელემენტებისათვის იზოლირებული ატომის ვალენტური შრის *S* და *P* მდგომარეობებს შორის ენერგეტიკული დაცილება. *S* მდგომარეობაში არის 2 ადგილი და მათზე 2 ელექტრონია: *P* მგომარეობაშიში არის 6 ადგილი და მათზეც მხოლოდ 2 ელექტრონია. მეორე ატომთან მისი ურთიერთქმედების შედეგად ორი ატომის *S* და *P* დონეებისაგან იქმნება SP^3 ვიტუალური დონე, რომელზეც ელექტრონებისათვის ადგილების

რაოდენობა არის 8 და მასზე არის 4 ელექტრონი. ურთიერთქმედების შედეგად SP^3 დონე იხლიჩება ორ მბმელ σ და ანტიმბმელ დონეებად **ნახაზზე 2გ**. ატომის SP^3 დონეზე მყოფი ოთხივე ელექტრონი რჩმ დასხდეს მბმელ დონეზე, მაშინ ანტიმბმელი დონე იქნება ცარიელი. ასეთი, ელექტრონებით გაჯერებული, მბმელი დონეები გვაძლევს ნივთიერებაში შევსებულ, ე.ი. ვალენტურ ზონას, ხოლო ცარიელი ანტიმბმელი დონეები – გამტარობის C ზონას (**ნახაზი 2დ**). ვალენტური ზონის ზედა კიდეს შეესაბამება სუფთა P მდგომარეობები, ხოლო გამტარობის ზონის ქვედა კიდეს – სუფთა S მდგომარეობები. P სიმეტრიის ტალღური ფუნქციები მკაცრად მიმართულნი არიან, ხოლო S სიმეტრიის ტალღური ფუნქციები სფერული სიმეტრიისაა. ეს დასკვნა კარგად ჩანს S და P მდგომარეობების შესაბამისი თერმების ატომთაშორის მანძილზე დამოკიდებულების დიაგრამიდან.

კოვალენტურ SP^3 ტიპის ბმის კრისტალურ ნივთიერებებში LCAO მიავლოებაში ერთ-ერთი მიმართულებით ტალღური ფუნქცია მოიცემა ასე:

$$\Psi(r) = \frac{1}{2}\Psi_S(r) + \frac{\sqrt{3}}{2}\Psi_{px}(r)\,. \qquad (4)$$

აქედან ნათლად ჩანს, რომ S მდგომარეობის წვლილი ამ ბმაში 3-ჯერ ნაკლებია P მდგომარეობის წვლილზე. თუ მოცემულ ატომთან გამოჩნდება მეხუთე ელექტრონი (ინჟექციით ან მინარევული ატომიდან), მაშინ იგი დაიკავებს SP^3-ის ანტიმბმელ ნახლეჩზს. თუ საბაზისო ფუნქციებად გამოვიყენებთ SP^3 ჰიბრიდულ ბმის ტალღურ ფუნქციებს და გავითვალისწინებთ პაულის პრინციპს, LCAO ასეთი მდგომარეობისათვის (3) ნაცვლად გვაძლევს ასეთ ფუნქციას:

$$\Psi_1^1(r) = \frac{1}{2\sqrt{5}}\{(\sqrt{2}+3)\Psi_s(r) + \sqrt{3}(\sqrt{2}-1)\Psi_p(x)\}. \qquad (5)$$

ასეთ ბმაში S-ის წვლილი P-სთან შედარებით ~ 30-ჯერ მეტია. მაშასადამე, ანტიმბნელი ელექტრონის არსებობა მოცემულ ატომთან ძლიერ ცვლის მის კვანტურ მდგომარეობას, კერძოდ, მკაცრად მიმართული SP^3 ჰიბრიდული ბმები ხდება თითქმის სფერული სიმეტრიის. რაც შეეხება ბმის ენერგიის ატომებს შორის, იგი დაახლოებით 2-ჯერ მცირდება, მაგრამ თავისუფლების ხარისხი ატომებისა ერთმანეთის მიმართ, როცა მათთან ანტიმბმელ დონეზე იმყოფება ელექტრონ,ი ძლიერ იზრდება.

მაშასადამე, ვაკეთებთ ასეთ დასკვნას: კოვალენტურ კრისტალებში თუ მოცემულ ატომებთან ბმებშია ანტიმბმელი ნაწილაკის (ანტიმბმელი ელექტრონი ან ხვრელი), მაშინ იცვლება ატომის ბმის კვანტური მდგომარეობა (იგი უფრო სფერულ-სიმეტრიული ხდება) და მცირდება ატომებს შორის ბმის ენერგია. ნივთიერების დნობისათვის მნიშვნელობა აქვს ატომის თავისუფლების ხარისხის ცვლილებას, კერძოდ, მათი ბმის ორბიტალის "გასფერულებას" და არა – ბმის ენერგიის ცვლილებას, თუნდაც ძლიერ შემცირებას.

იონურ კრისტალთა დნობის შესახებ

კრისტალურ მყარ სხეულებს, ნივთიერებათა სხვა აგრეგატული მდგომარეობიდან (სითხე, აირი, პლაზმა) განსხვავებით გააჩნია სტაბილური ფორმა და ისინი ხასიათდება ნაწილაკთა (ატომები, იონები, მოლეკულები) სითბური მოძრაობით წონასწორობის მახლობლობლად. მყარი სხეულის სტრუქტურის შექმნას განაპირობებს მის ნაწილაკებს შორის მოქმედი ძალები. ამ ძალათა ხასიათი, პირველ რიგში, განისაზღვრება ნაწილაკთა ელექტრონული გარსების აგებულებით. ნაწილაკთა

ურთიერთქმედების მიხედვით კრისტალებში განიხილავენ ოთხი ტიპის ბმას: კოვალენტურს, იონურს, ლითონურს და წყალბადისას. იონური ბმა წარმოიქმნება იონური კრისტალების დადებით და უარყოფით იონებს შორის კულონური ურთიერთქმედების შედეგად. იონური კრისტალების ტიპიური წარმომადგენლებია ტუტე ლითონთა ჰალოგენები: ლითიუმის, ნატრიუმის, კალიუმის ფტორიდები და ქლორიდები. ვინაიდან ჰალოგენები ძლიერი დამჟანგველებია, მათ მიტაცებული აქვთ ტუტე ლითონთა გარე შრის ელექტრონი (Li^+F^-, Na^+F^-, K^+F^-, Li^+Cl^-, Na^+Cl^-, K^+Cl^-). ამ კრისტალების სტრუქტურა მიეკუთვნება მარტივ კუბურ სისტემას.

რადგან კულონური ურთიერთქმედების ენერგია, $\pm kq_e^2/r$, ერთნაირი ნიშნის იონთა შემთხვევაში (განზიდვა) დადებითია, ხოლო საპირისპირო ნიშნის იონების დროს (მიზიდვა) – უარყოფითი, ამიტომ ნებისმიერი იონის მეზობელ იონებთან ურთიერთქმედების ენერგია წარმოდგება ნიშანცვლადი წევრებიან სწრაფად კრებადი მწკრივის სახით. კრისტალიდან პირობითად გამოვყოთ 125 იონისგან შემდგარი ელემენტი – კუბი, რომლის წიბო $4a$ ტოლია (a – მესრის პერიმეტრია). **ნახაზზე 3** მოცემულია ამ კუბის ცენტრზე გამავალი ჰორიზონტალური კვეთა. გამოვთვალოთ ურთიერთქმედების ენერგია ცენტრში მყოფი იონის (ნახაზზე ვარსკლავითაა აღნიშნული) მეზობელ 124 იონთან. დასაწყისში განვიხილოთ მისი ურთიერთქმედება უახლოეს 26 იონთან $2a$ წიბოს მქონე კუბის შიგნით (**ნახაზზე 3** შემოსაზღვრულია წყვეტილი ხაზით). იგი საპირისპირო ნიშნის მქონე 6 იონთან დაშორებული აღმოჩნდება $r = a$ მანძილით და $r = \sqrt{3}a$ მანძილით – 8 იონთან, ხოლო იმავე ნიშნის 12 იონთან – $r = \sqrt{2}a$ მანძილით. შესაბამისად, ამ იონის მეზობელ 26 იონთან ურთიერთქმედების ენერგია იქნება:

$$W_{26} = k\frac{q_e^2}{a}\left(-6-8\frac{1}{\sqrt{3}}+12\frac{1}{\sqrt{2}}\right)\approx -2.12k\frac{q_e^2}{a}. \qquad (6)$$

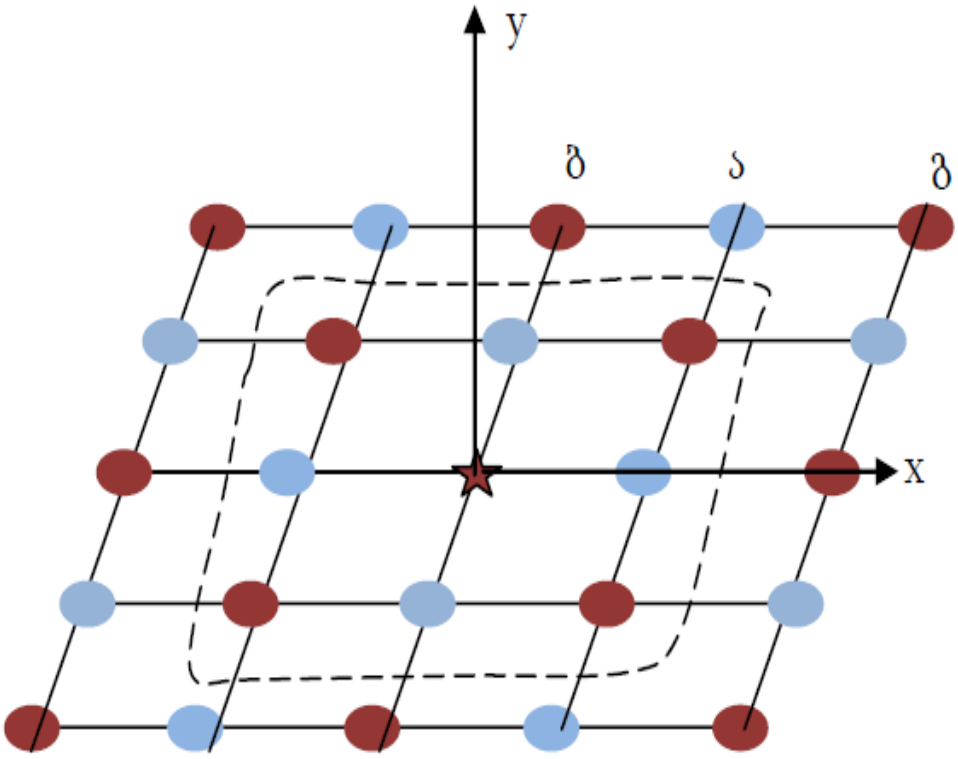

ნახაზი 3.

ამ კუბის გარეთ არსებულ 98 იონთან განსახილველ იონს გააჩნია შემდეგი მიმართება:

ძირითადი სიბრტყე ($x=\pm 2a;\quad y=0$): ა. მიზიდვა – 8 იონი, $r=\sqrt{5}a$; ბ. განზიდვა – 4 იონი, $r=2a$; გ. განზიდვა – 4 იონი, $r=\sqrt{8}a$.

ზედა + ქვედა სიბრტყე ($x=\pm 2a;\quad y=\pm 2a$): ა. მიზიდვა – 16 იონი, $r=3a$; ბ. განზიდვა – 8, იონი $r=\sqrt{8}a$. გ. განზიდვა – 8 იონი, $r=\sqrt{12}a$.

ზედა + ქვედა სიბრტყე ($x=\pm 2a;\quad y=\pm a$): ა. მიზიდვა – 8 იონი, $r=3a$; ბ. მიზიდვა – 8 იონი, $r=5a$; გ. განზიდვა – 16 იონი. $r=\sqrt{6}a$.

ზედა + ქვედა სიბრტყე ($x=\pm a;\quad y=\pm 2a$): ა. განზიდვა – 2 იონი, $r=2a$; ბ. განზიდვა – 8 იონი, $r=\sqrt{6}a$, გ. მიზიდვა – 8 იონი, $r=\sqrt{5}a$.

შესაბამისად, მოცემული იონის მათთან ურთიერთქმედების ენერგია იქნება:

$$W_{98}=k\frac{q_e^2}{a}\left(-8\cdot\frac{1}{\sqrt{5}}+4\frac{1}{2}+4\frac{1}{\sqrt{8}}-16\cdot\frac{1}{3}+8\frac{1}{\sqrt{8}}+8\cdot\frac{1}{\sqrt{12}}-8\cdot\frac{1}{3}-8\frac{1}{5}+\right.$$
$$\left.+16\frac{1}{\sqrt{6}}+\frac{2}{2}+8\frac{1}{\sqrt{6}}-8\frac{1}{\sqrt{5}}\right)=-0{,}76k\frac{q_e^2}{a}, \tag{7}$$

რადგან $|W_{\text{el}}|\sim r^{-1}$ ამიტომ უგულვებელვყოთ შემდგომ იონებთან ($4a$ წიბოს მქონე კუბის გარეთ) ურთიერთქმედების ენერგია. ენერგიათა შეკრებადობიდან გამომდინარე, მოცემული იონის დანარჩენ იონებთან ურთიერთქმედების პოტენციალური ენერგია იქნება:

$$W=W_{26}+W_{98}\approx -2.88k\frac{q_e^2}{a}\approx -6.64\cdot\frac{1}{a}\text{ ჯოული}. \tag{8}$$

ცხადია, ეს ენერგია უარყოფითია, ანუ იონი იმყოფება ბმულ-ფიქსირებულ მდგომარეობაში. გამოვითვალოთ იონთა ეფექტური რაოდენობა 125 იონისაგან შემდგარი ელემენტში, გავითვალისწინოთ, რომ ერთ იონს უშუალოდ ქიმიური კავშირი აქვს 6 უახლოეს იონთან. ამიტომ ზედაპირზე მყოფი იონებისათვის:

$$N_{\text{ზედ}}=8\cdot\frac{3}{6}+12\cdot 3\cdot\frac{4}{6}+9\cdot 6\cdot\frac{5}{6}=4+24+45=73. \tag{9}$$

კრისტალის გათბობისას იზრდება ნივთიერების შინაგანი ენერგია და როდესაც ტემპერატურა გაუტოლდება ისეთ სიდიდეს, როცა ადგილი ექნება ტოლობას:

$$W=\sigma\cdot N_{\text{ზედ}}\cdot\left(\frac{3}{2}\cdot kT\right), \tag{10}$$

მოცემული იონი ბმიდან განთავისუფლდება ანუ კრისტალი დაიწყებს დნობას.

დავადგინოთ σ კოეფიციენტის ფიზიკური აზრი. ცნობილია, რომ ზემოთ ჩამოთვლილი ოთხი ტიპის ბმიდან კრისტალებში "სუფთა" სახით არცერთი არ არსებობს. იონურ კრისტალებს მიაკუთვნებენ იმ კრისტალებს, სადაც დომინირებს იონური ბმა და ა.შ. იონურ კრისტალის შემადგენელი ელემენტები ხასიათდება მკვეთრად განსხვავებული ელექტროუარყოფითობით (გავიხსენოთ: ესაა ატომის უნარი თავისი გარე გარსის შევსებისთვის მიიზიდოს მეზობელი ატომის ელექტრონები). ტუტე ლითონების ელექტროუარყოფითობაა: Li – 0.98, Na – 0.93, K – 0.82. ჰალოგენებისათვის F – 3.98, Cl – 3.16. იონური ბმა მით უფრო დამახასიათებელია, რაც მეტია მოცემული იონური კრისტალის შემადგენელ ატომთა ელექტროუარყოფითობების ფარდობა β (იხ. **ცხრილი 1**).

ცხრილი 1.

	β	σ	a , 10^{-9} მ	$T_{\text{თეორია}}$	T	δT, %
NaF	4.06	0.84	0.463	1266	1129	11
NaCl	3.22	0.66	0.562	1073	1184	10
LiF	4.02	0.83	0.403	1121	1312	17
LiCl	3.19	0.66	0.514	887	1294	46
KF	4.85	1	0.535	1130	821	27
KCl	3.85	0.79	0.555	1123	1001	11

რადგან β ყველაზე დიდია KF შემთხვევაში, ჩავთვალოთ, რომ იგი "სუფთა" იონური კრისტალია და მის მიმართ სხვა კრისტალთა იონურობა დავახასიათოთ შემდეგი ფარდობით $\sigma = \beta / \beta_{\text{KF}}$. (8) და (10) გამოსახულებების გატოლებით მიიღება ტუტე ლითონთა ჰალოგენების დნობის ტემპერატურის შემდეგი ფორმულა:

$$T = \frac{0.439 \cdot 10^{-6}}{a\sigma}. \qquad (11)$$

როგორც ცხრილიდან ჩანს ამოსახულებიდან (11) მიღებული შედეგები დასაშვებ ცდომილებაშია ექსპერიმენტულ შედეგებთან (გამონაკლისია LiCl). თუმცა ცხადია, მოცემული მსჯელობა საჭიროებს შემდგომ დამუშავებას.

დასკვნა:

ნაშრომში მიღებულ შედეგებს არ გააჩნიათ სიზუსტეზე დიდი პრეტენზიები, თუმცა, ნაშრომის ღირსებას ნამდვილად წარმოადგენს, ამ უძველეს და უმნიშვნელოვანესი საკითხის კვლევაში უზუსტობების დანახვა და, ჩვენი აზრით, ამ საკითხის კვლევისადმი მართებული მიდგომების ჩამოყალიბება.

დამოწმებანი

1. А. Харрисон. Электронная структура и свойства твердых тел. 1983, Москва. 311 стр.
2. К. Дей, Д. Селбин. Теоретическая неорганическая химия. 1976, Москва, 576 стр.
3. Z. Gogua, G. Kantidze. Bull. Georg. Natl. Acad. Sci., 2006, 2, 4, 70-77.
4. Г. Г. Филиппов, А. И. Горбунов. Новый подход к выбору практической шкалы электроотрицательностей атомов. Росс. хим. журн., 1995, 39, 2, 39-42.

ТЕРМОСТОЙКИЕ КОМПОЗИЦИОННЫЕ НАНОМАТЕРИАЛЫ НА ОСНОВЕ ТВЕРДОГО МАГНИЙФОСФАТНОГО СВЯЗУЮЩЕГО

Н. С. Апанасевич [1], К. Н. Лапко [1], А. Н. Кудлаш [1], А. А. Сокол [1], В. А. Ломоносов [1], А. И. Лесникович [1], А. О. Плющ [2], П. П. Кужир [2], С. А. Максименко [2]

[1] Белорусский государственный университет
Научно-исследовательский институт физико-химических проблем
Минск, Беларусь
lapkokn@bsu.by
[2] Белорусский государственный университет
Институт ядерных проблем
Минск, Беларусь
polina.kuzhir@gmail.com

Принята 9 ноября 2015 года

Аннотация

Исследованы термостойкие композиционные материалы на основе твердого магнийфосфатного связующего (ТФМ) с многослойными углеродными нанотрубками (МУНТ). Наиболее оптимальное содержание твердого фосфатного связующего в изучаемой системе составляет 15 – 20 масс. %. Процесс окисления МУНТ в фосфатной композиции начинается на 150 – 200 °С выше, чем индивидуальных нанотрубок. Термообработка композиции на основе ТФМ с МУНТ до 800 °С приводит к последовательному увеличению прочности в 2-раза. Значения прочности и электропроводности композитов с МУНТ на основе ТФМ выше, чем аналогичных композитов на основе жидкого алюмофосфатного связующего (АФС).

Введение

Благодаря высокой тепло- и электропроводности, значительной химической стабильности и уникальной механической прочности углеродные нанотрубки представляют большой научный и практический интерес [1]. Одним из перспективных направлений современного материаловедения является создание электропроводящих термостойких неорганических композиционных материалов с углеродными нанотрубками.

Анализ литературных данных [2 – 5] показывает, что из большого многообразия термостойких неорганических материалов фосфатные являются наиболее технологичными. Они имеют низкие температуры отверждения и хорошо сочетаются с различными наполнителями, что в свою очередь, дает возможность широкого модифицирования их составов.

В работах [6 – 7] в качестве основы для приготовления композиционных материалов были использованы жидкое алюмофосфатное связующее и наполнитель, в

состав которого входили корунд (α-$A1_2O_3$) и нитрид алюминия. В качестве модифицирующих добавок использовали многослойные углеродные нанотрубки. Средний размер МУНТ: длина 10 – 20 мкм, толщина 9 – 20 нм. Установлено, что введение 2 масс. % МУНТ в термостойкую фосфатную матрицу приводит к росту проводимости на 13 порядков по сравнению с исходным материалом [6]. Получен соответствующий патент [7] на электропроводящие термостойкие фосфатные композиционные материалы.

При изготовлении материалов на основе жидких фосфатных связующих приходится сталкиваться с рядом трудностей. Такие связующие, как правило, неустойчивы при хранении: со временем в жидком связующем происходят процессы кристаллизации, приводящие к образованию довольно прочных осадков, и, как следствие этого, происходит изменение атомного отношения фосфора к металлу (P / Me) в оставшейся жидкой фазе. Последнее требует корректировки соотношения наполнитель / связка при изготовлении композиций. Еще одна трудность в процессе изготовления материалов связана с оптимальным подбором наполнителей по дисперсности, что существенным образом сказывается на прочностных свойствах получаемых материалов [8].

В отличие от технологии изготовления традиционных растворных смесей способ приготовления сухих смесей позволяет получать последние со строго оптимизированным фракционным составом наполнителей и точным дозированием исходных компонентов. Точное соблюдение требований по подготовке исходного сырья, его дозированию и перемешиванию обеспечивает получение сухих смесей и конечной продукции на их основе стабильно высокого качества [8].

С целью усовершенствования методики получения композитных материалов на основе фосфатных связующих в данной работе исследована возможность использования в качестве связующего твердого фосфата магния состава $Mg(H_2PO_4)_2 \cdot 4H_2O$.

Методика эксперимента

В работе использовали следующие реактивы: корунд α-Al_2O_3, нитрид алюминия AlN, дигидрофосфат магния $Mg(H_2PO_4)_2 \cdot 4H_2O$, многослойные углеродные нанотрубки (длина 10 – 20 мкм, толщина 9 – 20 нм). Основной наполнитель готовили путем смешивания порошков корунда α-Al_2O_3 и нитрида алюминия. Композит готовили путем смешивания определенных количеств основного наполнителя, МУНТ, твердого фосфатного связующего и воды. Установлено, что оптимальное содержание воды составляет 5 – 10 %. Добавление меньшего количества воды приводит к разупрочнению образцов, при введении воды более 10 % перетираемая масса становится пластичной, что существенно затрудняет дальнейшую обработку. Компоненты, используемые для изготовления композиционного материала, тщательно перетирали в ступке до получения однородной смеси, которую затем просеивали и прессовали. Образцы композитов отверждали при комнатной температуре в течение суток и затем термообрабатывали.

Физико-химические методы исследования

Сканирующая электронная микроскопия (СЭМ) образцов фосфатных композитов проведена на микроскопе LEO–1455 VP.

Термогравиметрические исследования выполнены на анализаторе NETZSCH STA 449 при нагревании образцов от 25 до 1000 °C со скоростью нагрева 10 ° / мин.

Навеска образца составляла 5 – 15 мг. Образцы для исследования готовили путем их растирания до порошкообразного состояния.

Испытания на прочность проведены на универсальной испытательной машине Instron 1195 при усилии нагружения 10 и 20 кН со скоростью 5 мм / мин. Погрешность измерения составляла 1 %. Прочностные свойства материалов изучали по величине предела прочности на сжатие ($\sigma_{сж.}$) образцов исходных фосфатных композитов (столбики высотой 10 и диаметром 10 мм) и образцов фосфатных композитов с МУНТ (высота 6 и диаметр 6 мм).

Электрическое сопротивление образцов измеряли четырехконтактным методом с помощью измерителя LCR meter HP4284A. Для измерения использовали две эквивалентные схемы. В первой измеряли емкость образца C и тангенс угла потерь $\mathrm{tg}\delta$, во второй схеме измеряли комплексный импеданс $Z^* = R + jX$, где R – активное сопротивление, jX – реактивное сопротивление. Образец представлял собой брусок поперечными размерами 7×3 мм, толщина образца составляла 0.7 мм. Для обеспечения контакта на поверхность образца наносили серебряную пасту.

Результаты и обсуждение результатов

Как известно, одной из трудностей, связанных с применением углеродных нанотрубок, является их равномерное диспергирование в матрице. Для изучения степени однородности распределения МУНТ в фосфатной матрице проведена СЭМ фосфатных композитов на основе ТФМ с 2 и 10 масс. % МУНТ. Микрофотографии представлены на **Рисунках 1** и **2**.

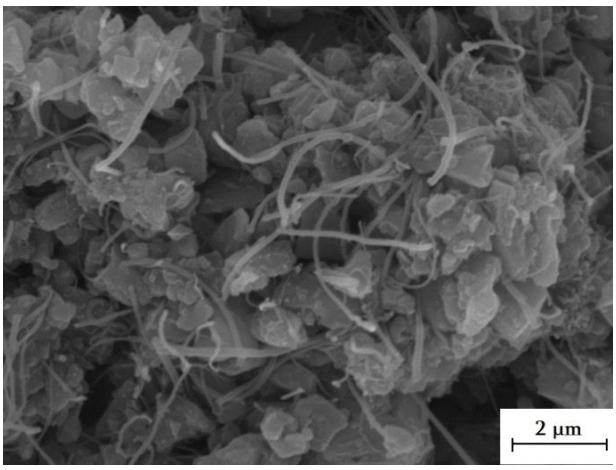

Рисунок 1. Микрофотография композита на основе ТФМ с 2 масс. % МУНТ (увеличение 20000).

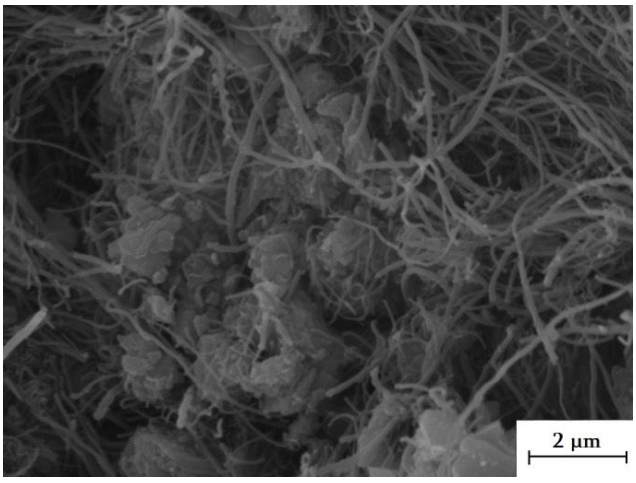

Рисунок 2. Микрофотография композита на основе ТФМ с 10 масс. % МУНТ (увеличение 20000).

Из приведенных микрофотографий следует, что МУНТ достаточно равномерно распределены по объему образца, и их агрегация не наблюдается. Таким образом, используемая методика приготовления образцов позволяет равномерно диспергировать МУНТ в композиционном материале.

Проведен термический анализ исходного фосфатного композита, состоящего из основного наполнителя и твердого магнийфосфатного связующего. Термограмма приведена на **Рисунке 3**.

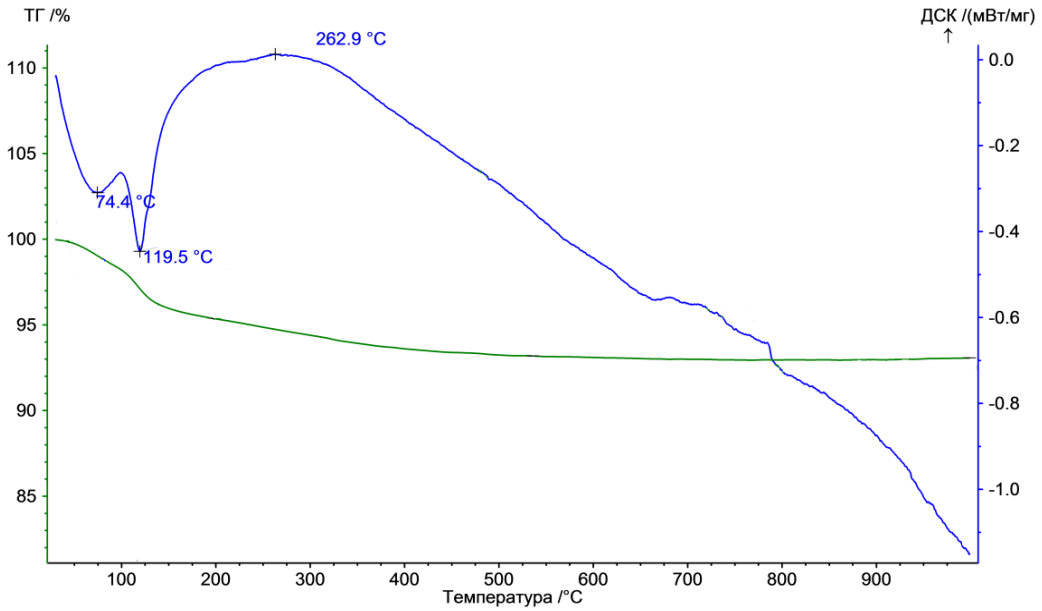

Рисунок 3. Термограмма исходного фосфатного композита.

Результаты проведенного термического анализа показывают, что при нагревании композиции до 200 °С проявляются 2 эндоэффекта с максимумами при 74 и 120 °С. Потеря массы составляет около 5 масс. %. В температурном интервале 200 – 1000 °С заметные термоэффекты отсутствуют. При этом происходит плавное уменьшение массы (около 2 масс. %). Такой характер поведения исследованной фосфатной композиции свидетельствует о перспективности её использования в качестве термостойкой матрицы для получения композиционных материалов.

Изучена термическая устойчивость индивидуальных углеродных нанотрубок и МУНТ в фосфатной матрице. Полученные термограммы представлены на **Рисунках 4** и **5**.

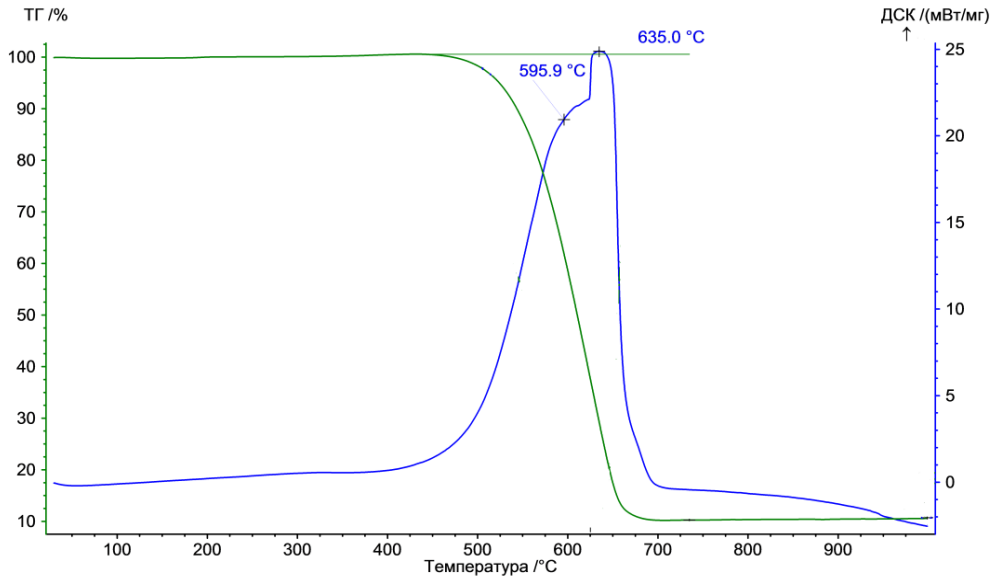

Рисунок 4. Термограмма МУНТ.

Из приведённых данных следует, что в атмосфере воздуха нанотрубки устойчивы к процессам окисления до 450 °С. Начиная с этой температуры и выше, происходит окисление МУНТ кислородом воздуха, что зафиксировано на кривой ДСК в виде экзо–эффекта с максимумом при 635 °С.

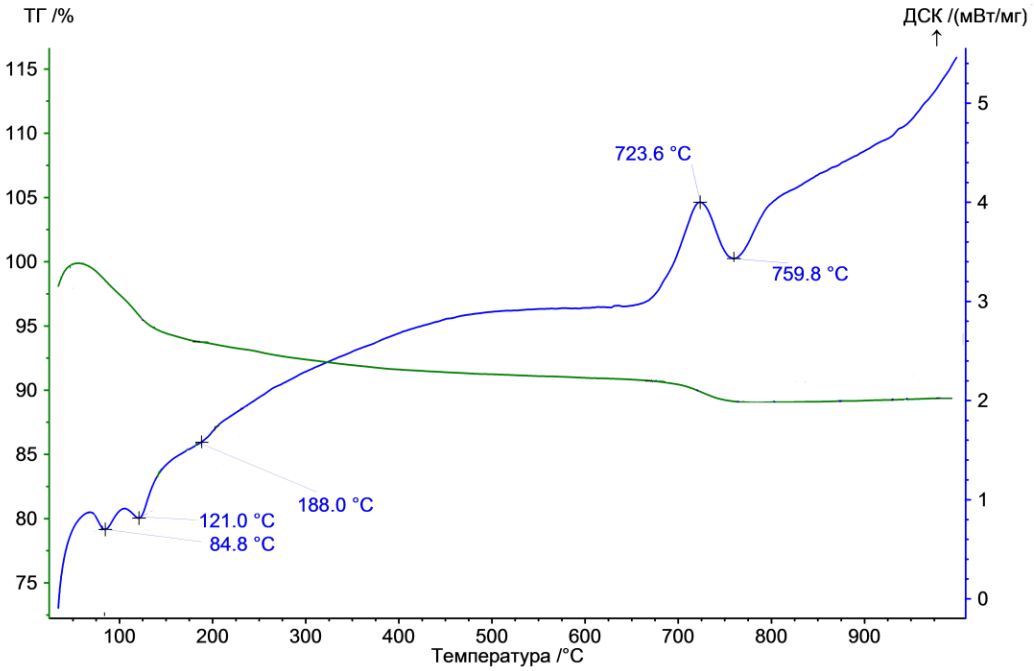

Рисунок 5. Термограмма фосфатного композита с 2 масс. % МУНТ.

Термический анализ фосфатного композита с 2 % масс. МУНТ показывает, что процесс окисления МУНТ в этом случае начинается при температуре около 650 °C. Максимум экзо-эффекта этого процесса на кривой ДСК наблюдается при 724 °C. Следовательно, процесс окисления МУНТ в фосфатной композиции происходит на 150–200 °C выше по сравнению с индивидуальными углеродными нанотрубками.

Изучено влияние содержания твердого магнийфосфатного связующего и температуры обработки на прочность фосфатных композитов. Результаты испытания образцов на сжатие приведены на **Рисунках 6** – **8**.

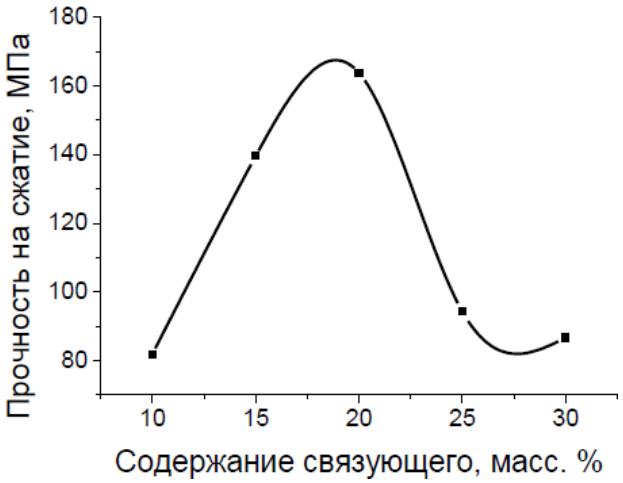

Рисунок 6. Зависимость прочности фосфатных композитов от содержания связующего.

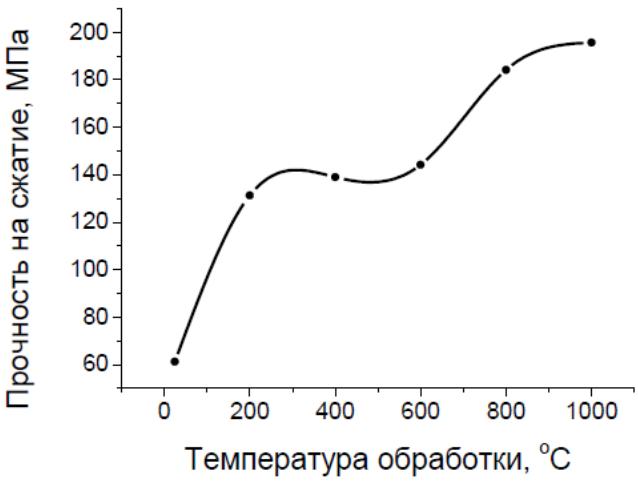

Рисунок 7. Зависимость прочности фосфатных композитов от температуры обработки.

Из приведенных данных следует, что наиболее оптимальное содержание твердого фосфатного связующего в изучаемых системах составляет 15 – 20 масс. %. Термообработка фосфатного композита до 1000 °C приводит к последовательному увеличению прочности композитов в 3 раза.

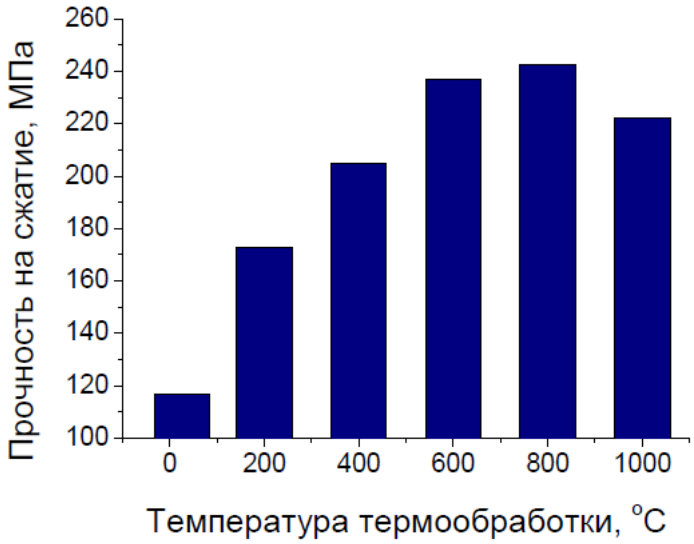

Рисунок 8. Зависимость прочности фосфатного композита, содержащего 0.5 масс. % МУНТ, от температуры обработки.

Гистограмма на **Рисунке 8** показывает, что термообработка композиции на основе ТФМ с МУНТ до 800 °C приводит к последовательному увеличению прочности композитов в 2 раза.

Для изготовления фосфатных композитов традиционно применяют жидкое алюмофосфатное связующее. Однако, как было указано выше, материалы на основе твердых связующих имеют ряд преимуществ. В работе проведено сравнение прочностных и электропроводящих свойств фосфатных композитов с МУНТ на основе различных типов связующих.

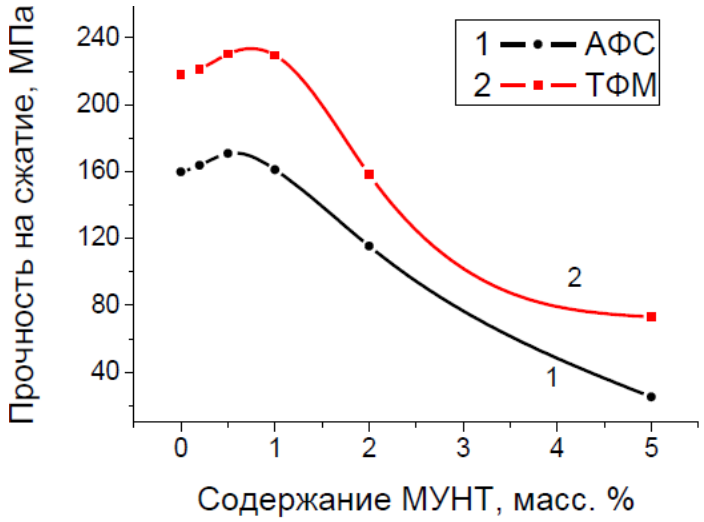

Рисунок 9. Зависимость прочности композитов от содержания МУНТ.

Изучена прочность образцов фосфатных композитов на основе жидкого алюмофосфатного связующего и твердого магнийфосфатного связующего. Результаты измерения прочности на сжатие представлены на **Рисунке 9**.

Зависимости на **Рисунке 9** показывают, что прочность композитов с МУНТ на основе ТФМ на 20 – 30 % выше прочности композитов на основе жидкого АФС. При введении более 2 масс. % МУНТ в фосфатную матрицу прочность композитов снижается значительно, но остается достаточно высокой для данных материалов.

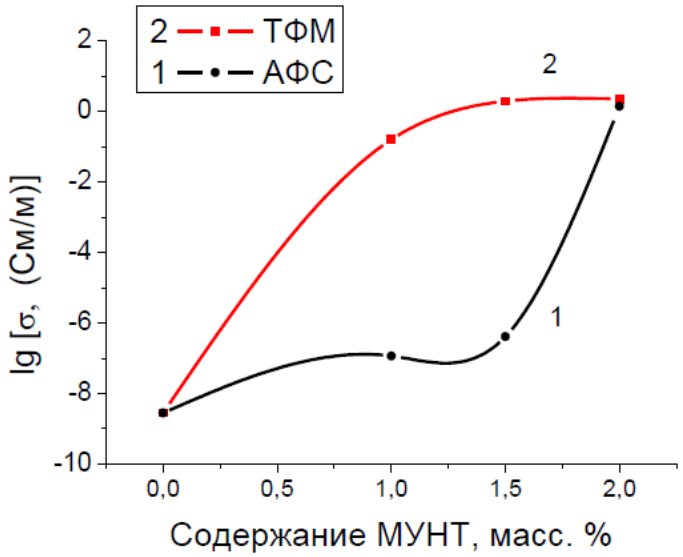

Рисунок 10. Зависимость электрической проводимости композитов на основе АФС и ТФМ от концентрации МУНТ .

Результаты сравнительного измерения электропроводности образцов фосфатных композитов на основе ТФМ и АФС с одинаковым содержанием углеродных нанотрубок представлены на **Рисунке 10**.

Из полученных результатов следует, что электропроводность композитов с 1 – 1.5 масс. % МУНТ на основе ТФМ на 6 – 7 порядков выше, чем композитов на основе жидкого АФС.

Выводы

В работе получены и исследованы термостойкие композиционные материалы на основе твердого магнийфосфатного связующего с многослойными углеродными нанотрубками. Показано, что характер термического поведения фосфатной композиции свидетельствует о перспективности её использования в качестве термостойкой матрицы для получения композиционных материалов. Установлено, что термообработка композиции на основе ТФМ до 1000 °С приводит к последовательному увеличению прочности в 3 раза. Изучена термическая устойчивость, прочностные и электропроводящие свойства материалов с МУНТ. Показано, что процесс окисления МУНТ в фосфатной композиции начинается на 150 – 200 °С выше по сравнению с чистыми нанотрубками. Прочность композитов с МУНТ на основе ТФМ выше прочности композитов на основе жидкого АФС. Электропроводность композитов с МУНТ на основе твердого магнийфосфатного связующего на 6 – 7 порядков выше, чем композитов на основе жидкого алюмофосфатного связующего. Использование твердого магнийфосфатного связующего позволяет более эффективно и с более воспроизводимыми характеристиками изготавливать полифункциональные термостойкие композиционные материалы.

Ссылки

1. П. Н. Дьячков. Углеродные нанотрубки: строение, свойства, применения. 2006, Москва, БИНОМ – Лаборатория знаний, 293 стр.
2. A. S. Wagh. Chemically Bonded Phosphate Ceramics. 2004, Elsevier, 284 pp.
3. С. Л. Голынко–Вольфсон, М. М. Сычев, Л. Г. Судакас, Л. И. Скобло. Химические основы технологии и применения фосфатных связок и покрытий. 1968, Ленинград, Химия, 189 стр.
4. М. М. Сычев. Неорганические клеи. 1986, Ленинград, Химия, 152 стр.
5. Л. Г. Судакас. Фосфатные вяжущие системы. 2008, Санкт-Петербург, РИА «Квинтет», 260 стр.
6. П. П. Кужир, К. Н. Лапко, С. А. Максименко, В. А. Ломоносов, О. А. Ивашкевич, А. И. Лесникович, А. Н. Окотруб, А. С. Курилин, П. В. Седышев, В. Н. Швецов. Термостойкие фосфатные композиции, модифицированные микроструктурными соединениями бора и углеродными нанотрубками, для использования в прикладной ядерной физике. Докл. НАН РБ, 2012, 56, 3, 68- 72.
7. Л. Г. Булушева, А. В. Окотруб, О. А. Ивашкевич, К. Н. Лапко, А. И. Лесникович, В. А. Ломоносов, П. П. Кужир, С. А. Максименко. Электропроводящий термостойкий фосфатный композиционный материал. Патент № 2524516 РФ, МПК H01B1/14, 27.07.2014.
8. П. И. Юхневский, Г. Т. Широкий. Строительные материалы и изделия (Учебное пособие). 2004, Мин.ск, УП «Технопринт», 340 стр.

ИССЛЕДОВАНИЕ ПРОЦЕССА ПОЛУЧЕНИЯ НАНО-КРИСТАЛЛИЧЕСКИХ БОРОСОДЕРЖАЩИХ ЛИГАТУР

А. А. Гачечиладзе [1], А. Л. Оклей [1], Б. Г. Маргиев [1], Р. В. Чедия [2], Л. С. Чхартишвили [1], О. А. Цагарейшвили [1]

[1] Институт металлургии и материаловедения им.Ф. Н. Тавадзе
Тбилиси, Грузия
archilgachechiladze@gmail.com
[2] Сухумский физико-технический институт им. И. Векуа
Тбилиси, Грузия

Принята20ноября 2015 года

Аннотация

Приведены результаты исследования по получению нанокристаллических сплавов Fe–B и Fe – B–Al_2O_3, пригодныхдля модифицирования сталей.

Перспективы развития чёрной металлургии определяются не только совершенствованием металлургических агрегатов и процессов, но и возможностью удовлетворения постоянно растущих требований к качеству металла при минимальном расходовании легирующих компонентов. Использование бора открывает новые возможности для получения экономнолегированных сталей, эксплуатационные характеристики которых во многих случаях не только не уступают, но и превосходят уровень свойств сталей, получаемых с применением традиционной системы легирования.

Бор существенно повышает качество металла при добавке в чугуны и стали в количестве $10^{-4} – 10^{-3}$ %, а это на 2 – 4 порядка меньше расхода других легирующих элементов (например, хрома, марганца, молибдена или никеля), применение которых позволяет получить соответствующие результаты по повышению прокаливаемости и прочности низко- и среднелегированных сталей [1].

Бор, как микролегирующий элемент, известен давно и широко практикуется его использование на сталеплавильных заводах в виде ферробора и борсодержащих лигатур. Однако при добавках этих сплавов, существенные различия плотности фаз и значительный перегрев металла (300 – 500 °C) над температурой ликвидуса перед его выпуском из печи, приводит к ликвации практическти всех контролируемых элементов по высоте и сечению стального слитка. Это обуславливает уменьшение эффективности «действия» бора и стабильности получаемых результатов.

Поэтому нужны новые подходы и поиск новых технологических решений для получения и применения микролегирующих сплавов с бором.

Нами проводятся исследованияпо получению нанокристаллических сплавов для модифицирования стали [2].

В представленной работе приведены результаты исследования по получению сплавов Fe – B и Fe – B – Al_2O_3.

В качестве шихтовых материалов использовались:

– для получения сплава Fe – B: хлорид железа – $FeCl_3 \cdot 6H_2O$, борный ангидрид – B_2O_3 и сахароза – $C_{12}H_{22}O_{11}$;

– для получения сплава Fe – B – Al_2O_3: хлорид железа – $FeCl_3 \cdot 6H_2O$, хлорид алюминия –$Al_2O_3 \cdot 6H_2O$, борный ангидрид –B_2O_3 м сахароза – $C_{12}H_{22}O_{11}$.

Трехэтапный технологический процесс получуения сплавов Fe – B и Fe – B – Al_2O_3, в общих чертах, заключается в следующем.

На первом этапе, исходный шихтовой раствор заданного стехиометрического состава распыляется на корундовую подложку, нагретую до 250 – 300 °C. Образующийся порошок помещается в реторту, где происходит восстановление водородом при температуре 800 – 870 °C (второй этап). На третьем этапе, восстановленный порошок помещается в другую реторту, где выдерживается при 1100 – 1200 °C в атмосфере аргона.

Фаза FeB начинает формироваться при 1000 °C. С повышением температуры начинает формироваться фаза Fe_2B и при 1200 °C образуется двухфазная система FeB - Fe_2B (**Рисунки 1** и**2**).

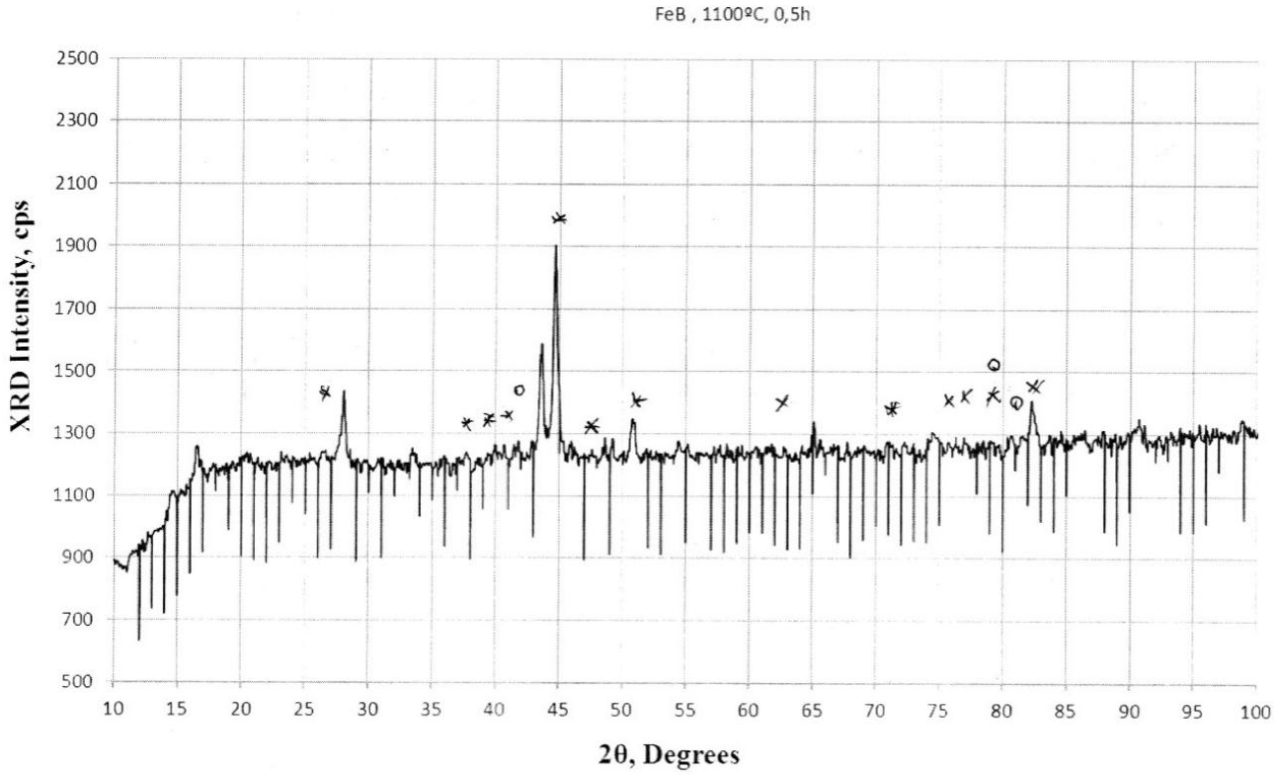

Рисунок 1. Рентгенодифрактограмма FeB при 1100 °C (* – FeB и ° – Fe_2B).

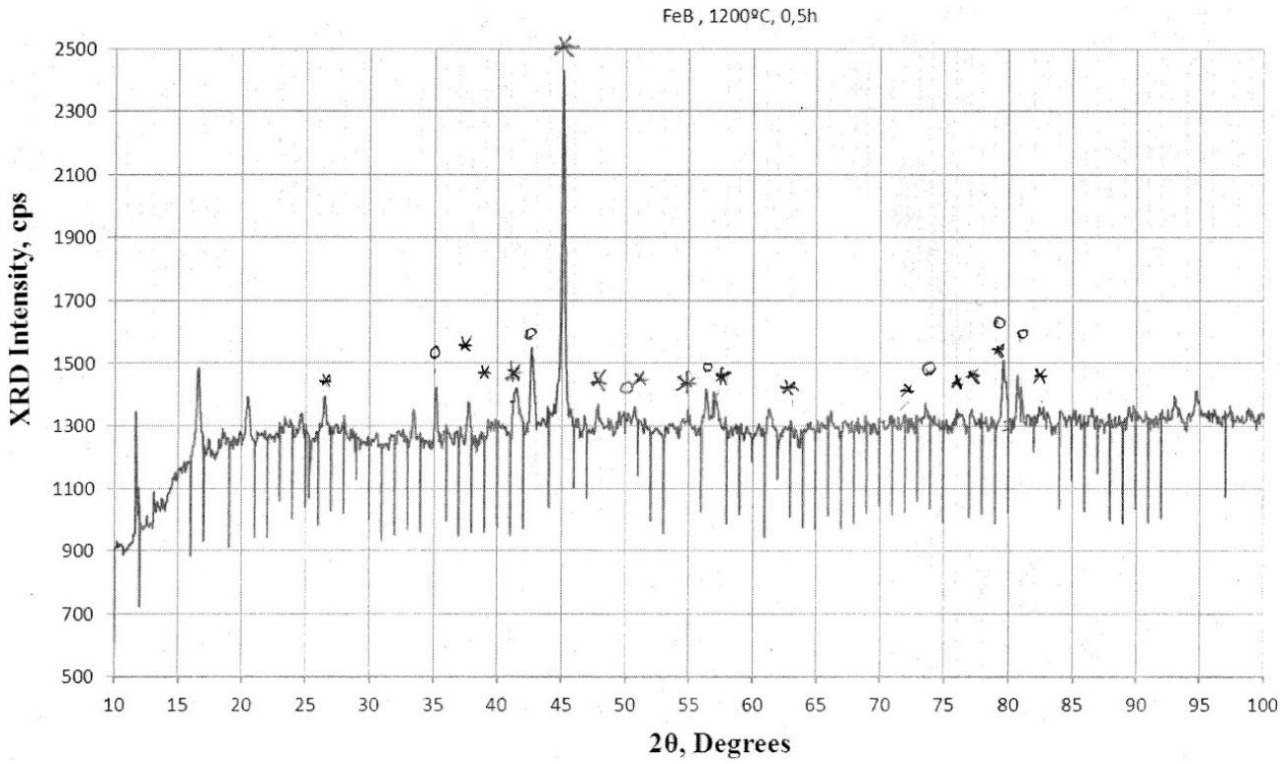

Рисунок 2. Рентгенодифрактограмма FeB при 1200 °C (* – FeB и ° – Fe_2B).

Оценка геометрических размеров наночастиц по расширению рентгенодифракционных максимумов (метод Шерера) показала, что они находятся в пределах 40 – 80 нм. Это подтверждается электромикроскопическими исследованиями.

Образующиеся в исследуемой лигатуре соединения железа и бора характеризуется высокой дисперсностью вероятно будеть играт рола дисперсных включенийв металлической матрице, и следовательно являтся эффективными барьерами для движущихся при пластической деформации дислокации. В месте с этим они не блокируют передвижение дислокаций, что определяет повышение предела прочности материала с сохранением исходных пластических характеристик матрицы [3].

Установление реализуремого в изучаемых сплавах механизма дисперсного упрочнения является предметом последующих исследолвании.

Применения нанокристаллических лигатур содержащих высокодисперсные соединения железа и бора позволит повысить предел прочности легирующих сталей с сохранением пластических характеристик.

Мелкодисперсная структура сталей, легированных разработанной нанокристаллической лигатурой несомненно повысит механические свойства сталей наряду с эффектом дисперсного упрочнения.

Ссылки

1. Н. П. Лякишев, Ю. Л. Плинер, С. И. Лаппо. Боросодержащие стали и сплавы. 1986, Москва, Металлургия, 191 стр.
2. A. Gachechiladze, B. Margiev, R. Chedia, A. Oakley, L. Chkhartishvili, O. Tsagareishvili. New nanoalloys for modifying the steel.In: Proceedings of the 2nd International Conference “Modern Technologies & Methods of Inorganic Materials Science”.2015, Tbilisi, Sachino, 228-231.
3. А. А. Гачечиладзе, Т. П. Микаберидзе, М. В. Тавадзе, Ф. Н. Тавадзе. Механические свойств и внутреннее трение дисперсноупочненного материала на основе железа. В сб.: Матер. Всесоюзногосеминара «Механизмы повреждаемостии прочность гетерогенных материалов». 1985, Ленинград, 143-145.

MENDELEEV AND THE PETROLEUM INDUSTRY

F. Habashi

Laval University
Department of Mining, Metallurgical &Materials Engineering
Quebec City, Canada
Fathi.Habashi@arul.ulaval.ca

Accepted January 28, 2015

Introduction

The discovery of the Periodic Table in 1869 by Dmitri Ivanovich Mendeleev (1834 – 1907) (**Figure 1**) is only one of his professional achievements. His work on petroleum was his major occupation. He wrote many articles on the subject and supported the theory that the origin of petroleum was the result of the reaction of carbides with water — a theory that is dismissed today in favour of the organic theory. He went to Baku in Azerbaijan many times to consult on oil production. Azerbaijan at that time was part of Imperial Russia and an oil well was drilled using primitive methods more than a decade before an oil well was drilled in North America. In 1901, it produced more than half of the world's oil. Today, it produces a small amount as compared with other producing countries.

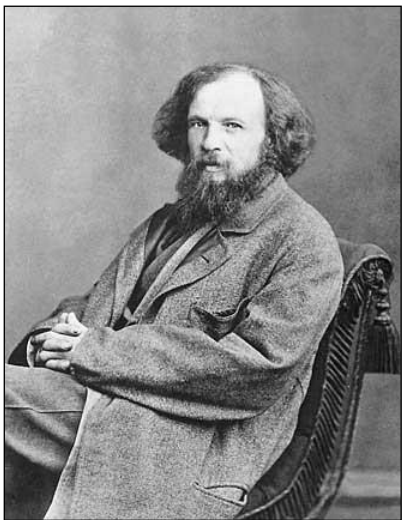

Figure 1. Dmitri Ivanovich Mendeleev (1834 – 1907).

Kerosene

In 1846 a small kerosene factory was built. Barrels were used to collect and store the oil that is why today oil is measured and sold per barrel. Kerosene is a clear liquid obtained from the fractional distillation of petroleum between 150 and 275 °C. In the second half of the 19th century Baku turned into the biggest oil region of Russia. Kerosene was widely used in households cooking in Primus stoves invented in 1892 (**Figure 2**) and lighting fuel in lamps and

lanterns (**Figures 3** and **4**) before electrical distribution became available. Its name is derived from Greek meaning wax, which was registered as a trademark in 1854. Kerosene burned longer and with a brighter light than other oils.

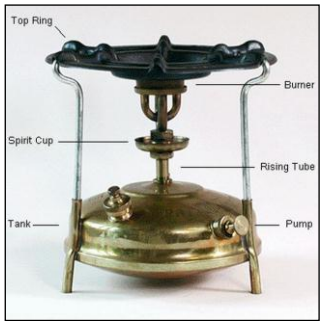

Figure 2. Kerosene cooking in portable stoves.

Figure 3. Kerosene lamps.

Figure 4. Kerosene lantern.

The widespread availability of cheaper kerosene was the principal factor in the decline in the whaling industry in the late 19th century, as the leading product of whaling was oil for lamps. Kerosene also replaced turpentine obtained from the distillation of wood as a fuel. Kerosene stoves have replaced traditional wood-based cooking appliances. Kerosene was sold in some filling stations or in tank cars (**Figure 5**). The vast Russian empire needed more of the new light than anyone else as St. Petersburg, the capital, barely had six hours of daylight in the winter. Interestingly, after crude oil was processed, one of the by-products (gasoline) at that time was simply dumped or used as solvent.

Figure 5. Selling kerosene from a tank cars.

Today, kerosene is mainly used in fuel for jet engines in several grades. One form is burned with liquid oxygen as rocket fuel. Kerosene is used to store active metals that react with air or water such as potassium, sodium, lithium, etc. It also used a pesticide.

Mendeleev in Baku

Mendeleev was 29 years old when he was invited by the Russian oil businessman Vasily Alexandrovich Kokorev (1817 – 1889) (**Figure 6**) to visit his oil refinery in Baku constructed in the 1850s and make recommendation since it had become less profitable. Mendeleev at that time was professor at Saint Petersburg University, just returned from Heidelberg in Germany where he was sent by the Russian Government in 1859 to 1861 to study. Apparently he became

known to Kokorev through Germans who supplied him with some equipment. Mendeleev left for Baku on September 6, 1863, stayed in Moscow at Kokorev's mansion across the Moscow River from the Kremlin. He then left to Nizhniy Novgorod and onwards aboard a ship along the Volga then to Baku. He returned on October 8.

Figure 6. Vasily Alexandrovich Kokorev (1817 – 1889).

After the visit, Mendeleev proposed building a pipeline for oil transportation from wells to the sea, where oil was to be stored in reservoirs then transported across the Caspian Sea by tanker till Volga and from there till Nizhniy Novgorod where a factory for processing oil to various products should be built (**Figure 7**). He argued further that Cheleken, then part of Turkmenistan – now known as Hazar (**Figure 8**), would be occupied by the Russian military for exploitation of its oil resources. The project did not appear to have gone ahead. Incidentally Turkmenistan was annexed by Russia in 1881 but became independent in 1991.

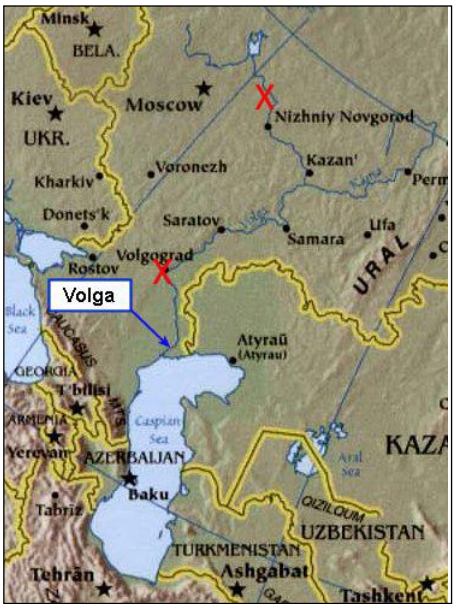

Figure 7. Map showing Baku on the Caspian Sea and Nizhniy Novgorod and Volgograd, formerly Tsaritsyn (1589 – 1925), And Stalingrad (1925 – 1991) on the Volga, X.

Figure 8 . Map showing Baku and Cheleken, X.

Kokorev suggested that Mendeleev become technical director of the new refinery to be built near Nizhniy Novgorod. Mendeleev tempted to give up his low-paying academic position in order to work full-time in the oil industry for much more money but he declined the offer because his wife did not like the idea. He was even offered later to become a co-owner of the refinery but after much thought he declined. Six years later in 1869 Mendeleev became famous for formulating the Periodic Table.

The refineries around Baku moved their oil from the wells to Baku in wooden barrels on carts, which was inefficient. Manufacturing barrels was made worse by the lack of wood in the region. The barrels were prone to leaking. Oil was shipped by boat up the Volga. In order to improve efficiency, refiners asked the Caucasus and Mercury Shipping Company owned by Kokorev to install cisterns so that oil could be shipped along the Volga in bulk but the company refused.

Mendeleev and the oil industry

Mendeleev took part with the Russian delegation for the Paris World Fair in 1867 as an expert on chemistry. In 1868, two government commissions were formed — one in Tbilisi and one in St. Petersburg. The Tiblisi commission noted that the United States, which was not tied by a leasing system, experienced growth. In Russia the oilmen did not open up new wells because of the leasing system. As a result it was impossible for modernization. The St. Petersburg commission found the need to end the leasing system. In 1875, America made some huge oil discoveries and in the absence of any taxes, the price of oil fell. The threat of the influx of cheap American kerosene was taken seriously and a commission was created to examine the question of taxes on oil. As a result the Russian Government decided to send Mendeleev to examine the American system.

Mendeleev departed from St. Petersburg on May 30, 1876 with his English speaking assistant, and returned September 11. The trip was sponsored by the Minister of Finance to understand the modern technology of the oil business in America, the tax policy on oil, and to understand the reasons for the lowering of kerosene prices. Mendeleev visited the oil fields in Pennsylvania and the Philadelphia World Fair to examine the oil display. He took a trip to Niagara Falls and visited the meteorological centre in Washington. Meteorology was a subject which he would later study for the Russian Government. On his return, Mendeleev wrote to the Minister of Finance, *Memorandum regarding the abolition of lighting oil taxes*.

Mendeleev mentioned the necessity of cancelling the petroleum tax. American oil started to decrease when taxes on crude oil and its refining were abolished. The result was an increase in use. Mendeleev discussed fire hazards and kerosene, dangers of its transportation and storage, refining of oil by-products, oil pipelines, how to attract capital to the Russian oil industry, and how to encourage its growth. Furthermore, because there was insufficient technical information on Russian oil, it was necessary that a study of the industry be undertaken including the heavy oil, its uses and its marketing. He argued that the refineries should not only be in Baku but along the Volga and in the centre of use, close to those places where barrels are cheap. Mendeleev wrote that it was necessary that different people do the construction, sales, give technical advice, drilling, construction of reservoirs and other apparatus. He also commented on the state of the bureaucracy and the employment of women in America, and the arrival of the first gas piston engine in America.

Mendeleev noted that only half of America's kerosene was consumed at home while the rest was exported. He observed that America used three times kerosene per capita as Europe while Russia was using less than Europe. America's economic strengths, was the result of the quality of their oil, which produced much greater quantities of kerosene than Russia's. Mendeleev believed that the Baku oil fields could compete with the American product if the Russian government similarly abolished the taxes it assessed on the industry. Once Russian kerosene was plentiful and reached a low price then Russia, should export to Europe by using pipelines, special barges, and wagons.

Nobels in Baku

The Petroleum Production Company Nobel Brothers was set up by Ludvig Nobel (1831 – 1888) (**Figure 9**) and Baron Peter von Bilderling (1844 – 1900) in 1876 in Baku. It was headquartered in St. Petersburg and became one of the largest oil companies in the world producing 50 % of the world's oil. Ludvig Nobel was an engineer and a businessman. The Nobel family was from Sweden but lived many years in Saint Petersburg. The company had been facing financial difficulties since the end of the Crimean War in 1856 due to a severe cut in the military budget ordered by the new Tsar Alexander II, and eventually, in 1862, the firm was sold.

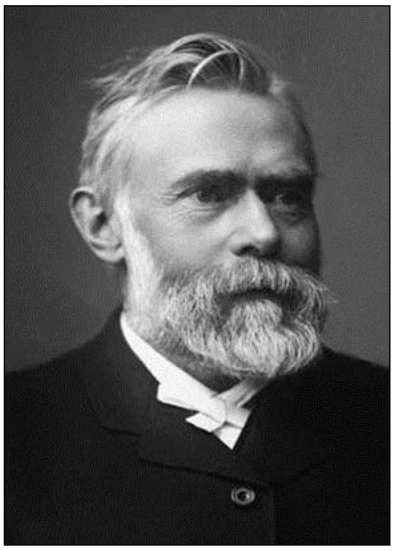

Figure 9. Ludvig Nobel (1831 – 1888).

Figure 10. Robert Nobel (1829 – 1896).

Figure 11. Alfred Nobel (1833 – 1896).

With some funds he had managed to save, Ludvig opened a new firm, the Machine-Building Factory. Initially producing cast-iron shells, the factory became in a few years one of the largest producers of gun carriages of Russia. When his brother Robert (1829 – 1896) (**Figure 10**) bought a refinery in Baku, Ludvig invested in refinery modernization. He established technical chemical research labs employing dozens of scientists, finding ways to treat oil, developing new uses for oil, and developing new products derived from oil.

By 1876, the Nobel brothers established themselves as the most competent refiner in Baku and sent the first shipment of illuminating oil to St. Petersburg. By 1879, Ludvig turned the business into a shareholding company, Branobel, with brothers Robert and Alfred (1833 – 1896) (**Figure 11**) and others.

Improvement in the Azerbaijan oil industry

Great changes were introduced in the area of oil storage, for example, iron reservoirs were used. In 1877, construction of the first oil pipeline linking Surakhany oil field and refinery in Baku was completed. By 1890, there were more than 25 pipelines. The Nobel Brothers were the first to introduce railway tanks (cisterns) for oil transportation in 1883. In 1884, the oil producers in Baku established the Oil Extractors Congress Council under the direction of Ludvig Nobel. They created the magazine, Neftyanoe Delo (Oil Business). Ludvig and Robert Nobel built Villa Petrolea which received on October 9, 1888 Emperor Alexander III of Russia with his family; currently functions as a museum. Ludvig Nobel invented oil tankers; the world's first tanker was *Zoroaster* (**Figure 12**) designed in Sweden in 1878 and made its first trip from Baku to Astrakhan.

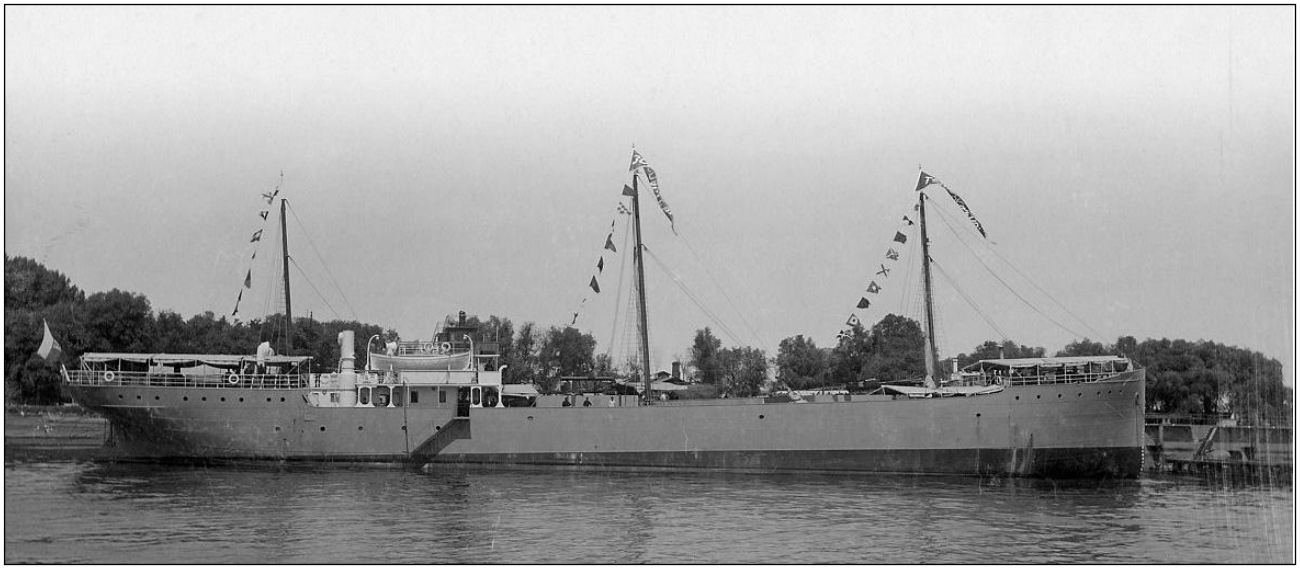

Figure 12. The world's first oil tanker Zoroaster, 1878.

By 1890, 345 tankers, including 133 steam vessels and 212 sailing vessels were sailing on the Caspian Sea. The oil-saturated earth in Baku was covered by fertile soil and fresh water was imported from the Volga on ships travelling from Astrakhan which used it as ballast instead of sacks of sand. Large companies started to employ geologists to describe and map prospective structures. By early 20th century, innovation started to improve the backward well drilling practices. Tankers played an important role in shipping fuel. For example, on July 22, 1892 the first tanker sailed from Britain to Batum to be filled with kerosene, subsequently passed through the Suez Canal [opened in 1869] on August 23 for the Far East.

Mendeleev's other trips to Baku

Mendeleev made a second trip to Caucasus in 1880 and was befriended with Azerbaijani oil industrialist Haji Zeynalabdin Taghiyev (1821? – 1924) (**Figure 13**). In 1884 (October 26 – November 8) he took an active part in the Congress of Baku Oil Industrialists. In May 1886 he made another trip to Baku and gave speeches about the conditions of development of oil business. On March 1887 he presented a report to the minister of state properties about the issue of oil and kerosene pipelines.

Figure 13. Haji Zeynalabdin Taghiyev (1821? – 1924).

In 1880, Mendeleev proposed the construction of Baku–Batum pipeline to transport oil to the world market (**Figure 14**). The project was postponed as premature, and the construction started only in 1896 and finished in 1906. The first pipeline was kerosene pipeline. It was at that time the longest pipeline in the world. It was Alfred Nobel's dynamite that helped build the pipeline through the mountains. Other pipelines were later constructed.

Figure 14. Baku – Batum pipeline (Sangachal – Supsa), 1906.

Rothschild brothers in Baku

In 1883 the Caspian – Black Sea Oil Industry & Trade Society was established by Alphonse Rothschild (1827 – 1905) (**Figure 15**) the son of Paris banker James Rothschild (1792 – 1868). After his father's death, Alphonse took on the management of the Paris banking business. Alphonse Rothschild opened branches of his company in many cities in the Volga area, in the Baltic States, in Belorussia, and in and Poland. After his death his younger brother Baron Edmond Rothschild (1845 – 1934) (**Figure 16**) took over. The construction of the Transcaucasia railway (**Figure 17**) connecting Baku and Batumi was finished in 1883 thanks to a Rothschild loan. In the early 1900s, the Nobel Brothers and the Rothschilds concluded an agreement to prevent the American Standard Oil from entering the Caucasus.

Figure 15. Baron Alphonse Rothschild (1827 – 1905).

Figure 16. Baron Edmond Rothschild (1845 – 1934).

Figure 17. Transcaucasia railway connecting Baku and Batumi.

World Wars

On the eve of the World War I, the Russian General Oil Company, Royal Dutch Shell, and Partnership of Nobel Brothers controlled 60 % of oil production. In 1912, Anglo – Dutch firm Shell obtained 80 % shares of Caspian – Black Sea Society Mazut, which had belonged to Rothschilds.

After the Russian Revolution, nationalization of the industry was decreed by the Baku commune in June 1918. As a result of World War I no oil export was possible, oil storage facilities were damaged, and wells were idle. The government of Democratic Republic of Azerbaijan was unable to restore the damage done to the oil industry.

On 28 April 1920, the Bolsheviks seized power in Baku and confiscated and nationalized the industry. They formed Azneft State Company. Scientific exchange started with the USA and engineers from Baku visited the oil fields in Pennsylvania, Oklahoma, California, and Texas. The Azerbaijan State Oil Academy was established in 1920 to train oil specialists.

By World War II, the Nazis were determined to capture the oil fields of the Caucasus. Their defeat at Stalingrad forced a retreat. Oil production from the existing fields started to decline after World War II, as a result of over-production.

In the early 1930s, engineers constructed the first offshore wells and in 1949 important discoveries were made. In 1957 several large oil and gas fields were discovered and put into production.

Figure 18. Baku – Tbilisi – Ceyhan pipeline, 2006

After gaining independence Azerbaijan the Baku – Tbilisi – Ceyhan pipeline was opened in 2006 to transport crude oil (**Figure 18**). It is the second longest oil pipeline in the world — the longest being the Druzhba pipeline from Russia to central Europe.

Extensive references *to the original literature is in Ph.D. Thesis of Mark Butorac, "Mendeleev, the West and the Russian Oil Industry", presented at the Faculty of Graduate Studies and Research, McGill University, Montreal, 2001 (252 pages).*

The illustrations *are by the present author and are in the public domain.*

მე-11 საერთაშორისო კონფერენცია "გამოსხივებათა ურთიერთქმედება მყარ სხეულებთან"

მე-11 საერთაშორისო კონფერენცია "გამოსხივებათა ურთიერთქმედება მყარ სხეულებთან" მიმდინარეობდა 2015 წლის 23–25 სექტემბერს ბელარუსის დედაქალაქ მინსკში, ბელარუსის სახელმწიფო უნივერსიტეტში.

ბელარუსის სახელმწიფო უნივერსიტეტის ფიზიკის ფაკულტეტის ძველი (მარცხნივ) და ახალი (მარჯვნივ) კორპუსები

კონფერენცია მიზნად ისახავდა თავი მოეყარა მსოფლიოდან იმ მეცნიერების, ინჟინრების, მაღალტექნოლოგიური წარმოებისა და მეცნიერების პოლიტიკის წარმომადგენლებისათვის, რომლებიც მოღვაწეობენ მყარი სხეულების რადიაციული ტექნოლოგიის სწრაფად განვითარებად სფეროში, რათა მათ მისცემოდათ საშუალება ერთმანეთისათვის გაეცნოთ თავიანთი უახლესი მიღწევები, გაეზიარებინათ შედეგები და დაემყარებინათ ურთიერთსასარგებლო კონტაქტები, განევითარებინათ სამომავლო თანამშრომლობა.

საზეიმო გახსნა. მარცხნიდან მარჯვნივ: ვიქტორ ანიშჩიკი (პროგრამული კომიტეტის თავმჯდომარის მოადგილე), სერგეი აბლამეიკო (ამ კომიტეტის თავმჯდომარე, ბელარუსის სახელმწიფო უნივერსიტეტის რექტორი), გენადი მესიაცი (ამ კომიტეტის წევრი, რუსეთის მეცნ. აკად. ვიცე-პრეზიდენტი)

საერთო ჯამში კონფერენციის მუშაობაში მონაწილეობა მიიღო 150-მდე მეცნიერმა 67 ქვეყნიდან (გერმანია, ისრაელი, ლატვია, ლიტვა, თურქეთი, პაკისტანი, პოლონეთი, სამხრეთ აფრიკის რესპუბლიკა, საქართველო, სომხეთი, უზბეკეთი, რუსეთის ფედერაცია, უკრაინა, ყაზახეთიდა ა.შ.). კონფერენციის მუშაობაში აქტიურად იყვნენ ჩართული სტუდენტებიც – შესაბამისი დარგების ასპირანტები და დოქტორანტები – ასევე, სხვა ახალგაზრდა მეცნიერები ბელარუსის სხვადასხვა უმაღლესი სასწავლებლიდან და კვლევითი ინსტიტუტიდან.

პლენარულ სხდომაზე წარმოადგინეს მოწვეული მოხსენებები მყარ სხეულებზე რადიაციის ზემოქმედების შედეგად მათი ფიზიკური მახასიათებლების ცვლილებისა და მყარი სხეულების რადიაციული ტექნოლოგიის რიგი მნიშვნელოვანი და აქტუალური მიმართულებით:

- რადიაციული ეფექტები იონებით იმპლანტირებულ β-Ga_2O_3-ში;
- ნაწილაკების ნივთიერებაში გავლის მოდელირების კასკადურ-ალბათური მოდელი;
- გერმანიუმის ზონური სტრუქტურის მოდიფიკაცია პირდაპირზონური ლუმინესცენციის მიღებისათვის: თანამედროვე მდგომარეობა და პერსპექტივები;
- რუსეთის მეცნიერებათა აკადემიის მაღალი სიზუსტის ელექტრონიკის ინსტიტუტში შემუშავებული ახალი იონურ-პლაზმური მოწყობილობა და მასალების ზედაპირების დამუშავების კომპლექსური პროცესები.

კონფერენციის მონაწილეთა ერთი ჯგუფი

პროფ. გ. ჩირაძე და ლესია უკრაინკას სახ. ნაციონალური უნივერსიტეტის თეორიული და მათემატიკური ფიზიკის დეპარტამენტის პროფესორი პიოტრ ტროხიმჩუკი

კონფერენციის თემატიკის მრავალფეროვნებაზე მეტყველებს აგრეთვე სექციების დასახელებებიც:

- გამოსხივებათა და პლაზმის მყარ სხეულებთან ურთიერთქმედების პროცესები;
- რადიაციული ეფექტები მყარ სხეულებში;
- მასალათა თვისებების მოდიფიკაცია;
- ნანომასალებისა და ნანოსტრუქტურების ფორმირების სხივური მეთოდები;
- ზედაპირების დანაფარების სტრუქტურა და თვისებები;
- თანამედროვე მოწყობილობები და ტექნოლოგიები.

წარმოდგენილი მოხსენებების სრული ტექსტების კრებული დაურიგდათ მონაწილეებს და განთავსდა კონფერენციის საიტზე. სარედაქციო ჯგუფის ექსპერტიზის შედეგად რამდენიმე მოხსენებას მიეცა რეკომენდაცია, რათა ისინი სტატიების სახით გამოქვეყნდეს ბელარუსის სახელმწიფო უნივერსიტეტის სამეცნიერო ჟურნალში და ასევე სხვა პერიოდულ გამოცემებში.

კონფერენციის ლოგო

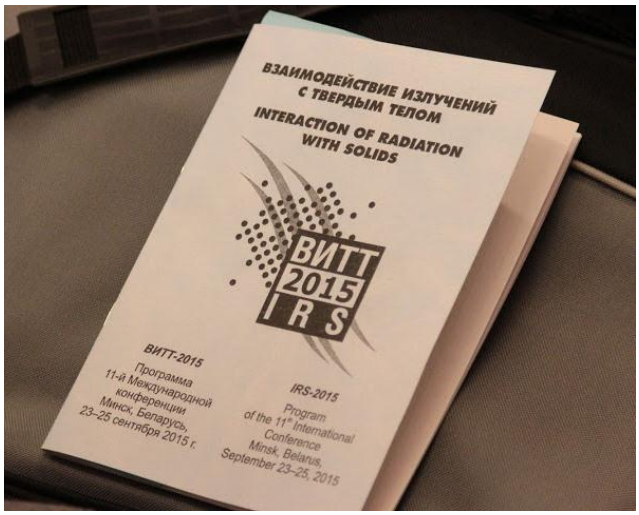

კონფერენციის პროგრამის გარეკანი

კონფერენციის სამუშაო პროგრამა საკმაოდ დატვირთუყლი იყო. გაიმართა ორი პლენარული სხდომა, თითქმის ათამდე სხდომა სექციებში, სამი პოსტერული სესია. თითოეული სესიის ბოლოს გამოყოფილი იყო დრო დისკუსიისათვის, რომელიც საკმაოდ აქტიური კითხვა-პასუხის რეჟიმში მიმდინარეობდა.

პროფ. გ. ჩირაძე გამოდის მოხსენებით

დისკუსიის დროს

საქართველოდან კონფერენციის მუშაობაში მონაწილეობდა აკაკი წერეთლის სახელმწიფო უნივერსიტეტის ფიზიკის დეპარტამენტის პროფესორი გიორგი ჩირაძე (მისი მგზავრობა დააფინანსა ქუთაისის მერიამ, ხოლო კონფერენციაში მნონაქწილეობის დანარჩენი ხარჯები – აკაკი წერეთლის სახელმწიფო უნივერსიტეტმა). მან წარმოადგინა მოხსენება “ნარჩენი ფოტომექანიკური ეფექტის გამოკვლევა ჩქარი ნეიტრონებით გასხივებულ სილიციუმში” (თანაავტორი: ალექსი გერასიმოვი – საქართველოს ტექნიკური უნივერსიტეტის საინჟინრო ფიზიკის დეპარტამენტის პროფესორი), რომელმაც საკმაოდ დიდი ინტერესი გამოიწვია. საკმარისია ითქვას, რომ პროფ. გ. ჩირაძემ მიიღო წინადადება, რომ მოხსენება გაფართოვდეს და გამოიცეს ცალკე მონოგრაფიის სახით.

პროფ. გ. ჩირაძე და ხარკოვის ნაციონალური სამეცნიერო ცენტრის “ფიზიკა-ტექნიკის ინსტიტუტი” დირექტორი, აკად. ივან ნეკლიუდოვი

პროფ. გ. ჩირაძე და ვარშავის ტელერადიო კვლევების ინსტიტუტის პროფესორი პიოტრ კონარსკი

კონფერენციის მიმდინარეობის პერიოდში პროფ. გ. ჩირაძე შეხვდა და ესაუბრა მყარი სხეულების რადიაციული ტექნოლოგიების დარგის მთელ რიგ წამყვან სპეციალისტებს. მათ შორის არიან: ალექსანდრე კუპჩიშინი (ალ-ფარაბის სახ. ყაზახეთის ნაციონალური უნივერსიტეტი), ნიკოლაი კოვალი (რუსეთის მეცნ. აკად. ციმბირის განყ. ტომსკის მაღალი სიზუსტის ელექტრონიკის ინსტიტუტი), რუსლან ბატალოვი (რუსეთის მეცნ. აკად. ყაზანის ფიზიკა-ტექნიკის ინსტიტუტი) და ელკე ვანდლერი (იენის ფრიდრიხ შილერის უნივერსიტეტის მყარი სხეულების ფიზიკის ინსტიტუტი).

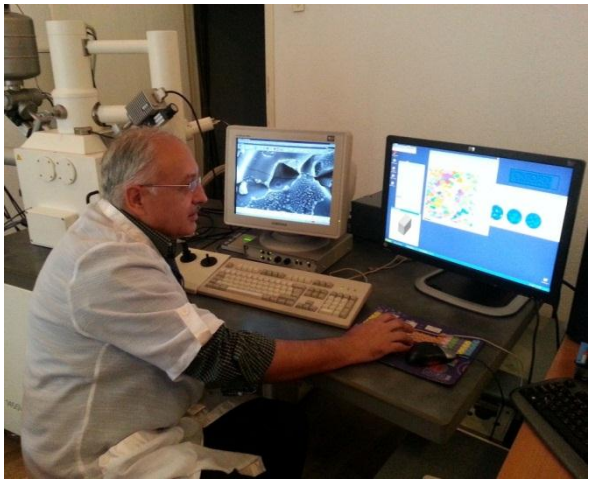

პროფ. გ. ჩირაძე ბელარუსის სახელმწიფო უნივერსიტეტის ფიზიკის ფაკულტეტის რასტრული ელექტრონული მიკროსკოპიის ლაბორატორიაში მუშაობისას

დიდი სამამულო ომის საბრძოლო დიდების მუზეუმის დათვალიერებისას პროფ. გ. ჩირაძე პროფესორ ვიქტორ ანიშჩიკს გლობუსზე უჩვენებს მანძილს, რომელიც მან გამოიარა თბილისიდან მინსკამდე

განსაკუთრებით აღსანიშნავია ის ფაქტი, რომ მინსკში ყოფნის დროს ხელი მოეწერა ურთიერთთანამშრომლობის მემორანდუმს აკაკი წერეთლის სახელმწიფო უნივერსიტეტსა და ბელარუსის სახელმწიფო უნივერსიტეტს შორის. მემორანდუმი ითვალისწინებს თანამშრომლობას სამეცნიერო და შემოქმედებით სფეროში. იდეას ამ უკანასკნელის შესახებ საფუძველი ჩაეყარა 2013 წელს – წინა კონფერენციაზე, რომელიც რიგით მე-10 იყო და, შეაბამისად, საიუბილეო (მაშინ პროფ. გ. ჩირაძის გამგზავრება დაფინანსდა შოთა რუსთაველის ეროვნული სამეცნიერო ფონდის მოკლევადიანი ინდივიდუალური სამოგზაურო გრანტის ფარგლებში).

ბელარუსის ნაციონალური ბიბლიოთეკა

ეს სამეცნიერო ფორუმი, რომელიც მრავალფეროვან საექსკურსიო პროგრამასაც ითვალისწინებდა, საზეიმოდ დაიხურა 25 სექტემბერს.

მე-11 საერთაშორისო კონფერენციის “გამოსხივებათა ურთიერთქმედება მყარ სხეულებთან” მონაწილეებმა ერთმანეთს წარმატებები უსურვეს და მომავალი საქმიანი შეხვედრების იმედი გამოთქვეს.

გიორგი ჩირაძე

2015 წლის 17 ნოემბერი

მე-3 საერთაშორისო სამეცნიერო-პრაქტიკული კონფერენცია “ნანოტექნოლოგია და ნანომასალები”

2015 წლის 26 – 29 აგვისტოს ლვოვში – ისტორიული გალიციის დედაქალაქში და თანამედროვე უკრაინის ერთ-ერთ მთავარ კულტურულ ცენტრში – გაიმართა მე-3 საერთაშორისო სამეცნიერო-პრაქტიკული კონფერენცია “ნანოტექნოლოგიები და ნანომასალები”.

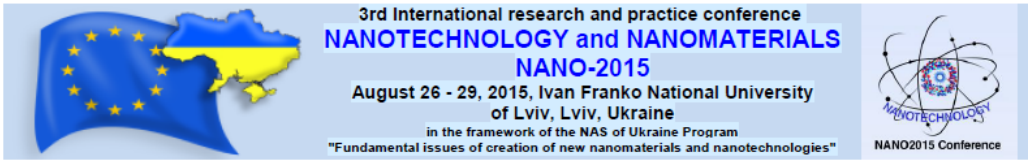

კონფერენციის ლოგო

ამ ფართო წარმოდგენლობის სამეცნიერო ფორუმს ივან ფრანკოს ლვოვის ეროვნული უნივერსიტეტი მასპინძლობდა – როგორც პლენარული, ისე სექციური სხდომები უნივერსიტეტის დიდ საკონფერენციო დარბაზში მიმდინარეობდა..

კონფერენციის გახსნა ივან ფრანკოს ლვოვის ეროვნულ უნივერსიტეტში. მარცხნიდან მარჯვნივ: უნივერსიტეტის რექტორი პროფ. ვ. პ. მელნიკი, უკრაინის განათლებისა და მეცნიერების მინისტრის მოადგილე პროფ. მ. ვ. სტრიხა, უკრაინის მეცნიერებათა ეროვნული აკადემიის ფიზიკის ინსტიტუტის დირექტორი აკად. ლ. პ. იაცენკო და ადგილობრივი საორგანიზაციო კომიტეტის ხელმძღვანელი დოქტ. ო. მ. ფესენკო

კონფერენცია უკრაინის ეროვნული ჰიმნის შესრულებით გაიხსნა

კონფერენციის თანაორგანიზატორები იყვნენ:

- უკრაინის მეცნიერებათა ეროვნული აკადემიის ფიზიკის ინსტიტუტი (უკრაინა),
- ივან ფრანკოს ლვოვის ეროვნული უნივერსიტეტი (უკრაინა),

- ეროვნული სამეცნიერო კვლევითი ცენტრის (ესკც) პიერ და მარია კიურების ინსტიტუტი (საფრანგეთი),
- ტურინის უნივერსიტეტი (იტალია),
- ტარტუს უნივერსიტეტი (ესტონეთი), და
- ორგანიზაცია “ევროპული პროფილები” (საბერძნეთი).

გახსნის პლენარული სესიის გარდა, ზეპირი მოხსენებები წარმოდგენილი იყო რვა სექციაში, რომელთა თემატიკაც საკუთარ თავში ნანოტექნოლოგიისა და ნანომასალათმცოდნეობის ყველა პრაქტიკულად მნიშვნელოვან პრობლებას მოიცავდა:

- ნანოობიექტების მიკროსკოპია,
- ნანოკომპოზიტები და ნანომასალები,
- ნანოდასტრუქტურებული ზედაპირები,
- ნანოოპტიკა და ფოტონიკა,
- ნანოპლაზმონიკა და ზედაპირის ფაქიზი სპექტროსკოპია,
- ნანოქიმია და ბიოტექნოლოგია,
- ნანომასშტაბის მოვლენების ფიზიკა, და
- ფიზიკურ-ქიმიური ნანომასალათმცოდნეობა.

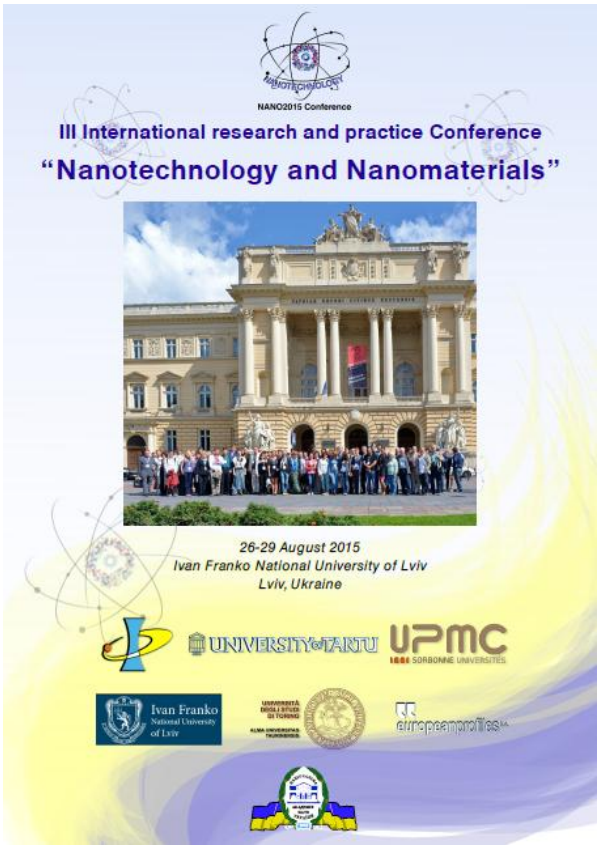

კონფერენციის პროგრამის გარეკანი

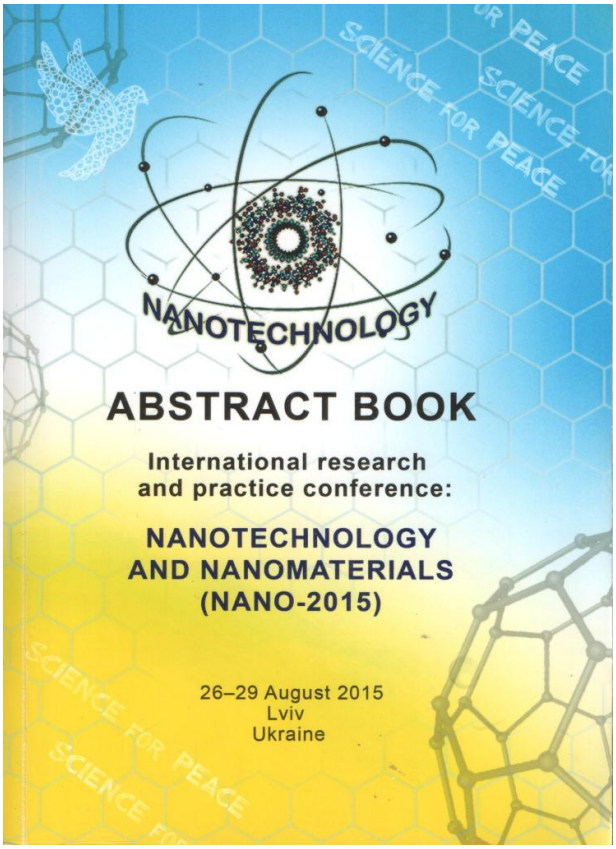

მოხსენებათა თეზისების კრებულის გარეკანი

ცალკე კრებულის სახით გამოიცა კონფერენციის მოხსენებათა თეზისების კრებული. ხოლო ყველა იმ მოხსენების სრული ტექსტი, რომელიც გაივლის ფეერ-რეცენზირების პროცედურას, გამოქვეყნდება ცნობილი საერთაშორისო სამეცნიერო გამომცემლობის Springer კონფერენციისადმი მიძღვნილი წიგნის თავის ანდა ამავე გამომცემლობის ნანომასშტაბური ობიექტებისა და მოვლენების გამოკვლევაზე სპეციალიზებული ჟურნალის Nano Scale Research Letters სტატიის სახით.

კონფერენციაზე მოხსენებები წარდგენილი ჰქონდათ ავტორებს მსოფლიოს 36 ქვეყნიდან (ავსტრია, ალჟირი, აშშ, ბელარუსი, ბელგია, ბულგარეთი, გერმანია, დიდი ბრიტანეთი, ესპანეთი, ესტონეთი, თურქეთი, ირანი, ისრაელი, იტალია, ლატვია, ლიტვა, მექსიკა, მოლდოვა, ნეპალი, ნიდერლანდები, პოლონეთი, რუმინეთი, რუსეთი, საბერძნეთი, სამხრეთ კორეა, საფრანგეთი, საქართველო, სლოვაკეთი, ტაივანი, უკრაინა, უნგრეთი, ფინეთი, შვედეთი, ჩეხეთი, ჩინეთი და ყაზახეთი). საბოლოო ჯამში 20-ზე მეტი ქვეყნის მონაწილეთა მიერ დაახლოებით 420 ზეპირი (პლენარული და სექციური) და სტენდური მოხსენება გაკეთდა. ღირსეულად იყო წარმოდგენილი საქართველოც.

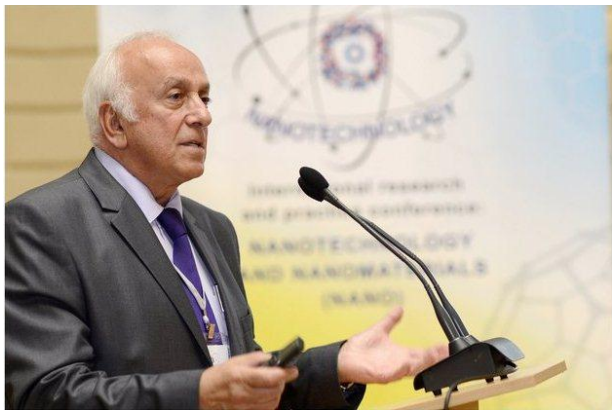


აკად. გ. კვესიტაძის გამოსვლა პლენარულ სხდომაზე

საქართველოს მეცნიერებათა ეროვნული აკადემიის პრეზიდენტი აკად. გიორგი კვესიტაძე გამოვიდა პლენარული მოხსენებით “მიკროორგანიზმებიდან მიღებული სტაბილური ენზიმები ბიოტექნოლოგიებისათვის”, რომელშიც დასაბუთებული იყო, რომ ამ ნივთიერებათა წარმოება ნანობიოტექნოლოგიის ახალ და უაღრესად პერსპექტულ მიმართულებას წარმოადგენს. მისმა მოხსენებამ ნანოტექნოლოგიის დამსწრე სპეციალიტთა შორის დიდი ინტერესი გამოიწვია.


პროფ. ლ. ჩხარტიშვილი გამოდის მოხსენებით

საქართველოს ტექნიკური უნივერსიტეტის საინჟინრო ფიზიკის დეპარტამენტის პროფესორმა ლევან ჩხარტიშვილმა სექციაში “ნანომასშტაბის მოვლენების ფიზიკა” წარმოადგინა მოხსენება თემაზე: “ელექტრული ველი ფენოვანი სტრუქტურის ბინარული ნაერთების ნანონაწილაკების ზედაპირთან”. ამ მოხსენებაში აღწერილ იქნა ახალი ნანომასშტაბური ეფექტი – სტატიკური ელექტრული ველის წარმოქმნა ნანონაწილაკების ზედაპირის მახლობლად,. ზედაპირული ატომური ფენის სპეციფიკური სტრუქტურული რეკონსტრუირების შედეგად.

არამარტო ზეპირი, არამედ პოსტერული სესიებიც აზრების განსაკუთრებით ინტენსიური გაცვლის რეჟიმში მიმდინარეობდა. სესიებს შორის შესვენებების დროს სხვადასხვა ქვეყნის მკვლევარებმა ბევრი საინტერესო შეხვედრა გამართეს ერთმანეთთან. მაგალითად, პროფ. ლ. ჩხარტიშვილი და დოქტორი ოლენა ლავრინენკო (უკრაინის მეცნიერებათა ეროვნული აკადემიის ფ. დ. ოვჩარენკოს ბიო-კოლოიდური ქიმიის ინსტიტუტი, კიევი, უკრაინა) შეთანხმდნენ სამომავლო თანამშრომლობაზე ბორის ფუძეზე ისეთი ნანომასალების შექმნაზე, რომლებიც კოროზიისაგან ფოლადების ეფექტური დაცვისათვის იქნებიან გამოსადეგი.

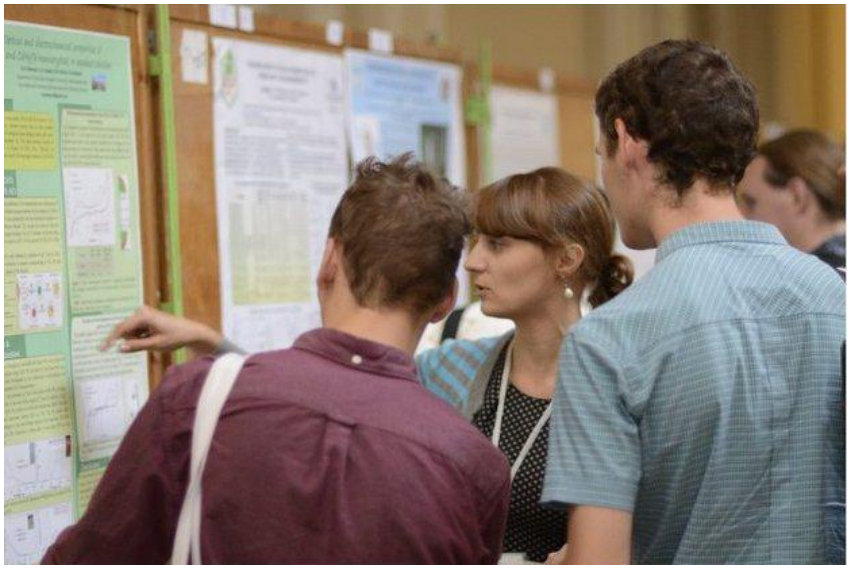

პოსტერულ სესიაზე

პროფ. ლ. ჩხარტიშვილი და დოქტ. ო. ლავრინენკო

კონფერნციის დღეებში ჯერ კიდევ გრძელდებოდ ომი აღმოსავლეთ უკრაინაში. ამიტომაც იყო, რომ იგრძნობოდა პოლიტიკური დაძაბულობა და ეკონომიკური ვარდნის შედეგები.

უნივერსიტეტის წინ მდებარე პარკში, ივან ფრანკოს მონუმენტთან, ერთობლივი ფოტოს გადაღებისას კონფერენციის მონაწილეებმა მშვიდობის მტრედები გაუშვეს

კონფერენციის ერთი დღე უკრაინის რადიკალური პარტიის მიტინგის ფონზე მიმდინარეობდა

მეფის ქანდაკება (ბრინჯაო), რომელიც ლვოვის ერთ-ერთ გზაჯვარედინზე დგას

კონფერენციის სოციალური პროგრამაც საინტერესო აღმოჩნდა მისი მონაწილეთათვის. ის ითვალისწინებდა: უკრაინული ხალხური სიმღერის ანსამბლის "ჩერიომუში" კონცერტს, ექსკურსიას ლვოვის ოპერის თეატრში, ექსკურსიას ხალხური არქიტექტურის მუზეუმში და სადილს სასტუმრო "დნისტროს" რესტორანში.

მონაწილეთა მეგობრულ სადილზე რესტორან "დნისტროში"

ანსამბლ "ჩერიომუშის" კონცერტზე

გუცულების სახლები ძველად

ხის ეკლესია ტყეში, გადმოტანილი მუზეუმში

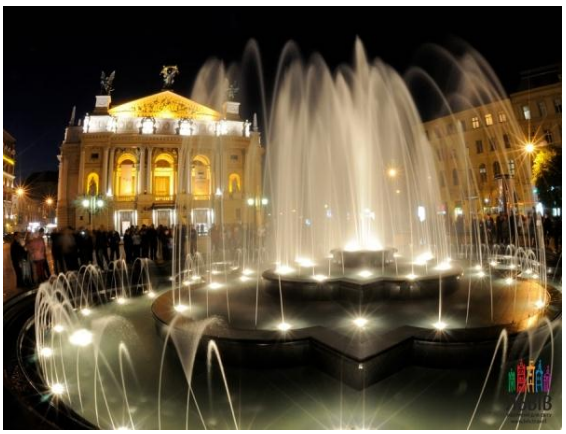

ლვოვის ოპერის თეატრის ექსტერიერი და ინერიერი

მონაწილეთა საერთო აზრით, მე-3 საერთაშორისო სამეცნიერო-პრაქტიკულმა კონფერენციამ “ნანოტექნოლოგიები და ნანომასალები” (2015 წლის 26 – 29 აგვისტო, ლვოვი, უკრაინა) მაღალ მეცნიერულ დონეზე ჩაიარა და კარგად იყო ორგანიზებული. დახურვის სხდომაზე გამოცხადდა, რომ მომავალ წელს კონფერენცია კვლავაც დასავლეთ უკრაინის რომელიმე ქალაქში გაიმართება.

ლევან ჩხარტიშვილი

2015 წლის 1 სექტემბერი

ISSN 1987-8826